EDITORIAL BOARD

Academic Press is an imprint of Elsevier
Linacre House, Jordan Hill, Oxford OX2 8DP, UK
32 Jamestown Road, London NW1 7BY, UK
225 Wyman Street, Waltham, MA 02451, USA
525 B Street, Suite 1900, San Diego, California 92101-4495, USA

First edition 2011

Library of Congress Cataloging-in-Publication Data
A catalog record for this book is available from the Library of Congress

British Library Cataloguing-in-Publication Data
A catalogue record for this book is available from the British Library

ISBN: 978-0-12-387720-8
ISSN: 1554-4516

For information on all Academic Press publications visit our website at www.elsevierdirect.com

Printed and bound in USA

11 12 13 10 9 8 7 6 5 4 3 2 1

Preface

Volume 14 of *Advances in Planar Lipid Bilayers and Liposomes* continues with the tradition of the past volumes and includes the invited chapters on the broad range of topics that are not limited to the planar lipid bilayers and liposomes only and in this way reflects the intensive development in the field of physics, biology, and chemistry of biological membranes and their micro- and nanostructures. This volume is dedicated to the statistical thermodynamics of adhesion points in supported membranes, the study of stability of exocytotic fusion pore, membrane instability of a planar lipid bilayer in an electric field, possible mechanisms of raft formation in cell membranes, computer simulations of multicomponent lipid bilayers and liposomes using coarse-grained models, thermal fluctuations of lipid vesicles, and interactions of biologically important molecules with lipid molecules. I would like to express my gratitude to the following authors contributing their chapters: Drs. P. Pieranski, R. Zorec, J. Jorgačevski, F. Ziebert, D. Lacoste, R. Reigada, K. Lindenberg, O. Farago, M. Wahab, H.J. Mogel, P. Schiller, M. Laradji, P.B. Sunil Kumar, F. Mravec, M. Klučáková, M. Pekar, V. Vitkova, C. Misbah, A.V. Popova, A.S. Andreeva, and their coauthors. Special thanks go to the member of Editorial Board of APLBL Prof. Sylvio May. I wish to express my gratitude and thanks to Ben Davie from Elsevier Office in London together with his coworkers from Elsevier's Chennai Office in India, Paul Prasad Chandramohan, Sunita Sundararajan, and Vijayaraj Purush. I am deeply grateful to my wife Veronika Kralj-Iglič for her constant support and help.

Aleš Iglič
Editor

Contributors

Atanaska S. Andreeva
Department of Condensed Matter Physics, Faculty of Physics, Sofia University, Sofia, Bulgaria

Oded Farago
Department of Biomedical Engineering and Ilse Katz Institute for Nanoscale Science and Technology, Ben-Gurion University of the Negev, Be'er Sheva, Israel

Ajda Flašker
Laboratory of Neuroendocrinology–Molecular Cell Physiology, Faculty of Medicine, University of Ljubljana, Ljubljana, Slovenia

Miha Fošnarič
Laboratory of Biophysics, Faculty of Electrical Engineering, University of Ljubljana, Ljubljana, Slovenia

Aleš Iglič
Laboratory of Biophysics, Faculty of Electrical Engineering, University of Ljubljana, Ljubljana, Slovenia

Jernej Jorgačevski
Laboratory of Neuroendocrinology–Molecular Cell Physiology, Faculty of Medicine, University of Ljubljana, and Celica, Biomedical Center, Tehnološki park 24, Ljubljana, Slovenia

Martina Klučáková
Centre for Materials Research, Faculty of Chemistry, Brno University of Technology, Brno, Czech Republic

Veronika Kralj-iglič
Laboratory of Clinical Biophysics, Faculty of Medicine, University of Ljubljana, Ljubljana, Slovenia

Marko Kreft
Laboratory of Neuroendocrinology–Molecular Cell Physiology, Faculty of Medicine, University of Ljubljana, and Celica, Biomedical Center, Tehnološki park 24, Ljubljana, Slovenia

D. Lacoste
Laboratoire de Physico-Chimie Théorique - UMR CNRS Gulliver 7083, ESPCI, 10 rue Vauquelin, Paris, France

Mohamed Laradji
Department of Physics, The University of Memphis, Memphis, Tennessee, USA

Katja Lindenberg
Department of Chemistry and Biochemistry 0340, and BioCircuits Institute, University of California San Diego, La Jolla, California, USA

H.-J. Mögel
TU-Freiberg, Institute of Physical Chemistry, Freiberg, Germany

Chaouqi Misbah
Laboratoire interdisciplinaire de physique (LiPHy), CNRS and Université J. Fourier Grenoble I, Saint Martin d'Hères, France

Filip Mravec
Centre for Materials Research, Faculty of Chemistry, Brno University of Technology, Brno, Czech Republic

Miloslav Pekař
Centre for Materials Research, Faculty of Chemistry, Brno University of Technology, Brno, Czech Republic

Pawel Pieranski
Laboratoire de Physique des Solides, UMR8502, Université Paris-Sud, Orsay, France

Antoaneta V. Popova
Institute of Biophysics and Biomedical Engineering, Bulgarian Academy of Sciences, Sofia, Bulgaria

Maja Potokar
Laboratory of Neuroendocrinology–Molecular Cell Physiology, Faculty of Medicine, University of Ljubljana, and Celica, Biomedical Center, Tehnološki park 24, Ljubljana, Slovenia

Ramon Reigada
Departament de Química Física, Universitat de Barcelona, Avda. Diagonal 647, Barcelona, Spain

Boštjan Rituper
Laboratory of Neuroendocrinology–Molecular Cell Physiology, Faculty of Medicine, University of Ljubljana, Ljubljana, Slovenia

P. Schiller
TU-Freiberg, Institute of Physical Chemistry, Freiberg, Germany

Matjaž Stenovec
Laboratory of Neuroendocrinology–Molecular Cell Physiology, Faculty of Medicine, University of Ljubljana, and Celica, Biomedical Center, Tehnološki park 24, Ljubljana, Slovenia

P.B. Sunil Kumar
Department of Physics, Indian Institute of Technology Madras, Chennai, India

Nina Vardjan
Laboratory of Neuroendocrinology–Molecular Cell Physiology, Faculty of Medicine, University of Ljubljana, and Celica, Biomedical Center, Tehnološki park 24, Ljubljana, Slovenia

Victoria Vitkova
Liquid Crystals Laboratory, Institute of Solid State Physics, Bulgarian Academy of Sciences, Sofia, Bulgaria

M. Wahab
TU-Freiberg, Institute of Physical Chemistry, Freiberg, Germany

F. Ziebert
Laboratoire de Physico-Chimie Théorique - UMR CNRS Gulliver 7083, ESPCI, 10 rue Vauquelin, Paris, France; Physikalisches Institut, Albert-Ludwigs-Universität, Freiburg, Germany, and Institut Charles Sadron, 23 rue du Loess, Strasbourg, France

Robert Zorec
Laboratory of Neuroendocrinology–Molecular Cell Physiology, Faculty of Medicine, University of Ljubljana, and Celica, Biomedical Center, Tehnološki park 24, Ljubljana, Slovenia

CHAPTER ONE

Faceting of Soft Crystals

Pawel Pieranski*

Contents

* Corresponding author. Tel.: +33-1-69157285; Fax: +33-1-69156086.
E-mail address: pawel.pieranski@u-psud.fr

Laboratoire de Physique des Solides, UMR8502, Université Paris-Sud, Orsay, France

Advances in Planar Lipid Bilayers and Liposomes, Volume 14
ISSN 1554-4516, DOI: 10.1016/B978-0-12-387720-8.00001-7

Abstract

The denomination "soft crystals" has been coined by Nozières *et al.* with the purpose to mark out a special class of liquid crystalline phases—thermotropic and lyotropic cubic mesophases. Their structure, being periodic in three dimensions, is crystalline. At the same time, it is also liquid because contents of huge unit cells are partially liquid. Due to such "liquid crystalline" structures, cubic mesophases have special physical properties such as the "soft elasticity." Here, we are dealing with another salient property of soft crystals—faceting of their interfaces. We focus on several topics such as (1) special methods allowing observation of faceted shapes, (2) description and classification of characteristic shapes seen as fingerprints of space group symmetries, (3) new phenomena occurring in faceted mesophases.

1. Introduction

1.1. Textures of Liquid Crystals

After the discovery of the phenomenon of "double melting" in esters of cholesterol by Friedrich Reinitzer [1], Otto Lehmann [2] used a polarizing microscope equipped with a heating stage for systematic observations of enigmatic textures occurring in many other substances. Puzzled by flows occurring in birefringent samples, he coined the oxymoron *liquid crystals* because in that time, the birefringence was considered as a fingerprint of crystalline structures. George Friedel [3] used the same optical technique and from his own observations of a few very characteristic textures he concluded that the Lehmann's liquid crystals are in fact new states of matter—*mesophases*—having molecular structures intermediate between

solid crystals and isotropic liquids. Friedel identified and named three such mesophases: nematic, smectic, and cholesteric.

Since this pioneer epoch, the Lehmann's technique was and still is widely used. Conjugated with X-ray crystallography and calorimetry, it was helpful for the discovery of dozens of other mesophases. In many cases, textures observed in a polarizing microscope are so specific that they are sufficient for identification of corresponding mesophases. For this purpose, textbooks on liquid crystal textures [4,5] containing their photographs, description, and explanation are very useful.

1.2. Cubic Mesophases: "True Liquid Crystals" or Soft Crystals

Among dozens of mesophases known today, cubic thermotropic and lyotropic mesophases are those for which the oxymoron "liquid crystals" seems to be the most adequate. Indeed, in special conditions, these cubic mesophases can show faceted shapes (see Figs. 1C and 2) similar to those of faceted minerals (or crystals in a common language) that are exposed in public or private collections. Our aim here will be:

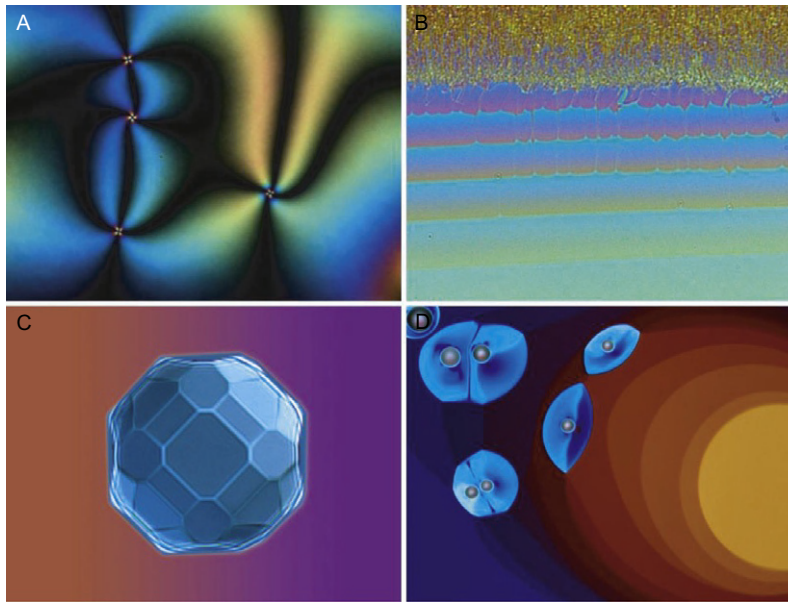

Figure 1 Textures of mesophases: (A) so-called schlieren texture of a nematic thin layer (6CB), (B) texture of a cholesteric mesophase in the Cano wedge, (C) monocristal of the *Im3m* lyotropic cubic phase (quaternary system Phytantriol/DSPG/Ethanol/water). (D) Inclusions of the inverted micellar phase in a free standing film of the lamellar phase (binary system C12EO6/water).

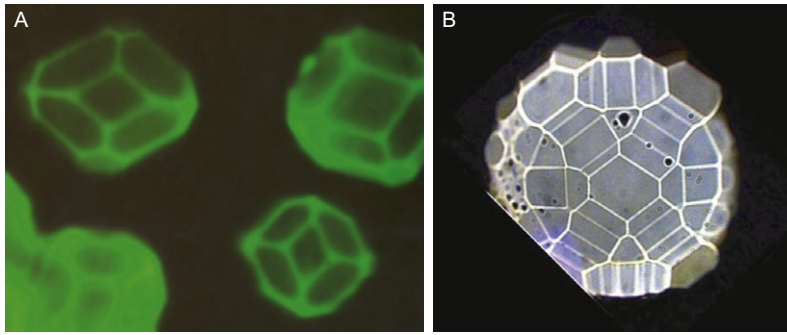

Figure 2 Thermotropic soft crystals: (A) monocrystals of the Blue Phase I surrounded by the isotropic phase observed in a reflecting microscope, (B) *Ia3d*-in-air monocrystal observed in an optical microscope in transmitted light (from Ref. [6]).

1. Describe methods tailored for observations of faceted shapes of cubic mesophases
2. Describe and classify observed shapes
3. Outline new phenomena occurring in faceted mesophases

Before that, let us consider faceting of mesophases from a more general point of view of fundamental concepts in physics.

1.3. Concepts Related to Symmetry and Topology

Among fundamental concepts related to symmetry and topology [7], those of long range order, order parameter, and topological defects are central in condensed matter physics dealing with solid crystals, superfluids, superconductors, or liquid crystals [8]. Within this framework of fundamental concepts, cubic mesophases are similar to solid crystals because they share with them symmetries described by space groups such as:

- $I4_132$ and $P4_232$ for thermotropic Blue Phases [9]
- *Ia3d* for a thermotropic cubic phase [6,10–12]
- *Ia3d*, *Im3m*, *Pn3m*, or *Pm3n* for lyotropic cubic phases [13–16]

Essentially for this symmetry reason, Blue Phases and lyotropic cubic phases are elastic [17–19], can contain mobile dislocations [20] or grain boundaries and their interfaces with isotropic phases can be faceted like interfaces of solid crystals with vapor or liquid phases. In order to emphasize this similarity with solid crystals, Nozières, Balibar, and Pistolesi who worked on the theory of faceting [21] called faceted mesophases *soft crystals*.

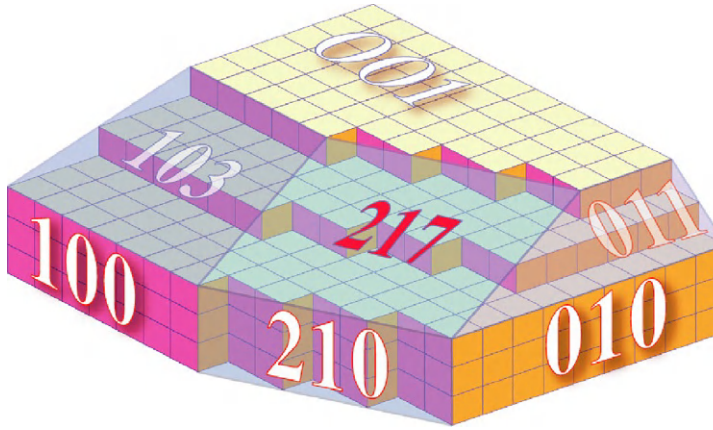

Figure 3 Haüy-like model of a faceted cubic crystal.

1.4. Crystallography without X-rays

Let us remind that this was the astonishing geometrical perfection of faceted shapes of solid crystals such as naturally occurring minerals or snow flakes that lead Haüy to considerations about periodic stackings of hypothetical ultimately small pieces of matter called atoms or molecules (Fig. 3). Subsequently, all possible types of such crystalline structures were classified with help of mathematicians in the framework of symmetry groups—14 Bravais lattices, 32 point groups and 230 space groups. This classification, initiated by observations of shapes of facets and measurements of angles between facets occurring on crystal shapes, was achieved prior to experiments of Bragg and von Laue that gave an experimental evidence for periodic structures of crystals and opened the door to the modern X-ray crystallography. One can find a very detailed discussion of space group and of corresponding crystal shapes in another generic writing of Georges Friedel—his "Leçons de cristallographie" [22]—as well as in a more recent book of F.C. Phillips [23].

1.5. Facets and Bragg Spots

The occurrence of facets on crystal shapes and of Bragg spots on diffraction diagrams are intimately related in the reciprocal space. Indeed, Bragg spots and facets are both indexed by Miller indices (*hkl*)—coordinates of nods of the reciprocal lattice:

$$\mathbf{q} = h\mathbf{a}^* + k\mathbf{b}^* + l\mathbf{c}^*, \tag{1}$$

which are nothing else but wave vectors of components of Fourier series

$$\rho(\mathbf{r}) = \sum \rho_{\mathbf{q}} e^{i\mathbf{q}\cdot\mathbf{r}} \tag{2}$$

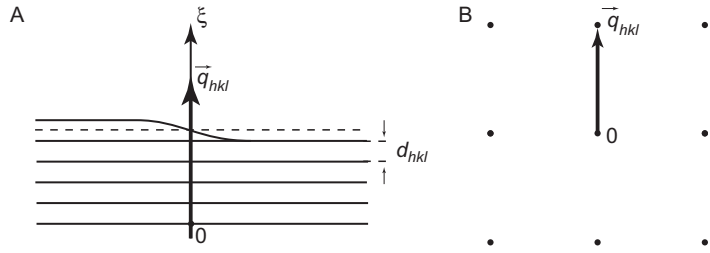

Figure 4 Selection rules for Bragg reflections and facets: (A) elementary step of height d_{hkl} on the (hkl) facet, (B) (hkl) node in the reciprocal lattice.

into which any scalar function $\rho(\mathbf{r})$ can be decomposed. In the context of X-ray diffraction, $\rho(\mathbf{r})$ represents the electronic density. In the theory of faceting, $\rho(\mathbf{r})$ would correspond to the pinning potential involved in formation of facets [24]. When a Fourier component $\rho_{\mathbf{q}}$ is nonzero, then, on one hand, there is a stationary electronic density wave with wavevector $\mathbf{q}$ which gives rise to a specific Bragg reflection (Fig. 4B). On the other hand, the component $\rho_{\mathbf{q}}$ of the pinning potential leads to the formation of a facet perpendicular to $\mathbf{q}$ (Fig. 4A). Inversely, when the amplitude $\rho_{\mathbf{q}}$ of some Fourier components vanishes for some symmetry reasons, then the corresponding (hkl) Bragg reflections and facets are forbidden. In such a case, it can happen that the "next" Fourier component with indices ($2h$,$2k$,$2l$) can be allowed. On the diffraction diagram, it is identified as a specific ($2h$,$2k$,$2l$) Bragg spot, however the corresponding ($2h$,$2k$,$2l$) facet has exactly the same orientation on the crystal surface as it would have the forbidden (h,k,l) facet. In order to index correctly such a facet, the height of steps occurring on it is helpful because it is given by the interplanar distance

$$d_{hkl} = \frac{2\pi}{|\mathbf{q}|}. \tag{3}$$

When it is impossible to measure this height, the knowledge of the facets size is helpful because it decreases with d_{hkl}. We will return to this so-called Donnay–Harker rule later.

1.6. Structures of Solid and Soft Crystals

The superposition of all nonzero density waves (i.e., components) in the Fourier series [Eq. (2)] leads to structures that share two common features:

1. They are all made of identical elementary unit cells which are parallelepipeds spanned on three base vectors **a**, **b**, and **c**

2. These unit cells are repeated by translations in three dimensions accordingly to the Bravais lattice which is defined as a set of translation vectors given by

$$\mathbf{r} = l\mathbf{a} + m\mathbf{b} + n\mathbf{c}, \tag{4}$$

where **a**, **b**, and **c** are base vectors and l, m, n are integers.

Now, the contents of unit cells is different is classical solid crystals and in soft crystals (Fig. 5).

1.6.1. Solid Crystals

In solid crystals, unit cells are relatively small and contain always *fixed numbers of atoms or molecules whose* (x,y,z) *positions* (and generally orientations) *inside unit cells are fixed too*. This means that in classical solid crystals there is a *long range order of positions* of atoms or molecules; when positions of atoms or molecules in the unit cell located at origin O are known then position of all other equivalent atoms or molecules are known with accuracy better than dimensions of unit cells no matter how far from the origin they are. Among other properties, the elasticity of solid crystals is a consequence of this long range order.

1.6.2. Soft Crystals

In soft crystals, unit cells are much larger and their contents is much more fuzzy:

1. They contain a large and *variable* number of molecules.
2. These swarms of molecules are organized into *partially liquid patterns* which are characterized, beside their symmetry, also by *topological* features.

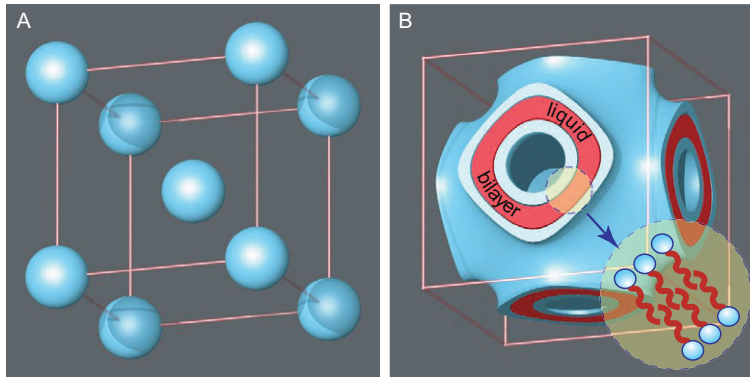

Figure 5 Solid and soft crystals: (A) bcc structure of iron, (B) *Pn3m* structure of the inverted cubic lyotropic phase Im3m.

2. Experimental Methods

2.1. Variety of Cubic/Isotropic Interfaces in Lyotropic Systems

In lyotropic systems, the variety of phases occurring as a function of temperature and composition in at least binary mixtures is plethoric [13,14]. Moreover, from the Gibbs phase rule results that coexistence of two phases in lyotropic systems is ubiquitous. In cases when at least one of the two coexisting phases is not isotropic, the interfacial tension is anisotropic. Theoretically, the equilibrium shapes of such an anisotropic interface given by the Wulff construction should be not spherical [24]. Here, we focus on the subset of cubic/isotropic interfaces which is wide on its own because several cubic lyotropic phases of different symmetries and/or topologies can coexist with at least four isotropic phases: the direct and inverted micellar phases $L1$ and $L2$, the sponge phase $L3$, and the water vapor (see Fig. 6). As we will see below, experiments have shown that only cubic/vapor and cubic/$L1$ interfaces are faceted.

The discovery of faceting in lyotropic systems was serendipitous, that is, made in experiments which were not tailored for this purpose. To our knowledge, first observation of faceting of a cubic/$L1$ interface has been made by Winsor [25]. Later, Sotta [26] observed faceted air bubbles included in the bulk $Ia3d$ phase of C12EO6/water system. Our own interest for faceting of soft crystals began with studies of thermotropic Blue Phases [9] (see Fig. 2A). Later, when working with free-standing films (surrounded by a humid atmosphere) of the lamellar phase of the C12EO6/water system, we have discovered accidentally the devil's staircase-type faceting of the $Ia3d$/vapor interface [27]. Subsequently, we have developed new setups specially tailored for experiments on faceting in lyotropic system. We describe them below.

2.2. Hygroscopic Methods for Studies of Cubic/Vapor Interfaces

The setup depicted schematically in Fig. 7 can be qualified as a hygroscope of third generation. In the very first system used for studies the devil's staircase faceting of $Ia3d$/vapor interface [27,28], humidity control was achieved by mixing dry and 100% humid gas fluxes. Subsequent experiments with C12EO6, monoolein, phytantriol, DTACl, and DDMAS have shown however that cubic phases occur generally in the humidity range between 95% and 100% where this system of humidity control is not the most accurate. For this reason, the principle of humidity control was changed in the second version of the hygroscopic setup [29]: the sample was enclosed in an almost tight metallic cell containing a small reservoir of

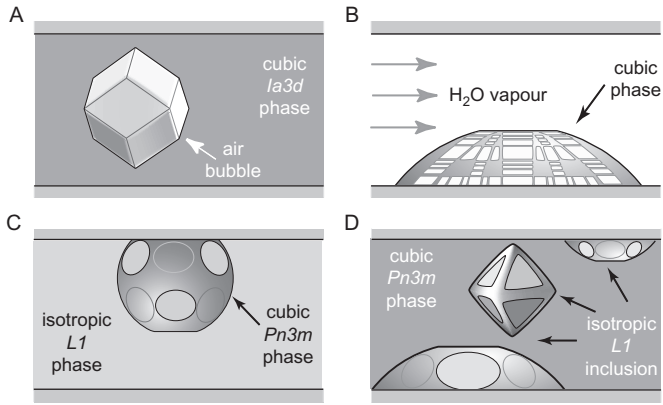

Figure 6 Conditions for observation of the faceting in lyotropic system: (A) air bubble in a cubic phase [26], (B) cubic phase surrounded by water vapor, (C) cubic phase surrounded by *L*1 phase in systems with solubility gap, (D) *L*1 inclusions in a cubic phase.

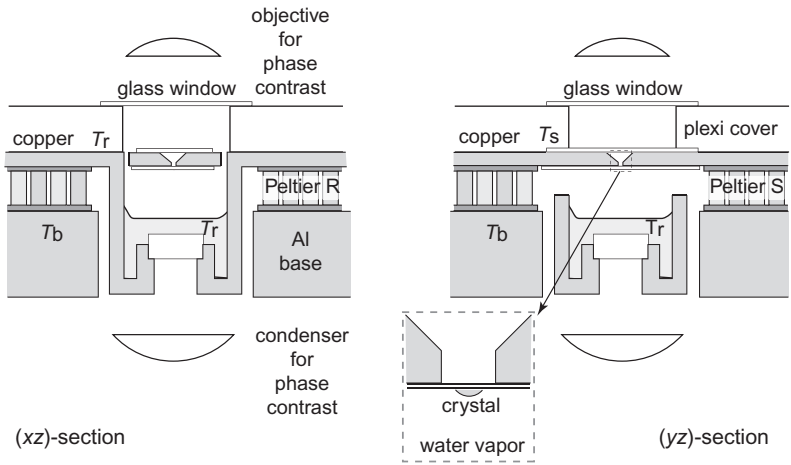

Figure 7 Experimental setup developed for hygroscopic studies of cubic/vapor interfaces. (Reproduced from Ref. [20] with kind permission of J. Phys. Condens. Matter.)

water and the relative humidity at the sample level was a function of the temperature difference between water, in good thermal contact with the cell, and the sample whose temperature was regulated independently. The same principle is used in the third generation hygroscopic system shown here in Fig. 7. It consists of three parts:

1. Large aluminum base of thickness 1.5 cm. Its temperature T_b is regulated by a circulation from a water bath.

2. Reservoir of water made of copper. The (xz)-section shows that it is supported by two Peltier elements that regulate its temperature T_r.
3. Sample holder made of copper. The (yz)-section shows that it is supported by a second pair of Peltier elements that regulate its temperature T_s.

In practice, temperatures T_r and T_s are regulated with accuracy better than 0.01 °C. As explained in Ref. [29], the relative humidity H at sample level is given by the formula

$$H(T_s, T_{res}) = \frac{p_s(T_r)}{p_s(T_s)} \times 100\%, \tag{5}$$

where $p_s(T)$ expresses dependence of the saturated vapor pressure at temperature T. Knowing the accuracy $\delta T = \pm 0.01$ °C of temperature regulation, the corresponding accuracy of the humidity control is about $\delta H = \pm 0.05\%$. Let us note that the sample holder has a smaller thermal inertia than the water reservoir. For this reason, in order to change the humidity, it is more convenient to keep the temperature T_r of the water reservoir constant and to vary the temperature $T_s = T_r + \Delta T$ of the sample holder. As a consequence, the T-vs.-H phase diagram is explored along slightly oblique paths such as those indicated by dashed lines in Fig. 8. For each path two parameters are pertinent: $T_r = \text{const}$ and $\Delta T = T_s - T_r$. The second major improvement in this new hygroscopic setup consisted in using the phase contrast optical set: a matched condenser–objective pair from a biological microscope. As the light beam from the condenser passes through the layer of water, the capillarity-induced curvature of the water surface can perturb the condenser–objective matching. For this reason, the diameter of the water reservoir was made large enough ($\approx$3 cm) to keep water surface flat. Images have been taken with a CCD camera.

2.3. The Isoplethal Method for Studies of Cubic/$L1$ Interfaces

For studies of faceting at cubic/$L1$ interfaces, we developed the experimental setup shown in Fig. 9 [31,32]. Here, the sample—*Pn*3*m* or *Im*3*m* crystals surrounded by the $L1$ phase—is located in a flat glass capillary of section 5 × 0.2 mm. The capillary is supported by two Peltier elements and by this means its temperature is regulated with accuracy of 0.01 °C. Ends of the capillary are connected to flexible tubes which are immersed in reservoirs A and B containing, for example, water or water/ethanol mixture. The reservoir A can be lifted or lowered with respect to B by means of a micrometer translation stage. By principle of communicating vessels, the composition of the $L1$ phase surrounding *Pn*3*m* or *Im*3*m* crystals can be changed. In the last version of this setup, this composition is regulated more

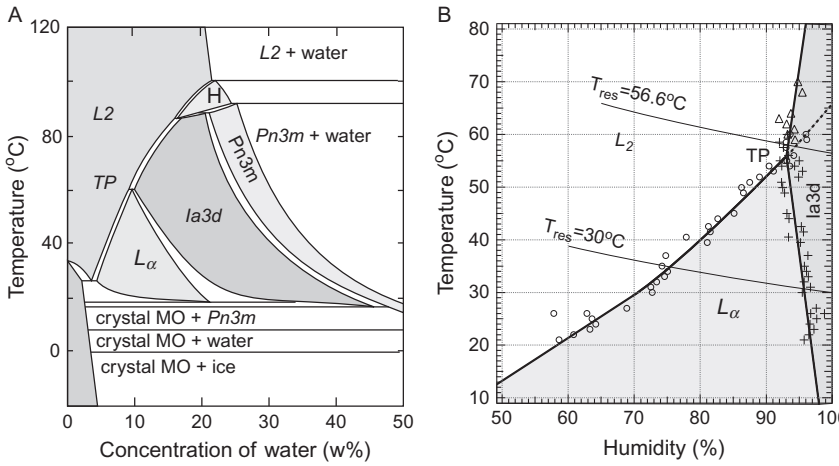

Figure 8 Principle of the hygroscopic method illustrated on the example of the monoolein/water system. (A) Classical *Temperature vs. Concentration* phase diagram from Qiu and Caffrey [30]. (B) Temperature vs. humidity phase diagram obtained by the hygroscopic method [29]. Dashed lines correspond to trajectories followed when the temperature T_r of the water reservoir is kept fixed and the temperature of the sample is varied. Nuclation of *Ia3d* monocrystals from *L2* droplets occurs when *L2* → *Ia3d* transition is crossed along an isothermal path a few degrees above triple point TP. (Reproduced from Ref. [20] with kind permission of J. Phys. Condens. Matter. Collaboration with J. Grenier.)

accurately by mixing fluxes from two motorized syringes containing water/ethanol mixtures of different concentrations.

Like in the hygroscopic setup, observation are made by means of a microscope objective forming the image of the sample directly on the CCD sensor of a digital camera. The preparation of samples has been described in details in Refs. [31–33]).

3. Faceting of Cubic/Vapor Interfaces

3.1. Direct *Ia3d* Cubic Phase (C12EO6)

3.1.1. Structure

The structure of the direct *Ia3d* cubic phase is represented schematically in Fig. 10. It consists of two distinct but entangled scaffoldings made of surfactant and immersed in water. These scaffoldings are made of cylinders connected three by three as shown in the insert of Fig. 10. One can say that this structure is intermediate between structures of the lamellar and hexagonal phases because, on one hand, it is made of rods like the hexagonal phase

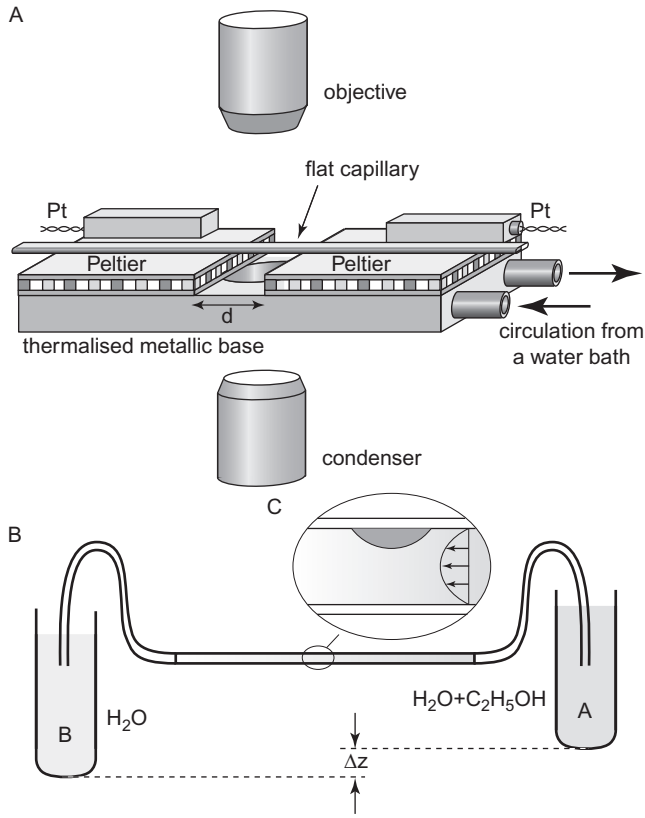

Figure 9 Experimental setup for studies of cubic/*L*1 interfaces. (Collaboration with M. Bouchih, N. Ginestet, and S. Popa-Nita.)

*H*1, and, on the other hand, each junction of three rods can be seen as a small patch of the lamellar phase Lα. Therefore in the phase sequence of, for example, C12EO6/water system [see Eq. (6)] *Ia*3*d* phase is intermediate between *H*1 and Lα phases. Such a structure corresponds perfectly to the definition of soft (or fuzzy) crystals given in Section 1.6.2; it is a periodic stack of cubic unit cells whose contents is partially liquid. Indeed, molecules of surfactant can diffuse freely inside each of the two scaffolding while water molecules can also diffuse freely in the space between the two scaffoldings.

3.1.2. Devil's Staircase-Type Faceting

It was surprising to find that such fuzzy crystals display the so-called devil's staircase faceting [27,28] expected for solid crystals at low temperatures [24]. As an example we show in Fig. 11A an image of a small monocrystal of the

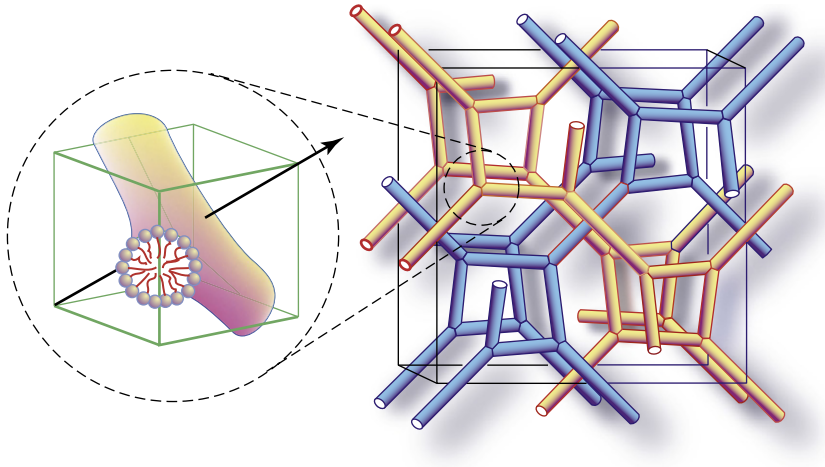

Figure 10 Structure of the *Ia3d* direct cubic phase.

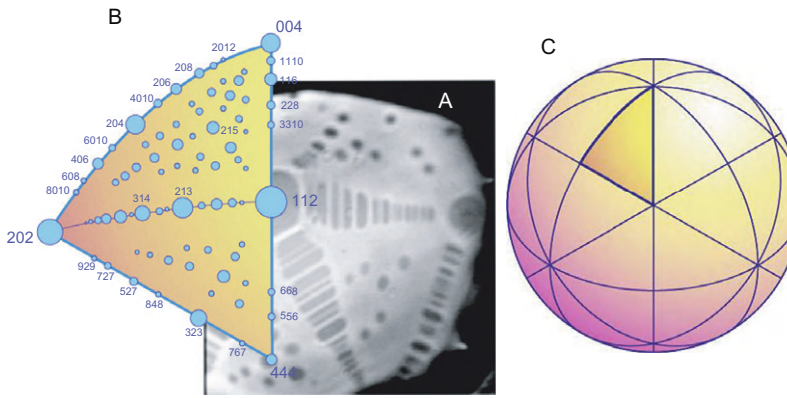

Figure 11 Devil's staircase-type faceting of the *Ia3d*/vapor interface in the C12EO6 system: (A) Image of a small *Ia3d* monocrystal located on a glass substrate, (B) indexing of facets on the elementary triangular patch, (C) surface of spherical *Ia3d* crystal covered by triangular patches.

Ia3d direct cubic phase in C12EO6/water system. We will see below that such a *rich* faceting occurs also in other lyotropic systems.

In Fig. 11A, the crystal has the global shape of a spherical cup whose diameter and contact angle at the base are $D \approx 1$ *mm* and $\theta \approx 30°$, respectively (see Fig. 6B). It was obtained by humidity processing (see below) of a small droplet of the nonionic surfactant C12EO6 deposited on a glass

substrate. When submitted to an atmosphere of increasing humidity at room temperature, the droplet undergoes the following sequence phase transitions.

$$L2 - 85\% - L\alpha - 95\% - Ia3d - 98\% - H1 - 100\% - L1. \qquad (6)$$

The transition from the initial $L2$ (inverted micellar) phase to the Lα (lamellar) phase takes place at $H \approx 85\%$ without any metastability, since the lamellar phase wets the micellar phase. After this transition into the lamellar phase, the initial spherical shape of the droplet changes: it acquires one facet on its top. Orientation of this facet unveils the texture of the drop: a stack of bilayers parallel the glass substrate.

The next transition from the lameller to the cubic phase $Ia3d$ is significantly metastable and occurs upon a sufficient supersaturation $\Delta H \approx 1\%$. Immediately after this phase transition $L\alpha \rightarrow Ia3d$, the surface of the drop becomes very irregular and one or two days of annealing are necessary to obtain the faceting shown in Fig. 11A.

Only a small patch of the whole crystal surface is visible here (other images can be found in Ref. [27,28]). The most striking feature of this photograph is an astonishing variety of facets with different Miller indices. All these facets form a highly symmetric pattern very similar to Laue diagrams. For indexing of facets, the simulation of faceting based on the Donnay–Harker rule shown in Fig. 11B is helpful. It shows one of the 48 identical elementary patches, related by the O_h point symmetry, covering the surface of a spherical crystal (see Fig. 11C). In this heuristic diagram, the diameters of circles have been set proportional to $d_{hkl} = a/\sqrt{h^2 + k^2 + l^2}$ since the occurrence and relative extension of facets is directly related to the interplanar distances d_{hkl} according to the elementary Donnay–Harker rule [23]. For the same reason, the general crystallographic selection rules for the $Ia3d$ symmetry were applied, so that only those facets were drawn for which the four following relations are satisfied: (1) $h + k + l = 2n$, (2) $hk0$: $h,k = 2n$, (3) hhl: $2h + l = 4n$, (4) $h00$: $h = 4n$. Using this method of indexing, about 60 facets with different Miller indices have been identified.

3.1.3. Fingerprints

In conclusion of this section devoted to the faceting of $Ia3d$ direct crystals, three fingerprint-like features can be emphasized:

- In agreement with the Donnay–Harker rule, the most prominent facets at the $Ia3d$/vapor interface are of (211) and (220) type.
- In most cases, these facets are located on the top of crystals which means that $Ia3d$ crystals are oriented with (211) or (220) reticular planes parallel to the glass or mica substrate.

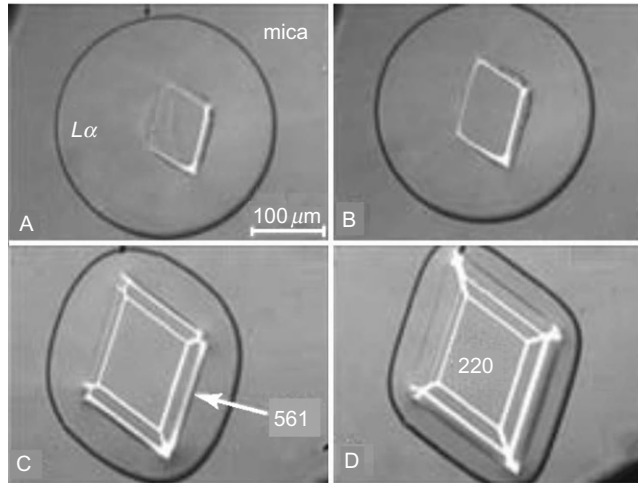

Figure 12 Slow growth of a *Ia3d* crystal from the lamellar phase.

- During a slow growth shown in Fig. 12, the orientation (220)/bilayers is inherited from the lamellar phase.

3.2. Inverted *Ia3d* Cubic Phase (Monoolein and Phytantriol)

3.2.1. Structure

The phase diagram temperature versus water concentration of the monoolein/water system [30] is shown in Fig. 8A. Due to a relatively small hydrophilic head of the monoolein molecule, the cubic phases *Ia3d* and *Pn3m* present here are inverted. In both phases, surfactant molecules are assembled into a continuous bilayer having shapes of infinite periodic minimal surfaces—G of symmetry *Ia3d* and D of symmetry *Pn3m*. In the *Ia3d* phase, the G surface divides the space into two entangled labyrinths having the topology of two scaffoldings made of surfactant in the direct *Ia3d* phase (see Fig. 10). Roughly speaking, water/surfactant patterns in *Ia3d* phases of monoolein/water and C12EO6/water systems are inverted.

3.2.2. Facet by Facet Surface Melting at the *Ia3d*/Vapor Interface

The phase diagram of monoolein is very interesting from the fundamental point of view of faceting's theory. In particular, it allows to shed new light on the problem of the *anisotropic melting of crystal surfaces* discussed by Nozières in Ref. [34]. Indeed, upon decreasing humidity, the *Ia3d* phase can be melted into the isotropic *L2* phase. It is therefore possible to see how the devil's staircase type faceting is modified when the *Ia3d* → *L2* transition

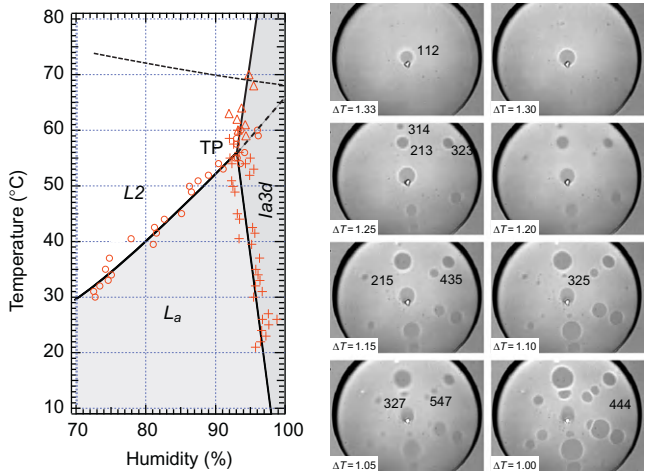

Figure 13 Facet by facet anisotropic melting at the *Ia3d*/vapor interface in the monoolein/water system. When T (in degree Celsius) increases (from the bottom to the top), the distance in terms of humidity from the *Ia3d*/*L2* transition decreases. As a consequence, (*hkl*) sets of facets disappear progressively. (Reproduced from [35] with kind permission of J. Phys. Condens. Matter. Collaboration with J. Grenier.)

is approached. Hygroscopic studies described in Ref. [29] have shown that the number of different facets types present at the *Ia3d*/vapor interface is decreasing as a function of the distance from the *Ia3d* → *L2* transition. As an example we show in Fig. 13 a series of pictures taken at different values of the temperature difference $\Delta T = T_s - T_r$ between the sample and the water reservoir.

The same behavior has also been observed in the phytantriol/water system whose phase diagram is very similar to that of monoolein. It is illustrated by two pictures in Fig. 14A and C taken at different distances from the *Ia3d* → *L2* transition. Simulations of faceting based on the Donnay–Harker rule shown in Fig. 14B and D allow indexing of facets visible on the surface of the *Ia3d* crystal.

3.3. Micellar *Pm3n* Cubic Phase (DTACl)

The devil's staircase-type faceting has also been observed by hygroscopy at the *Pm3n*/vapor interface in the DTACl/water system whose phase diagram has been established by Balmbra *et al.* [36].

3.3.1. Structure

The contents of the unit cell of the *Pm3n* micellar phase is shown in Fig. 15A. It is similar to the structure of Cr_3Si crystals in which atoms of silicon are located at vertices and in the center of the unit cell while those of

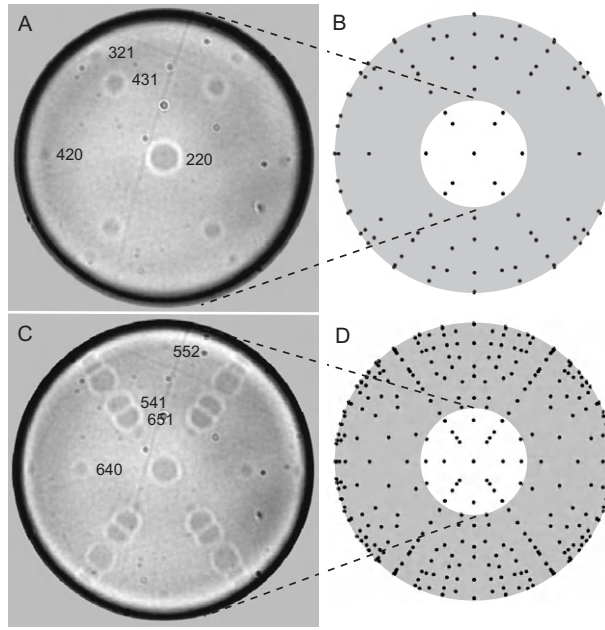

Figure 14 Indexing of facets at the *Ia3d*/vapor interface in the phytantriol/water system. (Collaboration with P. Faye and R. Sheska.)

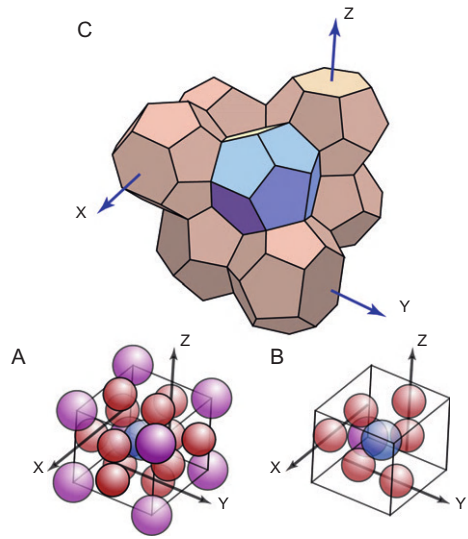

Figure 15 Structures having the *Pm3n* symmetry: (A) and (B) positions of micels (respectively Cr and Si atoms) in the unit cell of the *Pm3n* cubic lyotropic phase (respectively Cr_3Si crystal), (C) A15 minimal foam structure obtained from (B) by inflation of micels [37].

chrome are located two by two on faces of the unit cell. In the cubic micellar phase, micels occupy positions of Cr and Si atoms. As we will see later, it is important to note that the so-called A15 minimal froth invented by Weaire and Phelan (Fig. 15C) has also this *Pm*3*n* symmetry.

3.3.2. Faceting

As expected, hygroscopic experiments have shown that the faceting of the *Pm*3*n*/vapor interface is very rich. The obvious fourfold symmetry of the constellations of facets in Fig. 16A leads immediately to the conclusion that Miller indices of the central facet are (200). Indexing of other facets seems more difficult. Fortunately, simulation of faceting in Fig. 16B based on selection rules for the *Pm*3*n* symmetry (*hkl:* $l = 2n$, *h*00: $h = 2n$) and on the Donnay–Harker rule is helpful. Indexing of the central facet in Fig. 16A is less obvious but the simulation in Fig. 16B leads to conclusion that Miller indices of this facet are (211).

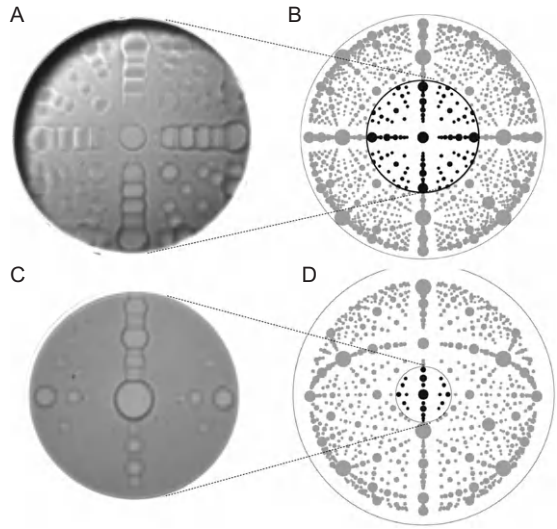

Figure 16 Devil's staircase-type faceting at *Pm*3*n*/vapor interface of the DTACl/water system (for the phase diagram see Fig. 17). (A) The photograph shows a *Pm*3*n* crystal obtained from a droplet of the *L*2 micellar phase at $T = 70\ ^{\circ}C$. The crystal is obviously oriented with its fourfold [100] axis orthogonal to the mica substrate. (B) Simulation of faceting of a spherical *Pm*3*n* crystal; only small part of the crystal surface is visible in A. (C) *Pm*3*n* crystal oriented with (211) planes parallel to the mica substrate. (D) Corresponding simulation of faceting.

3.4. RHCP Micellar Phase

3.4.1. Experimental Surprise: An Ephemeral Phase

Hygroscopic experiments with the DTACl/water system lead to the discovery of a new phase [35]. On the basis of the phase diagram established by Balmbra *et al.* [36]) the *Pm*3*n* phase should be obtained from the micellar phase *L*1 upon decreasing humidity by a direct phase transition. Hygroscopic experiments have shown, however, that below 70 °C, the transition from the *L*1 to the *Pm*3*n* phase is not direct. Indeed, in Fig. 17, pictures A and D correspond, as expected, to the *L*1 and *Pm*3*n* phases but the texture of the sample in picture B is abnormal and clearly proves the existence of a new phase. This new phase has been called *ephemeral* for three reasons:

1. Its humidity range is very narrow.
2. It does not appear on the way back from *Pm*3*n* to *L*1.
3. It disappears completely in the presence of impurities.

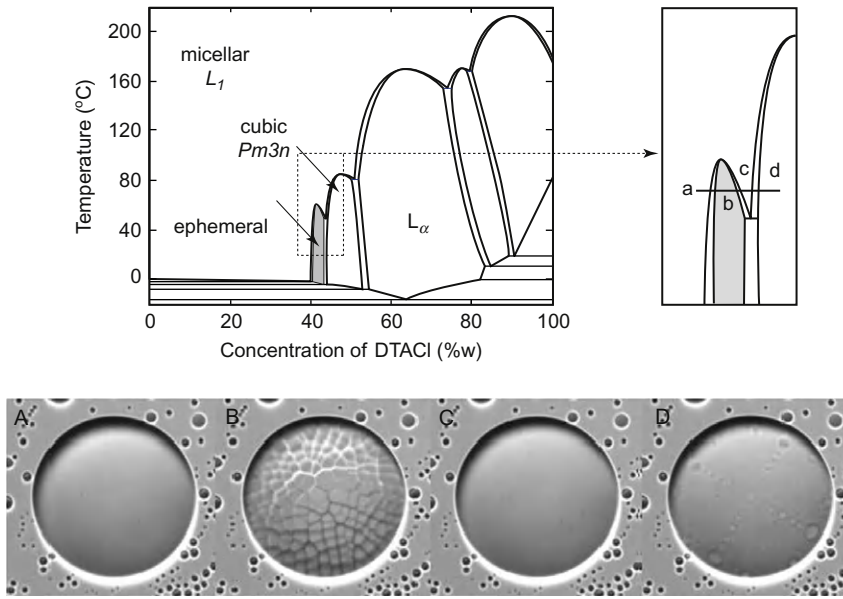

Figure 17 Experimental evidence for the ephemeral phase. The phase diagram of the DTACl/water mixture, established by Balmbra *et al.* [36] has been completed here by the addition of the ephemeral phase. The series of photographs (A)–(D) shows indeed that at $T = 60\ ^\circ C$, the transition from the micellar *L*1 phase to the cubic *Pm*3*n* phase is mediated by another unknown phase. (Reproduced from Ref. [35] with kind permission of J. Phys. Condens. Matter.)

What can be inferred about this new phase from the shape of its interface with the surrounding humid atmosphere? The polycrystalline initial texture of this new phase in Fig. 17B is useless. However, after a long enough annealing illustrated by the series of four images in Fig. 18 an enigmatic constellation of facets finally shows up (see Fig. 18D). This constellation has three remarkable features:

1. It has a sixfold symmetry.
2. Facets are distributed exclusively in six ranges surrounding the central facet.
3. Everywhere else, the crystal surface is rough.

Such an inhomogeneous distribution of facets suggests that the distribution of Bragg spots in the reciprocal space of the ephemeral phase should be very inhomogeneous as well. This feature is reminiscent of X-ray diffraction experiments with the so-called random hexagonal close packed (rhcp) structure in colloidal systems [38] where 2D hexagonal crystal planes form a random stack. Due to the disorder, two-third of the hcp Bragg spots are smeared out into diffuse rods while the other Bragg spots are preserved. In the DTACl/water system, the $L1$ and $Pm3n$ phases are micellar.

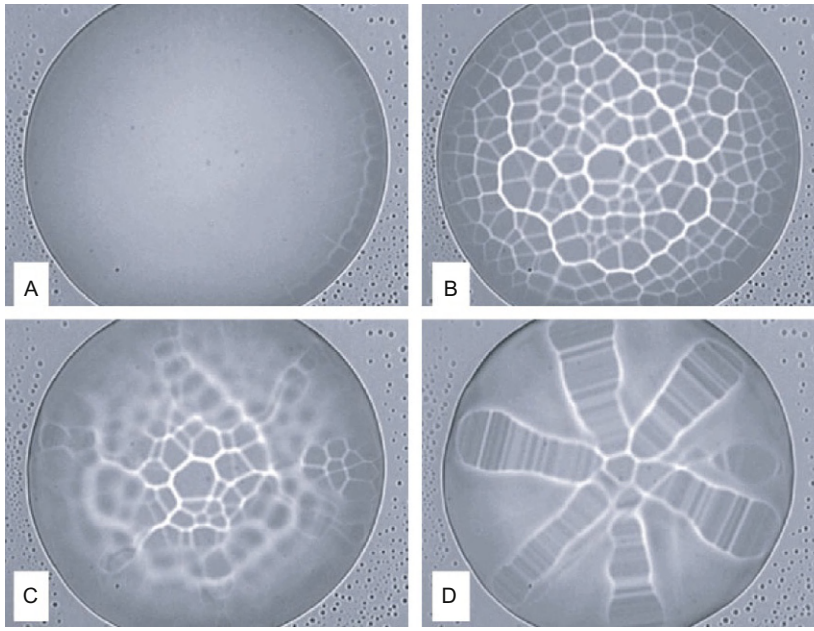

Figure 18 Faceting of the ephemeral phase in the DTACl/water system: (A) beginning of the $L1 \rightarrow$ rhcp phase transition, (B) mosaic polycrystalline structure, (C) beginning of the annealing, (D) faceting after annealing.

The intermediate ephemeral phase should, therefore, be micellar as well. By analogy with colloidal crystals, the order of micelles could be rhcp.

This hypothesis is reinforced by the theoretical predictions of Ziherl and Kamien [39] concerning the phase sequence in a system of soft spheres such as polymer or surfactant micelles. Following this theory, when the density increases, the phase sequence can be: liquid → close packed(fcc, hcp, or rhcp) → bcc → *Pm*3*n*.

4. Faceting of Cubic/*L*1 Interfaces

4.1. Rich and Poor Faceting of Soft Crystals

Following to Nozières *et al.* [21], the rich faceting of cubic/vapor interfaces is due to the conjunction of a large size of unit cells (≈10 nm) with a relatively large tension at the cubic/vapor interface (≈25 dyn/cm). The lyotropic systems provide us with an opportunity to test this theory because the cubic/isotropic interfacial tension can be varied in a large extent. Indeed, as emphasized already in Section 2.1, cubic phases can coexist also with isotropic liquid phases *L*1, *L*2, or *L*3 and in such cases the interfacial tension is expected to be much smaller.

4.2. *Pn*3*m*/*L*1 Interface

4.2.1. Discovery of Faceting

The discovery of faceting at the *Pn*3*m*/*L*1 interface was made by Lynch *et al.* [40] who established the phase diagram of the binary system C12EO2 (see Fig. 19A). Here, the inverted *Pn*3*m* phase can coexist with all three phases *L*1, *L*2, and *L*3. Lynch *et al.* observed that upon a rapid heating of the *Pn*3*m* phase, faceted inclusions of the *L*1 phase were growing in it. This reaction *Pn*3*m* → *Pn*3*m* + *L*1 is indicated in Fig. 19 as the trajectory *a* → *b*.

4.2.2. *Pn*3*m*-in-*L*1 Crystals (C12EO2)

With the aim to test predictions of Nozières *et al.* the special-purpose isoplethal setup (Fig. 7) was used subsequently for more detailed studies of the *Pn*3*m*/*L*1 interface in two complementary geometries: *Pn*3*m*-in-*L*1 crystals and *L*1-in-*Pn*3*m* inclusions [32]. The conclusion of experiments with the C12EO2/water system is that, in this system, only (111)-type facets coexisting with rough surfaces are present at the *Pn*3*m*/*L*1 interface. This feature is illustrated in Fig. 19B by a typical image of a *Pn*3*m*-in-*L*1 crystal located at the capillary glass wall. In the light of experiments on the facet-by-facet surface melting (see Section 3.2.2) such an *extremely poor* faceting is obviously due to the very narrow temperature range of the *Pn*3*m*/*L*1 coexistence domain in the phase diagram of C12EO2: below

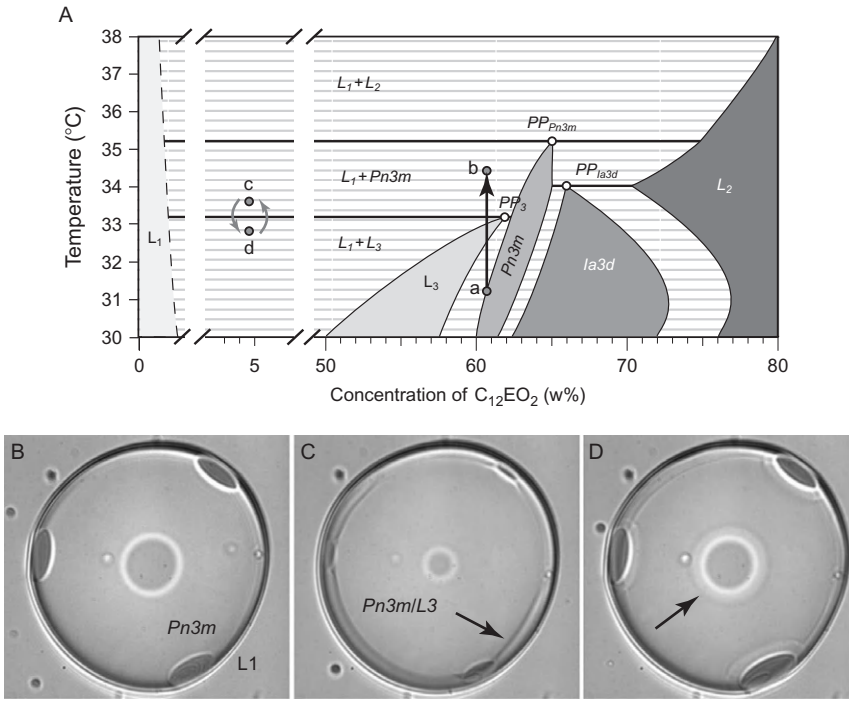

Figure 19 (A) Phase diagram of the binary system C12EO2/water established by Lynch *et al.* [40]. (B) Typical image of a *Pn3m*-in-*L1* crystal located on the capillary wall. It is oriented with its threefold [111] axis orthogonal to the substrate. (C) Upon cooling ($c \rightarrow d$ trajectory) rough parts of the *Pn3m*/*L1* "melt" into a layer of the sponge phase. Facets remain unmelted but their size decreases. (D) Upon heating ($d \rightarrow c$ trajectory) the sponge layer "recrystallizes". (Reproduced from Ref. [35] with kind permission of J. Phys. Condens. Matter.)

the peritectic triple point *PP3*, the *Pn3m* phase melts into the sponge phase, while above the peritectic triple point *PPPn3m* it melts into the *L2* phase.

4.2.3. Anisotropic Surface Melting at the *Pn3m*-in-*L1* Interface (C12EO2)

The two other images C and D of this series illustrate the phenomenon of the anisotropic surface melting considered theoretically by Nozières [34]. Here, upon cooling (trajectory $c \rightarrow d$ in Fig. 19A), a layer of the *L3* phase of a macroscopic thickness is growing exclusively on rough parts of the *Pn3m*/*L1* interface while the (111)-type facets remain intact although their size decreases. In order to visualize better geometry of this three-phase coexistence, we show in Fig. 20 its perspective view. Here, edges of facets

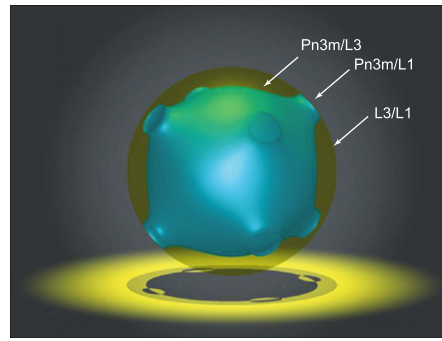

Figure 20 Anisotropic melting at the *Pn3m*/*L*1 interface supress (Povray simulation).

are triple lines of contact of three interfaces: *Pn3m*/*L*1, *Pn3m*/*L*3, and *L*3/*L*1. The *L*3/*L*1 interface is obviously isotropic so that its mean curvature must be constant. In a good approximation, it is spherical. The *Pn3m*/*L*3 interface is almost isotropic so that its mean curvature is approximately constant too. Finally, the *Pn3m*/*L*1 facets are flat. Following Nozières' theory, such an equilibrium configuration of three phases is possible below the peritectic point *PP*3 *if and only if* above the peritectic point the junction between rough parts of the *Pn3m*/*L*1 interface and facets is angular. From the presence of a bright ring surrounding the central facet in Fig. 19B, one can infer that this is the case.

4.3. *L*1-in-*Pn3m* Inclusions (C12EO2)

The isoplethal setup has also been used for studies of *L*1-in-*Pn3m* inclusions in the C12EO2/water system. When such inclusion are nucleated at capillary walls, their triangular shapes shown in Fig. 21 are similar to those of *Pn3m*-in-*L*1 crystals. Shapes of inclusions nucleated and grown in bulk (see Fig. 21A–D) reveal the cubic symmetry of the surrounding *Pn3m* crystal: regular octahedra limited by eight (111)-type facets.

4.4. *Pn3m* → *Fd3m* Symmetry Breaking

The Donnay–Harker selection rule [23] applied to *Pn3m* crystals predicts the prominence of twelve (110)-type facets (see Fig. 22B) which alone would form a dodecahedral shape. Obviously, this theoretical dodecahedral shape does not agree with real shapes of *Pn3m*-in-*L*1 crystals prepared with C12EO2/water mixtures [33] where, as shown in Fig. 22A, eight (111)-type facets are prominent and present in all temperature range of the *Pn3m*/*L*1 coexistence (see Fig. 19). Six small (200)-type facets occur only in the

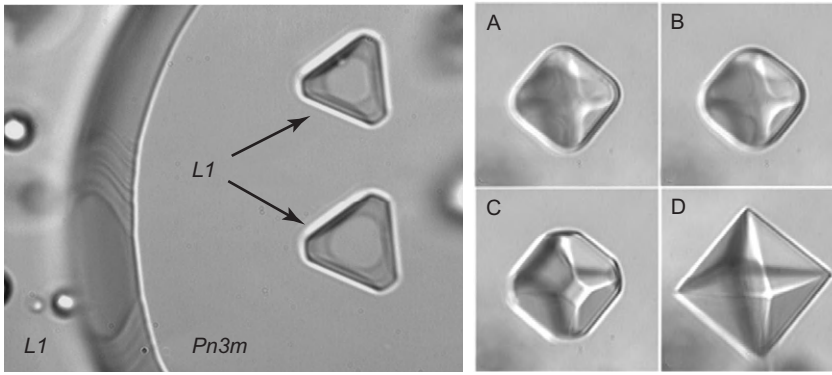

Figure 21 Faceted *L*1-in-*Pn*3*m* inclusions. In the image on the left, two inclusions were nucleated and grown at the capillary wall inside a large, pancake-shaped *Pn*3*m* crystal. The series of four images (A)–(D) shows the growth of a bulk inclusion. The final completely faceted shape of the inclusion is that of a regular octahedron limited by (111)-type facets. (Reproduced from Ref. [33] with kind permission from Springer Science+Business Media.)

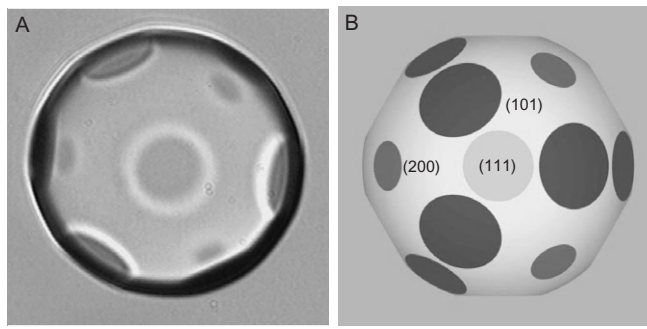

Figure 22 Shapes of *Pn*3*m*-in-*L*1 crystals: (A) observed in experiments with C12EO2/water system [33], (B) predicted by the Donnay–Harker rules of faceting [23]. The observed predominance of (111)-type facets and the absence of (110)-type do not agree with the theoretical shape made of (110)-, (111)-, and (100)-type facets.

middle of the *Pn*3*m*/*L*1 coexistence range. Moreover, no (110)-type facets were visible in any conditions. To explain this flagrant disagreement with the Donnay–Harker rules, we argued in Ref. [33] that *Pn*3*m* → *Fd*3*m* symmetry breakdown was induced by the requirement of the bilayer continuity at the *Pn*3*m*/water interface. We will come back to this problem in the next section.

5. Faceting in the Ternary and Quaternary Mixtures

5.1. On the Choice of Phytantriol/Water/Ethanol and Monoolein/Water/Ethanol Systems

As we have seen above, one of characteristics of the C12EO2/water binary system is that the $Pn3m+L1$ coexistence domain has here a narrow, 2 °C temperature range (see Fig. 19A). On cooling below the $Pn3m/L1/L3$ triple point, $Pn3m$ crystals are melting into the sponge $L3$ phase. Similarly, on heating above the $Pn3m/L1/L2$ triple point, $Pn3m$ crystals melt into the inverted micellar $L2$ phase. The surface melting of $Pn3m$ crystals into the sponge phase is an advantage because it allows to prepare $Pn3m$-in-$L1$ crystals of a globally spherical shape. Unfortunately, due to the narrow $Pn3m/L1$ coexistence range, the shape of the $Pn3m$-in-$L1$ crystals is dominated by the anisotropic surface premelting as discussed extensively in Ref. [32]: for this reason, the (200)-type facets are hardly visible and all other types of facets are missing.

With the aim to enlarge the temperature range of the $Pn3m/L1$ coexistence domain, we selected surfactants that are used for production of cubosomes [41,42]: monoolein (glycerol monooleate) and phytantriol (3,7,11,15-tetramethyl-1,2, 3-hexadecanetriol). Their binary phase diagrams (temperature vs concentration of water) have identical geometrical structures and differ only by numerical values of characteristic concentrations and temperatures. As an example, we show here, in Fig. 23, the phase diagram of the phytantriol/water system, established by Barauskas and Landh [43]. It displays the $Pn3m/L1$ coexistence domain of wide temperature range, limited from above by the $Pn3m/L1/H$ triple point at $T = 40$ °C. In experiments presented here, we used a sample of phytantriol from a different source [44] and have found that temperatures of all triple points were higher by several degree Celsius. In particular, we have found the $Pn3m/L1/H$ triple point at $T_{P1H} = 56$ °C. In the case of the monoolein/water system, the temperature of the $Pn3m/L1/H$ triple point is even higher: $T_{P1H} = 90$ °C [30]. If the binary phytantriol/water and monoolein/water systems have the suitable wide $Pn3m+L1$ coexistence range, they have also one drawback: upon heating, $Pn3m$ crystals can be melted into the hexagonal phase but this process does not generate suitable globally spherical shapes. Stimulated by the method of Spicer and Hayden of preparation of cubosomes [41,45–47], we decided to check whether $Pn3m$-in-$L1$ crystals could be melted into an isotropic phase when ethanol is added to the $L1$ phase. Our experiments with phytantriol(or monooelin)/water/ethanol ternary mixtures proved that this is effectively the case. The $Pn3m/L2$ transition can be driven in two ways (see Fig. 24):

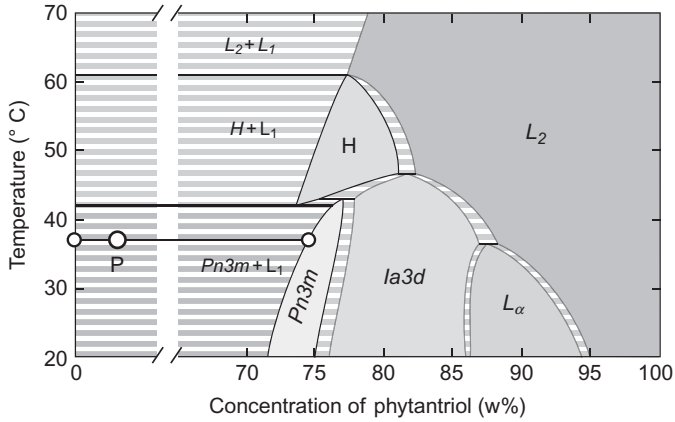

Figure 23 Phase diagram of the phytantriol/water mixture established by Barauskas and Landh [43]. In our experiments performed with a sample of phytantriol from another source [44], temperatures of all triple points were higher by several degree Celsius. At point P, *Pn3m* crystals are surrounded by the *L*1 phase which is composed of almost pure water. When 3% of ethyl alcohol is added to water, the hexagonal phase is suppressed and *Pn3m*-in-*L*1 crystals melt directly into the *L*2 phase at 55.5 °C.

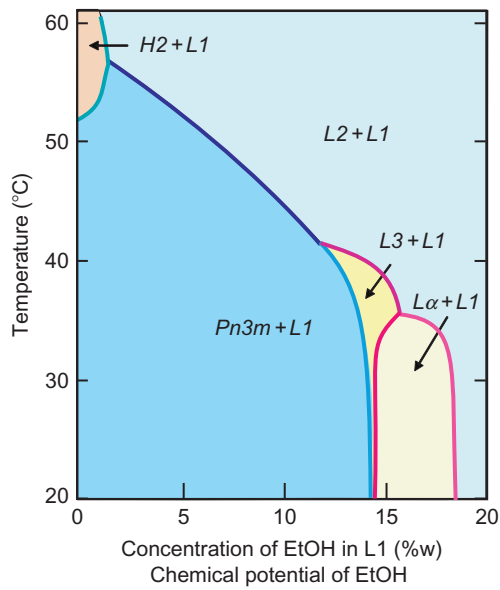

Figure 24 Phase diagram of the ternary mixture phytantriol/water/ethanol [48]. *Pn3m*-in-*L*1 crystals can be melted either into *L*2 or *L*3 phases.

1. Either at constant temperature, by adding ethanol to the *L*1 phase surrounding *Pn*3*m* crystals
2. Or by increasing the temperature at a constant adequate concentration of ethanol in *L*1

5.2. Facet-by-Facet Melting at the *Pn*3*m*/*L*1 Interface

The series of pictures shown in Fig. 25 was taken at a fixed concentration (4%) of ethanol in *L*1 phase. On the initial shape of the crystal (47.0 °C), several types of facets having different sizes coexist with rough surfaces.

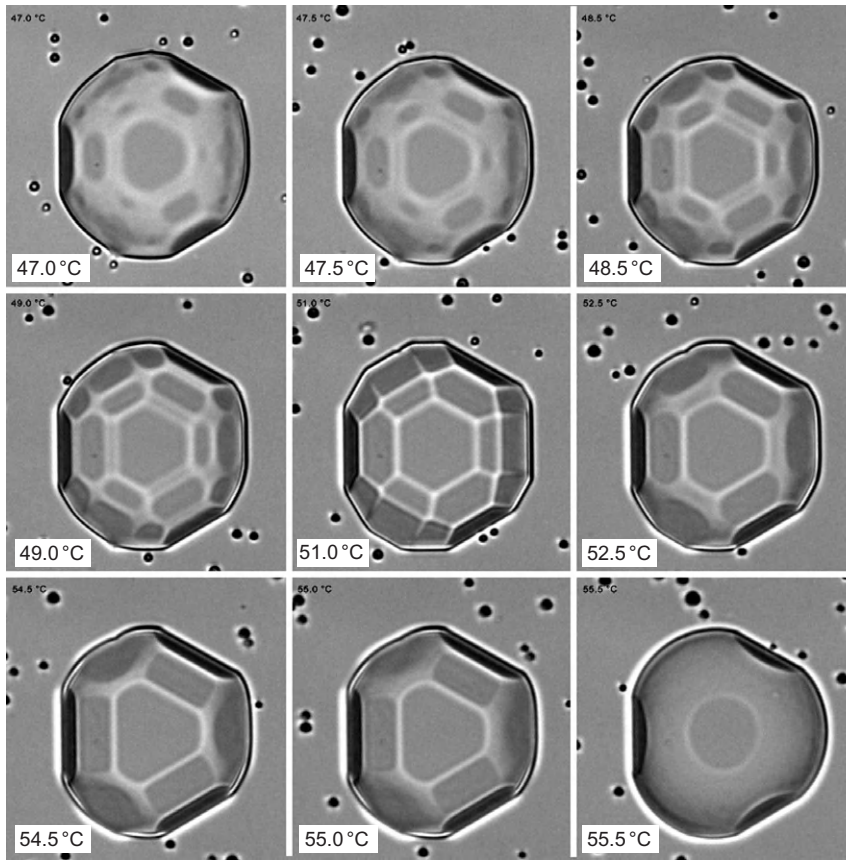

Figure 25 Facet-by-facet anistropic melting of the *Pn*3*m*/*L*1 interface. A droplet of the *L*2 phase is transformed into a spherical *Pn*3*m* crystal and cooled down to 47 °C: five types of facets are present. Subsequently, the temperature is raised by increments of 0.5 °C. At 48.5 °C, (511)-type facets disappear. (311)-type facets disappear at 52.5 °C, (400) at 55.0°C, (220) at 55.5 °C and at 55.6 °C (111)-facets are wet by the *L*2 phase. (Collaboration with J. Grenier and J. Okal.)

Upon heating from 47.0 to 51.0 °C, facets grow at the expense of rough surfaces which are completely eliminated at 51.0 °C. This phenomenon will be discussed later in Section 7.1. Upon further heating from 51.0 to 55.5 °C, the facet-by-facet surface melting occurs.

5.3. Indexing of Facets at the *Pn*3*m*/*L*1 Interface

Further description of crystal shapes observed in experiments requires the knowledge of facets' indices. For indexing of facets, it is convenient to consider a completely faceted shapes such as those in Fig. 26A and C. Here, the crystal in picture (A) has the shape similar to the one labeled "51.0 °C" in Fig. 25. With the hypothesis of the *Pn*3*m* → *Fd*3*m* symmetry breakdown in mind, *Pn*3*m* (Fig. 26B) and *Fd*3*m* (Fig. 26C) shapes expected theoretically from the Donnay–Harker selection rules have been generated.

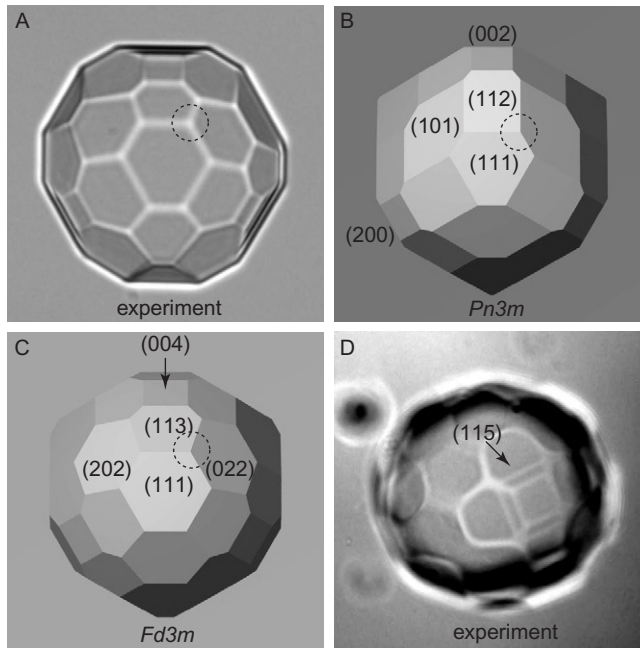

Figure 26 Indexing of facets on experimentally observed crystal shapes in terms of *Pn*3*m* and *Fd*3*m* symmetries: (A) completely faceted *Pn*3*m*-in-*L*1 crystal of phytantriol. (B) shape of *Pn*3*m* crystals expected from Donnay–Harker rules, (C) shape of *Fd*3*m* crystals expected from Donnay–Harker rules, (D) vicinity of the [001] axis. (Collaboration with P. Faye and R. Sheska.)

In terms of these rules, the corresponding series of facets, in order of their prominence (based on interplanar distances) are:

- *Pn*3*m*, D-H: (110), (111), (200), (211), (221), (310)
- *Fd*3*m*, D-H: (111), (220), (311), (400), (331), (511)
- Experiment: (111), (220), (400), (311)

Clearly, the *Fd*3*m* theoretical shape in Fig. 26C (limited to four types of facets) matches the experimental one better than the *Pn*3*m* one in Fig. 26B. This discussion will be resumed in Section 6.

5.4. *Im*3*m*-in-*L*1 Crystals in Phytantriol/DSPG/Water/Ethanol system

To complete our study of faceting of bicontinuous cubic phases, we had to find a system in which the *Im*3*m* phase would coexist with the *L*1 phase. To our knowledge, there are no binary systems having this property however it has been pointed our recently by Wadsten-Hindrichsen *et al.* [42] that the *Pn*3*m* phase is replaced by the *Im*3*m* one when a small amount of DSPG (distearoylphospatidylglycerol) is added to the phytantriol. We have found that at the concentration of 1.8 w% of DSPG in phytantriol, the phase diagram of the ternary mixture phytantriol/water/ethanol (see Fig. 24) is slightly modified: the *Im*3*m* phase appears inside the domain of the *Pn*3*m* phase for concentrations of ethanol larger than 8 w%.

5.5. Indexing of Facets at the *Im*3*m*/*L*1 Interface

The series of nine images in Fig. 27 shows the evolution of a *Im*3*m*-in-*L*1 crystal upon a slow lowering of the ethanol concentration in the surrounding *L*1 phase. Indexing of facets is at the *Im*3*m*/*L*1 interface is very easy. From the fourfold symmetry of the crystal shape, one can conclude that the central facet is (100). The (111) facet is also easy to identify because its shape becomes triangular in Fig. 27I. The facet situated halfway between (100) and (010) must be (110). Finally, the small facet intermediate between (100) and (111) can be (211). Let us compare this series of facets with predictions of the Donnay–Harker rule for the *Im*3*m* and the *Pm*3*m* symmetry resulting from the "outside-inside" symmetry breaking:

- Experiment: (100), (111), (110), (211)
- D-H, *Im*3*m*: (110), (200), (211), (310), (222)
- D-H, *Pm*3*m*: (100), (110), (111), (210), (211)

The conclusion is that the experimental results fit much better with the lower *Pm*3*m* symmetry.

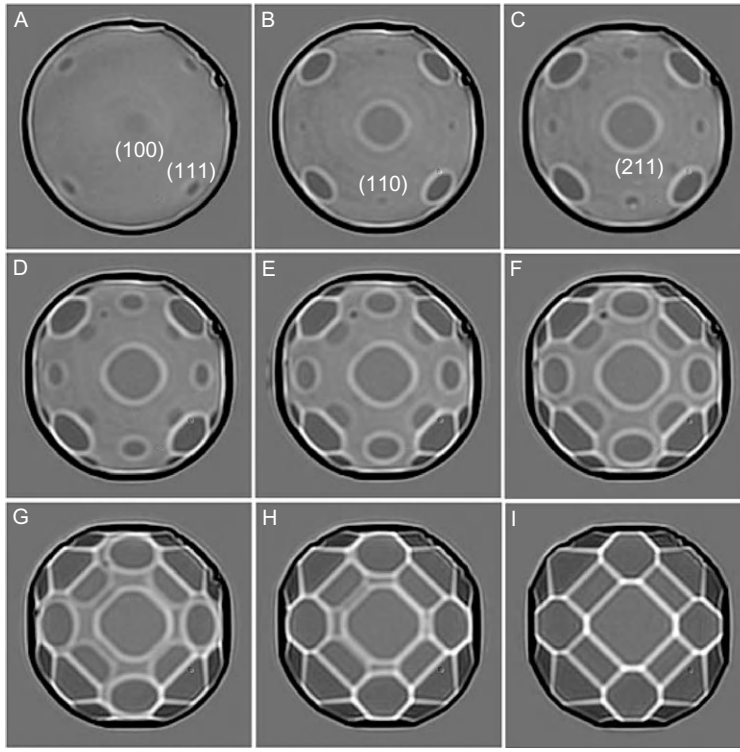

Figure 27 Faceting of a *Im3m*-in-*L*1 crystal. This series of pictures shows how the shape of the *Im3m*/*L*1 interface varies when the concentration of ethanol in *L*1 phase is lowered from 13% to 8%. (Collaboration with L. Latypova.)

6. Faceting and Topology

Experiments on faceting of bicontinuous inverted cubic phases are summarized in the lower row of Fig. 28 where typical fingerprint-like shapes of *Ia3d*-in-vapor, *Pn3m*-in-*L*1, and *Im3m*-in-*L*1 crystals are shown. The upper row of this figure displays spherical sections of so-called "level surfaces approximation" of IPMS having the *Ia3d*, *Pn3m*, and *Im3m* symmetries.

6.1. Symmetry Breakdown in Balanced Bicontinuous Structures

To start the discussion of the topological symmetry breakdown at the *Pn3m*/*L*1 interface, it seems useful to remind some general facts about symmetries of the bicontinuous lyotropic phases.

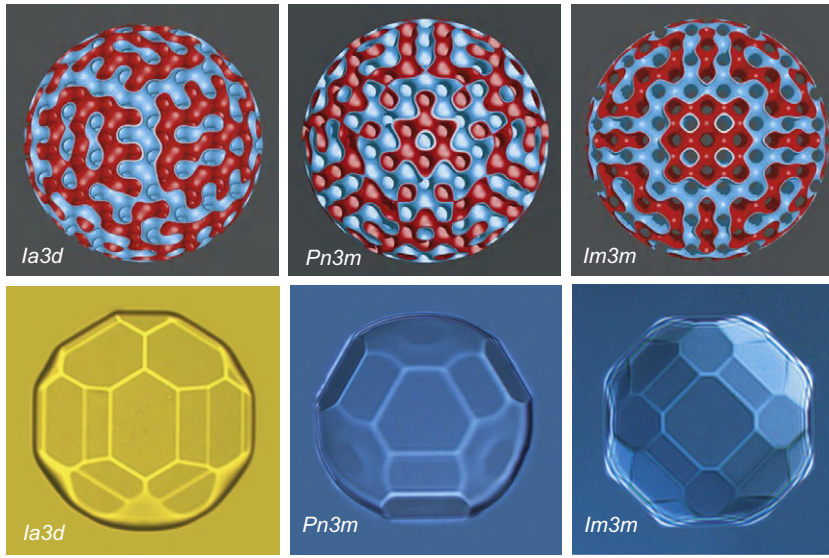

Figure 28 Bicontinuous cubic lyotropic phases. Pictures of level surfaces in the upper row illustrate shapes of the surfactant bilayer. Pictures in the lower row are images of real crystals observed in a transmission optical microscope: a *Ia3d*-in-vapor monocrystal grown by the hygroscopic techniquemonoolein/water system, a *Pn3m*-in-*L*1 monocrystal grown by the isoplethal technique in the phytantriol/water system and a *Im3m*-in-*L*1 monocrystal in the phytantriol/DSPG/water/ethanol mixture.

In the bulk of a perfect bicontinuous lyotropic cubic phase, surfactant molecules are self-assembled into a continuous non-selfintersecting bilayer separating two labyrinths filled with water. In drawings, different colors can be attributed to these two labyrinths or to the two monolayers forming the bilayer. In Fig. 29, we use Bright and Dark tones of gray (or Blue and Daffodil colors) so that we will call them B and D.

Triply Periodic Minimal Surfaces (TPMS) or Level Surfaces (LS) of suitable symmetry can be used for analytical approximations of the bilayer's shape. The TPMS representation which appears naturally in the framework of the Ginzburg–Landau model [15] has a better physical legitimacy but here, in the context of arguments involving exclusively symmetry and topology, the LS representation [49] is more convenient for drawings.

Following Schwarz and Gompper [15], a LS (or TPMS) surface is called *balanced* if there exists an Euclidean transformation α which maps the B labyrinth onto the D one and *vice versa*. Translation $\overrightarrow{b_M}$ in Fig. 29 is an example of such an operation in the case of the *Pn3m* bicontinuous structure.

Therefore, the bicontinuous structures are characterized by two space groups: if the bi-tone structure has space group H, the mono-tone structure

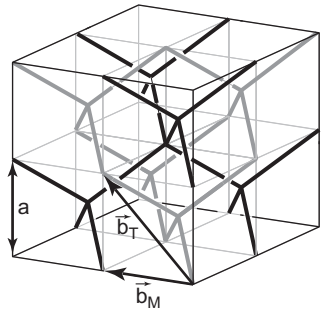

Figure 29 Illustration of the relationship between Bravais lattices of the *Pn*3*m* and *Fd*3*m* space groups. The shortest vectors of sc and fcc Bravais lattices are shown.

has space group $G = \{H, \alpha H\}$. In terms of group theory, one can say more precisely that the group G is composed of two cosets with respect to its subgroup H. All symmetry operation from the first coset H map B and D labyrinths on themselves, while those from the second coset αH map B on D and vice versa.

The names *Ia*3*d*, *Pn*3*m*, and *Im*3*m* of cubic lyotropic phases correspond to symmetries G of mono-tone structures; the two labyrinths are assumed to be equivalent in the bulk of perfect crystals. The corresponding subgroups H of bi-tone structures are then: $H = I4_132$, *Fd*3*m*, and *Pm*3*m*. We will argue below, that for topological reasons, in *Pn*3*m* crystals surrounded by the $L1$ phase the two water labyrinths cannot be strictly equivalent. This difference between the two labyrinths, no matter how large it is, breaks the symmetry *Pn*3*m* to *Fd*3*m*. The same arguments applied to *Ia*3*d* and *Im*3*m* phases, would lead respectively to $Ia3d/I4_132$ and *Im*3*m*/*Pm*3*m* symmetry breakdowns.

6.2. Topological Constraints, Prohibited Bilayer's Edges

In order to understand topological constraints imposed on the structure by the *Pn*3*m*/$L1$ interface, let us imagine that the interface has been created by a three-step geometrical process:

1. The bicontinuous phase is first divided into two parts by some secant surface.
2. One of the two parts is replaced by the $L1$ phase composed of almost pure water.
3. The interface created in this way is reconstructed.

Obviously, after the first two steps, the surfactant bilayer is necessarily intersected and the energetically prohibited edges are created. First, we will

find shapes and topology of these edges as a function of the orientation and position of the secant surface and after that we will reconstruct the interface with the aim to suppress bilayer's edges. In the case of the cubic bicontinuous phase *Pn*3*m*, the bilayer's edges are easy to find using the Level Surface [49] given by the equation:

$$D(x, y, z) = \cos(x)\cos(y)\cos(z) - \sin(x)\sin(y)\sin(z) = 0. \quad (7)$$

In Fig. 30B, these prohibited free edges are well visible. One can stitch them up so that the integrity of the bilayer is recovered. This can be done in two ways because one of the B or D colors can be chosen for the outer side of the closed surface. Results of these surgeries are shown in Fig. 30A and C. Clearly, these two finite closed surfaces are slightly different. One can say that a surface-induced topological *Pn*3*m*/*Fd*3*m* symmetry breakdown occurred here.

6.3. Disorientations

So far, we were dealing with surfaces and facets of perfect single crystals. However, real crystals can contain dislocations. In solid crystals, dislocations emerging on facets give rise to steps which can be detected with, for example, SEM or AFM methods. As already mentioned in Section 1.3, dislocations have also been detected in soft crystals [9,20] by means of observation of steps at interfaces.

From the fundamental point of view, dislocations are characterized by Burgers vectors which, by definition, are translations belonging to Bravais lattices. Two such Burgers vectors belonging to the simple cubic Bravais lattice of the *Pn*3*m* space group are shown in Fig. 29. We called them $\vec{b}_{\mathrm{T}}$

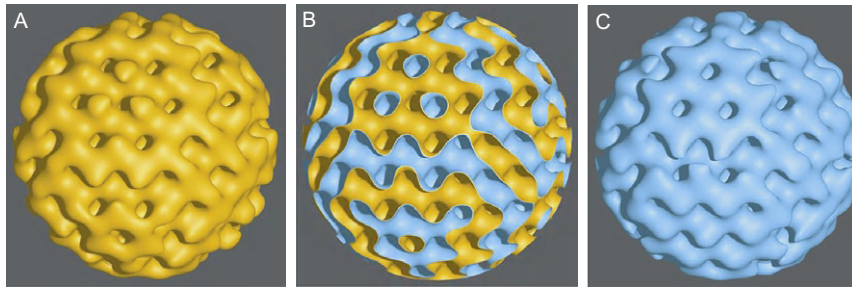

Figure 30 The Level Surface *Pn*3*m* in a has two different colors on its two sides. The spherical section produces prohibited free edges. One can stitch them up so that the surface becomes closed. This can be done in two ways because one or the other color for the outer side can be chosen. In both cases, the topological *Pn*3*m* → *Fd*3*m* symmetry breakdown occurs.

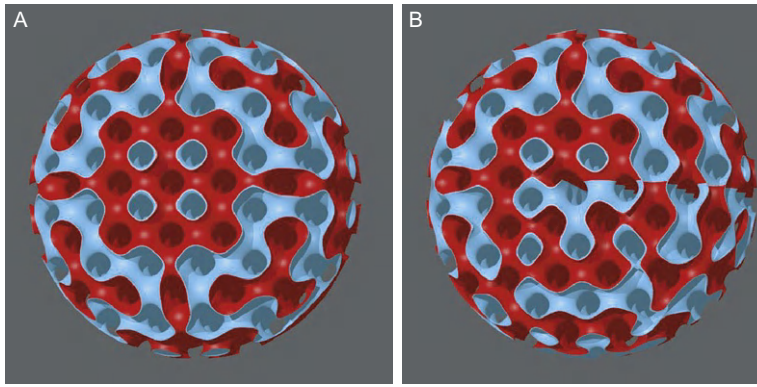

Figure 31 Disorientation: a new topological defect. (A) Spherical domain of the *Im*3*m* level surface. Free edges of the bilayer visible here can stitched up exactly in the same manner as in the case of the *Pn*3*m* surface in Fig. 30. (B) In the presence of a disorientation, the surface becomes nonorientable (see the color discontinuity) and the free edge connected to the disorientation can not be stitched up.

and $\overrightarrow{b_M}$ with the aim to emphasize that they give respectively *Trivial* and *Möbius* dislocations. A detailed explanation of this terminology can be found in Ref. [50]. Here, in Fig. 31, we show that when a *Pn*3*m* crystal contains a Möbius dislocation, the bilayer becomes nonorientable exactly as it is the Möbius strip. From the point of the surface reconstruction discussed in the previous section, the Möbius dislocation introduces a vary drastic perturbation because the integrity of the bilayer cannot be restored by stitching up free edges of the bilayer.

7. Phenomena Out of Equilibrium

Theories of crystal shapes are usually focused on the concept of the equilibrium shape corresponding to the unique absolute minimum of the total surface energy of a crystal at a constant volume. In such theories, the minimum is taken with respect to variations in crystal shapes, which are supposed implicitly to be free which means that there are no energy barriers to overcome when matter is transferred from one portion of the crystal surface to another one.

In solid crystals, as emphasized by Nozières in Ref. [21], "This should be kept in mind: *facets size do not reflect equilibrium* unless great care is taken to allow their vertical growth". It is so because ". . . a facet is often *trapped* at a given height z. While it can *enlarge* easily by adjusting the surrounding curved parts, it cannot nucleate new terraces; the facet is then *metastable*".

This thermodynamic property remains true also in the case of soft crystals interfaces and has several unexpected consequences.

7.1. Growth by Redistribution

The phenomenon of growth-by-redistribution is one of such consequences. It occurs, for example, in following conditions:

1. The temperature T is risen in C12EO2/water, MO/water and Phytantriol/water systems.
2. The chemical potential of water $\mu_{H_2O}(H)$ is lowered in C12EO6/water system.
3. The chemical potential of ethanol μ_{EtOH} (concentration of ethanol in the $L1$ phase) is lowered in phytantriol/water/ethanol system.

In all these cases, for small enough variations of the intensive parameters T, $\mu_{H_2O}(H)$, or μ_{EtOH}, facets existing already at interfaces extend their sizes while the rough parts of interfaces are shrinking. Here, this phenomenon has already been mentioned in Section 5.2 (see Fig. 25).

This phenomenon has no counterpart in usual crystal/melt(solution) systems because it occurs at a constant number N_s of surfactant molecules in *Pn3m*, *Ia3d*, or *Im3m* crystals. Called "pseudo-growth" or "growth-by-redistribution," it is characteristic of soft crystals in which the number of surfactant (or water) molecules per unit cell can vary continuously as a function of T, $\mu_{H_2O}(H)$, or μ_{EtOH}. If for instance the number of surfactant molecules per unit cell n_{uc} decreases upon the above-mentioned changes then, at constant N_s, new unit cells have to be created as if crystals were growing.

Now, in the case when facets are *metastable*, that is, when nucleation is prohibited on facets, the growth (in terms of the total number of unit cells $N_{uc} = N_s/n_{uc}$) takes place only on rough parts of crystal surfaces and as a consequence, facets extend their sizes (see Fig. 32).

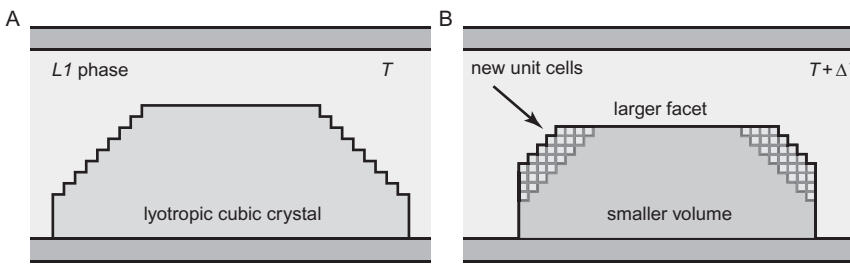

Figure 32 Growth-by-redistribution of soft crystals. (A) Flat facets coexists with rough surfaces made of steps. (B) The excess surfactant is used for construction of new unit cells on rough surfaces.

7.2. Ratchet Effect

Experiments have shown that the growth-by-redistribution phenomenon is in general not perfectly reversible; when the initial values of the intensive parameters are restored too rapidly, facets generally do not recover their initial sizes but remain larger. Therefore, one can expect that upon such back-and-forth saw tooth-like cycling of intensive parameters, facets may grow in size until elimination of rough surfaces is complete. In Ref. [31], this phenomenon called *ratchet effect* is discussed in all details. Here, it is illustrated in Fig. 33 showing variations of the shape of a *Im*3*m*-in-*L*1 crystal in the quaternary phytantriol/DSPG/water/ethanol system submitted to temperature cycling.

7.3. Thermal Permeation

In 1982, P.G. de Gennes wrote two articles on two apparently disjoined subjects: (1) Ludwig–Soret effect in porous media filled with pure liquids [51] and (2) bicontinuous structures in microemulsions [52]. In the study of bicontinuous cubic lytropic crystals submitted to temperature gradients [53], these two subjects are intimately related. Experiments reported in Ref. [53] consisted in observation, by means of an optical microscope, of crystal shapes in three types of phase coexistence: *Ia*3*d*-in-vapor, *Pn*3*m*-in-*L*1, and *Im*3*m*-in-*L*1. Here, we show in Fig. 34A a series of six pictures

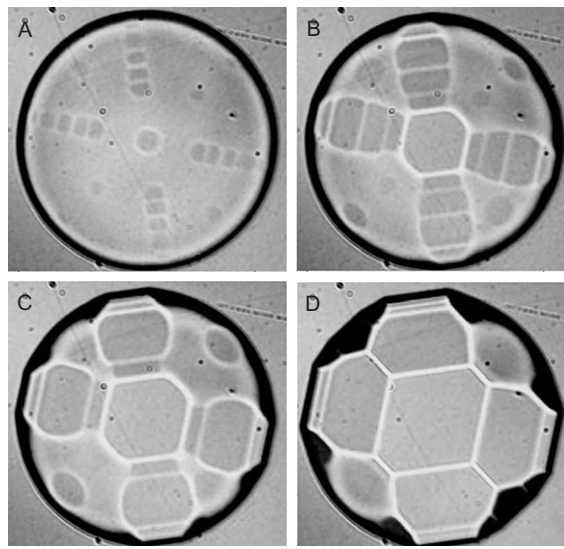

Figure 33 Ratchet effect: variations of the shape of a *Im*3*m*-in-*L*1 crystal in the quaternary phytantriol/DSPG/water/ethanol system submitted to temperature cycling. (Collaboration with T. Plötzing and L. Latypova.)

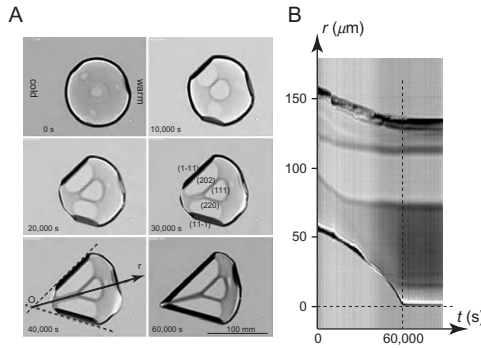

Figure 34 Deformation of *Pn3m*-in-*L*1 crystal submitted to a temperature gradient in the phytantriol/water/ethanol ternary system. The concentration of ethanol in the *L*1 phase is 4%. The temperature gradient is 2.4 K/mm. (A) Series of six images selected from a video. (B) Spatiotemporal section along the axis *r* defined in the picture labeled "40000 sec", extracted from a video taken at the rate of 1 image per 400 s. (Reproduced from Ref. [53] with kind permission of Liquid Crystals. Collaboration with S. Popa-Nita, J. Rizzi, and G. Saquet.)

illustrating the evolution of a *Pn3m*-in-*L*1 crystal submitted to a horizontal temperature gradient of 2.4 K/mm. It is evident here that the colder part of the crystal is growing and the warmer is simultaneously deconstructed. Quantitative features of this behavior can be obtained from the spatiotemporal cross-section shown in Fig. 34B. It has been extracted from a video by the reslice command (ImageJ freeware) along the axis *r* defined in Fig. 34A. In particular, it is obvious that:

1. The velocity of the cold extremity of the crystal increases monotonically and suddenly falls to zero at time $t_c = 60{,}000$ s.
2. This transition takes place when the faceting of the cold extremity is achieved, that is, when the mobile rough part of the crystal surface located between facets disappears.
3. The velocity of the warmer extremity of the crystal decreases progressively and tends to zero at the same time t_c.

It is obvious that these growth and deconstruction processes involve transport of the surfactant from warm to cold extremities of crystals. In the case of *Ia3d*-in-vapor crystals, this transport cannot occur through the vapor phase because C12EO6 surfactant is not volatile, that is, its vapor pressure at room temperatures is extremely low. In the case of *Pn3m*-in-*L*1 and *Im3m*-in-*L*1 crystals, the transport of surfactant can neither occur through the *L*1 phase because the concentration of surfactants (C12EO2 or phytantriol) in it is negligible. We know that from the fact that the volume of *Pn3m* and *Im3m* crystals does not decrease on the time scale of weeks in spite of the fact that fresh water or fresh water/ethanol solution is permanently flowing

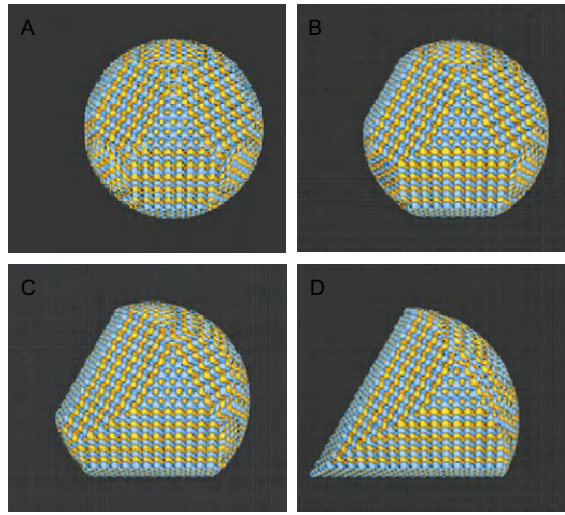

Figure 35 Simulation of the Soret effect in the *Pn*3*m* phase (see Fig. 34). (Reproduced from Ref. [53] with kind permission of Liquid Crystals. Collaboration with S. Popa-Nita, J. Rizzi and G. Saquet.)

around them. Moreover, if the surrounding solvent ($L1$ phase) was involved in the transport of surfactant, the observed changes in crystal shapes would be affected by flow of the solvent which is not the case.

Therefore, we are left with the unique possibility of the transport of the surfactant through the crystal. We should even say—*transport of the surfactant through the lattice made of the unique bilayer*—because the crystal lattice is at rest with respect to capillary walls; we know that from the fact that cold facets are at rest. This important conclusion is illustrated in Fig. 35 by four drawings of the *Pn*3*m* level surface inside the crystal changing its shape (to be compared with Fig. 34). This kind of transport is similar to the permeation of molecules through smectic layers or through cholesteric helix. Therefore, our final conclusion is that *temperature gradients drive the transport of surfactant by permeation, along triply periodic bilayers, from warm toward cold sides of crystals.*

8. Exploring Facets of Soft Crystals with AFM

8.1. Vicinal Facets as Systems of Ordered Steps

The devil's staircase faceting mentioned in Section 3.1.2 is, strictly speaking, a purely theoretical concept valid at $T = 0$ K for crystals of infinite size. It involves the Haüy-like representation of facets with arbitrarily high Miller

indices as ordered systems of steps and kinks belonging to principal facets. The principle of this so-called FSK (facets, steps, and kinks) model has already been represented in Fig. 3 where, for example, the (103) facet, intermediate between (100) and (001) facets, is obviously made of regularly spaced steps belonging to the (001) facet. In general, any (*m*0*n*) facets can be represented as an ordered systems of such steps.

One can ask whether such ordered systems of steps really exist on facets with high Miller indices in experiments with soft crystals where the devil's staircase-like faceting was reported to occurs.

The optical phase contrast used in experiments with the Monooelin/water system reported in Ref. [20] allows to detect isolated steps on (112) or (202) facets. Unfortunately, the diffraction limited lateral resolution of this technique (of the order of 1 μm) is too low for imaging ordered systems of steps on vicinal facets of relatively small crystals.

In terms of the vertical and lateral resolution, the Atomic Force Microscopy is perfectly adapted for this purpose but it is difficult to use in the humidity range close to 100% required for the existence of *Ia*3*d*-in-vapor crystals. We are thus left with the last alternative choice—the thermotropic cubic mesophases—where, on the contrary, the atmosphere surrounding crystals should preferentially be dry.

8.2. Cubic Thermotropic Mesophase

In experiments reported in Ref. [6], a series of 4′-alkoxy-3′-nitrobiphenyl-carboxylic acids (ANBC) derivatives were used [6,10–12]. For the $n = 9$ compound, the cubic *Ia*3*d* mesophase occurs between 95.8 and 145.6 °C (respectively between 92.6 and 149.8 °C for the $n = 10$ one). Upon cooling, the cubic mesophase appears at 135.7 °C for $n = 9$ (respectively, 142 °C for $n = 10$) and remains metastable till room temperature. Moreover, in the case of small droplets, the metastable cubic mesophase can be kept at room temperature during several weeks after which it recrystallizes slowly. It is precisely this metastability of the cubic mesophase that allowed to study droplets of this phase with the AFM at room temperature.

8.3. AFM Images of Vicinal Facets

In Fig. 36, two AFM images of small portions of the free surface of an *Ia*3*d* monocrystal are shown. The global shape of the crystal has been determined from optical observations (see, e.g., Fig. 2B) and from other low-resolution AFM images reported in Ref. [6]. It is a spherical cup with the base of 10 μm in diameter and the contact angle of about 30°. Using the same low-resolution images indexing of 15 facets covering this crystal has been performed.

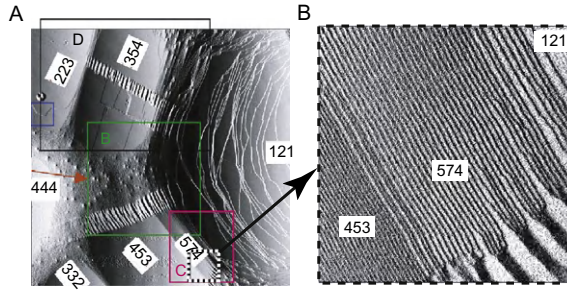

Figure 36 Systems of ordered steps detected by AFM on vicinal facets. (Reproduced from Ref. [6] with kind permission of Springer Science+Business Media.)

Figure 36A shows the topography of a square area 15 × 15 μm in size located on the top of the crystal. Isolated steps on the (121) facet are well visible here but vicinal facets have still a smooth aspect. A small 1 × 1 μm square area surrounded by the dotted line in Fig. 36A has been enlarged in Fig. 36B. This image confirms the validity of the FSK theoretical model proposed for explanation of the devil's staircase-type faceting.

9. Conclusions

Facetted shapes of cubic thermotropic and lyotropic mesophases are beautiful and intriguing. On many images shown in this review, constellations of facets at cubic/isotropic interfaces appear as highly symmetric and allow to identify immediately fourfold, threefold, and twofold axes. Simultaneous occurrence of these three point symmetries is a finger-print of cubic space groups: *Ia*3*d*, *Pn*3*m*, *Im*3*m*, and *Pm*3*n*. Discrimination between these groups is possible after indexing of an appropriate number facets. In conclusion, shapes of monocrystals of cubic mesophases are like characteristic textures of other mesophases: they allow to identify symmetries without the help of X-ray diffraction.

Let us stress that production of monocrystals of cubic lyotropic mesophases requires special methods tailored for this purpose. The *hygroscopic method* described in Section 2.2 is adapted for studies of cubic/vapor interfaces in surfactant/water binary systems. The *isoplethal method* described in Section 2.3 has been developed for studies of cubic/*L*1 interfaces in binary or ternary systems with the solubility gap.

In the hygroscopic method, the chemical potential of water μ_{water} is controlled through regulation of the water vapor pressure. By this means, T-vs.-μ_{water} diagrams can be explored much more precisely than the

corresponding T-vs.-c_{water} classical diagrams build tediously from a large set of samples with different concentrations. Thanks to this feature, the *RHCP ephemeral phase* has been discovered in DTACl/water system.

Another unexpected outcome of hygroscopic studies was the generic discovery of the *devil's staircase-type faceting* at *Ia*3*d*/vapor interface. In the light of this result, lyotropic systems appeared as a model system for studies of the faceting phenomena considered from the fundamental point of view. In particular, the so-called *anisotropic melting of crystal surfaces* analyzed theoretically by Nozières [34] has been found to occur at cubic/vapor interface. In the case of binary surfactant/water systems, the anisotropic melting at the cubic/vapor interface occurs when the cubic → *L*2(*L*3) transition is approached. More precisely, different (*hkl*)-type of facets melt one after another as a function of the decreasing distance from the cubic → L2(L3) transition.

From theoretical considerations of Nozières *et al.* [21] results that the richness of faceting in soft crystals depends on the interfacial tension. At the cubic/*L*2(*L*3) interface this tension is so low that the whole interface is rough. In systems with the solubility gap, the cubic/*L*1 coexistence shows up and the corresponding interfacial tension is larger. Experiments have shown that as expected, faceting occurs in this case even if it is less "exuberant" then at cubic/vapor interfaces.

Studies of faceting in lyotropic systems lead also to discoveries of several other effects that have no equivalence in solid crystals. The *growth by redistribution*, the *ratchet effect*, and the *thermopermeation* are three of them. Let us stress that this last out-of-equilibrium effect is connected to former work P.G. de Gennes from whom the author learned so much.

ACKNOWLEDGMENTS

It is a pleasure to thank Patricia Cladis who initiated research on Blue Phases at LPS in Orsay and with whom first observations of faceting of Blue Phases I and II were done. The author is also grateful to Paul Sotta whose observations of faceted air bubbles inside a lyotropic cubic phase triggered the long series of experiments on faceting of interfaces in lyotropic systems presented here. Most of these experiments were made with the help of undergraduated and graduated students: D. Rohe, M. Bouchih, N. Ginestet, S. Popa-Nita, T. Plötzing, J. Grenier, S. Leroy, J. Okal, P. Faye, R. Sheshka, G. Saquet, J. Rizzi. I am very indebted to them. I address also my thanks to W. Gozdz, A. Ciach, and L. Latypova with whom the last series of studies on faceting of the *Im*3*m*/*L*1 interface was done. Enlightening discussions with B. Pansu, C. Even, and M. Imperor-Clerc were crucial for comprehension of phenomena occurring in lyotropic systems. The author is also grateful to Sebastien Balibar and Philippe Nozières for illuminating remarks on the theory of faceting. Contributions of V. Klein, S. Saranga, D. Brunello and J-L. Signoret were crucial for conception and realization of experimental setups. We are very grateful to Madame Sylvie Messager from Laserson Chimie Fine for providing us with a sample of phytantriol.

REFERENCES

[1] F. Reinitzer, Monatshefte für Chemie (Wien) 9 (1888) 421.
[2] O. Lehmann, Zeitschrift für Physikalische Chemie 4 (1889) 462.
[3] G. Friedel, Annales de Physique 18 (1922) 273.
[4] D. Demus, L. Richter, Textures of Liquid Crystals, Verlag Chemie, Weinheim, 1978.
[5] I. Dierking, Textures of Liquid Crystals, Wiley-VCH, Weinheim, 2003.
[6] C. Even, M. Impéror-Clerc, P. Pieranski, Eur. Phys. J. E 20 (2006) 89.
[7] A.P. Balachandran, Foundations of Physics 24 (1994) 455.
[8] P.M. Chaikin, T.C. Lubensky, Principles of Condensed Matter Physics, Cambridge University Press, Cambridge, 1995.
[9] P. Oswald, P. Pieranski, Nematic and Cholesteric Liquid Crystals: Concepts and Physical Properties, Taylor and Francis, New York, 2005, chapter 8.
[10] M. Impéror-Clerc, P. Sotta, Liq. Cryst. 27 (2000) 1001.
[11] M. Impéror-Clerc, M. Veber, A.-M. Levelut, ChemPhysChem 8(9) (2001) 533.
[12] C. Even, A. Gourbil, M. Impéror-Clerc, P. Pieranski, M. Veber, ChemPhysChem 12 (2002) 1031.
[13] K. Fontell, Colloid Polym. Sci. 268 (1990) 264.
[14] R.G. Laughlin, The Aqueous Phase Behavior of Surfactants, Academic Press, London, 1994.
[15] U. Schwarz, G. Gompper, Bicontinuous surfaces in self-assembling amphiphilic systems, in: K.R. Mecke, D. Stoyan (Eds.), Morphology of Condensed Matter: Physics and Geometry of Spatially Complex Systems, Lecture Notes in Physics, 600 Springer, Heidelberg, 2002, p. 107.
[16] M.L. Lynch, P.T. Spicer (Eds.), Bicontinuous Liquid Crystals, Surfactant Science Series vol. 127, Taylor and Francis, New York, 2005.
[17] M. Gradzielski, H. Hoffmann, G. Oetter, Colloid Polym. Sci. 268 (1990) 167.
[18] S. Radiman, C. Toprakcioglu, T. McLeish, Langmuir 10 (1994) 61.
[19] R. Bruinsma, J. Phys. II 2 (1992) 425.
[20] S. Leroy, P. Pieranski, J. Phys. Condens. Matter 18 (2006) 6453.
[21] P. Nozières, F. Pistolesi, S. Balibar, Eur. Phys. J. B 24 (2001) 387.
[22] G. Friedel, Leçons de Cristallographie, Librairie Scientifique Albert Blachard, Paris, 1964.
[23] F.C. Phillips, An Introduction to Crystallography, Longmans, New York, 1960.
[24] P. Nozières, Shape and growth of crystals, in: C. Godrèche (Ed.), Solids Far from Equilibrium, Cambridge University Press, Cambridge, 1992.
[25] P.A. Winsor, The influence of composition and temperature on the formation of mesophases in amphiphilic systems. The R-Theory of fused micellar phases, in: G.W. Gray, P.A. Winsor (Eds.), Liquid Crystals and Plastic Crystals, vol. 1, Halster, New York, 1974, chapter 5, fig. 5.13, p. 224.
[26] P. Sotta, J. Phys. II 1 (1991) 763.
[27] P. Pieranski, P. Sotta, D. Rohe, M. Imperor-Clerc, Phys. Rev. Lett. 84 (2000) 2409.
[28] P. Pieranski, L. Sittler, P. Sotta, M. Imperor-Clerc, Eur. Phys. J. E 5 (2001) 317.
[29] S. Leroy, J. Grenier, D. Rohe, C. Even, P. Pieranski, Eur. Phys. J. E 20 (2006) 19.
[30] H. Qiu, M. Caffrey, Biomaterials 21 (2000) 223.
[31] T. Plötzing, P. Pieranski, Eur. Phys. J. E 13 (2004) 179.
[32] J. Grenier, T. Plötzing, D. Rohe, P. Pieranski, Eur. Phys. J. E 19 (2006) 223.
[33] P. Pieranski, M. Bouchih, N. Ginstet, S. Popa-Nita, Eur. Phys. J. E 12 (2003) 239.
[34] P. Nozières, J. Phys. 50 (1989) 2541.
[35] P. Pieranski, J. Phys. Condens. Matter 17 (2005) S3333.
[36] R.R. Balmbra, J.S. Clunie, J.F. Goodman, Nature 222 (1969) 1159.
[37] D. Weaire, R. Phelan, Phil. Mag. Lett. 69 (1994) 107.

[38] A.V. Pethukov, I.P. Delbnya, D.G.A.L. Aarts, G.J. Vroege, H.N.W. Lekkerkerker, Phys. Rev. Lett. 90 (2003) 028304.
[39] P. Ziherl, R.D. Kamien, Phys. Rev. Lett. 85 (2000) 3528.
[40] M.L. Lynch, K.A. Kochvar, J.L. Burns, R.G. Laughlin, Langmuir 16 (2000) 3537.
[41] P.T. Spicer, K.L. Hayden, Langmuir 17 (2001) 5748.
[42] P. Wadsten-Hindrichsen, J. Bender, J. Unga, S. Engstrom, J. Coll. Interface. Sci. 315 (2007) 701.
[43] J. Barauskas, T. Landh, Langmuir 19 (2003) 9562.
[44] A sample offered by Madame Sylvie Messager from Laserson Chimie Fine..
[45] K. Larsson, J. Phys. Chem. 93 (1989) 7304.
[46] T. Landh, J. Phys. Chem. 98 (1994) 8453.
[47] J. Gustafsson, H. Ljusberg-Wahren, M. Almgren, K. Larsson, Langmuir 12 (1996) 4611.
[48] L. Latypova, From small cubic lyotropic crystals to cubosomes, Ph.D. thesis.
[49] H.G. von Schnering, R. Nesper, Z. Phys. B Condens. Matter 83 (1991) 83.
[50] P. Pieranski, Euro. Phys. Lett. 81 (2008) 66001.
[51] P.-G. de Gennes, C.R.A.S. 295 (1982) 959.
[52] P.-G. de Gennes, C. Taupin, J. Phys. Chem. 86 (1982) 2294.
[53] P. Pieranski, Liq. Cryst. 36 (2009) 1049.

CHAPTER TWO

How to Make a Stable Exocytotic Fusion Pore, Incompetent of Neurotransmitter and Hormone Release from the Vesicle Lumen?

Jernej Jorgačevski,[1,2] Boštjan Rituper,[1] Miha Fošnarič,[3] Ajda Flašker,[1] Nina Vardjan,[1,2] Matjaž Stenovec,[1,2] Maja Potokar,[1,2] Marko Kreft,[1,2] Veronika Kralj-iglič,[4] Aleš Iglič,[3] *and* Robert Zorec[1,2,*]

Contents

* Corresponding author. Tel.: +386 1 543 70 20; Fax: +386 1 543 70 36.
E-mail address: robert.zorec@mf.uni-lj.si

[1] Laboratory of Neuroendocrinology–Molecular Cell Physiology, Faculty of Medicine, University of Ljubljana, Ljubljana, Slovenia
[2] Celica, Biomedical Center, Tehnološki park 24, Ljubljana, Slovenia
[3] Laboratory of Biophysics, Faculty of Electrical Engineering, University of Ljubljana, Ljubljana, Slovenia
[4] Laboratory of Clinical Biophysics, Faculty of Medicine, University of Ljubljana, Ljubljana, Slovenia

Advances in Planar Lipid Bilayers and Liposomes, Volume 14
ISSN 1554-4516, DOI: 10.1016/B978-0-12-387720-8.00002-9

Abstract

In multicellular organisms, signaling is a necessity and an important mode of communication between cells is mediated by neurotransmitters, hormones, and other chemical messengers that are stored in secretory vesicles. In stimulated conditions secretory vesicles, which are trafficked to be docked at the plasma membrane, enter exocytosis, characterized by vesicle and plasma membrane merger. Due to repulsive forces of negatively charged membrane surfaces, it was long believed that the fusion pore is merely a short lived intermediate state leading irreversibly to a complete merger of both membranes. However, recent results show that the fusion pore is a rather stable structure, which can reversibly reopen to subnanometer diameters; dimensions too narrow to permit the exit of the cargo into the extracellular space. The aim of this chapter is to first review how can such a structure attain stability and compare two models in which membrane constituents are either isotropic or anisotropic in nature. Then we address the molecular nature of such a stable, release-unproductive fusion pore. We conclude that membrane constituents of the stable fusion pore membrane, being made of proteins and/or lipids, very likely consist of architectural elements that exhibit anisotropicity. The dynamics of fusion pore diameter is then determined by the density and architectural properties of these membrane constituents at fusion pore locales.

1. Introduction

When eukaryotic cells evolved from a prokaryotic precursor 1000 to 2000 million years ago, this was associated with a significant cell volume increase. This prompted a new structural organization to evolve, since diffusion-based signaling, efficient at nanometer distances, is inadequate to support the function of single nucleated cells, and consequently all multicellular organisms, which emerged once nucleated cells evolved. Besides the nucleus and other membrane-bound organelles, a key structural invention of eukaryotic cells is the secretory vesicle. This subcellular organelle has a complicated structure; its membrane consists of lipids and proteins. It is playing an essential role in the function of animals, including humans, where chemical signals, such as neurotransmitters and hormones, are stored. The highly concentrated chemical signals in the secretory vesicle are released into the extracellular medium following a stimulus delivery, which is thought to mediate the fusion of the secretory vesicle membrane with the plasma membrane. This latter event is part of the process of exocytosis.

Exocytosis involves the formation of the fusion pore-an aqueous channel between the vesicle and the plasma membranes. Despite intense investigation of the regulatory mechanisms of exocytosis in the last decades, the nature of the fusion pore remains obscure [1]. The main obstacle has been an inability to directly monitor the cargo release through single fusion

pores. Over the past decade, methodologies have been developed to monitor neurotransmitter release during single exocytotic events by detecting the amperometric oxidation current of the released transmitter [2–4]. However, neurotransmitter release proceeds in at least two main stages [5]. First, the vesicle establishes a stable fusion pore and then the pore suddenly enlarges (Fig. 1). In support of this view, amperometric spike-like currents are preceded by a small pedestal, called the "foot" of the spike [2]. Combined patch-clamp and amperometric studies have indicated that the foot represents neurotransmitter release through the initially formed fusion pore [6], although recent results have failed to confirm this [7]. On the other hand, the neurotransmitter released during the foot and during the main spike is the same [3], demonstrating the existence of a dynamic fusion pore. However, from the amperometric approach one can not conclude about the nature of dynamism of the fusion pore directly. In particular, it is not clear whether the relatively small release of transmitter during the initially formed fusion pore is due to a narrow fusion pore diameter and/or due to restrained kinetics-short effective fusion pore dwell-time. Moreover, the rather small signal associated with the foot versus the spike-like current and the transient and short-lived nature of the fusion pore preclude a detailed experimental investigation of the early fusion pore stages, which may not necessarily lead to the subsequent increased neurotransmitter/hormone flux rate. Furthermore, to learn more about the nature of the fusion pore in its initial stages, it would be ideal to have a preparation in which the initial fusion pore exhibits robust appearance and rarely proceeds to the full fusion stage (Fig. 1), thus permitting the study of the fusion pore properties more directly by electrophysiological means. A preparation that meets these criteria is the pituitary peptidergic vesicle [8].

The mechanism(s), by which the initial fusion pore attains stability, is poorly understood. Once formed, the fusion pore either fully widens, leading to the complete merger of vesicle membrane with the plasma

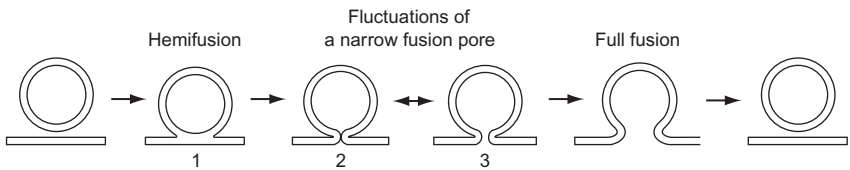

Figure 1 Stages a secretory vesicle has to undergo in exocytosis. Stages a secretory vesicle has to undergo to attain vesicle membrane merger with the plasma membrane via the hemifusion stage (1), the fusion pore formation (2), which exhibits stability and the fusion pore diameter may fluctuate to a wider stage (3) before full fusion, that is, full integration of the vesicle membrane into the plasma membrane. The integrated vesicle membrane may return to the cytosol via the process of endocytosis as depicted by the last stage on the right in the scheme.

membrane (full fusion exocytosis; [9]) or can reversibly close (kiss-and-run exocytosis; [10]). The patch-clamp membrane capacitance measurements [11] revealed that the fusion pore can also fluctuate between an open and a closed state in the subsecond time domain before full fusion [12] or can retain the transient nature of opening and closing for several tens of minutes [8,13,14]. Reopening of the same fusion pore indicates a remarkable stability, a property not observed previously. This and the fact that single exocytotic events can be observed with fluorescence microscopy in real time with styryl dyes [15], and by electrophysiological methods [16] render pituitary cells convenient preparations to study elementary properties of fusion events. Therefore, these cells were used to develop a mathematical model describing the observed energetic stability of the transient fusion pore [17].

2. Narrow Fusion Pores Are Stable Due to the Accumulation of Anisotropically Shaped Molecules in the Highly Curved Membrane Regions

One can consider that highly curved membrane domains consist of specially shaped membrane constituents. These can be classified as isotropic and anisotropic as is defined in Fig. 2 [see 18–20]. The appropriate ordering of such specially shaped membrane constituents in the highly curved membrane regions can likely increase the stability of the membrane region. Therefore, the model describing the fusion pore stability of peptidergic vesicles [17] sources on these considerations, and is based on the elasticity of the membrane layers which includes orientational ordering of membrane constituents that are anisotropic with respect to the axis perpendicular to the membrane [21]. Membrane constituents can be single molecules or small complexes of molecules, which have high negative intrinsic (spontaneous) curvatures [22]. Figure 3 summarizes the results of the model (taken with permission from [17]), showing that the correct ordering of membrane constituents result in the stable fusion pore. Figure 3A captures three states of a vesicle connected to the plasma membrane with fusion pores of different diameters. Top three diagrams show that the relative area density of anisotropic membrane constituents is increased in the membrane region of the fusion pore, which connects the vesicle with the plasma membrane. Note that the relative density of anisotropic membrane constituents in the pore region is increased as the fusion pore diameter is narrowed. Figure 3B reports the calculated membrane free energy (ΔF) as a function of the fusion pore diameter, for different inner diameters of the fusion pore Δ. It can be observed in Fig. 3B that for highly anisotropic membrane constituents a minimum of ΔF at certain Δ is predicted, as if the fusion pore can attain

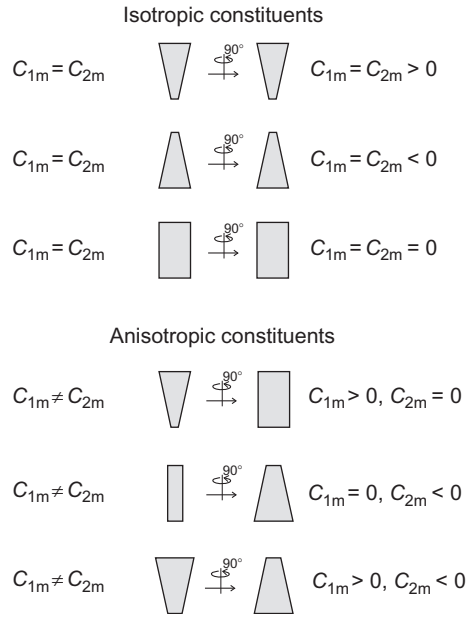

Figure 2 Isotropic and anisotropic shapes of membrane in highly curved membrane locales. Different possible intrinsic shapes (isotropic and anisotropic) of small membrane constituents in relation to intrinsic principal curvatures C_{1m} and C_{2m} [18–20].

distinct stable fusion pore diameters. Experimental evidence in support of discrete diameter states of a stable fusion pore was provided recently by studying the role of Munc18-1 proteins in fusion pore physiology [24]. A similar, although indirect, conclusion was reported previously [25]. Figure 3C shows that the stable equilibrium fusion pore diameter is narrower, if the membrane constituents have higher anisotropy. Moreover, Fig. 3D depicts the narrowness of such stable fusion pores in relation to the membrane thickness. Furthermore, it is important to note that such a model includes properties related to the observed relationship between the vesicle size and fusion pore properties [4,17].

3. Isotropic Membrane Constituents Are Unable to Generate Narrow Stable Fusion Pores?

A logical question is whether isotropic constituents (as defined in Fig. 2, with $C_{1m} = C_{2m} < 0$) can replace the anisotropic ones? The results on Fig. 4 show that this is not the case. Isotropic membrane constituents

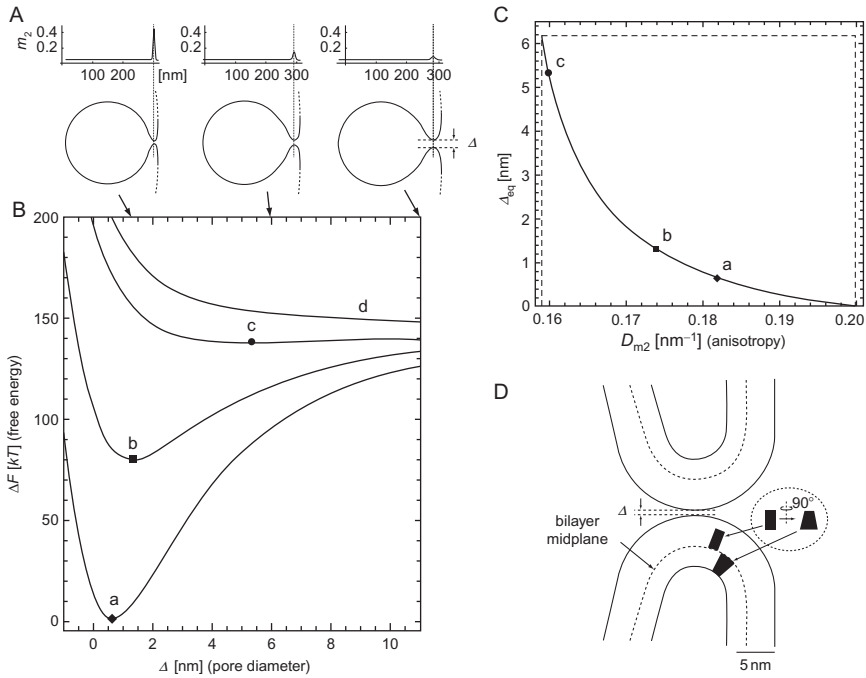

Figure 3 Stable configuration of the fusion pore (vesicle fused to the plasma membrane) as a function of the fusion pore diameter and intrinsic anisotropy of the membrane constituents. (A) The sum of the relative area densities of the anisotropic (type 2) membrane constituents ($m_2 = m_{2,1} + m_{2,2}$) in both membrane monolayers, shown for three different vesicle shapes (see panel below) of 300 nm in diameter, fused to the inner membrane surface. Anisotropic membrane constituents have $C_{1m,2} \approx 0$ and $C_{2m,2} = -1/3$ nm^{-1} which corresponds to $H_{m,2} = -D_{m,2} = -1/6$ nm^{-1}. (B) Free energy of the two component bilayer membrane (ΔF) as a function of the fusion pore diameter (Δ) calculated for different values of the intrinsic curvature deviator of the anisotropic (type 2) membrane constituents in the membrane bilayer $H_{m,2} = -D_{m,2}$: $-1/5.75$ nm^{-1} (a), $-1/6$ nm^{-1} (b), $-1/6.2$ nm^{-1} (c), $-1/6.5$ nm^{-1} (d). Arrows show the values of Δ(nm) corresponding to the shapes presented in panel A. (C) The calculated equilibrium fusion / pore diameter (Δ_{eq}), corresponding to the minimum of ΔF (see panel B) as a function of the anisotropy $D_{m,2} = |H_{m,2}|$ (see Appendix A and Materials and Methods in [17]). Note that on the left side of the vertical dotted line, the local minimum of ΔF does not exist (see curve (d) in panel B). Values of the model parameters are: $H_{m,1} = D_{m,1} = 0$, $K_1 = 10$ kT nm^2 [21,23], $K_2 = 100$ kT nm, $K_2 = -70$ kT nm^2, $w = -0.25$, $z_2 = 6$, $\bar{m}_{2,in} = \bar{m}_{2,out} = 0.02$, $m_0 = 1.67$ nm^{-2} and $R_0 = 1000$ nm, taken with permission from [17]. (D) Schematic representation of the fusion pore with anisotropic constituents in both membrane layers and a fusion pore diameter (Δ) of $\sim$0.6 nm. The thickness of the membrane layer containing glycolipids ($\sim$4 nm) is larger than the thickness of the membrane layer without them ($\sim$2.5 nm).

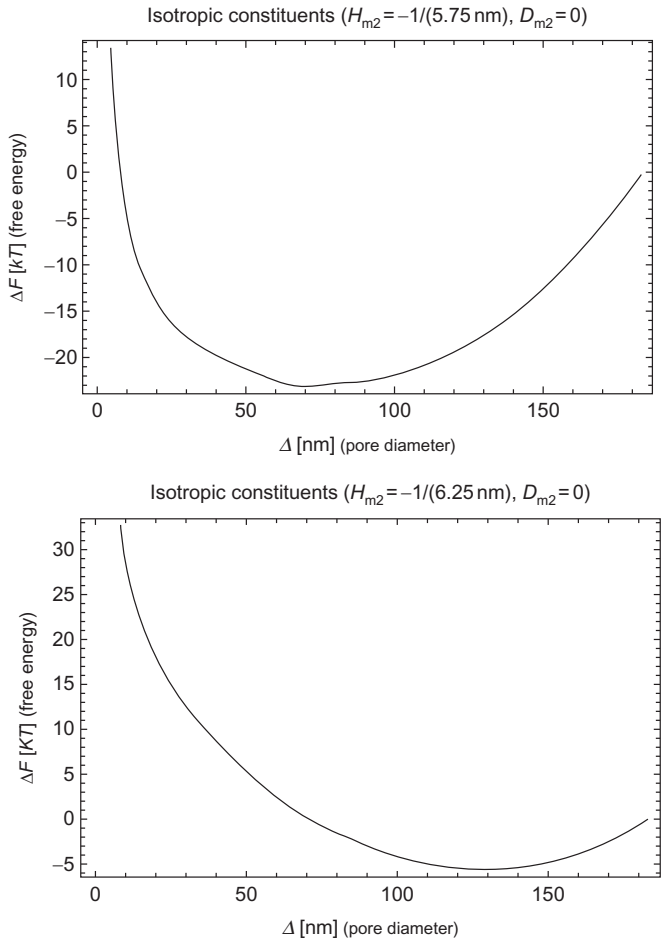

Figure 4 Membrane free energy as a function of the stable pore diameter with isotropic membrane constituents. Isotropic membrane constituents have intrinsic curvatures as marked in the figure. Values of other model parameters are given in the caption to Fig. 3.

only weakly accumulate in the inner and outer membrane layers in the vicinity of the saddle-like fusion pore and only form less stable fusion pores with diameters that are at least two orders of magnitude wider than those obtained by the anisotropic membrane constituents (with $C_{2m} < 0$ at $C_{1m} \approx 0$, compare the ordinates and abscissas with Fig. 3B). While the effects of isotropic inverted conical constituents on the membrane elasticity due to the mismatch of the intrinsic mean curvatures and the actual mean curvature of both layers in the two membrane layers partly cancel each other

due to opposing signs of the principal curvature in the two membrane layers, the effect of the average orientational ordering of the anisotropic constituents from both layers is summed up (since the average orientation of the anisotropic membrane constituents is different in both membrane layers of the fusion pore). This is one of the main reasons for the most striking difference between the effect of anisotropic membrane constituents and the isotropic inverted conical membrane constituents. Namely, the anisotropic membrane constituents (with $C_{2m} < 0$ at $C_{1m} \approx 0$) can stabilize the fusion pore geometry (as shown in Fig. 3B), while isotropic membrane constituents (with $C_{1m} = C_{2m} < 0$) cannot.

Thus, the answer is that a narrow stable fusion pore is likely made of anisotropic, rather than by isotropic membrane constituents. The nature of these, however, is not clear yet.

4. Protein and Lipids Affect Exocytosis and Fusion Pore Properties

Figure 3D shows the cross section of the fusion pore with a stable narrow diameter. It is remarkable that fusion pores with a diameter of about one-tenth of the membrane thickness can be formed. The question is, how and with which molecules such a structure can be built. It is clear that such a narrow pore is physiologically release unproductive (unable to release the vesicle cargo-neurotransmitters and hormones), since the pore is narrower than the size of even the smallest chemical messengers such as glutamate and acetylcholine [14,17,26]. Once such narrow pores are formed, they can enter into a release competent mode by stimulation [8,14,26], that is, the pore diameter widens or even generates the full fusion vesicle state (see Fig. 1).

In the next section, we discuss some of the key candidate molecules that may regulate the fusion pore formation and properties (Fig. 5). Although physiological results are still incomplete of how proteins and lipids affect the stages of exocytosis defined in Fig. 1, mainly biochemical and genetic studies (reviewed in [27]) place the SNARE proteins as prominent players in these processes, as it is shown in Fig. 5.

5. SNARE Zippering and SM-Proteins

The formation of the fusion pore may be driven by a conformational change of the SNARE complex (N-ethylmaleimide-sensitive fusion (NSF)-attachment protein receptor) [28]. Together with other interacting proteins (i.e., SM-proteins, for Sec1/Munc-18 like proteins), this complex is considered important in membrane merger [1], that is, in the overcoming

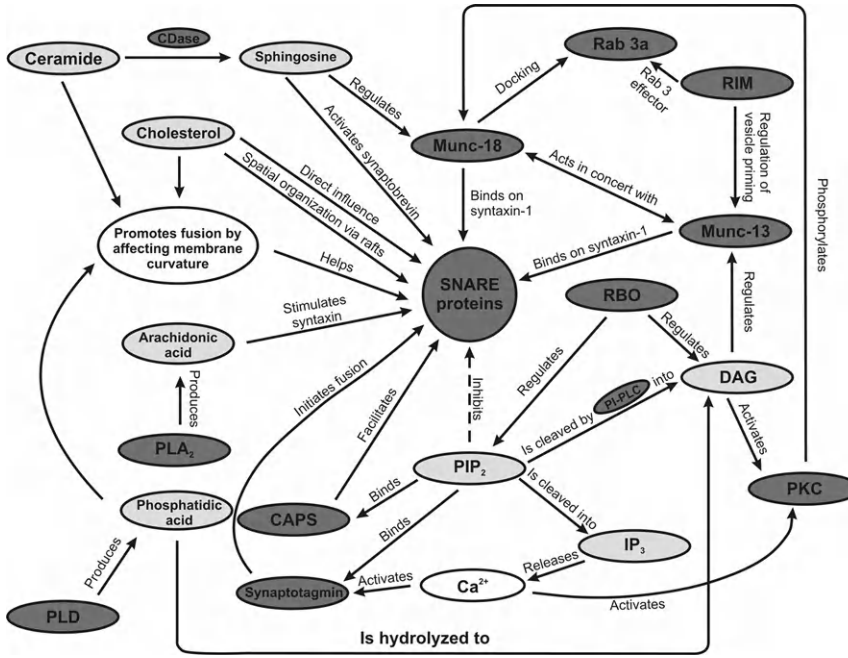

Figure 5 Interactions between lipids and proteins affecting exocytosis and fusion pore properties. Lipids and lipid derivatives are depicted in light gray, proteins are depicted in dark grey. Taken with permission from [27].

the repulsive electrostatic forces between phospholipid bilayers of the apposing membranes.

According to the "zipper hypothesis" [29], assembly is initiated at the N-terminal ends of the SNARE motifs and then progresses downhill an energy gradient toward the C-terminal membrane anchors, thus pulling the membranes together and initiating fusion. However, it is still contested as to how exactly SNARE zippering contributes to the membrane merger and in particular how these proteins relate to the fusion pore stability and the postfusion stages of exocytosis (Fig. 1).

For example, the trigger for secretions, an elevation of cytosolic [Ca^{2+}] is thought to be translated into dynamic fusion pore changes via the interaction of synaptotagmin-1, a Ca^{2+}-binding protein, with the SNARE complex [23]. Moreover, the SM family of proteins play a role in SNARE-mediated events, though their exact role(s) remains enigmatic. Neuronal isoform of mammalian Munc18, Munc18-1, was originally found to bind with high affinity to syntaxin-1, a SNARE member protein [30], which appears to have a role in determining fusion pore structure [31]. However, whether alterations in fusion pore dynamics involve specifically

changes in fusion pore conductance or/and fusion pore kinetics is unknown. The interpretation of fusion pore dynamics by SNARE mediated mechanisms is further complicated by the discovery that changing vesicle size affects its fusion pore [4,17]. In addition to proteins, negatively charged lipid molecules strongly affect the probability of exocytosis [22]. Thus, to understand how these complex mechanisms affect the dynamics of the fusion pore, one needs to consider a mechanism that can describe the stability of the fusion pore forming initially [17], and also predicts how interacting molecules (proteins and/or lipids) mediate changes in pore stability leading to fusion pore diameter enlargement. Which are the lipids that affect exocytosis and fusion pore properties? Do they modulate exocytosis indirectly (signaling) or directly?

6. Cytosolic Plasma Membrane PIP_2 Organizes Exocytotic Machinery

Phosphatidylinositol 4,5-biphosphate (PIP_2) is a member of membrane phospholipids of eukaryotic cells. Its inositol headgroup can be phosphorylated at single or multiple sites to give rise to a variety of phosphoinositides [32]. In addition to phosphorylation, hydrolysis of PIP_2 by PI-phospholipase C (PI-PLC) yields soluble inositol 1,4,5-tris-phosphate (IP_3) and membrane-resident diacylglycerol (DAG), both second messengers, playing multiple signaling roles [33]. PIP_2 is mainly located on the cytoplasmic leaflet of the plasma membrane and is known to be engaged in a series of regulated processes, including endocytic and exocytic membrane trafficking [34]. It is a necessary prerequisite for Ca^{2+}-dependent exocytosis [35]. Following activation of membrane fusion, plasma membrane PIP_2 becomes transiently depleted by phospholipase C activity downstream of Ca^{2+} signaling. Using PC12 cells, two enzymes (phosphatidylinositol transfer protein and phosphatidylinositol-4-phosphate-5-kinase) involved in metabolism of PIP_2, were identified to be required for vesicle priming [36]. Recently, it was shown that increase or decrease of plasmalemmal PIP_2 levels results in increase or decrease of primed vesicle pool [37] and that siRNA knockdown of previously mentioned enzymes results in impaired exocytosis of insulin [38]. PIP_2 self-organizes in lipid microdomains and colocalizes well with syntaxin clusters, which appears to be essential for Ca^{2+}-dependent exocytosis [39,40]. Interestingly, a substantial fraction of PIP_2 microdomains also colocalizes with calcium activated protein for secretion (CAPS) protein [40], which indicates that PIP_2 signals the recruitment of proteins required for exocytosis to sites necessary for vesicle docking and membrane merger.

Concentration of PIP_2 in lipid microdomains is estimated to be relatively high in comparison to the surrounding regions [41], which inhibits SNARE-dependent fusion in the absence of CAPS, most likely due to its inverted cone shape and positive curvature, which antagonizes highly negative curvature stalk models needed for transition to full fusion [41,42]. However, positively charged juxtamembrane regions of SNAREs may sequester PIP_2 from membrane regions that undergo high curvature transition during fusion, thus SNAREs themselves may help promote the curvature needed for completion of SNARE complex formation and transition to full fusion [43]. James *et al.* [41] suggest two mechanisms by which PIP_2 helps to regulate membrane fusion. First, inhibition is due to intrinsic positive curvature of PIP_2. Second, PIP_2 strongly facilitates rates of membrane fusion by PIP_2-binding proteins such as CAPS, synaptotagmin, or rabphilin which possess additional properties that promote SNARE function in fusion [41]. Thus, if one would regulate enzymes, that control PIP_2, then one could influence exocytosis. Indeed, the rolling blackout (*rbo*) gene encodes lipases, which are putative integral plasma membrane lipolytic enzymes that have an essential role in phospholipase C-dependent PIP_2/DAG signaling [44]. In rbo^{ts} (temperature-sensitive) *Drosophila* mutants, exocytosis appears to be blocked shortly before fusion step with accumulation of docked vesicles at presynaptic active zones, indicating a role for RBO protein downstream of vesicle docking [45], for example, through stabilization of the fusion pore in its narrow configuration which does not permit neurotransmitter release [17]. It is believed that RBO protein may be important for the local production of DAG and for the local regulation of PIP_2. Thus, if RBO protein is blocked, elevated concentrations of PIP_2 may negatively regulate Ca^{2+} channels thereby blocking Ca^{2+} influx and arresting docked synaptic vesicle fusion [45].

7. Polyunsaturated Fatty Acids Modulate Exocytosis via SNARE Proteins

Polyunsaturated fatty acid (PUFA) and phospholipases, which release them, have been known to play an important role in exocytosis [46]. Especially two types of PUFAs, omega-6 (arachidonic) and omega-3 (docosahexaeonic) variants, are essential in membrane fusion [47]. Besides ion channel modulation and cytoskeleton functions, PUFAs act on proteins that are pivotal in vesicle fusion—syntaxins. PUFAs are also major building blocks of cellular membranes [48] and possess favorable biophysical properties such as flexibility and solubility, which promote membrane fluidity [46]. It is known that a mutation of PUFA-related enzymes as well as PUFA deficient diet causes mental retardation [49] and deficient brain function

[50]. However, until recently not much has been known about mechanism of PUFAs actions. It was proposed [47] that omega-3 and omega-6 fatty acids act on syntaxin by changing its conformation thus allowing formation of Munc18-syntaxin-SNAP25 tripartite complex and promoting completion of SNARE complex formation [47,51].

8. Lipid Rafts, Ceramide, Sphingosine, and Cholesterol

Ceramide, a membrane sphingolipid, is unable to spontaneously transfer between lipid bilayers and has a tendency to self-aggregate into microdomains (lipid rafts) in association with other sphingolipids and cholesterol [52,53]. It was thought that ceramide acted as a secondary messenger. However, it is more likely that it acts by modifying interactions within lipid rafts, with consequences for raft coalescence, membrane curvature, and signaling emanating from these domains [54]. Additionally, with its small hydroxy headgroup and a cone shape, ceramide facilitates membrane fusion and fission by inducing negative membrane curvature [54].

Sphingosine is the backbone molecule of sphingolipids [55]. After being cleaved by ceramidase from ceramide, sphingosine is involved in many cellular functions, some of those being inhibition of voltage-operated calcium channels [56], modulation of excitability and/or transmitter release in the nervous system [57], control of apoptosis [58], and more. Recently, it was also discovered that sphingosine facilitates SNARE complex assembly by acting on synaptobrevin-2 [59] (Fig. 5) and that it regulates syntaxin-1 interaction with Munc18-1 [60], thus making it one of the most important lipids in regulation of exocytosis.

Cholesterol is a major lipid component of cellular membranes and is known to aggregate with saturated phospholipids and sphingolipids in lipid microdomains or rafts [61], where it plays a key organizing role in enhancing the tendency of saturated phospholipids and sphingolipids to segregate from unsaturated phospholipids [62]. Rafts themselves are considered to serve as sites for specific protein–lipid interactions [63] and several proteins necessary for the exocytotic process have been shown to associate with these cholesterol-rich domains, including SNAREs [64]. Thus, it is very likely that lipid rafts or specialized membrane sites serve as sites at or near which membrane fusion occurs [65,66].

There are several mechanisms by which cholesterol is capable of contributing to membrane fusion [67,68]. First, as a component of lipid rafts, cholesterol can organize essential proteins and lipids at the fusion site [67]. Removal of cholesterol from plasma/vesicle membrane breaks the structure of lipid microdomains causing dispersal of critical proteinaceous and lipidic

fusion machinery, thus interfering with efficient exocytosis. It was shown that removal of cholesterol by using methyl-β-cyclodextrin (MβCD) causes dose-dependent inhibition of the extent of triggered fusion and progressive shift to a higher [Ca^{2+}] [69]. Interestingly, the effect can be rescued by exogenous delivery of cholesterol or other molecules with similar or greater negative intrinsic curvature (α-tocoferol and dioleoylphosphatidyl-ethanolamine [DOPE]). However, only cholesterol can recover both the efficiency of fusion and the fundamental ability of vesicles to fuse [69,70]. Second important role of cholesterol in membrane fusion is its modulation of physical properties of the membrane, such as fluidity and/or curvature [71], the latter being extremely high in the fusion pore area [17]. Finally, as a functional ligand or cofactor, cholesterol can directly modulate the activity of proteins essential to the fusion process [67], for instance, synaptophysin/synaptobrevin interaction, which is necessary for efficient exocytosis, seems to critically depend on the cholesterol content at the fusion site [72]. At this site, cholesterol may participate in the relatively high density of anisotropic membrane components [17].

Cholesterol also appears to play an important role in fusion pore dynamics. It is believed that cholesterol regulates the persistence of the semi-stable fusion pore as shown electrophysiologically in single vesicle studies of pituitary peptidergic vesicles [17]. It is interesting to note that it is the cholesterol located in the cytosolic leaflet that may stabilize the fusion pore and not the one in the extracellular leaflet [73]. Wang *et al.* [73] indicate that all three previously depicted properties of cholesterol: viscosity of membrane, stiffness of lipid monolayer, negative intrinsic molecular curvature, and modulation of fusion proteins may contribute to this effect. These mechanisms may generate an anisotropically rich environment that is required for highly curved membrane structures [17]. Together, these properties make it energetically favorable to form and maintain the narrow waistline of the fusion pore. Thus, cholesterol removal on the cytoplasmic leaflet of the fusion pore lowers the overall probability for successful fusion [73].

9. Conclusions

We here discussed the fusion pore, a membranous intermediate that is formed upon the merger of vesicle and plasma membranes. Initially, it is an energetically stable, but release unproductive structure, if its diameter is in the subnanometer domain. The subsequent steps may lead to fusion pore dilation or even into full fusion stage, where the vesicle membrane collapses into the plasma membrane. The later stages are characterized by an enlarged pore diameter and are release productive. The stable and narrow fusion pore is likely established by accumulation of anisotropic membrane constituents

within the neck of the fusion pore. Which molecules exactly contribute to the anisotropic nature of the fusion pore is presently unknown; however, we here discussed some key proteins and lipids that play significant role. Future studies will focus in delineating the exact role of classes of molecules relevant for stabilizing the pore and also address the questions of narrow pore widening upon a physiological trigger.

ACKNOWLEDGMENTS

This work was supported by grants P3 521 0381, P3 0310 0381, J3-3632-1683; Z3-3510-1683, J3-9219-0381-06, P2-0232-1578, and CipKeBip from the Ministry of Higher Education, Science and Technology of the Republic of Slovenia.

REFERENCES

[1] M. Jackson, E. Chapman, The fusion pores of Ca^{2+}-triggered exocytosis, Nat. Struct. Mol. Biol. 15 (2008) 684–689.
[2] R.H. Chow, L. von Rüden, E. Neher, Delay in vesicle fusion revealed by electrochemical monitoring of single secretory events in adrenal chromaffin cells, Nature 356 (1992) 60–63.
[3] R.M. Wightman, J.A. Jankowski, R.T. Kennedy, K.T. Kawagoe, T.J. Schroeder, D.J. Leszczyszyn, J.A. Near, E.J. Diliberto, O.H. Viveros, Temporally resolved catecholamine spikes correspond to single vesicle release from individual chromaffin cells, Proc. Natl. Acad. Sci. USA 88 (1991) 10754–10758.
[4] L. Sombers, H. Hanchar, T. Colliver, N. Wittenberg, A. Cans, S. Arbault, C. Amatore, A. Ewing, The effects of vesicular volume on secretion through the fusion pore in exocytotic release from PC12 cells, J. Neurosci. 24 (2004) 303–309.
[5] L.J. Breckenridge, W. Almers, Currents through the fusion pore that forms during exocytosis of a secretory vesicle, Nature 328 (1987) 814–817.
[6] G. Alvarez de Toledo, R. Fernández-Chacón, J. Fernández, Release of secretory products during transient vesicle fusion, Nature 363 (1993) 554–558.
[7] M. Segovia, E. Alés, M.A. Montes, I. Bonifas, I. Jemal, M. Lindau, A. Maximov, T.C. Südhof, G. Alvarez de Toledo, Push-and-pull regulation of the fusion pore by synaptotagmin-7, Proc. Natl. Acad. Sci. USA 107 (2010) 19032–19037.
[8] M. Stenovec, M. Kreft, I. Poberaj, W. Betz, R. Zorec, Slow spontaneous secretion from single large dense-core vesicles monitored in neuroendocrine cells, FASEB J. 18 (2004) 1270–1272.
[9] J. Heuser, T. Reese, Evidence for recycling of synaptic vesicle membrane during transmitter release at the frog neuromuscular junction, J. Cell Biol. 57 (1973) 315–344.
[10] B. Ceccarelli, W. Hurlbut, A. Mauro, Turnover of transmitter and synaptic vesicles at the frog neuromuscular junction, J. Cell Biol. 57 (1973) 499–524.
[11] E. Neher, A. Marty, Discrete changes of cell membrane capacitance observed under conditions of enhanced secretion in bovine adrenal chromaffin cells, Proc. Natl. Acad. Sci. USA 79 (1982) 6712–6716.
[12] J. Fernandez, E. Neher, B. Gomperts, Capacitance measurements reveal stepwise fusion events in degranulating mast cells, Nature 312 (1984) 453–455.

[13] J. Jorgacevski, M. Stenovec, M. Kreft, A. Bajić, B. Rituper, N. Vardjan, S. Stojilkovic, R. Zorec, Hypotonicity and peptide discharge from a single vesicle, Am. J. Physiol. Cell Physiol. 295 (2008) C624–C631.
[14] N. Vardjan, M. Stenovec, J. Jorgacevski, M. Kreft, R. Zorec, Subnanometer fusion pores in spontaneous exocytosis of peptidergic vesicles, J. Neurosci. 27 (2007) 4737–4746.
[15] A.J. Cochilla, J.K. Angleson, W.J. Betz, Monitoring secretory membrane with FM1-43 fluorescence, Annu. Rev. Neurosci. 22 (1999) 1–10.
[16] R. Zorec, S. Sikdar, W. Mason, Increased cytosolic calcium stimulates exocytosis in bovine lactotrophs. Direct evidence from changes in membrane capacitance, J. Gen. Physiol. 97 (1991) 473–497.
[17] J. Jorgacevski, M. Fosnaric, N. Vardjan, M. Stenovec, M. Potokar, M. Kreft, V. Kralj-Iglic, A. Iglic, R. Zorec, Fusion pore stability of peptidergic vesicles, Mol. Membr. Biol. 27 (2010) 65–80.
[18] V. Kralj-Iglic, A. Iglic, H. Hägerstrand, P. Peterlin, Stable tubular microexovesicles of the erythrocyte membrane induced by dimeric amphiphiles, Phys. Rev. E. 64 (2000) 4230–4234.
[19] V. Kralj-Iglic, A. Iglic, G. Gomiscek, V. Arrigler, H. Hägerstrand, Microtubes and nanotubes of phospholipids bilayer vesicles, J. Phys. A. Math. Gen. 35 (2002) 1533–1549.
[20] M. Fosnaric, V. Kralj-Iglic, K. Bohinc, A. Iglic, S. May, Stabilization of pores in lipid bilayers by anisotropic inclusions, J. Phys. Chem. B. 107 (2003) 12519–12526.
[21] V. Kralj-Iglic, B. Babnik, R.D. Gauger, S. May, A. Iglic, Quadrupolar ordering of phospholipid molecules in narrow necks of phospholipid vesicles, J. Stat. Phys. 125 (2006) 727–752.
[22] M.A. Churchward, T. Rogasevskaia, D. Brandman, H. Khosravani, P. Nava, J. Atkinson, J. Coorssen, Specific lipids supply critical negative spontaneous curvature: an essential component of native Ca^{2+}-triggered membrane fusion, Biophys. J. 94 (2008) 3976–3986.
[23] J. Bai, C. Wang, D. Richards, M. Jackson, E. Chapman, Fusion pore dynamics are regulated by synaptotagmin t-SNARE interactions, Neuron 41 (2004) 929–942.
[24] J. Jorgačevski, M. Potokar, S. Grilc, M. Kreft, W. Liu, J.W. Barclay, J. Bückers, R. Medda, S.W. Hell, V. Parpura, R.D. Burgoyne, R. Zorec, Munc18-1 tuning of vesicle merger and fusion pore properties, J. Neurosci. 31 (2011) 9055–9066.
[25] M. Bretou, C. Anne, F. Darchen, A fast mode of membrane fusion dependent on tight SNARE zippering, J. Neurosci. 28 (2008) 8470–8476.
[26] N. Vardjan, M. Stenovec, J. Jorgacevski, M. Kreft, R. Zorec, Elementary properties of spontaneous fusion of peptidergic vesicles: fusion pore gating, J. Physiol. 585 (2007) 655–664.
[27] B. Rituper, B. Davletov, R. Zorec, Lipid–protein interactions in exocytotic release of hormones and neurotransmitters, J. Clin. Lipidol. 5 (2010) 747–761.
[28] R. Jahn, T. Lang, T. Südhof, Membrane fusion, Cell 112 (2003) 519–533.
[29] R. Jahn, R. Scheller, SNAREs: engines for membrane fusion, Nat. Rev. Mol. Cell Biol. 7 (2006) 631–643.
[30] R. Fisher, J. Pevsner, R. Burgoyne, Control of fusion pore dynamics during exocytosis by Munc18, Science 291 (2001) 875–878.
[31] X. Han, C. Wang, J. Bai, E. Chapman, M. Jackson, Transmembrane segments of syntaxin line the fusion pore of Ca^{2+}-triggered exocytosis, Science 304 (2004) 289–292.
[32] S. Corvera, A. D'Arrigo, H. Stenmark, Phosphoinositides in membrane traffic, Curr. Opin. Cell Biol. 11 (1999) 460–465.
[33] D. Poccia, B. Larijani, Phosphatidylinositol metabolism and membrane fusion, Biochem. J. 418 (2009) 233–246.

[34] T.F. Martin, Phosphoinositide lipids as signaling molecules: common themes for signal transduction, cytoskeletal regulation, and membrane trafficking, Annu. Rev. Cell Dev. Biol. 14 (1998) 231–264.
[35] D.A. Eberhard, C.L. Cooper, M.G. Low, R.W. Holz, Evidence that the inositol phospholipids are necessary for exocytosis. Loss of inositol phospholipids and inhibition of secretion in permeabilized cells caused by a bacterial phospholipase C and removal of ATP, Biochem. J. 268 (1990) 15–25.
[36] J.C. Hay, P.L. Fisette, G.H. Jenkins, K. Fukami, T. Takenawa, R.A. Anderson, T.F. Martin, ATP-dependent inositide phosphorylation required for Ca^{2+}-activated secretion, Nature 374 (1995) 173–177.
[37] I. Milosevic, J.B. Sørensen, T. Lang, M. Krauss, G. Nagy, V. Haucke, R. Jahn, E. Neher, Plasmalemmal phosphatidylinositol-4,5-bisphosphate level regulates the releasable vesicle pool size in chromaffin cells, J. Neurosci. 25 (2005) 2557–2565.
[38] L. Waselle, R.R. Gerona, N. Vitale, T.F. Martin, M.F. Bader, R. Regazzi, Role of phosphoinositide signaling in the control of insulin exocytosis, Mol. Endocrinol. 19 (2005) 3097–3106.
[39] L.J. Pike, J.M. Miller, Cholesterol depletion delocalizes phosphatidylinositol bisphosphate and inhibits hormone-stimulated phosphatidylinositol turnover, J. Biol. Chem. 273 (1998) 22298–22304.
[40] K. Aoyagi, T. Sugaya, M. Umeda, S. Yamamoto, S. Terakawa, M. Takahashi, The activation of exocytotic sites by the formation of phosphatidylinositol 4,5-bisphosphate microdomains at syntaxin clusters, J. Biol. Chem. 280 (2005) 17346–17352.
[41] D.J. James, C. Khodthong, J.A. Kowalchyk, T.F. Martin, Phosphatidylinositol 4,5-bisphosphate regulates SNARE-dependent membrane fusion, J. Cell Biol. 182 (2008) 355–366.
[42] L.V. Chernomordik, J. Zimmerberg, Bending membranes to the task: structural intermediates in bilayer fusion, Curr. Opin. Struct. Biol. 5 (1995) 541–547.
[43] T.J. Melia, D. You, D.C. Tareste, J.E. Rothman, Lipidic antagonists to SNARE-mediated fusion, J. Biol. Chem. 281 (2006) 29597–29605.
[44] F.D. Huang, E. Woodruff, R. Mohrmann, K. Broadie, Rolling blackout is required for synaptic vesicle exocytosis, J. Neurosci. 26 (2006) 2369–2379.
[45] N. Vijayakrishnan, K. Broadie, Temperature-sensitive paralytic mutants: insights into the synaptic vesicle cycle, Biochem. Soc. Trans. 34 (2006) 81–87.
[46] F. Darios, E. Connell, B. Davletov, Phospholipases and fatty acid signalling in exocytosis, J. Physiol. 585 (2007) 699–704.
[47] F. Darios, B. Davletov, Omega-3 and omega-6 fatty acids stimulate cell membrane expansion by acting on syntaxin 3, Nature 440 (2006) 813–817.
[48] L. Svennerholm, Distribution and fatty acid composition of phosphoglycerides in normal human brain, J. Lipid Res. 9 (1968) 570–579.
[49] I. Meloni, M. Muscettola, M. Raynaud, I. Longo, M. Bruttini, M.P. Moizard, M. Gomot, J. Chelly, V. des Portes, J.P. Fryns, H.H. Ropers, B. Magi, C. Bellan, N. Volpi, H. G. Yntema, S.E. Lewis, J.E. Schaffer, A. Renieri, FACL4, encoding fatty acid-CoA ligase 4, is mutated in nonspecific X-linked mental retardation, Nat. Genet. 30 (2002) 436–440.
[50] P.E. Wainwright, Dietary essential fatty acids and brain function: a developmental perspective on mechanisms, Proc. Nutr. Soc. 61 (2002) 61–69.
[51] E. Connell, F. Darios, K. Broersen, N. Gatsby, S.Y. Peak-Chew, C. Rickman, B. Davletov, Mechanism of arachidonic acid action on syntaxin-Munc18, EMBO Rep. 8 (2007) 414–419.
[52] K. Venkataraman, A.H. Futerman, Ceramide as a second messenger: sticky solutions to sticky problems, Trends Cell Biol. 10 (2000) 408–412.
[53] J.B. Massey, Interaction of ceramides with phosphatidylcholine, sphingomyelin and sphingomyelin/cholesterol bilayers, Biochim. Biophys. Acta 1510 (2001) 167–184.

[54] W.J. van Blitterswijk, A.H. van der Luit, R.J. Veldman, M. Verheij, J. Borst, Ceramide: second messenger or modulator of membrane structure and dynamics, Biochem. J. 369 (2003) 199–211.
[55] S. Lahiri, A.H. Futerman, The metabolism and function of sphingolipids and glycosphingolipids, Cell Mol. Life Sci. 64 (2007) 2270–2284.
[56] A. Titievsky, I. Titievskaya, M. Pasternack, K. Kaila, K. Törnquist, Sphingosine inhibits voltage-operated calcium channels in GH4C1 cells, J. Biol. Chem. 273 (1998) 242–247.
[57] L. Colombaioni, M. Garcia-Gil, Sphingolipid metabolites in neural signalling and function, Brain Res. Brain Res. Rev. 46 (2004) 328–355.
[58] O. Cuvillier, Sphingosine in apoptosis signaling, Biochim. Biophys. Acta 1585 (2002) 153–162.
[59] F. Darios, C. Wasser, A. Shakirzyanova, A. Giniatullin, K. Goodman, J. Munoz-Bravo, J. Raingo, J. Jorgacevski, M. Kreft, R. Zorec, J. Rosa, L. Gandia, L. Gutiérrez, T. Binz, R. Giniatullin, E. Kavalali, B. Davletov, Sphingosine facilitates SNARE complex assembly and activates synaptic vesicle exocytosis, Neuron 62 (2009) 683–694.
[60] A. Betz, U. Ashery, M. Rickmann, I. Augustin, E. Neher, T.C. Südhof, J. Rettig, N. Brose, Munc13-1 is a presynaptic phorbol ester receptor that enhances neurotransmitter release, Neuron 21 (1998) 123–136.
[61] H.A. Lucero, P.W. Robbins, Lipid rafts–protein association and the regulation of protein activity, Arch. Biochem. Biophys. 426 (2004) 208–224.
[62] J.R. Silvius, Role of cholesterol in lipid raft formation: lessons from lipid model systems, Biochim. Biophys. Acta 1610 (2003) 174–183.
[63] R. Lindner, H.Y. Naim, Domains in biological membranes, Exp. Cell Res. 315 (2009) 2871–2878.
[64] T. Lang, D. Bruns, D. Wenzel, D. Riedel, P. Holroyd, C. Thiele, R. Jahn, SNAREs are concentrated in cholesterol-dependent clusters that define docking and fusion sites for exocytosis, EMBO J. 20 (2001) 2202–2213.
[65] C. Salaün, D.J. James, L.H. Chamberlain, Lipid rafts and the regulation of exocytosis, Traffic 5 (2004) 255–264.
[66] P. Gonçalves, M. Stenovec, H. Chowdhury, S. Grilc, M. Kreft, R. Zorec, Prolactin secretion sites contain syntaxin-1 and differ from ganglioside monosialic acid rafts in rat lactotrophs, Endocrinology 149 (2008) 4948–4957.
[67] K.L. Furber, M.A. Churchward, T.P. Rogasevskaia, J.R. Coorssen, Identifying critical components of native Ca^{2+}-triggered membrane fusion. Integrating studies of proteins and lipids, Ann. N. Y. Acad. Sci. 1152 (2009) 121–134.
[68] M.A. Churchward, J.R. Coorssen, Cholesterol, regulated exocytosis and the physiological fusion machine, Biochem. J. 423 (2009) 1–14.
[69] M.A. Churchward, T. Rogasevskaia, J. Höfgen, J. Bau, J.R. Coorssen, Cholesterol facilitates the native mechanism of Ca^{2+}-triggered membrane fusion, J. Cell Sci. 118 (2005) 4833–4848.
[70] M.A. Churchward, T. Rogasevskaia, D. Brandman, H. Khosravani, P. Nava, J. Atkinson, J. Coorssen, Specific lipids supply critical negative spontaneous curvature: an essential component of native Ca^{2+}-triggered membrane fusion, Biophys. J. 94 (2008) 3976–3986.
[71] E.J. Dufourc, Sterols and membrane dynamics, J. Chem. Biol. 1 (2008) 63–77.
[72] D. Mitter, C. Reisinger, B. Hinz, S. Hollmann, S.V. Yelamanchili, S. Treiber-Held, T.G. Ohm, A. Herrmann, G. Ahnert-Hilger, The synaptophysin/synaptobrevin interaction critically depends on the cholesterol content, J. Neurochem. 84 (2003) 35–42.
[73] N. Wang, C. Kwan, X. Gong, E.P. de Chaves, A. Tse, F.W. Tse, Influence of cholesterol on catecholamine release from the fusion pore of large dense core chromaffin granules, J. Neurosci. 30 (2010) 3904–3911.

CHAPTER THREE

A Planar Lipid Bilayer in an Electric Field: Membrane Instability, Flow Field, and Electrical Impedance

F. Ziebert[1,2,3] *and* D. Lacoste[1,*]

Contents

* Corresponding author. Tel.: +33-140-795140; Fax: +33-140-794731.
E-mail address: david.lacoste@gmail.com

[1] Laboratoire de Physico-Chimie Théorique - UMR CNRS Gulliver 7083, ESPCI, 10 rue Vauquelin, Paris, France
[2] Physikalisches Institut, Albert-Ludwigs-Universität, Freiburg, Germany
[3] Institut Charles Sadron, 23 rue du Loess, Strasbourg, France

Advances in Planar Lipid Bilayers and Liposomes, Volume 14
ISSN 1554-4516, DOI: 10.1016/B978-0-12-387720-8.00003-0

Abstract

For many biotechnological applications it would be useful to better understand the effects produced by electric fields on lipid membranes. This review discusses several aspects of the electrostatic properties of a planar lipid membrane with its surrounding electrolyte in a normal DC or AC electric field.

In the planar geometry, the analysis of electrokinetic equations can be carried out quite far, allowing to characterize analytically the steady state and the dynamics of the charge accumulation in the Debye layers, which results from the application of the electric field. For a conductive membrane in an applied DC electric field, we characterize the corrections to the elastic moduli, the appearance of a membrane undulation instability and the associated flows which are built up near the membrane. For a membrane in an applied AC electric field, we analytically derive the impedance from the underlying electrokinetic equations. We discuss different relevant effects due to the membrane conductivity or due to the bulk diffusion coefficients of the ions. Of particular interest is the case where the membrane has selective conductivity for only one type of ion. These results, and future extensions thereof, should be useful for the interpretation of impedance spectroscopy data used to characterize, for example, ion channels embedded in planar bilayers.

1. Introduction

Bilayer membranes formed from phospholipid molecules are an essential component of the membranes of cells. The mechanical properties of equilibrium membranes are characterized by two elastic moduli, the surface tension and the curvature modulus [1], which typically depend on the electrostatic properties of the membranes and its surroundings [2]. Understanding how these properties are modified when the membrane is driven out of equilibrium is a problem of considerable importance to the physics of living cells. A membrane can be driven out of equilibrium in many ways, for instance by ion concentration gradients or by electric fields.

Quite generally one can distinguish between systems in which the electric field is applied externally and systems which are able to self-generate electric fields.

1.1. Membranes in Externally Applied Electric Fields

The external application of electric fields on lipid films is used to produce artificial vesicles (electroformation), as well as to create holes in the membrane (electroporation) [3]. Both processes are important for biotechnological applications and they are widely used experimentally. However, they are still not well understood theoretically. The research on electroformation is motivated by the hope to produce artificial lipid vesicles in a controlled

and simple way, which will be key to many biotechnological applications. Cell electroporation is a popular technology and biomedical applications of *in vivo* cell electropermeabilization [4] are gaining momentum for drug and nucleic acids electrotransfer and for the destruction of tumor cells for cancer treatment [5].

In view of the importance of these applications, many research efforts have been devoted to study and understand deformations of giant unilamellar vesicles (GUVs) due to the application of electric fields. In the presence of an AC electric field, GUVs show a rich panel of possible behaviors and morphological transitions depending on experimental conditions—electric field frequency, conductivities of the medium and of the membrane, salt concentration, etc., [6,7]. A theoretical framework involving hydrodynamics and a continuum mechanics description of the membrane has been developed, which accounts quantitatively for the observed equilibrium and nonequilibrium shapes taken by the vesicles in the presence of an AC electric field [8,9]. For a clear and self-contained presentation of this theoretical framework, we recommend the chapter "Non-equilibrium dynamics of lipid membranes: deformation and stability in electric fields" by P. Vlahovska [53].

The application of external fields is also interesting as a means to move fluids via electro-osmosis [10,11] and to self-assemble colloidal particles, for various technological applications. Moreover, the ability to move fluids and nanoparticles at small scales is used in many biological systems. For instance, membrane-bound ion pumps and channels are able to transport water (for instance in aquaporin channels) and ions (in ionic pumps and channels) in a particularly selective and efficient way, which one would like to reproduce in artificial or biomimetic microfluidic devices.

1.2. Membranes in Self-generated Electric Fields

In some cases of biological relevance, membranes are able to self-generate an electric field, due to embedded ion channels or pumps. This can be achieved because the channels are able to transport ions from one side of the membrane to the other in a selective way, either down their concentration gradient in passive transport or against it in active transport, for example, coupled to the hydrolysis of Adenosine triphosphate or activated by light. Probably the best known example is the opening and closing of ion channels in nerve cells allowing the transmission of an electric signal via action potentials [12]. For all these reasons, ion channels and pumps play an essential role in many biological functions of a cell [13].

In order to better understand how nerve cells operate *in vivo*, it would be helpful to construct an in vitro biomimetic equivalent which would have some key features of the *in vivo* system, such as the ability to generate an action potential, but without the complexity of a real nerve cell. Active

membranes, which are GUVs containing ion pumps such as bacteriorhodopsin [14–16] are a promising system to achieve this goal.

The main purpose of this review is to propose and analyze a simple model to foster the understanding of various effects resulting from electric fields acting on a planar lipid membrane. Although we are mostly interested in applications to biological or biomimetic systems composed of lipid membranes, we would like to point out that the theoretical framework presented here is very general. It can be easily adapted to analyze the electrical properties of artificial membranes which can have very different properties from biological membranes (as far as, e.g., ionic conductivities or the bending stiffness are concerned).

This review is organized as follows: in Section 2 we present the model for a planar lipid membrane and its surrounding fluid in an applied electric field. In this section, we will restrict ourselves to the case of a DC field. In particular we will focus on (i) the electrostatic and electrokinetic steady-state corrections to the elastic moduli of the membrane due to the application of the electric field, see Section 2.3; (ii) the flow fields which can be predicted from such an approach, at steady state and in the case that the membrane is ion-conductive, see Section 2.4. In Section 2.5 we will compare the model predictions to two relevant experiments. More details on this theoretical framework, as well as an extension to the nonlinear electrostatic regime using the Poisson–Boltzmann (PB) equation, can be found in Refs. [17–20]. Finally, in Section 3 we present an analysis of the model in the presence of time-dependent AC electric fields. We provide derivations for the impedance of the system from the underlying electrokinetic equations, for situations where the membrane is either blocking or selectively conductive for ions.

2. A Quasi-Planar Membrane in a DC Electric Field

The mechanical properties of membranes at equilibrium are characterized by two elastic moduli, the surface tension and the bending modulus. These moduli typically depend on electrostatic properties, and their modifications in the case of charged membranes or surfaces in an electrolyte have been examined theoretically in various situations: in the linearized Debye–Hückel approximation as well as in the nonlinear PB regime, for lipid monolayers and symmetric bilayers [2,21–23]. More recently, charged asymmetric bilayers with unequal Debye lengths on both sides of the membrane [24] and an uncharged membrane in a DC field [25] have been investigated.

In all the works mentioned above, a free energy approach has been used. Note that while this method works well for equilibrium membranes, it is not applicable to situations in which the membrane fluctuations have a nonequilibrium origin, as in the case of active membranes containing ion channels [14,15,26,27] or in the case of a membrane in a time-dependent electric field. In our recent work [17–20], we thus have studied this problem using an electrokinetic approach, which does not have the limitations of a free energy formulation. In this framework we allow for a finite conductivity of the membrane due to, for example, ion channels or pumps, and the ion transport is described using a Poisson–Nernst-Planck (PNP) approach [28–30]. The electrostatic corrections to the elastic moduli and the fluid flows in the electrolyte are then obtained by imposing the overall force balance at the membrane.

Two additional points are worth emphasizing: first, our approach is able to correctly describe the capacitive effects of the membrane and of the Debye layers while keeping the simplicity of the "zero-thickness approximation" on which most of the literature on lipid membranes is based. This is accomplished by the use of an effective Robin-type boundary condition (BC) at the membrane. Second, as the method is based on a calculation of the general force balance at the membrane, additional nonequilibrium processes could be included into the model rather easily. For simplicity we investigate here only the effects of ionic currents flowing through the membrane, which in turn affect the fluid flow near the membrane. Other nonequilibrium effects that could be included as well are for instance ion channel stochasticity or active pumping.

2.1. Model Equations: Electrostatics

Figure 1 shows a sketch of the planar geometry that is studied: we consider a steady current driven by a DC voltage drop V across two electrodes separated by a fixed distance L. The membrane is quasi-planar and located at $z = 0$. It is embedded in an electrolyte of monovalent ions with number densities n^+ and n^-. It contains channels for both ion species but is itself neutral, that is, does not carry fixed charges. The channels or pumps are assumed to be homogeneously distributed in the membrane and enter only in the effective conductance G, as introduced below. A point in the membrane is characterized in the Monge representation by the height function $h(\mathbf{r}_\perp)$, where $\mathbf{r}_\perp$ is a two-dimensional in-plane vector. The base state of this problem is a flat membrane. Hence the electric field, assumed to be perfectly aligned in z-direction, is perpendicular to it. We assume a quasi-static approach [18,25] in which membrane fluctuations are much slower than the characteristic diffusion time $\tau = 1/D\kappa^2$ for the ions to diffuse a Debye length.

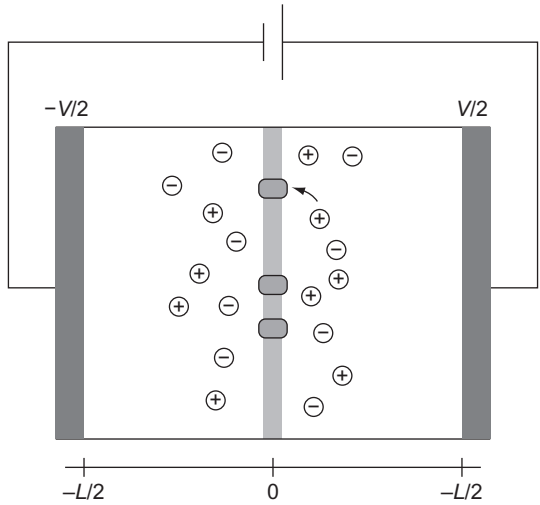

Figure 1 Sketch of a quasi-planar membrane embedded in a symmetric electrolyte. The initially flat bilayer membrane is represented by the plane $z = 0$. The membrane fluctuations around this base state have not been represented. A voltage $\pm V/2$ is applied on each electrode, which are separated by a distance L. The membrane carries ion channels which give rise to a conductance G.

In the electrolyte, the electric potential ϕ obeys Poisson's equation

$$\nabla^2\phi = -\frac{1}{\varepsilon}(en^+ - en^-) = -\frac{2}{\varepsilon}\rho. \tag{1}$$

Here e is the elementary charge, ε is the dielectric constant of the electrolyte and we have introduced *half* of the charge density,

$$\rho = e\frac{n^+ - n^-}{2}. \tag{2}$$

For the sake of simplicity, we assumed a symmetric 1:1 electrolyte, thus far away from the membrane $n^+ = n^- = n^\star$, and the total system is electrically neutral. The densities of the ion species obey the PNP equations

$$\partial_t n^\pm + \nabla\cdot\mathbf{j}^\pm = 0, \quad \mathbf{j}^\pm = D\left(-\nabla n^\pm \mp n^\pm \frac{e}{k_\mathrm{B}\mathrm{T}}\nabla\phi\right), \tag{3}$$

where $\mathbf{j}^\pm$ are the particle current densities of the ions and $k_\mathrm{B}T$ is the thermal energy. We will assume here that both ion types have the same diffusion coefficient D. Note that we will discuss the effects of differing diffusion coefficients for an applied AC voltage in Section 3.4.

Since we are primarily interested in the behavior close to the membrane, for the BCs far away from the membrane we assume

$$\phi(z = \pm L/2) = \pm V/2, \tag{4}$$

$$\rho(z = \pm L/2) = 0. \tag{5}$$

Equation (4) states that the potential at the electrodes is held fixed externally. This BC is quite oversimplified for real electrodes, but captures the main effects of the electric field, see the discussion in Ref. [19]. We have also assumed that the distance between the electrodes is much larger than the Debye length, $L \gg \lambda_D = \kappa^{-1}$, where

$$\kappa = \sqrt{\frac{2e^2 n^*}{\varepsilon k_B T}} = \lambda_D^{-1}. \tag{6}$$

Hence, as already mentioned above, the bulk electrolyte is quasi-neutral with negligible charge density (compared to the total salt concentration) and far from the membrane Eq. (5) holds.

The BC at the membrane is crucial to correctly account for capacitive effects. We use the Robin-type BC (see Appendix for a derivation)

$$\lambda_m(\mathbf{n}\cdot\nabla)\phi_{|z=h^+} = \lambda_m(\mathbf{n}\cdot\nabla)\phi_{|z=h^-} = \phi(h^+) - \phi(h^-), \tag{7}$$

where $\mathbf{n}$ is the unit vector normal to the membrane and

$$\lambda_m = \frac{\varepsilon}{\varepsilon_m} d. \tag{8}$$

λ_m is a length scale containing the membrane thickness d and the ratio of the dielectric constants $\varepsilon/\varepsilon_m$ of the electrolyte and the membrane. Note that in Eq. (7), the membrane plays a similar role as the Stern layer in the description of Debye layers near a charged interface. This BC was rederived for electrodes sustaining Faradaic current [31,32] or charging capacitively [33], and was applied for membranes in Refs. [18,19,30]. There it was shown to properly account for the jump in the charge distribution which occurs near the membrane as a result of the dielectric mismatch between the membrane and the surrounding electrolyte.

In addition to Eq. (7), we impose the continuity of the bulk current $j^\rho_{|z=0}$ at the membrane. This BC involves the ohmic law

$$j^\rho_{|z=0} = -\frac{G}{e}[\mu^\rho]_{z=0}, \tag{9}$$

where G denotes the membrane conductance per area and μ^{ρ} the electrochemical potential. The electrostatic potential and the ion densities can now be obtained by solving Eqs. (1, 2) in the linear Debye–Hückel approximation and one obtains [19]:

(i) the jump of the charge density at the membrane, ρ_m,
(ii) the current through the membrane, j_m, and
(iii) the electric field inside the membrane, E_0^m:

$$\rho_m = \frac{(\varepsilon\kappa^2/2)V - (j_m/D)(L+\lambda_m)}{2+\kappa\lambda_m}, \tag{10}$$

$$j_m = -j^{\rho} = \frac{GV}{1+(2/\varepsilon\kappa^2 D)GL}, \tag{11}$$

$$E_0^m = -\frac{1}{d}\left[\frac{2}{\varepsilon\kappa^2}\left(-\frac{j_m L}{D} - 2\rho_m\right) + V\right]. \tag{12}$$

For simplicity, in the derivation of Eqs. (10)–(12) we assumed equal ion conductivities ($G^+ = G^- = G$) and a symmetric electrolyte on both sides of the membrane ($\kappa^{>0} = \kappa^{<0} = \kappa$). Note that the method presented in this section can be easily extended to cover more general cases. In addition, the nonlinear electrostatic problem (keeping the PB equation) can be still solved analytically in the non-conductive case. The nonlinear generalizations of Eqs. (10)–(12) can be found in Ref. [20].

2.2. Model Equations: Hydrodynamics and Force Balance at the Membrane

The hydrodynamics of the electrolyte is described by the incompressible Stokes equation, $-\nabla p + \eta\nabla^2 \mathrm{v} + \mathbf{f} = 0$ with $\nabla \cdot \mathbf{v} = 0$, where $\mathbf{v}$ is the velocity field of the electrolyte, η its viscosity, p the hydrostatic pressure and $\mathbf{f} = -2\rho\nabla\phi$ the electric driving force. From the solution of the electrostatic and the hydrodynamic problem, one obtains the total stress tensor

$$\tau_{ij} = -p\delta_{ij} + \eta\left(\partial_i v_j + \partial_j v_j\right) + \varepsilon\left(E_i E_j - \frac{1}{2}\delta_{ij}E^2\right), \tag{13}$$

which contains the pressure, the viscous stresses in the fluid and the Maxwell stresses.

The lipid bilayer membrane, on the other hand, behaves as a two-dimensional fluid which can store elastic energy in bending deformations.

More precisely, its elastic properties can be described by the standard Helfrich free energy

$$F_{\mathrm{H}} = \frac{1}{2}\int d^2\mathbf{r}_\perp \left[\Sigma_0(\nabla h)^2 + K_0\left(\nabla^2 h\right)^2\right], \tag{14}$$

where Σ_0 is the bare surface tension and K_0 the bare bending modulus of the membrane.

All forces present in the system, the electrostatic, viscous, and elastic ones, have to fulfill the force balance equation. The latter states that the discontinuity of the normal–normal component of the stress tensor, as defined in Eq. (13) and evaluated at the membrane position, must equal the restoring force due to membrane elasticity, hence

$$-\left(\tau_{z\,z,1|z=h^+} - \tau_{zz,1|z=h^-}\right) = -\frac{\partial F_{\mathrm{H}}}{\partial h(\mathbf{r}_\perp)} = \left(-\Sigma_0 k_\perp^2 - K_0 k_\perp^4\right) h(\mathbf{k}_\perp)\cdot \tag{15}$$

Here the index 1 in the stress tensor refers to the order of an expansion with respect to the membrane height field $h(\mathbf{r}_\perp)$. Note that at zeroth order, the membrane is flat and thus only electric forces and osmotic pressure balance. By expanding to linear order in the height field $h(\mathbf{r}_\perp)$, and using

$$h \propto h_0 \mathrm{e}^{i\mathbf{k}_\perp\cdot\mathbf{r}_\perp + s(\mathbf{k}_\perp)t}, \tag{16}$$

Equation (15) yields the growth rate $s(\mathbf{k}_\perp)$ of membrane fluctuations. Details of the derivation of $s(\mathbf{k}_\perp)$ can be found in Refs. [17–19]. We would like to emphasize that the force localized at the membrane surface is a priori unknown in this problem. Thus it must be determined self-consistently from the BCs for the velocity and the stress.

2.3. Growth Rate and Renormalized Elastic Moduli

The force balance Eq. (15) determines the growth rate $s(\mathbf{k}_\perp)$ entering the normal stress difference,

$$\eta k_\perp s(\mathbf{k}_\perp) = -\frac{1}{4}(\Sigma_0 + \Delta\Sigma)k_\perp^2 - \Gamma_\kappa k_\perp^3 - \frac{1}{4}(K_0 + \Delta K)k_\perp^4\cdot \tag{17}$$

The electrostatic corrections to the surface tension, $\Delta\Sigma = \Delta\Sigma_\kappa + \Delta\Sigma_m$, and to the bending modulus, $\Delta K = \Delta K_\kappa + \Delta K_m$ can be decomposed into:

(i) an outside contribution due to the charges accumulated in the Debye layers and denoted with the index κ;

(ii) an inside contribution due to the voltage drop at the membrane and denoted with an index m. They are given by

$$\Delta\Sigma_\kappa = -4\frac{\rho_m^2}{\varepsilon\kappa^3} - 16\frac{\rho_m j_m}{\varepsilon\kappa^4 D}, \quad \Delta K_\kappa = \frac{3\rho_m^2}{\varepsilon\kappa^5} \tag{18}$$

for the contribution due to the Debye layers and by

$$\Delta\Sigma_m = -\varepsilon_m\left(E_0^m\right)^2 d, \quad \Delta K_m = \varepsilon_m\left(E_0^m\right)^2\left(\frac{d^3}{12} - \frac{\rho_m}{E_0^m}\frac{d}{\varepsilon\kappa^3}\right) \tag{19}$$

for the contribution due to the field inside the membrane.

Note that in Eq. (17), one also obtains a purely nonequilibrium correction $\Gamma_\kappa = (4\rho_m j_m)/(\varepsilon\kappa^5 D)$. It would correspond to a term proportional to $k_\perp^3$ in an "effective membrane free energy" incorporating the Maxwell stresses. At equilibrium such a term is forbidden by symmetry, but in a nonequilibrium situation, where the membrane sustains a current $j_m \neq 0$, it is allowed. For realistic parameters, however, this term is very small, see Ref. [18] for a detailed discussion.

The inside contribution to the membrane surface tension is always negative, see Eq. (19). The same is typically true for the outside contribution, see Eq. (18) and note that $\rho_m, j_m > 0$. Hence these contributions can overcome the bare surface tension Σ_0. If this is the case, an instability towards membrane undulations sets in. Such an instability had already been described for the high salt limit in Ref. [34]. Note that the linearized theory developed here describes only the early stages of the instability, but it is more general than previous works since it is not limited to the high salt limit and in addition accounts for hydrodynamic effects. The linear growth rate of the membrane fluctuations given by Eq. (17) is shown in Fig. 2 in rescaled units. We scaled the wave vector by κ, hence $k' = k_\perp/\kappa$ and the time by the typical time for ions to diffuse a Debye length, $\tau = 1/D\kappa^2$. The control parameter of the instability is the external voltage V. Figure 2 shows the growth rate for three different levels of the voltage: the dashed line is for $V = 0.7$ V, which lies below the threshold of the instability, all wave numbers are damped and the membrane is stable. The solid and the dash-dotted line correspond to $V = 0.75$ and 0.8 V. These values are above threshold and the growth rate is positive for a finite wave number window.

For a more detailed discussion of the dependence of the corrections to the elastic moduli, the instability threshold and the characteristic wave number as a function of salt concentration and membrane conductivity, we refer the reader to Refs. [18,19].

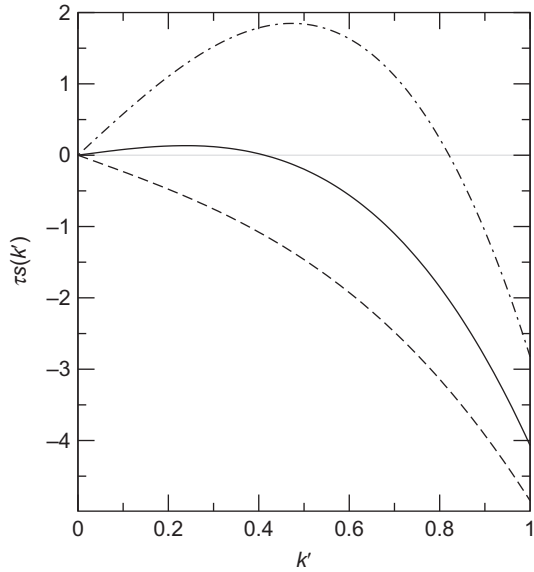

Figure 2 The renormalized growth rate or dispersion relation, τs, as a function of the rescaled wave number $k' = k_\perp/\kappa$ for three voltages: $V = 0.7$ V (dashed line), $V = 0.75$ V (solid line), and $V = 0.8$ V (dash-dotted line). We have used the following parameters: dielectric constants $\varepsilon = 80\varepsilon_0$ and $\varepsilon_m = 2\varepsilon_0$; membrane thickness $d = 5$ nm leading to $\lambda_m = (\varepsilon/\varepsilon_m)d = 200$ nm; diffusion coefficient of ions $D = 10^{-9}\text{m}^2\text{s}^{-1}$; viscosity $\eta = 10^{-3}$ Pas; inverse Debye length $\kappa = 2 \times 10^7$ m^{-1}; bare surface tension $\Sigma_0 = 1$ mN m^{-1}; bare bending modulus $K_0 = 10\ k_\text{B}T$. Here we assumed a non-conductive membrane, $G = 0$.

2.4. Flow Fields Near a Driven Membrane

We now summarize the main features of the fluid flows which arise near the membrane when it is driven by ionic currents [18]. Figure 3 was generated by selecting the fastest growing wave number and using the corresponding maximum growth rate. The shape of the membrane undulation is represented with the black solid curves. Figure 3C shows the flow field for a high membrane conductance and low salt, in the regime where the membrane is unstable due to the electrostatic correction to the surface tension and thus starts to undulate. The resulting flow is a superposition of two distinct flows: first, the typical flow associated to a membrane bending mode [35] as shown in Fig. 3A. Second, the flow which results from the ion transport across the membrane. The latter flow has the typical counter-rotating vortices of an ICEO flow [36], as shown in Fig. 3B. Clearly, the superposition of these two flow contributions, Fig. 3C, results in a parallel flow close to the membrane, in contrast to the usual bending mode flow given by Fig. 3A.

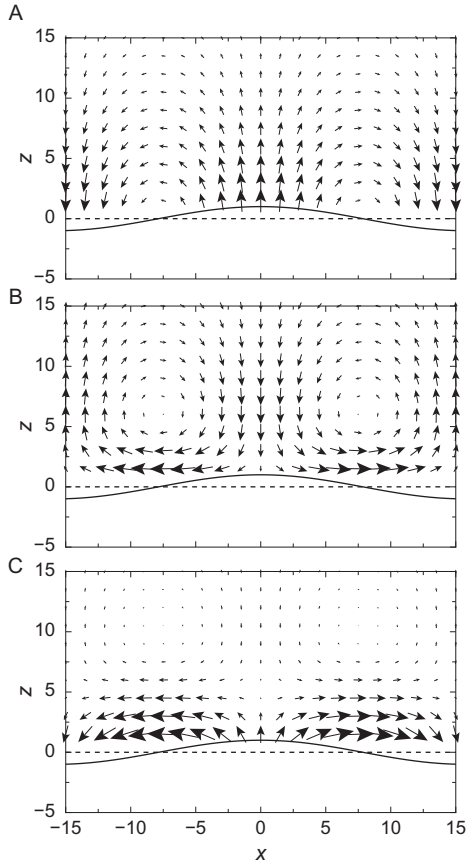

Figure 3 Representation of the flows around the membrane beyond the instability threshold. The orientation of the electric field is toward negative values of z. (A) shows the flow generated by the membrane bending mode. (B) shows the ICEO flow. Finally, (C) shows the actual flow, which is the superposition of the former two and results in a strong flow near the membrane, oriented parallel to the surface. Both axes are scaled by the Debye length κ^{-1}. Parameters are as in Fig. 2 except $V = 3.165$ V, $\kappa = 10^7$ m^{-1}, $G = 10$ Sm^{-2} and $L = 10$ μm.

For most realistic parameters—modest conductivities, not too low salt—the flow generated by membrane bending is usually dominating and hides the small ICEO contribution. To be able to observe the flows of Fig. 3, a high membrane conductance G and low salt are needed. Also, since for macroscopic electrode distances L (e.g., of the order of millimeters), the voltage needed to induce the instability is very high, we have assumed a microscopic electrode distance of $L = 10$ μm. While it might still be possible to observe flows for higher salt and macroscopic electrode

separations, such situations cannot be analyzed within the Debye–Hückel approximation used here.

Note that somewhat similar looking flow patterns have been recently observed experimentally in vesicles subject to AC electric fields in Ref. [6]. On closer inspection, however, it appears that these flows most probably have a different origin from the ICEO flows, since they are more likely to result from electrophoresis of charged lipids within the membrane.

2.5. Applications to Specific Experiments

Here we will briefly discuss how the framework presented above can be applied to recent experiments: the first experiment studied supported membranes subject to an electric field [37], while the second one investigated active membranes [14–16].

Lecuyer *et al.* [37] recently performed neutron reflectivity measurements on a system consisting of two nearby membrane bilayers in an external AC electric field. One of the bilayers was close to the bottom electrode and used to protect the second one from interacting with the wall. The bare values of the elastic moduli were known from X-ray off-specular experiments for a similar system [38], yielding $\Sigma_0 \simeq 0.5$ mN m^{-1} and $K_0 \simeq 15\ k_B T$. The experiments were performed in an AC electric field at several frequencies. For the lowest frequency (10 Hz) and for a voltage of $V = 5$ V, the electrostatic corrections to the surface tension and bending modulus were found to be $\Delta\Sigma \simeq -1 \pm 0.15$ mN m^{-1} and $\Delta K \simeq 185 \pm 15\ k_B T$.

Assuming that the membrane is non-conductive, $G = 0$, and using an inverse Debye length of $\kappa = 2 \times 10^7$ m^{-1} (milli-Q water) and the experimental electrode distance of $L = 1$ mm, our model yields $\Delta\Sigma \simeq -2$ mN m^{-1} and $\Delta K \simeq 190\ k_B T$. Thus the model successfully accounts for the order of magnitude of the electrostatic corrections observed in this experiment. Note, however, that the linearized Debye–Hückel approach is not a good approximation in this case, as applied voltages are rather high. For this reason, we recently extended our work to the PB regime [20].

The second experiments we would like to discuss concerns active membranes, which are artificial lipid vesicles containing bacteriorhodopsin ionic pumps [14–16]. These pumps are able to transfer protons unidirectionally across the membrane by undergoing light-activated conformational changes. The transport of protons across the membrane eventually builds up a transmembrane potential. In Refs. [15,26,27], a hydrodynamic theory has been developed to describe the nonequilibrium fluctuations of the membrane induced by the activity of the pumps. This work triggered substantial theoretical interest in the problem, mainly focusing on the proper description for these nonequilibrium effects associated with protein conformational changes [39–43].

In these models for active membranes, the electrostatic effects associated with the ion transport were not explicitly described. The framework presented in this review provides a more detailed description of the ion transport, which could be useful to understand some aspects of active membrane experiments. From a contour analysis of giant active vesicles, the fluctuation spectrum of the membrane was measured in Ref. [16], and a lowering of the membrane tension produced by the activity of the pumps was reported. Only the correction to the surface tension has been accurately measured in this experiment and many aspects of the transport of ions are still unknown. However, for simplicity we can assume that the passive state corresponds to a non-conductive membrane, $G = 0$, and the active state to a membrane with conductance $G = 10\ Sm^{-2}$. If we also assume a typical transmembrane potential of the order of 50 mV, we can use the results for the corrections to the surface tension obtained above. Accounting for the rather high amount of salt using $\kappa \simeq 5 \times 10^8\ m^{-1}$, we find a reasonable estimate for the observed tension lowering, $\Delta\Sigma \simeq 3 \times 10^{-7}\ Nm^{-1}$. We also find that there is no measurable difference for the bending modulus between the active and passive state, in agreement with the experiments. The model further predicts a current density of $j_m \simeq 1\ Am^{-2}$ when the pumps are active, which corresponds to an overall current of 1 pA on a vesicle of size 1 μm.

This accord in orders of magnitude for the electrostatic corrections is quite promising. For a more detailed comparison between experiments and the presented model, it would be necessary to do experiments in varying conditions (ionic strength, conductance of the membrane, or orientation of the pumps in the membrane for instance). Combined measurements of the membrane current and the transmembrane potential in the same experiment, using, for example, patch-clamp techniques, would also be desirable.

3. Impedance of a Planar Membrane in an AC Electric Field

Impedance spectroscopy [44] is an effective tool to obtain a characterization of the electric properties of lipid bilayer membranes. The method has been used in particular for supported lipid bilayers, which are a promising experimental system to characterize membrane proteins, channels or inclusions and more generally constitute the basis of highly sensitive detection technologies, that is, biosensors [45]. In the recent work [46], for instance, impedance spectroscopy has been used to characterize gramicidin D channels in pore suspending membranes. Nowadays, many biotechnology companies develop systems to measure the impedance of whole cells for screening or drug delivery.

In many cases, the interpretation of the data obtained by impedance spectroscopy is not that straightforward. Typically one uses equivalent circuits, which are sometimes controversial, since different models can be used for fitting the data. Moreover, there is often a lack of knowledge concerning the conditions of validity of these equivalent circuits to describe the diffuse charging in electric Debye layers. To answer these questions, one possibility is to start with an electrokinetic description based on the PNP equations. With such an approach, the dynamics of diffuse charging [33] and the current–voltage relation in electrochemical thin films have been successfully analyzed [32]. This approach is also useful for relating impedance measurements to the properties of the diffuse layers near charge selective interfaces such as electrodes or ion-exchange membranes [47].

In the following, we extend the model studied in the previous sections to the case of an applied AC electric field. For simplicity the membrane will be assumed to be *strictly planar and non-fluctuating*. We use the PNP equations to evaluate the impedance of this system, which can be then compared to simple equivalent circuits. We will first present the generic time-dependent equations for the perturbation induced by the applied AC field. Then we proceed to calculate the impedance for the following cases: (i) an ideally blocking membrane with equal diffusion coefficients for the two ion species, (ii) the same system but with unequal ion diffusion coefficients and finally (iii) an ideally non-blocking membrane which conducts selectively only one type of ion.

3.1. Time-dependent Electric Fields

The PNP equations for an electrolyte have already been given in Section 2.1. Taking the time derivative of the Poisson equation, Eq. (1), one obtains

$$-\varepsilon\partial_t\nabla^2\phi = e(\partial_t n^+ - \partial_t n^-) = -e(\nabla\cdot\mathbf{j}^+ - \nabla\cdot\mathbf{j}^-), \tag{20}$$

where in the last equation, the conservation of ion densities, Eq. (3), has been used. Through integration over space (assuming a one-dimensional geometry), and using the definition of the electric field, $\mathbf{E} = -\nabla\phi$, it follows that [48,49]

$$\mathbf{I} = \varepsilon\partial_t\mathbf{E} + e\mathbf{J}, \tag{21}$$

where the constant in of integration, $\mathbf{I}$, is the total electric current density. The first term on the R.H.S in Eq. (21) is the displacement current. The second term, $\mathbf{J} = \mathbf{j}^+ - \mathbf{j}^- = 2\mathbf{j}_\rho$, is the particle current density. The displacement current was absent in the previous section because we assumed a

stationary state, but for the time-dependent case it is crucial to obtain the response to an externally applied AC electric potential. We note that by virtue of the Poisson equation, Eq. (1), the total current density is divergence-free, $\nabla \cdot \mathbf{I} = 0$, at all times. Further note that the experimentally measurable quantity is given by the total electric current. For this reason, it is the relevant quantity to calculate the impedance as shown below.

3.2. Equations for Time-periodic Perturbations of an Equilibrium Base State

Let us assume an established equilibrium solution $c_0^+(z)$, $c_0^-(z)$ and $\phi_0(z)$ for the electrolyte in the absence of the AC field, which could be caused by an additional DC field or a Nernst potential. For convenience we consider here the *charge* densities $c^\pm$. Note that $c^\pm = en^\pm$ and $\kappa^2 = 2ec_0/(\varepsilon k_B T)$. The equations for the electrostatic problem, see Eqs. (1) and (3) above, read

$$\varepsilon \partial_z^2 \phi = c^- - c^+, \tag{22}$$

$$\partial_t c^\pm = -\partial_z j^\pm, \tag{23}$$

$$j^\pm = -D^\pm \left(\partial_z c^\pm \mp c^\pm \frac{e}{k_B T} \partial_z \phi \right). \tag{24}$$

Linearization around the base state like

$$c^+ = c_0^+ + \eta C^+, \quad c^- = c_0^- + \eta C^-, \quad \phi = \phi_0 + \eta \Phi,$$

where η is a small book-keeping parameter, leads at order $\mathcal{O}(\eta^0)$ to

$$c_0^\pm = c_0 e^{\pm \frac{e\phi_0(z)}{k_B T}}, \quad \text{with } \phi_0 \text{ solution of } \varepsilon \partial_z^2 \phi_0 = c_0 \left(e^{\phi_0} - e^{-\phi_0} \right).$$

This restates that the equilibrium solution has to fulfill the classical PB equation. At order $\mathcal{O}(\eta^1)$ in the perturbations, we get

$$\varepsilon \partial_z^2 \Phi = C^- - C^+, \tag{25}$$

$$\partial_t C^\pm = D^\pm \partial_z \left(\partial_z C^\pm \mp c_0^\pm \frac{e}{k_B T} \partial_z \Phi \mp C^\pm \frac{e}{k_B T} \partial_z \phi_0 \right). \tag{26}$$

As already discussed in the general case above, taking the time derivative of Eq. (25), insertion of the linearized PNP equations, Eq. (26), and integration in z yields

$$\varepsilon\partial_z\partial_t\Phi - D^-\left(\partial_z C^- - c_0^-\frac{e}{k_\mathrm{B}\mathrm{T}}\partial_z\Phi - C^-\frac{e}{k_\mathrm{B}\mathrm{T}}\partial_z\phi_0\right) + D^+\left(\partial_z C^+ + c_0^+\frac{e}{k_\mathrm{B}T}\partial_z\Phi + C^+\frac{e}{k_\mathrm{B}\mathrm{T}}\partial_z\phi_0\right) = I(t).$$

The integration constant $I(t)$ is the total electric current density. As we are interested in the response to an AC external voltage, $V(t) = V_0\mathrm{e}^{\mathrm{i}\omega t}$, introducing $I(t) = I_0\mathrm{e}^{\mathrm{i}\omega t}$ and $\Phi \propto \mathrm{e}^{\mathrm{i}\omega t}$, we arrive at

$$\left(\mathrm{i}\omega\varepsilon + \frac{e}{k_\mathrm{B}\mathrm{T}}\left(D^+c_0^+ + D^-c_0^-\right)\right)\partial_z\Phi + D^+\partial_z C^+ - D^-\partial_z C^- + \left(D^+C^+ + D^-C^-\right)\frac{e}{k_\mathrm{B}\mathrm{T}}\partial_z\phi_0 = I_0. \tag{27}$$

The first term on the L.H.S is the displacement current. The remaining terms are currents due to concentration gradients and a current induced by the equilibrium potential at the membrane. All these contributions taken together yield the total current I_0 in response to the external AC field.

We are left with the problem to solve Eqs. (26) and (27) with the external voltage entering via the BC, just like in Section 2.

3.3. Impedance for an Ideally Blocking Non-conductive Membrane

The equations derived in the last section are general as they describe the first order perturbation in an electrolyte induced by an AC voltage externally imposed at some boundaries. Let us now apply them to the planar membrane geometry as sketched in Fig. 1. The membrane is assumed to be flat and located at $z = 0$. The AC voltage will be externally applied at the electrodes at $z = \pm L/2$. For simplicity, we assume that there is no additional DC electric field or Nernst potential, that is, that the equilibrium solution is given by the homogeneous solution $\phi_0 = 0$, $c_0^+ = c_0$.

First we will treat the simplest case of an ideally blocking, non-conductive membrane, $j^\pm(0) = 0$. We also assume equal diffusion coefficients for the positive and negative ions, $D^+ = D^- = D$. Then the above Eqs. (26) and (27) for the perturbations reduce to

$$\mathrm{i}\omega C^\pm = D\partial_z\left(\partial_z C^\pm \mp c_0\frac{e}{k_\mathrm{B}T}\partial_z\Phi\right), \tag{28}$$

$$\left(\mathrm{i}\omega\varepsilon + 2Dc_0\frac{e}{k_B\mathrm{T}}\right)\partial_z\Phi + D(\partial_z C^+ - \partial_z C^-) = I_0. \tag{29}$$

Due to the symmetry of our system, one has

$$\Phi(z,t) = -\Phi(-z,t), \quad \rho(z,t) = -\rho(-z,t), \quad c(z,t) = c(-z,t). \tag{30}$$

Hence it is enough to solve the problem in $z \in [-L/2,0]$. The BCs in the chosen geometry read

$$C^+(-L/2) = 0, \tag{31}$$

$$C^-(-L/2) = 0, \tag{32}$$

$$\Phi(-L/2) = -V_0/2, \tag{33}$$

$$\partial_z C^+(0) + c_0\frac{e}{k_\mathrm{B}\mathrm{T}}\partial_z\Phi(0) = 0 = j^+(0)/D, \tag{34}$$

$$\partial_z C^-(0) - c_0\frac{e}{k_\mathrm{B}\mathrm{T}}\partial_z\Phi(0) = 0 = j^-(0)/D, \tag{35}$$

$$\lambda_m\partial_z\Phi(0) = \Phi(0^+) - \Phi(0^-). \tag{36}$$

Equations (31)–(33) fix the densities and the potential at the electrodes, as has already been discussed in Section 2.1. The next two Eqs. (34) and (35) state that the membrane is non-conductive for both ion types. Finally the last equation, Eq. (36), is again the Robin-type BC describing the capacitive behavior of the membrane with the effective length scale $\lambda_m = (\varepsilon/\varepsilon_m)d$. We will use the first five BCs to fix the five integration constants of Eqs. (28) and (29). Then imposing the last condition will yield the current–voltage relation and finally the impedance.

Extracting an equation for $C_\mathrm{s} = C^+ + C^-$ by adding the two cases $\pm$ in Eq. (28) yields $\mathrm{i}\omega C_\mathrm{s} = D\partial_z^2 C_\mathrm{s}$. From the BCs $\partial_z C_\mathrm{s}(0) = 0 = \mathrm{C_s}(-1/2)$ it follows $C_\mathrm{s}(\mathrm{z}) = 0$, that is, the total density of particles (positively and negatively charged) remains homogeneous. Introducing $\rho = C^+ - C^-$ and subtracting Eq. (28) yields

$$\mathrm{i}\omega\rho = D\partial_z^2\rho + D\varepsilon\kappa^2\partial_z^2\Phi, \tag{37}$$

$$\left(\mathrm{i}\omega\varepsilon + D\varepsilon\kappa^2\right)\partial_z\Phi + D\partial_z\rho = I_0, \tag{38}$$

where we have used $c_0 e/k_\mathrm{B}T = \varepsilon\kappa^2/2$. Eq. (38) can be integrated, yielding

$$\Phi(z) = c_1 + \frac{I_0 z - D\rho(z)}{D\varepsilon\kappa^2 + \mathrm{i}\omega\varepsilon}.$$

The BCs $\rho(-L/2) = 0$, $\Phi(-L/2) = -V_0/2$ fix the constant of integration to

$$c_1 = -\frac{V_0}{2} + \frac{I_0 L/2}{D\varepsilon\kappa^2 + \mathrm{i}\omega\varepsilon}.$$

Insertion of the obtained potential into Eq. (37) for ρ yields

$$\frac{D\kappa^2 + \mathrm{i}\omega}{D}\rho = \partial_z^2 \rho. \tag{39}$$

Using again the obtained potential transforms the BC $\partial_z\rho(0) + \varepsilon\kappa^2\,\partial_z\Phi(0) = 0$ into the simpler form $\partial_z\rho(0) = \mathrm{i}(I_0\kappa^2/\omega)$. Together with $\rho(-L/2) = 0$, the solution of Eq. (39) can be given as

$$\rho(z) = \mathrm{i}\frac{I_0\kappa^2}{\beta\omega\cosh(\beta L/2)}\sinh[\beta(z + L/2)] \tag{40}$$

with the (complex) inverse length scale

$$\beta = \sqrt{\kappa^2 + \mathrm{i}\omega/D}. \tag{41}$$

The remaining BC, Eq. (36), is a jump condition at the membrane. What we have calculated above are the solutions $\Phi^{<0}$, $\rho^{<0}$ on $z \in [-L/2, 0]$. Using the symmetry of our problem, Eq. (30), one directly obtains $\Phi^{>0}$, $\rho^{>0}$ on $z \in [0, L/2]$. Imposing Eq. (36), $\lambda_m\partial_z\Phi(0) = \Phi^{>0}(0) - \Phi^{<0}(0)$, then yields

$$\begin{aligned}\lambda_m\frac{I_0 - D\partial_z\rho(0)}{D\varepsilon\kappa^2 + \mathrm{i}\omega\varepsilon} &= c_1^{>0} + \frac{-D\rho^{>0}(0)}{D\varepsilon\kappa^2 + \mathrm{i}\omega\varepsilon} - \left[c_1^{<0} + \frac{-D\rho^{<0}(0)}{D\varepsilon\kappa^2 + \mathrm{i}\omega\varepsilon}\right] \\ &= -2c_1^{<0} - 2\frac{-D\rho^{<0}(0)}{D\varepsilon\kappa^2 + \mathrm{i}\omega\varepsilon}.\end{aligned}$$

Solving for the external voltage V_0—note that it enters in the integration constant c_1 of the electric potential—one gets

$$V_0 = \frac{I_0 L}{D\varepsilon\kappa^2 + \mathrm{i}\omega\varepsilon} - 2\frac{D\rho(0)}{D\varepsilon\kappa^2 + \mathrm{i}\omega\varepsilon} + \lambda_m\frac{I_0 - D\partial_z\rho(0)}{D\varepsilon\kappa^2 + \mathrm{i}\omega\varepsilon}.$$

This is the current–voltage relation. The impedance is defined as $Z(\omega) = V(\omega)/AI(\omega) = V_0/(AI_0)$, with A the membrane area normal to

the z-direction. Using the expression for the density, Eq. (40), one arrives at the following expression for the impedance of a non-conductive membrane

$$Z = \frac{L/A}{D\varepsilon\kappa^2 + \mathrm{i}\omega\varepsilon} - i\frac{(L/A)(D\kappa^2/\omega)}{D\varepsilon\kappa^2 + \mathrm{i}\omega\varepsilon}\frac{\tanh[\beta(L/2)]}{\beta L/2} + \frac{(\lambda_m/A)(1 - i(D\kappa^2/\omega))}{D\varepsilon\kappa^2 + \mathrm{i}\omega\varepsilon}. \tag{42}$$

Let us discuss the obtained result. The first term is the contribution of the electrolyte. This can be seen by rewriting it as

$$Z_{\mathrm{B}} = \frac{1}{R_{\mathrm{B}}^{-1} + \mathrm{i}\omega C_{\mathrm{B}}} \tag{43}$$

and identifying the capacitance of the bulk, $C_{\mathrm{B}} = \varepsilon A/L$, which is in parallel with the resistance of the bulk $R_{\mathrm{B}} = (1/D\varepsilon\kappa^2)(L/A) = Lk_{\mathrm{B}}T/2Dc_0eA$. A similar interpretation holds for the term $(\lambda_m/A)/D\varepsilon\kappa^2\mathrm{i}\omega\varepsilon$ in Eq. (42), which can be written as

$$Z_{\mathrm{S}} = \frac{1}{R_{\mathrm{S}}^{-1} + i\omega C_{\mathrm{S}}}. \tag{44}$$

This is again a RC-circuit with the capacitance $C_{\mathrm{S}} = \varepsilon A/\lambda_m = \varepsilon_m A/d$ of the membrane and a resistance $R_{\mathrm{S}} = (1/D\varepsilon\kappa^2)(\lambda_m/A)$. It arises from the Robin-BC which involves the effective length scale λ_m defined in Eq. (8). One can thus recast Eq. (42) into the form

$$Z = Z_{\mathrm{B}} + Z_{\mathrm{S}} - \frac{\mathrm{i}}{\omega}\frac{D\kappa^2}{R_{\mathrm{B}}^{-1} + \mathrm{i}\omega C_{\mathrm{B}}}\left[\frac{\tanh[\beta(L/2)]}{\beta L/2} + \frac{\lambda_m}{L}\right]. \tag{45}$$

The last term in this equation, let us call it Z_{C}, is due to charging of the double layer and the membrane. This can be best seen in the limit $\lambda_D/L = 1/(\kappa L) \ll 1$, that is, when the Debye length is small compared to the system size. Then $\tanh[\beta(L/2)]/(\beta L/2) \simeq 2/(\kappa L)$ and in the prefactor, the resistance R_{B}^{-1} dominates over the capacitance. One gets

$$Z_{\mathrm{C}} \simeq \frac{1}{\mathrm{i}\omega C_{\mathrm{eff}}}, \tag{46}$$

with the effective capacitance $C_{\mathrm{eff}} = \varepsilon[A/(2\lambda_D + \lambda_m)]$. Note that the thickness of the corresponding planar capacitor is the sum of the two Debye layers thicknesses $(2\lambda_D)$ and the effective length λ_m describing the capacitive effects of the membrane.

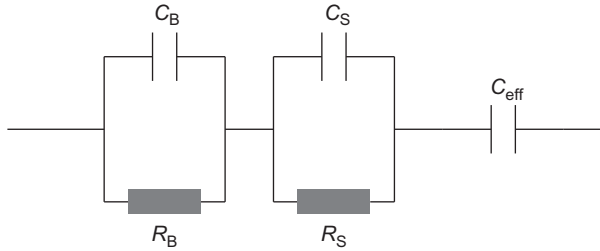

Figure 4 Effective circuit for the ideally blocking non-conductive membrane, Eq. (47): Two RC-circuits, one for the bulk and one for the membrane are in series with the effective charging capacitance of the membrane.

As shown in Fig. 4, for the blocking non-conductive membrane one effectively has an association in series of the RC-circuit of the bulk, the RC-circuit of the membrane and the effective capacitance of the charging membrane

$$Z = Z_B + Z_S + Z_C = \frac{1}{R_B^{-1} + i\omega C_B} + \frac{1}{R_S^{-1} + i\omega C_S} + \frac{1}{i\omega C_{eff}}, \qquad (47)$$

as long as $\lambda_D/L \ll 1$ holds. As $\lambda_m \simeq 200$ nm, the impedance contribution Z_S is usually small compared to the bulk resistance and can be neglected for $L \gg \lambda_m$. However, the contribution described by λ_m to the charging impedance Z_C can be of similar order as the one from the Debye layers and might even dominate the charging.

The best way to visually present the impedance is by a so-called Nyquist plot [44]. There one traces the negative imaginary part, $-\mathrm{Im}[Z(\omega)]$, of the impedance as a function of its real part, $\mathrm{Re}[Z(\omega)]$, for varying frequency ω. Nyquist plots for the full impedance, Eq. (45), and for the limit $\lambda_D/L \ll 1$, Eq. (47), are shown in Fig. 5. Panel (A) shows the case of a macroscopic system size, $L = 1$ mm. One clearly notices the RC-semi-circle terminating for high frequencies at the origin. For the given parameters one enters this semi-circle at $\omega \simeq 50$ Hz; the maximum is achieved for $\omega_{RC} = D\kappa^2 = 1$ kHz. The low frequency branch is dominated by the membrane charging capacitively at $R \simeq R_B + R_S$, thus for low frequencies one has a divergence like $(i\omega C_{eff})^{-1}$. As $\lambda_D/L \simeq 10^{-3}$, the effective circuit and the full calculation agree well.

Figure 5B shows the case of a microscopic system size, $L = 10$ μm. Here the bulk RC-signal is much less pronounced and charging dominates entirely. The full calculation (solid curve) yields a lower resistance for the charging process at low frequencies than the effective circuit obtained by the small-Debye layer approximation (dashed curve).

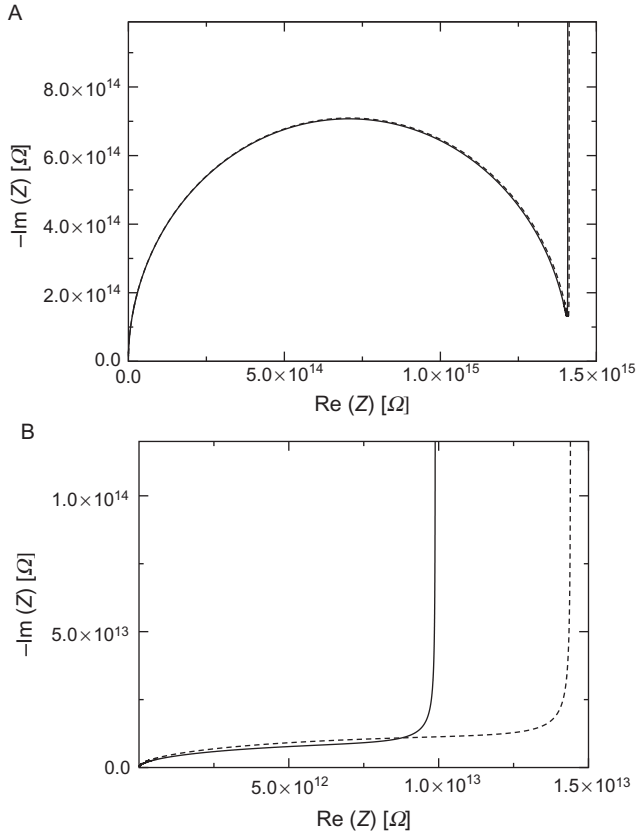

Figure 5 (A) Shows a Nyquist plot for a macroscopic system size, $L = 1$ mm. At low frequency the behavior is governed by the charging of the membrane. The semi-circle is governed by the bulk-RC-circuit. As $\lambda_D/L \simeq 10^{-3}$, the effective circuit and the full calculation agree well. (B) shows a Nyquist plot for a microscopic system, $L = 10$ μm. As L decreases, the bulk becomes less important and the RC-semi-circle less pronounced. The full calculation (solid curve) yields a lower resistance for the charging process at low frequencies than the effective circuit (dashed curve). Parameters as in Fig. 2 except for $\kappa = 10^{-6}$ m^{-1} (pure water); membrane area $A = 1$ μm^2.

3.4. Non-conductive Membrane: Effect of Unequal Diffusion Coefficients

In this section we investigate the effect of differing diffusion coefficients for the two ion species, $D^+ \neq D^-$, on the impedance of a blocking non-conductive membrane. Except for this assumption, the calculation is analogous to the one of the previous section. Equations (26) and (27) for the perturbations now read

$$\mathrm{i}\omega C^{\pm} = D^{\pm}\partial_z\left(\partial_z C^{\pm} \mp \frac{\varepsilon\kappa^2}{2}\partial_z\Phi\right), \tag{48}$$

$$\left(\mathrm{i}\omega\varepsilon + (D^{+}+D^{-})\frac{\varepsilon\kappa^2}{2}\right)\partial_z\Phi + D^{+}\partial_z C^{+} - D^{-}\partial_z C^{-} = I_0. \tag{49}$$

The BCs are still given by Eqs. (31)–(36). Since the equations for the charge densities do not decouple as before, it is useful to introduce $C = C^{+} + C^{-}$ and $\rho = C^{+} - C^{-}$ again, yielding

$$\begin{aligned}
&\mathrm{i}\omega C = \partial_z^2[\bar{D}C + \delta\rho + 2\delta\bar{c}\Phi],\\
&\mathrm{i}\omega\rho = \partial_z^2[\delta C + \bar{D}\rho + 2\bar{D}\bar{c}\Phi],\\
&(\mathrm{i}\omega\varepsilon + 2\bar{D}\bar{c})\partial_z\Phi + \delta\partial_z C + \bar{D}\partial_z\rho = I_0.
\end{aligned}$$

Here we introduced the abbreviation $\bar{c} = c_0\, e/k_B T$ as well as the average and the difference of the two diffusion coefficients

$$\bar{D} = (D^{+} + D^{-})/2, \quad \delta = (D^{+} - D^{-})/2. \tag{50}$$

Integration of the equation for the potential Φ yields

$$\Phi(z) = c_1 + \frac{I_0 z - (\delta C(z) + \bar{D}\rho(z))}{\bar{D}\varepsilon\kappa^2 + \mathrm{i}\omega\varepsilon} \quad \text{with}\, c_1 = -\frac{V_0}{2} + \frac{I_0 L/2}{\bar{D}\varepsilon\kappa^2 + \mathrm{i}\omega\varepsilon}.$$

Insertion into the equations for C and ρ yields a matrix equation

$$\begin{pmatrix} \mathrm{i}\omega - \left[\bar{D} - \delta^2\varepsilon\kappa^2/N\right]\partial_z^2 & -[\delta\mathrm{i}\omega\varepsilon/N]\partial_z^2 \\ -[\delta\mathrm{i}\omega\varepsilon/N]\partial_z^2\mathrm{i}\omega & -[\bar{D}\mathrm{i}\omega\varepsilon/N]\partial_z^2 \end{pmatrix}\cdot\begin{pmatrix} C \\ \rho \end{pmatrix} = 0, \tag{51}$$

where we have introduced $N = \bar{D}\varepsilon\kappa^2 + \mathrm{i}\omega\varepsilon$. Assuming solutions of the form $C, \rho \propto \mathrm{e}^{\beta z}$, Eq. (51) yields four solutions for the decay length β. In the case of equal diffusion coefficients studied previously, $\delta = 0$ and the equations are decoupled. In that case $\bar{D} = D$ and one simply gets $\beta_1^2 = \mathrm{i}\omega/D$ associated to the relaxation of the total particle density C and $\beta_2^2 = N/D\varepsilon = (D\kappa^2 + \mathrm{i}\omega)/D$ associated to the relaxation of ρ, see Eq. (39). In the case of unequal diffusion coefficients, the equations are coupled and the general solutions are

$$\beta_{1,2}^2 = \frac{\mathrm{i}\omega\bar{D} + \left(\bar{D}^2 - \delta^2\right)\kappa^2/2 \mp \sqrt{(\kappa^2/2)^2\left(\bar{D}^2 - \delta^2\right)^2 - \delta^2\omega^2}}{\left(\bar{D}^2 - \delta^2\right)}. \tag{52}$$

Here the minus sign applies to β_1 and the plus sign to β_2. Consequently, Eq. (51) is solved by the ansatz

$$\begin{pmatrix} C \\ \rho \end{pmatrix} = \sum_{i=1,2} \left[A_i \begin{pmatrix} E_i \\ 1 \end{pmatrix} \sinh[\beta_i(z+L/2)] + B_i \begin{pmatrix} E_i \\ 1 \end{pmatrix} \cosh[\beta_i(z+L/2)] \right]$$

with the eigenvectors given by

$$E_i = \frac{[\delta \mathrm{i}\omega\varepsilon/N]\beta_i^2}{\mathrm{i}\omega - \left[\bar{D} - \delta^2\varepsilon\kappa^2/N\right]\beta_i^2}.$$

The effective BCs read: $\partial_z C(0) = 0$ and $\partial_z \rho(0) = \mathrm{i}(2\bar{c}I_0/\omega\varepsilon)$ at $z = 0$; $C(-L/2) = 0$ and $\rho(-L/2)$ at $z = -L/2$. The last two BCs yield $E_1B_1 + E_2B_2 = 0$ and $B_1 + B_2 = 0$. As $E_1 \neq E_2$ this implies $B_1 = 0 = B_2$, that is, the cosh-contributions in the solution vanish. After some algebra one obtains

$$\rho = \mathrm{i}\frac{I_0\kappa^2}{\omega}\frac{E_1E_2}{E_2 - E_1}\left[\frac{\sinh[\beta_1(z+L/2)]}{E_1\beta_1\cosh(\beta_1 L/2)} - \frac{\sinh[\beta_2(z+L/2)]}{E_2\beta_2\cosh(\beta_2 L/2)}\right],$$
$$C = \mathrm{i}\frac{I_0\kappa^2}{\omega}\frac{E_1E_2}{E_2 - E_1}\left[\frac{\sinh[\beta_1(z+L/2)]}{\beta_1\cosh(\beta_1 L/2)} - \frac{\sinh[\beta_2(z+L/2)]}{\beta_2\cosh(\beta_2 L/2)}\right].$$

Using the Robin-type BC, Eq. (36), and once again the symmetry of the problem one gets

$$\lambda_m \frac{I_0 - (\delta\partial_z C(0) + \bar{D}\partial_z\rho(0))}{2\bar{D}\bar{c} + \mathrm{i}\omega\varepsilon} = -2c_1^{<0} - 2\frac{-(\delta C^{<0}(0) + \bar{D}\rho^{<0}(0))}{2\bar{D}\bar{c} + \mathrm{i}\omega\varepsilon}.$$

Solving for V_0, insertion of the obtained solutions for C and ρ and applying $Z = V_0/(I_0A)$ one obtains the impedance

$$\begin{aligned} Z = {} & \frac{L/A}{\bar{D}\varepsilon\kappa^2 + \mathrm{i}\omega\varepsilon} + \frac{(\lambda_m/A)(1 - \bar{D}\mathrm{i}(\kappa^2/\omega))}{\bar{D}\varepsilon\kappa^2 + \mathrm{i}\omega\varepsilon} \\ & - \mathrm{i}\frac{2\kappa^2/A}{(\bar{D}\kappa^2 + \mathrm{i}\omega)\omega\varepsilon}\frac{E_1E_2}{E_2 - E_1}\left(\delta + \frac{\bar{D}}{E_1}\right)\frac{\tanh[\beta_1 L/2]}{\beta_1} \\ & + \mathrm{i}\frac{2\kappa^2/A}{(\bar{D}\kappa^2 + \mathrm{i}\omega)\omega\varepsilon}\frac{E_1E_2}{E_2 - E_1}\left(\delta + \frac{\bar{D}}{E_2}\right)\frac{\tanh[\beta_2 L/2]}{\beta_2}. \end{aligned} \tag{53}$$

The first two contributions are already familiar to us, they stem from the bulk and the Stern-like description of the membrane. Note that $\bar{D}$ enters instead of D.Let us discuss the newly arising terms. As an expansion in $\lambda_D/L \ll 1$ is a bit tedious, let us consider only the simpler limit $\kappa \to \infty$. Equation (52) for β_1^2 has a minus sign in front of the square root, the two κ-terms cancel and

$$\beta_1^2 = \frac{\mathrm{i}\omega\bar{D}}{\left(\bar{D}^2 - \delta^2\right)} \to \beta_1 = \pm\sqrt{\mathrm{i}\omega/D_{\mathrm{eff}}} \tag{54}$$

with $D_{\mathrm{eff}} = (\bar{D}^2 - \delta^2)/\bar{D}$. For β_2^2 one has the plus sign in front of the square root, the terms in κ^2 dominate and one simply gets $\beta_2 = \pm\kappa$. For the eigenvectors to leading order one has $E_1 = (\bar{D}^2 - \delta^2)\kappa^2/\delta\mathrm{i}\omega$, $E_2 = -(1/E_1)$ and $(E_1E_2/E_2 - E_1)(\delta + (\bar{D}/E_1)) = \mathrm{i}\omega\delta^2/\kappa^2(\bar{D}^2 - \delta^2)$, $(E_1E_2/E_2 - E_1)(\delta + (\bar{D}/E_2)) = -\bar{D}$.

Consequently, the last term in Eq. (53) exactly reduces to the Debye-layer part of the charging contribution. Finally one obtains at leading order in λ_D

$$Z = \bar{Z}_{\mathrm{B}} + \bar{Z}_{\mathrm{S}} + Z_{\mathrm{C}} + Z_{\mathrm{W}} \tag{55}$$

with

$$Z_{\mathrm{W}} = \frac{2\lambda_D^2}{\bar{D}\varepsilon A/L}\frac{\delta^2}{\left(\bar{D}^2 - \delta^2\right)}\frac{\tanh[\beta_1 L/2]}{\beta_1 L}. \tag{56}$$

The first two terms are the RC-contributions of the bulk and the membrane (note that $\bar{D} = (D^+ + D^-)/2$ enters instead of D). The charging capacitance Z_{C} of the membrane is unchanged. The last term is the so-called Warburg impedance, with $\beta_1 = \sqrt{\mathrm{i}\omega/D_{\mathrm{eff}}}$ and $D_{\mathrm{eff}} = (\bar{D}^2 - \delta^2)/\bar{D}$. Note that this contribution is only present for unequal diffusion coefficients $\delta = (D^+ - D^-)/2 \neq 0$. It is proportional to λ_D^2 at leading order.[1]

The effective circuit corresponding to the obtained impedance is shown in Fig. 6. The contribution Z_{W} has been first described by Warburg [50,51] for electrochemical systems; in a nutshell, it arises from damped concentration oscillations close to an interface, here the membrane. We note however, that with typical differences in diffusion coefficients $D^+/D^- = 0.1$–10, a Nyquist

[1] For simplicity, we used the limit $\kappa \to \infty$ to derive this term. Taking this limit strictly, the contribution would vanish—as then both charge types diffuse infinitely rapidly across the zero-thickness Debye-layer. In real systems, however, κ remains always finite and thus one should include the leading order contribution, Z_W, in the impedance.

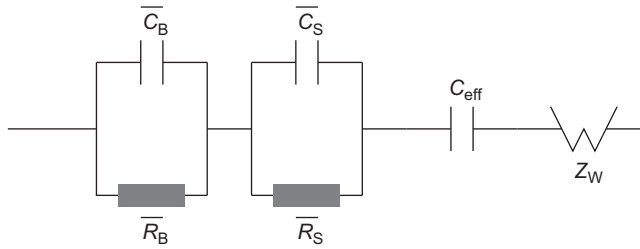

Figure 6 Effective circuit for the ideally blocking non-conductive membrane with differing diffusion coefficients, Eq. (55): Two RC-circuits, one for the bulk and one for the membrane are in series with the effective charging capacitance and a Warburg resistance.

plot of Eq. (55) is indistinguishable from Fig. 5 obtained for equal diffusion coefficients. This is due to the fact that in the geometry under investigation, the charging of the membrane is highly dominating the low-frequency behavior as it is proportional to ω^{-1}. Nevertheless, experiments often display a Warburg-like impedance at low frequencies, see, for example, Ref. [46]. In the next section we will investigate the case of a slightly conductive ion-selective membrane and will find that in this case one indeed obtains a Warburg impedance. We thus postpone a discussion of Z_W to the next section.

3.5. Impedance for an Ideally Non-blocking Conductive Membrane

For many applications it is interesting to account for a small but nonzero membrane conductivity. This is important for instance in the context of the characterization of ion channel proteins or pumps embedded in a lipid membrane using impedance spectroscopy. In contrast to Section 2.1, where we discussed the effects of a DC voltage on a conductive membrane that lets pass both types of charged ions ($G^+ = G^- = G$), here we will treat the case of a *selective membrane*, which lets pass only the positive ions. Thus, we assume a linearized relation $j^+ = G^+ \Delta\mu^+$ where G^+ is the effective conductance per unit area. The negative ions are not allowed to pass the membrane, hence $j^- = 0$ or effectively $G^- = 0$. This situation is relevant for biomembranes, where ion channels allow the passage of positively charged ions like Na^+ or K^+, but not of negatively charged ions like Cl^- which are typically larger.

To simplify the analysis, we will not describe the structure of the Debye layers as explicitly as in the previous sections. Instead we rely on two known approximations used in the study of electrochemical systems:

(i) the bulk is to a good approximation *locally* electroneutral. More precisely, deviations from electroneutrality occur only in the third order in an expansion of λ_D/L, which is very small for usual system sizes. This result can be obtained using a matched asymptotic expansion [33]. Consequently, we will assume for all z, $\rho(z) = 0$, or $C(z) = C^+(z) = C^-(z)$ for the perturbation of the charge densities.

(ii) Although we do not treat the Debye layers explicitly, we still impose effective BC for the electrochemical potential at the membrane. Thus, we implicitly assume that the electrochemical potential is continuous across the Debye layers.

We keep the geometry as before, that is, a flat membrane located at $z = 0$ with given AC voltage V_0 at the electrodes located at $z = \pm L/2$. We again assume that there is no additional DC field or Nernst potential, and equal diffusion coefficients[2] for positive and negative ions. Using the above-discussed approximations, we obtain

$$\mathrm{i}\omega C = D\partial_z^2 C, \tag{57}$$

$$\left(\mathrm{i}\omega\varepsilon + D\varepsilon\kappa^2\right)\partial_z\Phi = I_0. \tag{58}$$

Equation (58) is again easily integrated for $z \in [-L/2, 0]$ and together with the BC $\Phi(-L/2) = -V_0/2$ one gets

$$\Phi(z) = \frac{I_0(z + L/2)}{\mathrm{i}\omega\varepsilon + D\varepsilon\kappa^2} - V_0/2.$$

In addition we need three more BCs, namely

$$C(-L/2) = 0, \tag{59}$$

$$D(\partial_z C(0) - \bar{c}\partial_z\Phi(0)) = j^- = 0, \tag{60}$$

$$D(\partial_z C(0) + \bar{c}\partial_z\Phi(0)) = j^+ = \frac{G^+}{e}\left(\frac{\kappa_B T}{c_0}[C]_0 + e[\Phi]_0\right), \tag{61}$$

where $[C]_0 = C(0^+) - C(0^-)$ and analogously for $[\Phi]_0$. The second condition is the no-flux condition for the anions. The third condition states that the bulk current of cations equals the current through the membrane, and is assumed to follow Ohm's law. From Eqs. (57), (59), and (60), we obtain the following frequency dependent ion density distribution

[2] Note that in case of unequal diffusion coefficients, one gets a contribution like $\partial_z C$ in Eq. (58). The subsequent calculations can still be performed in a completely analogous way.

$$C(z) = \frac{\varepsilon\kappa^2 I_0}{2\alpha(\mathrm{i}\omega\varepsilon + D\varepsilon\kappa^2)\cosh(\alpha L/2)} \sinh(\alpha(z + L/2)),$$

where $\alpha = \sqrt{\mathrm{i}\omega/D}$ is of Warburg-type, cf. Eq. (54). Note that here the Warburg impedance arises from breaking the cation/anion symmetry, due to differences in membrane conductivities rather than due to differences in their diffusion coefficients as in the previous section. Also note that although the membrane is non-conductive for the anions, this is a collective effect in which both types of moving charges participate.

Finally, we use the BC for the cationic current, Eq. (61), to solve for the voltage V_0 and obtain the impedance via $Z = V_0/(I_0 A)$ as before

$$Z = Z_{\mathrm{B}} + \frac{D\kappa^2/(G^+ A)}{D\kappa^2 + \mathrm{i}\omega} + \frac{k_{\mathrm{B}}\mathrm{T}\kappa^2/(ec_0 A)}{\mathrm{i}\omega + D\kappa^2} \frac{\tanh(\alpha L/2)}{\alpha}. \tag{62}$$

Here we already have identified the bulk circuit, it is present as in the previous cases. The second term is the membrane contribution. It can be written as

$$Z_{\mathrm{M}} = \frac{1}{R_{\mathrm{M}}^{-1} + \mathrm{i}\omega C_{\mathrm{M}}}, \tag{63}$$

with the membrane's resistance, $R_{\mathrm{M}} = 1/(G^+ A)$, and capacitance, $C_{\mathrm{M}} = G^+ A/D\kappa^2$. The third term is the Warburg impedance, reading

$$Z_{\mathrm{W}} \simeq \frac{2\lambda_D^2}{D\varepsilon A/L} \frac{\tanh(\sqrt{\mathrm{i}\omega/D}L/2)}{\sqrt{\mathrm{i}\omega/D}L} \tag{64}$$

for small ω. Note that it is of the same form as Eq. (56) obtained for unequal diffusion coefficients, except for that in the latter appears an additional factor containing the diffusion coefficients.

We can conclude that as a result of the ionic membrane selectivity, a Warburg impedance arises. Figure 7 shows the effective circuit. A Nyquist plot is given in Fig. 8. One can identify the typical shape of a Warburg impedance for low frequencies: namely, for decreasing frequencies, on leaving the RC-signal of the bulk $-\mathrm{Im}[Z(\omega)]/\mathrm{Re}[Z(\omega)]$ acquires a slope of 45°. Finally, due to the finite system size $\mathrm{Im}[Z(\omega)]$ vanishes for $\omega \to 0$.

As already stated above, the calculation in this Section 3.5 is over-simplified. By assuming that the electrochemical potential is continuous across the Debye layers, there is no explicit contribution from the charging of the Debye layers to the impedance. Hence λ_m, which is important for the charging, does not enter—indeed we did not even use the Robin-type condition. As the membrane is conductive, at least for the cations, charging

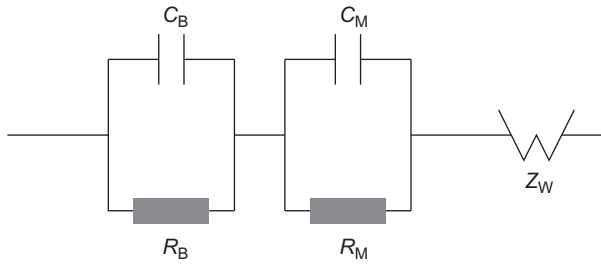

Figure 7 Effective circuit for the ideally blocking and selectively conductive membrane, Eq. (62): Two RC-circuits, one for the bulk and one for the membrane are in series with a Warburg resistance, caused by the ion selectivity of the membrane.

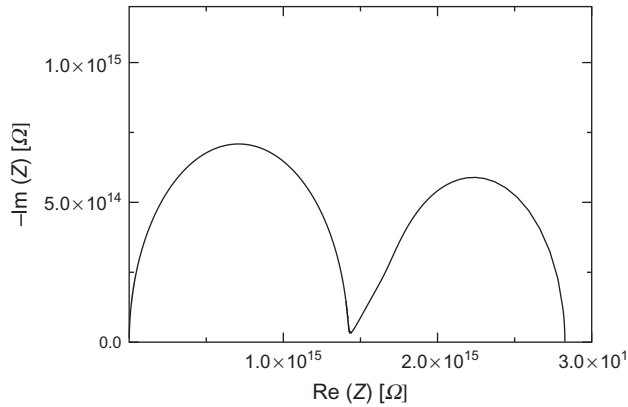

Figure 8 Nyquist plot for a selectively conducting membrane. At high frequencies one has an RC-semi-circle, which is either dominated by the bulk or by the membrane, depending on the membrane conductance and the dimensions of the system. The low-frequency behavior is governed by the Warburg impedance. Parameters as for Fig. 2 except for: $L = 1$ mm; $\kappa = 10^{-6}$ m^{-1} (pure water); $A = 1$ μm^2.

of the Debye layers is of minor importance for the overall impedance. With a proper treatment of the charging of the Debye layers, using a matched asymptotic calculation, the Robin-type condition will reoccur to match the two solutions and will reintroduce the length scale λ_m into the problem.

4. Conclusion

The study and theoretical description of the effects induced by electric fields on lipid membranes in an electrolyte is a vast, challenging, and far from fully explored problem, which is of relevance for many applications in biotechnology.

In this review, we have presented a theoretical framework to understand some of these effects in the simple case of a planar geometry. We have seen the importance of capacitive effects, occurring as a result of charge accumulation in the vicinity of the membrane, leading to renormalized elastic moduli and to membrane instabilities. We also have analyzed the flow fields which can be induced by currents due to small membrane conductivities. We discussed these effects only for time-independent (DC) electric fields, that is, in the steady-state regime.

Clearly, time-dependent electric fields lead to capacitive charging of the membrane and to time-dependent membrane dynamics. The capacitive charging can be described in two ways: the first approach is based on the leaky dielectric model developed by Taylor [52]. This approach is explained and illustrated in the contribution of P. Vlahovska [53]. One advantage of such an approach is that it captures the main physical effects associated with capacitive charging without the complexity of models which deal explicitly with the ion concentration fields. For this reason, it is useful to describe for instance the complex shape changes occurring in closed lipid vesicles [8].

The second approach, which we used in this work, is based on the electrokinetic PNP equations. This more refined level of description includes ion concentration fields, and therefore it is useful to describe specific effects associated for instance with the ion transport in ion channels or for effects occurring in low salt conditions. It is also needed to describe more precisely the capacitive charging, which as we have shown here includes several contributions coming from the bulk, the membrane impedance and the Debye layers themselves. In this review, we have tried to illustrate the strength of this approach for quantifying the impedance of a membrane-electrolyte system. In particular, we have shown how effective circuits used to interpret experimental data can be directly derived by this method. The membrane selectivity with respect to ion species is crucial to understand the conduction properties of membranes with embedded ion channels. We hope that our work will motivate further experimental and theoretical investigations in this field.

ACKNOWLEDGMENTS

We would like to thank particularly Martin Z. Bazant and Petia Vlahovska for many helpful discussions and access to unpublished work. We would also like to thank J. Prost, J. F. Joanny, P. Bassereau, L. Dinis, G. Toombes and S. Aimon for many inspiring discussions, and the ANR Artif-Neuron for funding. F. Z. thanks the DFG for partial funding via IRTG 1642 Soft Matter Science.

Appendix. Robin-type BC

In brief, this BC can be motivated for a flat membrane as follows: since the membrane is assumed to bear no fixed charges, the normal components of the electric displacement are continuous at the two interfaces between the membrane and the electrolyte,

$$\varepsilon\partial_z\phi(z=\pm d/2)=\varepsilon_m\partial_z\phi_m(z=\pm d/2), \tag{A.1}$$

where ϕ_m is the electric potential inside the membrane. Since the electric field $E_m=-\partial_z\phi_m$ is constant (to leading order) inside the membrane, the integral of the inside field can be written in the following way

$$E_m d=\int_{-d/2}^{d/2}E_m \mathrm{d}z=-[\phi_m(d/2)]-\phi_m(-d/2)]=-[\phi(d/2)-\phi(-d/2)],$$

where in the last step we used the continuity of the potential at the membrane surface. Together with Eq. (A.1) this yields

$$\lambda_m\partial_z\phi(z=\pm d/2)=\phi(d/2)-\phi(-d/2). \tag{A.2}$$

If we take the limit $d\to 0$ while keeping $\lambda_m=(\varepsilon/\varepsilon_m)d$ constant, one obtains Eq. (7) in the particular case of $h=0$ and $\mathbf{n}=\hat{z}$. The same derivation holds for the case of a slightly perturbed membrane surface $h(\mathbf{r}_\perp)$, where $\mathbf{r}_\perp$ is the in-plane vector.

REFERENCES

[1] U. Seifert, Configurations of fluid membranes and vesicles, Adv. Phys. 46 (1997) 13.
[2] D. Andelman, in: R. Lipowsky, E. Sackmann (Eds.), Handbook of Biological Physics vol. 1A, Elsevier, Amsterdam, 1995.
[3] E. Neumann, A.E. Sowers, C.A. Jordan, Electroporation and Electro-fusion in Cell Biology, Plenum Press, New York, 1989.
[4] P.T. Vernier, Y. Sun, M. Gundersen, Nanoelectropulse-driven membrane perturbation and small molecule permeabilization, BMC Cell Biol. 7 (2006) 37.
[5] H. Mekid, L.M. Mir, In vivo cell electrofusion, Biochim. Biophys. Acta Gen. Subj. 1524 (2000) 118–130.
[6] M. Staykova, R. Lipowsky, R. Dimova, Membrane flow patterns in multicomponent giant vesicles induced by alternating electric fields, Soft Matt. 4 (2008) 2168.
[7] R. Dimova, N. Bezlyepkina, M.D. Jordo, R.L. Knorr, K.A. Riske, M. Staykova, et al. Vesicles in electric fields: Some novel aspects of membrane behavior, Soft Matt. 5 (2009) 3201.

[8] P.M. Vlahovska, R.S. Graci, S. Aranda-Espinoza, R. Dimova, Electro-hydrodynamic model of vesicle deformation in alternating electric fields, Biophys. J. 96 (2009) 4789–4803.
[9] P. Peterlin, S. Svetina, B. Zeks, The prolate-to-oblate shape transition of phospholipid vesicles in response to frequency variation of an AC electric field can be explained by the dielectric anisotropy of a phospholipid bilayer, J. Phys.: Cond. Matt. 19 (2007) 136220.
[10] A. Ajdari, Pumping liquids using asymmetric electrode arrays, Phys. Rev. E 61 (2000) R45–R48.
[11] A. González, A. Ramos, N.G. Green, A. Castellanos, H. Morgan, Fluid flow induced by nonuniform AC electric fields in electrolytes on micro-electrodes. ii. a linear double-layer analysis, Phys. Rev. E 61 (2000) 4019–4028.
[12] B. Hille, Ion Channels of Excitable Membranes, Sinauer Press, Sunder-land, 2001.
[13] B. Alberts, Molecular Biology of the Cell, Garland, New York, 2002.
[14] J.B. Manneville, P. Bassereau, D. Lévy, J. Prost, Activity of transmembrane proteins induces magnification of shape fluctuations of lipid membranes, Phys. Rev. Lett. 82 (1999) 4356.
[15] J.B. Manneville, P. Bassereau, S. Ramaswamy, J. Prost, Active membrane fluctuations studied by micropipet aspiration, Phys. Rev. E 64 (2001) 021908.
[16] M.D.E.A. Faris, D. Lacoste, J. Pécréaux, J.-F. Joanny, J. Prost, P. Bassereau, Membrane tension lowering induced by protein activity, Phys. Rev. Lett. 102 (2009) 038102.
[17] D. Lacoste, M. Cosentino Lagomarsino, J.-F. Joanny, Fluctuations of a driven membrane in an electrolyte, Europhys. Lett. 77 (2007) 18006.
[18] D. Lacoste, G.I. Menon, M.Z. Bazant, J.F. Joanny, Electrostatic and electrokinetic contributions to the elastic moduli of a driven membrane, Eur. Phys. J. E 28 (2009) 243–264.
[19] F. Ziebert, M.Z. Bazant, D. Lacoste, Effective zero-thickness model for a conductive membrane driven by an electric field, Phys. Rev. E 81 (2010) 031912.
[20] F. Ziebert, D. Lacoste, A Poisson-Bolzmann approach for a lipid membrane in an electric field, New J. Phys. 12 (2010) 095002.
[21] M. Winterhalter, W. Helfrich, Effect of surface-charge on the curvature elasticity of membranes, J. Phys. Chem. 92 (1988) 6865–6867.
[22] H. Lekkerkerker, Contribution of the electric double-layer to the curvature elasticity of charged amphiphilic monolayers, Physica A 159 (1989) 319–328.
[23] M. Winterhalter, W. Helfrich, Bending elasticity of electrically charged bilayers - coupled monolayers, neutral surfaces, and balancing stresses, J. Phys. Chem. 96 (1992) 327–330.
[24] T. Chou, M. Jaric, E. Siggia, Electrostatics of lipid bilayer bending, Biophys. J. 72 (1997) 2042–2055.
[25] T. Ambjörnsson, M.A. Lomholt, P.L. Hansen, Applying a potential across a biomembrane: Electrostatic contribution to the bending rigidity and membrane instability, Phys. Rev. E 75 (2007) 051916.
[26] J. Prost, R. Bruinsma, Shape fluctuations of active membranes, Europhys. Lett. 33 (1996) 321.
[27] S. Ramaswamy, J. Toner, J. Prost, Nonequilibrium fluctuations, traveling waves, and instabilities in active membranes, Phys. Rev. Lett. 84 (2000) 3494.
[28] R.J. Hunter, Foundations of Colloid Science, Oxford University Press, Oxford, 2001.
[29] V. Kumaran, Electrohydrodynamic instability of a charged membrane, Phys. Rev. E 64 (2001) 011911.
[30] M. Leonetti, E. Dubois-Violette, F. Homblé, Pattern formation of stationary transcellular ionic currents in fucus, Proc. Natl. Acad. Sci. USA 101 (2004) 10243.

[31] E.M. Itskovich, A.A. Kornyshev, M.A. Vorotyntsev, Electric current across the metal-solid electrolyte interface. i. direct current, current-voltage characteristic, Phys. Status Solidi A 39 (1977) 229–238.
[32] K. Chu, M. Bazant, Electrochemical thin films at and above the classical limiting current, SIAM J. Appl. Math. 65 (2005) 1485–1505.
[33] M.Z. Bazant, K. Thornton, A. Ajdari, Diffuse charge dynamics in electrochemical systems, Phys. Rev. E 70 (2004) 021506.
[34] P. Sens, H. Isambert, Undulation instability of lipid membranes under an electric field, Phys. Rev. Lett. 88 (2002) 128102.
[35] F. Brochard, J.F. Lennon, Frequency spectrum of the flicker phenomenon in erythrocytes, J. Phys. (Paris) 36 (1975) 1035.
[36] M.Z. Bazant, T.M. Squires, Induced-charge electrokinetic phenomena: Theory and microfluidic applications, Phys. Rev. Lett. 92 (2004) 066101.
[37] S. Lecuyer, G. Fragneto, T. Charitat, Effect of an electric field on a floating lipid bilayer: A neutron reflectivity study, Eur. Phys. J. E 21 (2006) 153–159.
[38] J. Daillant, E. Bellet-Amalric, A. Braslau, T. Charitat, G. Fragneto, F. Graner, et al. Structure and fluctuations of a single floating lipid bilayer, Proc. Natl. Acad. Sci. USA 102 (2005) 11639–11644.
[39] N. Gov, Membrane undulations driven by force fluctuations of active proteins, Phys. Rev. Lett. 93 (2004) 268104.
[40] S. Sankararaman, G.I. Menon, P.B. Sunil Kumar, Electrostatic and electrokinetic contributions to the elastic moduli of a driven membrane, Phys. Rev. E 66 (2002) 031914.
[41] D. Lacoste, A. Lau, Dynamics of active membranes with internal noise, Europhys. Lett. 70 (2005) 418.
[42] H.-Y. Chen, Internal states of active inclusions and the dynamics of an active membrane, Phys. Rev. Lett. 92 (2004) 168101.
[43] M.A. Lomholt, Mechanics of nonplanar membranes with force-dipole activity, Phys. Rev. E 73 (2006) 061913.
[44] J.O.M. Bockris, A.K.H. Reddy, Modern Electrochemistry, Kluwer Academic/Plenum Press, New York, 2000.
[45] G. Wiegand, N. Arribas-Layton, H. Hillebrandt, E. Sackmann, P. Wagner, Electrical properties of supported lipid bilayer membranes, J. Phys. Chem. B 106 (2002) 4245–4254.
[46] E.K. Schmitt, C. Weichbrodt, C. Steinem, Impedance analysis of gramicidin d in pore-suspending membranes, Soft Matt. 5 (2009) 3347–3353.
[47] I. Rubinstein, B. Zaltzman, A. Futerman, V. Gitis, V. Nikonenko, Reexamination of electrodiffusion time scales, Phys. Rev. E 79 (2009) 021506.
[48] J.D. Jackson, Classical Electrodynamics, Wiley, New York, 1999.
[49] D. Andrieux, P. Gaspard, Stochastic approach and fluctuation theorem for ion transport, J. Stat. Mech. Theor. Exp. 2009 (2009) P02057.
[50] E. Warburg, Ueber das verhalten sogenannter unpolarisirbarer elektro-den gegen wechselstrom, Ann. Phys. (Lpz.) 67 (1899) 493(Ser. 3).
[51] E. Warburg, Polarization capacity of platinum, Ann. Phys. 6 (1901) 125.
[52] J.R. Melcher, G.I. Taylor, Electrohydrodynamics: a review of the role of interfacial shear stresses, Annu. Rev. Fluid Mech. 1 (1969) 111–146.
[53] P. Vlahovska, Adv. Planar Lipid Bilayers Liposomes 12(2010) (1969) 111–146.

CHAPTER FOUR

Raft Formation in Cell Membranes: Speculations About Mechanisms and Models

Ramon Reigada[1,*] *and* Katja Lindenberg[2,3]

Contents

Abstract

Spatial and temporal lipid organization in the plasmatic cell membrane is believed to be fundamental for the understanding of many cellular functions. The concept of lipid rafts as submicrometric cholesterol-rich lateral domains has been used to characterize the basic organizing principle of the cell membrane. Since such organization occurs at very small spatial scales, its experimental verification remains elusive. As a result, the raft hypothesis itself

* Corresponding author. Tel.: +34-934-039-290; Fax: +34-934-021-231.
E-mail address: reigada@ub.edu

[1] Departament de Química Física, Universitat de Barcelona, Avda. Diagonal 647, Barcelona, Spain
[2] Department of Chemistry and Biochemistry 0340, University of California San Diego, La Jolla, California, USA
[3] BioCircuits Institute, University of California San Diego, La Jolla, California, USA

Advances in Planar Lipid Bilayers and Liposomes, Volume 14
ISSN 1554-4516, DOI: 10.1016/B978-0-12-387720-8.00004-2

remains controversial. Meanwhile, different theoretical models are being proposed to fill this gap. Here, we survey our recent approaches to the theoretical study of the spatiotemporal organization of lipid bilayers perturbed in different ways. Transverse lipid transport and/or insertion of proteins results in domain organization that covers a wide range of submicrometric sizes and different levels of stability, suggesting plausible mechanisms for the control of nanoscale lipid organization in cell membranes. The relevance of our proposals to the understanding of lateral organization phenomena in biological cell membranes is also discussed.

1. Introduction

Contrary to the idea of the "fluid mosaic model" proposed more than three decades ago [1], there is increasing evidence that the cell membrane is a laterally heterogeneous medium with a complex nanoscale lipid organization [2]. To provide an accurate description, Simons and Ikonen [3] proposed the concept of the lipid raft to refer to lateral domains rich in saturated lipids and cholesterol, dispersed throughout a phase rich in unsaturated lipids. It has been suggested that these domains are crucial for targeting certain proteins in many signal transduction, cell polarization, adhesion, migration, and other cellular phenomena [4,5].

Despite the theoretical utility of the raft concept as a basic organizing principle of the plasma membrane, its verification is rather complicated since rafts develop at very small scales, within a range of tens to a few hundreds of nanometers [6]. Research in this field is now at a technical impasse because the experimental methods to study biomembranes at the characteristic raft length and timescales are only now being developed. For this reason, the raft hypothesis has been a matter of debate and vigorous controversy during the past decade. However, in view of recent progress in the understanding of the connection between structure and function in biomembranes, the raft issue is only controversial when it is viewed too simplistically. The simplistic hypothesis that stable and freely diffusing lipid rafts exist in plasma membranes is being replaced by a hierarchical picture of active lipid organization at different length scales that are exploited for distinct functions [7,8]. On the one hand, the existence of small, transient, and ordered lipid domains may induce short-lifetime protein interactions necessary to facilitate specific biochemical reactions in the membrane. On the other hand, larger stabilized rafts, resulting from the coalescence of small temporary domains, may be required for protein trafficking, endocytosis, and signaling. Such a picture opens new and challenging perspectives that update the raft hypothesis to take into account the dynamic nature of lipid assemblies at the surface of living cells [7,8].

Theoretical approaches have become a powerful tool to examine plausible membrane models to explain lipid heterogeneity in the cell membrane. Most of these approaches are based on the patterning abilities of simple model bilayers made of a few lipid components. Domain formation in multicomponent systems is commonly associated with differential affinities between their components. Bilayer mixtures of lipids with different melting temperatures such as unsaturated and saturated lipid species may eventually form ordered and disordered aggregates or phases rich in saturated and unsaturated lipids, respectively. Even more evident is the strong differential interaction of cholesterol with common membrane lipids. Cholesterol has a greater affinity for saturated lipids so that together they assemble into a more ordered, but still liquid, phase. This is experimentally observed in model bilayers [9] that promote liquid-ordered (lo) and liquid-disordered (ld) phases in giant vesicle membranes [10,11].

The general consensus up to this point is that the thermodynamics of lo and ld phases alone underlies raft formation and lipid heterogeneity in cell membranes so that lipid rafts may correspond to the liquid-ordered phase. However, this point of view immediately creates problems. In phase-separating model bilayers, initially nucleated ordered domains would progressively coalesce into macroscopic domains, in contrast to lipid rafts that remain small in the plasma membrane. Conversely, if the membrane lipid mixture is instead thought of as being in the one-phase region (miscible, no phase separation), only tiny ephemeral composition fluctuations would occur. In both cases, it is clear that thermodynamics alone cannot explain the hierarchical picture of rafts as dynamic and scale-dependent structures whose size and stability may dynamically change under specific signals or stimuli, contributing to the diversification of cellular responses. Theoretical approaches must therefore venture beyond the purely thermodynamic viewpoint to consider additional factors that alter or modify the phase stability of the lipid mixture and provide plausible mechanisms for the control of the nanoscale lipid organization.

In this chapter, some of these options are investigated by combining different model approaches. Depending on the phase state of the lipid mixture, two different scenarios are explored (see Fig. 1), and a third study of the mixture behavior when crossing the phase separation boundary is also reviewed. First, we take the lipid system to be located in the two-phase region of the phase diagram, that is, where the lipid mixture separates into two phases. In this situation, segregated domains are generated and coarsening continues even as the domains reach macroscopic sizes, unless some externally induced kinetic process hinders phase separation beyond some size. A number of possible halting factors have been proposed including, for example, the effect of in-plane line tension reduction [12], the action of active cellular processes [13], and lipid exchange with the membrane medium [14–17]. In Section 2, we inspect this scenario for a

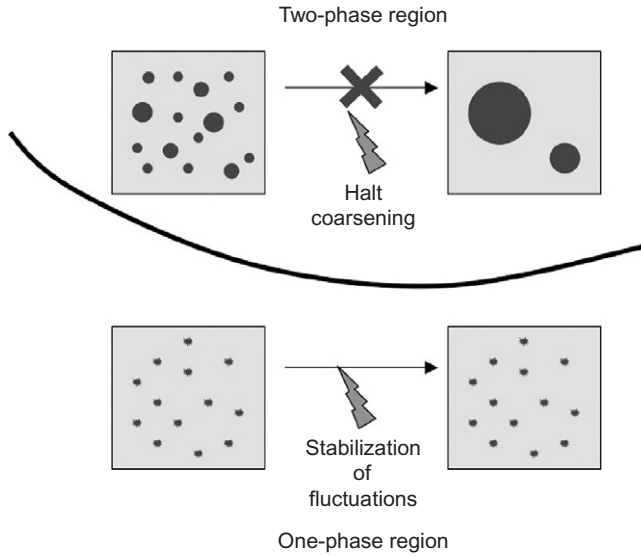

Figure 1 Schematic representation of a lipid mixture phase diagram to illustrate the raft formation mechanisms reported in this chapter. If the lipid mixture is in the two-phase region, an external factor must be invoked to explain why lo domains do not coarsen until complete macroscopic segregation. Under miscible conditions (one-phase region), composition fluctuations must be stabilized.

phase-separating ternary mixture consisting of cholesterol, saturated lipids, and unsaturated lipids, subjected to cholesterol recycling [16,17]. Cholesterol is dynamically added and removed from the membrane, and this continuous transport process causes the phase separation process to be halted at some point, leading to stationary finite-size segregated domains. Both thermodynamics and transport contribute to the determination of the size, shape, and stability of these actively maintained lipid aggregates. This study is performed by means of a continuum model that describes the thermodynamics of the lipid mixture in terms of local compositional fields and derives the corresponding kinetic equations supplemented with a cholesterol recycling term. Numerical simulations and linear stability analysis are performed on the resulting equations.

Alternatively, other mechanisms for raft formation may not necessarily invoke phase separation. In the one-phase region of a phase diagram, the entropic contribution dominates: small lipid clusters ("composition fluctuations" in "critical phenomena" terminology) of like species are formed, but thermal noise rapidly disintegrates them. For example, donor quenching Fluorescence Resonance Energy Transfer (FRET) analysis detects nanoscale domains (from 10 to 40 nm) in lipid bilayers in regions of the phase

diagram in which confocal microscopy indicates the presence of a single homogeneous phase [18]. Similar observations are inferred from NMR measurements in apparently homogeneous giant vesicles containing cholesterol [19]. However, these ephemeral lipid aggregates can be stabilized and even promoted to larger sizes by the action of other membrane components. For example, transmembrane proteins may act as surfactants for lipid fluctuations, increasing their disintegration time and stabilizing them [20]. In Section 3, this possibility is analyzed for a simple binary lipid bilayer mixture into which either neutral or interacting proteins are inserted. We report two different stabilization mechanisms of lipid nanoclusters depending on the interactions between the membrane proteins and the lipid components [21]. In this scenario, since we are interested in small length and short timescales, both lipid and protein components are treated as discrete interacting particles on a lattice. A combination of Monte Carlo algorithms is then used to study the phase stability of the lipid/protein mixture and its spatial organization.

Finally, in Section 4, a third approach is presented for the particular case of a lipid mixture close to the phase separation boundary. This scenario is particularly interesting since any slight perturbation of the system's conditions is able to strongly modify the spatiotemporal organization of the lipid mixture. In this situation, the combination of the two previous modifications (cholesterol content variation and protein insertion) leads to the formation of lipid structures covering a wide range of submicrometric sizes and different levels of stability, thus providing a robust cooperative mechanism for the control of nanoscale lipid organization in cell membranes. In this study, the spatial and temporal scales involved again require the use of a discrete approach for both lipid and protein components treated as single particles. Here, following an approach different from that of Section 3, a lipid membrane explicitly containing cholesterol is modeled. To do so, we propose a combination of two complementary lattices, one for the saturated/unsaturated lipid mixture and the other for the cholesterol component. This double lattice system is dynamically evolved by an appropriate Monte Carlo algorithm.

2. Lipid Membranes with Cholesterol Recycling

Cell membranes are continuously subjected to intra- and extracellular fluxes involving energy and mass transport. Among many others, recent experiments [22,23] have revealed that raft organization is extremely sensitive to cholesterol homeostasis. Here, we illustrate how cholesterol recycling may regulate the size, shape, and stability of rafts in cell membranes under biological conditions.

2.1. The Model

Our approach is based on analytical and numerical treatments of a simple nonequilibrium model for a ternary membrane composed of saturated lipids (A), unsaturated lipids (B), and cholesterol (C), subjected to a continuous cholesterol recycling process. The energetic description of the system follows a Ginzburg–Landau approach based on two space- and time-dependent compositional variables, $\phi(\vec{r},t)$ and $c(\vec{r},t)$. ϕ corresponds to the differential composition of two lipid components ($\phi > 0$ indicating predominance of saturated lipid), whereas c stands for the fraction of cholesterol with respect to a maximum allowed unit concentration. The free-energy functional per molecule can be written as a typical Landau expansion in ϕ^2, ϕ^4, c^2, and c^4, plus the simplest (linear) coupling contribution [16,17,24]

$$\frac{f[\phi,c]}{k_{\mathrm{B}}T} = \left(\frac{1}{2}-J\right)\phi^2 + \frac{1}{12}\phi^4 - G\phi c + 4\left(c-\frac{1}{2}\right)^2 + \frac{8}{3}\left(c-\frac{1}{2}\right)^4, \quad (1)$$

where T is the temperature and k_{B} stands for the Boltzmann constant. The parameter J corresponds to the differential interaction between the two lipid components, whereas G stands for the differential interaction between the two lipids with cholesterol ($G > 0$ corresponds to a preferential affinity between cholesterol and saturated lipids). These parameters can be obtained from experiments with different lipid systems [25,26]; a reasonable estimation for our model leads to $J \in (0.1,0.35)$ and $G \in (1.5,3)$, both in $k_{\mathrm{B}}T$ units [17]. The free-energy functional of the entire system can be expressed as

$$\mathcal{F}[\phi,c] = N_0 \int_S \left(f[\phi,c] + \frac{\gamma}{2}|\vec{\nabla}\phi|^2 \right) \mathrm{d}S, \quad (2)$$

where the integration is performed over the membrane area S and N_0 is the number of molecules per unit area. The line tension γ between phases can be estimated from Cahn–Hilliard theory [27] as $\gamma \approx Jd_0^2$, where J is the typical lipid interaction energy and d_0 is the characteristic interfacial width.

The kinetic evolution of the compositional fields is obtained by applying the constitutive relations from linear nonequilibrium thermodynamics leading to the dimensionless kinetic equations [17]:

$$\frac{\partial\phi}{\partial t} = \nabla^2\left[(1-2J)\phi + \frac{1}{3}\phi^3 - Gc - \gamma\nabla^2\phi\right] + \sqrt{\epsilon_\phi}\,v_\phi, \quad (3)$$

$$\frac{\partial c}{\partial t} = D\nabla^2\left[-G\phi + 8\left(c-\frac{1}{2}\right) + \frac{32}{3}\left(c-\frac{1}{2}\right)^3\right] - \rho(c-\bar{c}) + \sqrt{\epsilon_c}\,v_c, \quad (4)$$

which obey the conservation laws $S^{-1}\int_S \phi(\vec{r},t)\mathrm{d}s = \bar{\phi}$ and $S^{-1}\int_S c(\vec{r},t)\mathrm{d}s = \bar{c}$. For the average membrane composition, we have chosen values plausible for cell membranes, $\bar{\phi} = -0.2$ and $\bar{c} = 0.214$ [28]. The second term of the kinetic Eq. (4) accounts for a generic nonequilibrium exchange process of cholesterol, the parameter ρ being the recycling frequency (in units of inverse time). This nonequilibrium term can be interpreted as a continuous and homogeneous intake flux of cholesterol and its continuous release at a rate dependent on its local concentration [16]. The proposed term is the simplest way to introduce a unique timescale, ρ^{-1}, for the recycling process in such a way as to keep a constant total amount of cholesterol $\bar{c}$ in the system. Finally, the last contributions to the kinetic Eqs. (3) and (4) correspond to Gaussian white noise terms representing thermal fluctuations taken to have zero mean, zero correlations, and noise intensities $\in_\phi = 2/N_0$ and $\in_c = 2D/N_0$, respectively.

The equations, variables, and model parameters are represented in their dimensionless form: energy is expressed in units of $k_B T$, length is scaled according to $x \to x/\sqrt{\gamma/J}$, and time units are scaled as $t \to tJD_\varphi/\gamma$. The diffusion coefficient D_c for cholesterol is expressed in units of the diffusion coefficient of the lipids D_φ, that is, D_c is rescaled to $D = D_c/D_\varphi$. These rescalings are equivalent to setting $k_B T$, $d_0 = \sqrt{\gamma/J}$ and D_φ equal to unity.

2.2. Linear Stability Analysis

Some qualitative results can be advanced by means of a linear stability analysis of the kinetic equations. We test the linear stability of the stationary homogeneous solution $\left(\phi(\vec{r}) = \bar{\phi}, c(\vec{r}) = \bar{c}\right)$ by introducing small wave perturbations $\delta\phi \exp[w(q)t + \mathrm{i}\vec{q}\cdot\vec{r}]$ and $\delta c \exp[w(q)t + \mathrm{i}\vec{q}\cdot\vec{r}]$ and linearizing Eqs. (3) and (4). The growth rate $w(q)$ of the perturbations is calculated as the largest eigenvalue of the Jacobian resulting from the linearization matrix [17].

In the absence of the recycling process ($\rho = 0$), the system evolves to two possible equilibrium states depending on the values of the interaction parameters. For weak interaction parameters, the system remains stable to small perturbations and no phase separation is predicted ($w(q) < 0 \;\forall\; q > 0$; see Fig. 2). When the interaction parameters are above their critical values, long wavelength modes become unstable, promoting complete phase separation (see Fig. 2). In the absence of component C, phase separation is predicted if $J > J_{c,eq,AB} = \bar{\phi}'/2$, where $\bar{\phi}' = 1 + \bar{\phi}^2$. If component C is added to the system, equilibrium phase separation occurs for $J < J_{c,eq,AB}$ when $G > G_{c,eq} = 4\left[2\left(J_{c,eq,AB} - J\right)\bar{c}'\right]^{1/2}$, where $\bar{c}' = 1 + 2\bar{c}(\bar{c} - 1)$. The scenario studied in this section corresponds to a miscible binary lipid mixture ($J < J_{c,eq,AB}$) that undergoes phase separation due to the inclusion of cholesterol ($G > G_{c,eq}$).

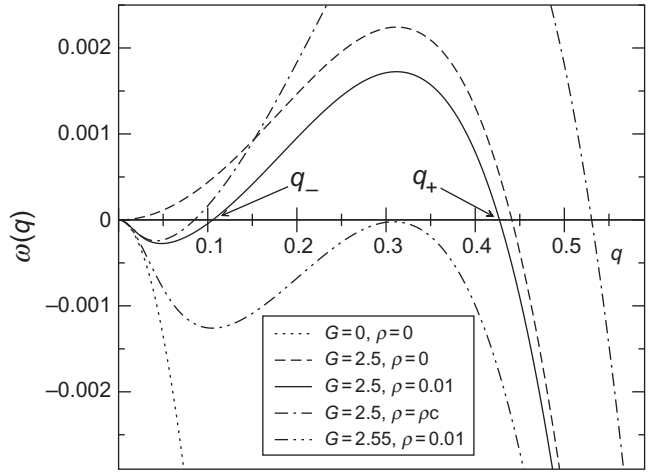

Figure 2 Growth rate $w(q)$ for different parameter values. For all curves, $J = 0.25$, $\gamma = 0.25$, $D = 1$, $\bar{\phi} = -0.2$, and $\bar{c} = 0.214$. The miscibility regime corresponds to $\rho = 0$ and $G = 0 < G_{c,eq} = 2.394$. When G is increased above its critical value ($G = 2.5 > G_{c,eq}$, $\rho = 0$), equilibrium phase separation is predicted. When a moderate recycling rate is applied ($G = 2.5$, $\rho = 0.01$), unstable modes appear at $q \in (q_-, q_+)$, leading to finite-size domains. Faster recycling increases the value of the minimum unstable mode q_- so that smaller domains are expected. If $\rho > \rho_c = 0.045$, unstable modes become stable and the miscibility of the mixture is recovered. A larger interaction parameter G (compare curves for $G = 2.5$ and $G = 2.55$) decreases the value of q_- so that larger domains are expected.

Under nonequilibrium conditions and moderate recycling rates, a range of unstable modes, $w(q) > 0$, appears at intermediate wavenumbers $q \in (q_-, q_+)$ (see Fig. 2). This means that the phase separation process evolves until segregating domains reach a maximum size, L, determined by the smallest unstable wavenumber, $L \sim \pi/q_-$. This result reflects the competition between thermodynamic ordering due to the preferential affinity between cholesterol and saturated lipids and nonequilibrium mixing actions caused by cholesterol recycling. The transport across the bilayer thus introduces a long-range mixing effect that eventually prevents complete phase separation. As a result, actively maintained finite-size segregation domains appear, their properties being regulated by the balance between thermodynamic and transport conditions.

The analytical determination of q_- provides an upper limit for the size of the stationary domains and its dependence on the model parameters. The analytical expression for q_- can easily be found in the limit $q_- \ll 1$ and reads [17]

$$q_-^2 \approx \frac{\rho\left(\bar{\phi}' - 2J\right)}{D\left(G^2 - 16\left(\bar{\phi}' - 2J\right)\bar{c}'\right)} = \frac{2\rho\left(J_{c,eq,AB} - J\right)}{D\left(G^2 - G_{c,eq}^2\right)}. \tag{5}$$

According to Eq. (5), a faster recycling rate leads to a smaller maximum size for lipid domains, whereas a deeper quench mixture (larger J and/or G interaction parameters) leads to a prediction of larger domain sizes.

When the recycling rate is higher than a critical value ρ_c, all positive wavenumber modes are stable, $w(q > 0) < 0$, meaning that the recycling process is so fast that the system is kinetically kept miscible. The critical value ρ_c can be obtained from the equality $q_- = q_+$ (see Fig. 2), leading to $\rho_c = D(G_{c,eq} - G)^2$

2.3. Numerical Results

The kinetic differential Eqs. (3) and (4) are solved numerically for the compositional fields ϕ and c on a two-dimensional (2D) square lattice of $N \times N$ sites. Periodic boundary conditions are applied. The discretization mesh size is chosen to be of the order of the characteristic interfacial width d_0 and set to $\Delta x = 1$, and the time step is set to $\Delta t = 0.001$. Both choices assure good numerical convergence. Simulations are started from a homogeneous distribution $\left[\phi(\vec{r},0) = \bar{\phi}, c(\vec{r},0) = \bar{c}\right]$ slightly perturbed with local variations of $\pm 1\%$.

The numerical simulation results are found to follow the predictions of the linear stability analysis. First, the effect of the parameter ρ is examined in a set of simulations varying the recycling frequency. The resulting temporal evolutions are presented in Fig. 3. Observe, as a general behavior, how the system is segregated into coarsening lo domains, and how the coarsening process is halted at smaller structures as the recycling frequency is increased. A more detailed characterization of the stationary domains is provided by the quantification of domain size histograms and roughness. We have defined segregated domains as all interconnected lattice sites with a composition variable three times larger than the average thermal fluctuations. Once the domains have been delimited, domain area distribution histograms are computed. Another feature that can be analyzed with this procedure is the roughness of the emerging domains. Specifically, the roughness index Ω_i of a domain i is computed as the square of the ratio between the perimeter P_i of the domain to the perimeter of the circle with the same area A_i, that is, $\Omega_i = P_i^2/4\pi A_i$. A circular domain has a roughness index $\Omega = 1$, whereas more irregular structures are characterized by $\Omega \gg 1$.

The domain area distributions have been computed for the last snapshots (stationary states) of each simulation and have been plotted in Fig. 4A. It is observed that the average domain area diminishes, as does its dispersion, when the exchange process is speeded up. The stationary mean domain size L_{st} corresponds to the square root of the mean domain area computed for each area distribution, and its value depends, as expected, on the applied exchange rate. A plot of $1/L_{st}$ as a function of $\rho^{1/2}$ is presented in Fig. 5, showing good

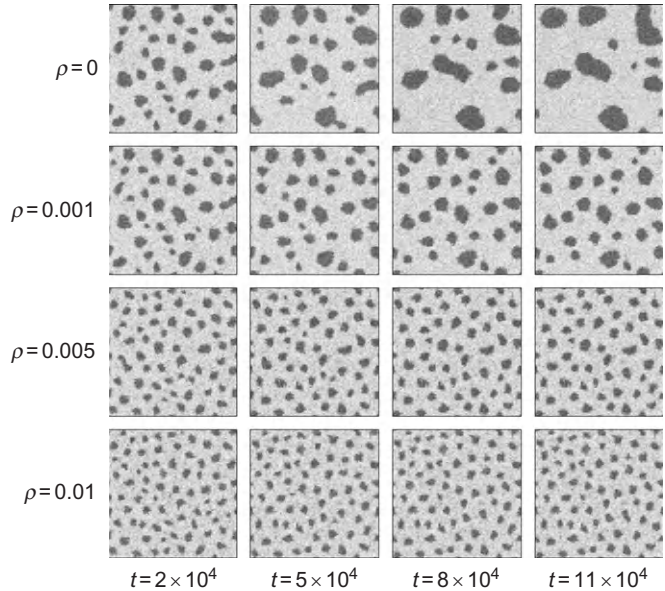

Figure 3 Temporal evolution of the simulation patterns in a 256×256 system for different recycling rates. The other parameters are $\bar{\phi} = -0.2, \bar{c} = 0.214$, $D = 1, \gamma = 0.25, J = 0.25,$ and $G = 2.5$. Each snapshot corresponds to a grayscale representation of the parameter ϕ. Darker regions correspond to higher values of this variable. The snapshots for c follow the same distribution (not shown). Only the last snapshots for the nonequilibrium cases ($\rho \neq 0$) are practically stationary.

agreement with the prediction $q_- \sim \rho^{1/2}$ in Eq. (5). As to the domain roughness, increasing ρ results in rougher domains (see the inset in Fig. 4A).

The stability of the generated domains is analyzed by means of the normalized temporal correlation functions for the ϕ field

$$T(\tau) = \frac{\langle \phi(\vec{r}, t)\phi(\vec{r}, t+\tau)\rangle - \langle \phi(\vec{r}, t)\rangle^2}{\langle \phi^2(\vec{r}, t)\rangle - \langle \phi(\vec{r}, t)\rangle^2}, \tag{6}$$

where the brackets stand for an average over positions $\vec{r}$ and time t. These functions are plotted in Fig. 4B for simulations with different values of ρ. It is clear that faster recycling leads to less stable domains.

The effects of modifying the thermodynamic conditions (i.e., changes in the distance to the phase boundary of the mixture) are analyzed by varying the interaction energy G while keeping the remaining parameters fixed. This analysis can be performed by comparing the data for $G = 2.5$ and 3 in Fig. 5 at equal values of ρ. An increase of the interaction energy G (namely,

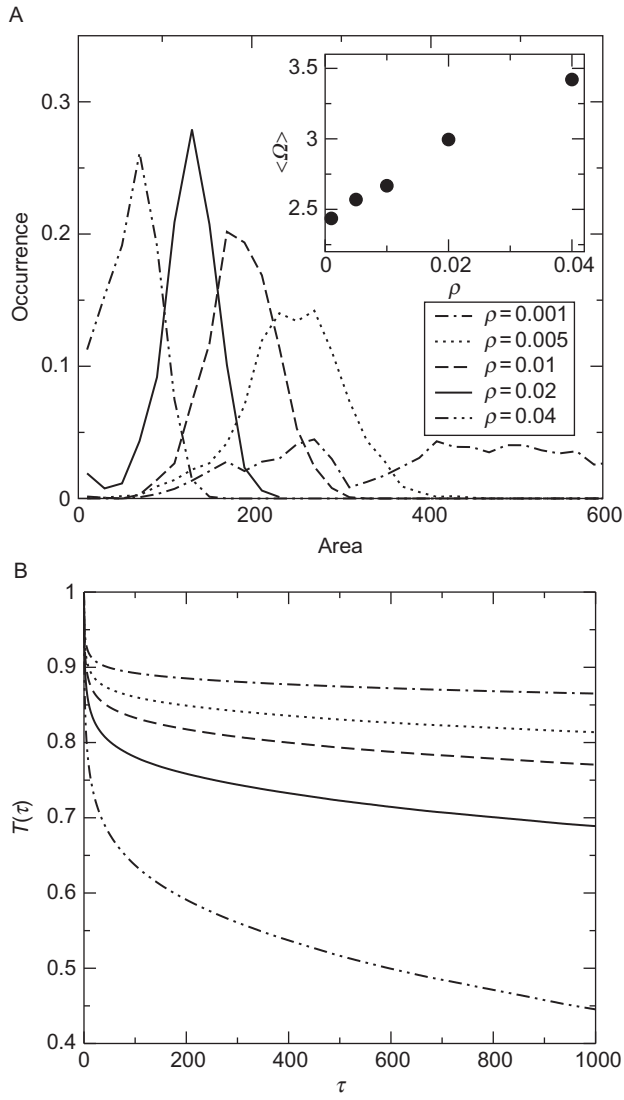

Figure 4 (A) Domain area distributions and mean roughness coefficient (inset). (B) Decay of time correlation functions for different values of ρ. In both panels, the other parameters are $\bar{\phi} = -0.2, \bar{c} = 0.214, \rho = 0.02, D = 1, \gamma = 0.25, G = 2.5$, and $J = 0.25$.

a deeper mixture quench) results in larger and also more circular and stable domains. Conversely, when the separating mixture is closer to the phase boundary (smaller value of G, but still larger than $G_{c,eq}$), the mixing effect due to the exchange process leads to smaller, more irregular less stable domains.

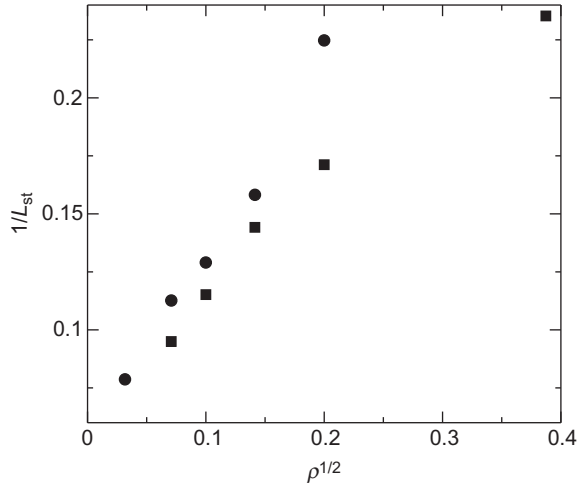

Figure 5 Inverse of the stationary domain linear size $1/L_{st}$ as a function of $\rho^{1/2}$ for $G = 2.5$ (circles) and $G = 3$ (squares). The other parameters are $\bar{\phi} = -0.2, \bar{c} = 0.214, D = 1, \gamma = 0.25$, and $J = 0.25$. The linear dependence $q_- \sim L_{st}^{-1} \sim \rho^{1/2}$ predicted in Eq. (5) is captured.

The proposed model and its results may be of interest in the study of the control of lipid heterogeneity and raft formation in plasmatic cell membranes. We have observed that, for a given set of parameters, the effect of increasing the recycling frequency favors the generation of monodisperse small, irregular, and unstable lo domains, whereas slow recycling leads to polydisperse, large, rounded, and stable structures. Taking the mixture closer to its phase boundary has the same effect as an increase of the recycling frequency. However, some caution must be exercised when comparing the spatial and temporal scales of the numerical examples provided in this section. For instance, the simulation with $G = 2.5$ in Fig. 5 leads to stationary domains of linear size $\approx$62.5 nm for $\rho = 40\ s^{-1}$ and $\approx$38.5 nm for $\rho = 400\ s^{-1}$. Both size values are in good agreement with typical raft characteristic lengths, but the estimated values for the recycling frequencies are much larger than biological values (of order s^{-1}) [29]. However, we have ameliorated this discrepancy by showing that similar small domain sizes can be attained for smaller recycling frequencies if the mixture is placed closer to the phase boundary, and this in fact corresponds to the accepted situation for lipid mixtures in cell membranes [22,23]. Therefore, the proposal presented in this section may fit raft formation phenomena in the limit of close proximity to the lipid mixture phase boundary.

3. Protein-Induced Nanodomain Stabilization in Lipid Membranes

Alternative proposals that do not invoke phase separation of the lipid mixture are based on the effect of other cell membrane components such as proteins. Actually, plasma cell membranes are highly crowded systems with a percentage of protein mass as high as 30–50%, which in some membrane regions could lead to surface coverages greater than 20%. It thus seems clear that the study of the lateral organization of biomembranes should also incorporate the effect of these nonlipid components. In particular, the effect of proteins on lipid phase stability has to be accounted for. A valuable example is provided in Ref. [20], which suggests that integral proteins that anchor the cytoskeleton to the membrane may prevent complete lipid phase separation. In this section, this scenario is analyzed in considerable detail by studying the influence on the lipid mixture phase stability of the protein size, protein coverage, and of its interactions with membrane lipids. Depending on the interplay of proteins and lipids, two molecular mechanisms for the stabilization of small domains are characterized, mechanisms that may be relevant in the cell membrane context [21].

3.1. The Model

The cell membrane is here described as a 2D square lattice of $N \times N$ sites and periodic boundary conditions. The lattice is occupied by either lipids or proteins. We consider only two types of lipids: the ones corresponding to the liquid-ordered phase (generally, saturated lipids and cholesterol) and those forming the liquid-disordered phase (mainly unsaturated lipids). Each lattice site i can be occupied by a liquid-ordered lipid (spin variable $S_i = +1$), by a liquid-disordered lipid ($S_i = -1$), or by protein ($S_i = 0$). Each lipid molecule occupies a single site, whereas proteins are allowed to occupy more than one site, depending on their size. Common membrane lipids in a fluid phase occupy an area per molecule of about 0.6–0.8 nm^2, so that the linear size for each lattice site can be fixed at $\Delta x = 0.8$ nm. The variable ϕ is defined as the fraction of lattice sites occupied by proteins. For the remaining sites, χ corresponds to the fraction occupied by liquid-ordered (saturated) lipids.

We concentrate on modeling integral membrane proteins. The function of many of them is to attach the cytoskeleton network to the membrane in order to provide mechanical support and cell shape. Therefore, unless otherwise stated, we consider these proteins to be statically inserted in the lipid mixture. Protein particles are initially placed randomly on the lattice

system. Protein size is determined by its cross-sectional radius r, given in lattice units. The most common transmembrane proteins are integrins and glycophorins that display a cross-sectional radius from 2 to 20 times the typical linear size of a lipid in the fluid phase [30].

The energetics of the membrane mixture follows the typical Ising Hamiltonian,

$$\mathcal{H} = -J_0 \sum_{\langle ij \rangle} S_i S_j + \lambda \sum_{i \in \Omega} S_i, \tag{7}$$

where J_0 is a positive parameter that accounts for the differential interaction energy between lipid species, Ω is the set of lipid sites which are neighboring a protein site, and λ corresponds to the lipid–protein interaction. Note that $\lambda > 0$ implies a preferential affinity of the proteins to be surrounded by unsaturated lipids, while $\lambda < 0$ lowers the energy of the system when proteins are surrounded by saturated lipids. A first estimation for J_0 can be extracted as follows. First, the application of the Hamiltonian in Eq. (7) on a square lattice leads to a critical value for the interaction parameter of 0.440 in units of $k_B T$, for a spin phase transition to occur in the absence of proteins. Second, a lo/ld phase transition occurs in giant vesicles at 40 °C [11]. Combining these pieces of information, the interaction parameter can be taken to be of order $J_0 = 0.274$ kcal/mol [20]. This value is consistent with the lipid interaction energy J used for the continuum approach in Section 3. The connection between interaction parameters in continuum and discrete models can be found in Ref. [24].

3.2. Effect of Proteins on Phase Stability

The study of the effects of neutral ($\lambda = 0$) proteins on the phase stability of the lipid mixture is performed using a nonconserved Monte Carlo spin dynamics based on the Swendsen–Wang algorithm [31,32]. For a given temperature, the Swendsen–Wang algorithm samples all lipid compositions with appropriate statistical weights [31], so that it can be used to construct the phase diagram of the mixture (see Refs. [20,21] for more details). During the simulation, protein sites act as static neutral obstacles and their spins are never changed.

The analysis of the simulations shows that the presence of neutral proteins leads to a significant shift of the coexistence curve to smaller temperatures, that is, to a reduction of the two-phase region of the phase diagram. The effect is more pronounced when the protein area fraction increases, but even at low values of ϕ, the effect is rather important; see, for example, the case with $\phi = 0.1$ and $r = 1$ in Fig. 6A. The reduction of the two-phase region is due to the protein surfactant action: neutral proteins

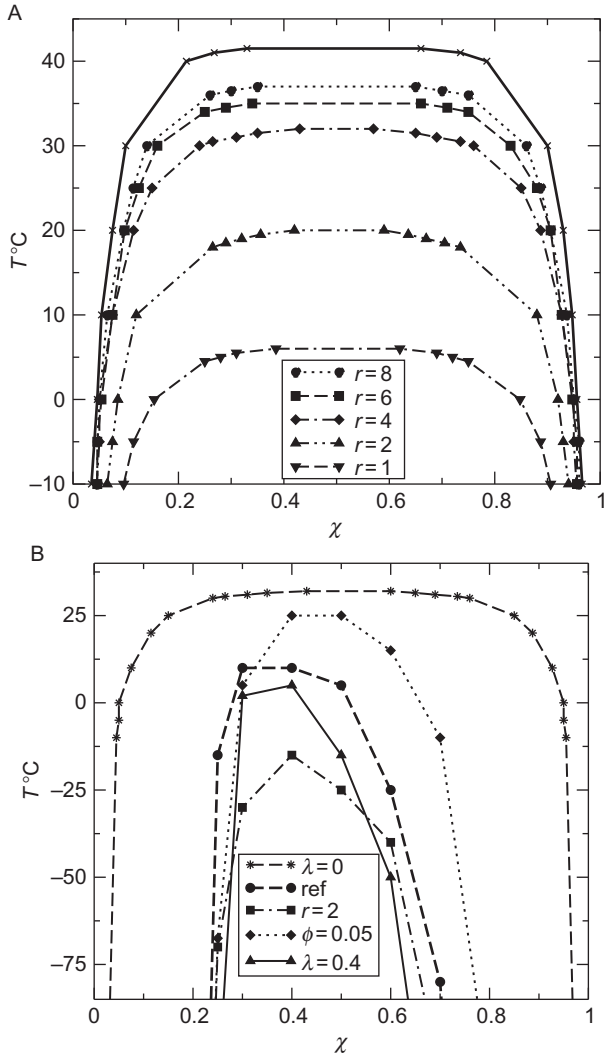

Figure 6 (A) (T, χ)-phase diagram for a lipid mixture with neutral ($\lambda = 0$) proteins. The top solid line corresponds to the protein-free mixture ($\phi = 0$), whereas the dashed curves stand for mixtures with 10% of the area occupied by neutral proteins of different sizes ($\phi = 0.1$). (B) (T, χ)-phase diagrams for different lipid mixtures The reference case corresponds to $r = 4$, $\phi = 0.1$, and $\lambda = 0.2$ kcal/mol, which is compared to its analogue with neutral proteins ($\lambda = 0$) in the figure. The legends indicate the model parameters that are varied with respect to the reference case. Coexistence curves for variations of protein size ($r = 2$), protein coverage ($\phi = 0.2$), and protein–lipid interaction ($\lambda = 0.4$) are plotted. In both panels, the lines connecting points are simply a guide to the eye. The two-phase regions are contained below each coexistence curve, and the lipid mixture has been simulated on a 300×300 lattice.

reduce the line tension between different lipid phases, stabilizing small lo domains that may be identified as nanometric lipid rafts [20,21].

Simulations with a protein area coverage of 10% have been run for different protein radii r. The corresponding phase diagrams are presented in Fig. 6A. A clear reduction of the protein effect reported above is observed when the size of the proteins is increased. Specifically, for a given protein coverage, an increase of protein size brings the coexistence curve closer to that of the protein-free situation. The reason for this behavior is simple. For given protein coverage, larger proteins lead to a smaller number of lipid–protein contacts, and therefore, the surfactant action of the proteins is diminished [21].

We now consider the fact that transmembrane proteins also interact with surrounding lipids via short-range interactions. These interactions may be due to different causes. Coulombic interactions with charged lipids or between charged groups of proteins and lipids may occur [33]. A more general effect can be caused by lateral packing preferences [7]. Another effect arises from the hydrophobic mismatch due to the fact that the hydrophobic span of the inserted protein and that of the lipid membrane do not coincide [34,35].

In order to estimate the value of the parameter λ, we could consider, for example, that transmembrane proteins may prefer to be surrounded by unsaturated lipids forming the liquid-disordered phase since they are more flexible and can be bent and stretched more easily to minimize the hydrophobic energy penalty. The exposure of a hydrophobic part of the protein or lipid to a polar environment implies an energy penalty proportional to the thickness mismatch, $\lambda = K|d_{\mathrm{p}} - d_{\mathrm{l}}|$, with an energy constant K that is experimentally quantified to be of the order of 0.25×10^{-13} erg/nm per lipid molecule [34,35]. Liquid-ordered and liquid-disordered phases display a difference in membrane thickness that, as an example, is of the order of 0.8 nm for the case of DOPC/SM/Chol mixtures [36]. Considering the lipid–protein hydrophobic mismatch to be of the order of this length, an interaction energy A of the order of several hundreds of cal/mol is found.

The straightforward implementation of the Hamiltonian in Eq. (7) for $\lambda \neq 0$ in the Swendsen–Wang algorithm has a major drawback. The lipid–protein interaction can be interpreted as the inclusion of an external field applied only to the lipid sites surrounding the proteins, and the Swendsen–Wang algorithm is extremely inefficient when external fields are applied to the system. Here, we have used the so-called two-replica algorithm, which has been used in other contexts [37] and has been shown to overcome this limitation (see details in Ref. [21]).

The (T, χ) coexistence curve for a lipid mixture with proteins of size $r = 4$ and $\lambda = 0.2$ kcal/mol covering 10% of the membrane area is plotted in Fig. 6B and is compared to its analogue with neutral proteins. Protein affinity for one of the lipid components causes a downward shift of the

coexistence curves along with a narrowing of the included two-phase region with respect to the case of noninteracting proteins. Moreover, as expected, the interaction breaks the symmetry of the phase diagram, shifting the maximum of the coexistence curve to higher concentrations of the favorable lipid component (changing $\lambda \rightarrow -\lambda$ leads to the same phase diagram if $\chi \rightarrow -\chi$). Therefore, the general effect of protein–lipid interactions for a given r and ϕ is to decrease the transition temperature at any given composition, favoring the miscibility of the mixture.

Starting from the case discussed above ($r = 4$, $\phi = 0.1$, and $\lambda = 0.2$) as a reference state, we analyze the effect of protein size, protein coverage, and protein–lipid interaction by constructing the phase diagrams for $r = 2$, $\phi = 0.05$, and $\lambda = 0.4$, respectively. The coexistence curves for these three cases are plotted in Fig. 6B. The comparison of these curves with the reference case reveals that the shift to lower transition temperatures and the narrowing of the two-phase region are more pronounced for smaller proteins, larger coverages, and stronger protein–lipid interactions.

From the results reported so far, it seems clear that the presence of protein static obstacles favors lipid miscibility by stabilizing small lipid aggregates and that this effect is greatly enhanced if proteins interact with their surrounding lipids. These consequences on the lipid phase stability are reduced if the size of the protein obstacles is large (larger than the lipid cross section). However, the latter effect is not particularly dramatic for interacting proteins, and even relatively large proteins may lead to a significant reduction of the transition temperature. The narrowing of the coexistence curves in Fig. 6B also plays in favor of this observation.

3.3. Two Mechanisms for Nanodomain Stabilization

So far we have focused on the changes in the phase diagram of membrane lipid mixtures due to the inclusion of static proteins. As a main result, we have shown that lipid mixtures that should be segregated into two different phases remain mixed when proteins are added to the membrane. Beyond this formal phase-stability study, the applicability of our results in the biological context relies on the *structural* mechanisms that stabilize nanometric lipid fluctuations, preventing complete phase separation. Two different mechanisms for nanodomain stabilization have been distinguished [21]. On the one hand, neutral proteins surround the incipient phase segregating lipid domains, therefore relaxing the energy between liquid-ordered and liquid-disordered domains and preventing coarsening. In this case, proteins mimic the action of a surfactant and reduce interdomain line tension (see Fig. 7A). On the other hand, interacting proteins nucleate aggregates of compatible lipids around them. In the case of static proteins, these nanoscale aggregates become pinned (see Fig. 7B) and are prevented from coarsening and forming a macroscopic separated phase domain. Such

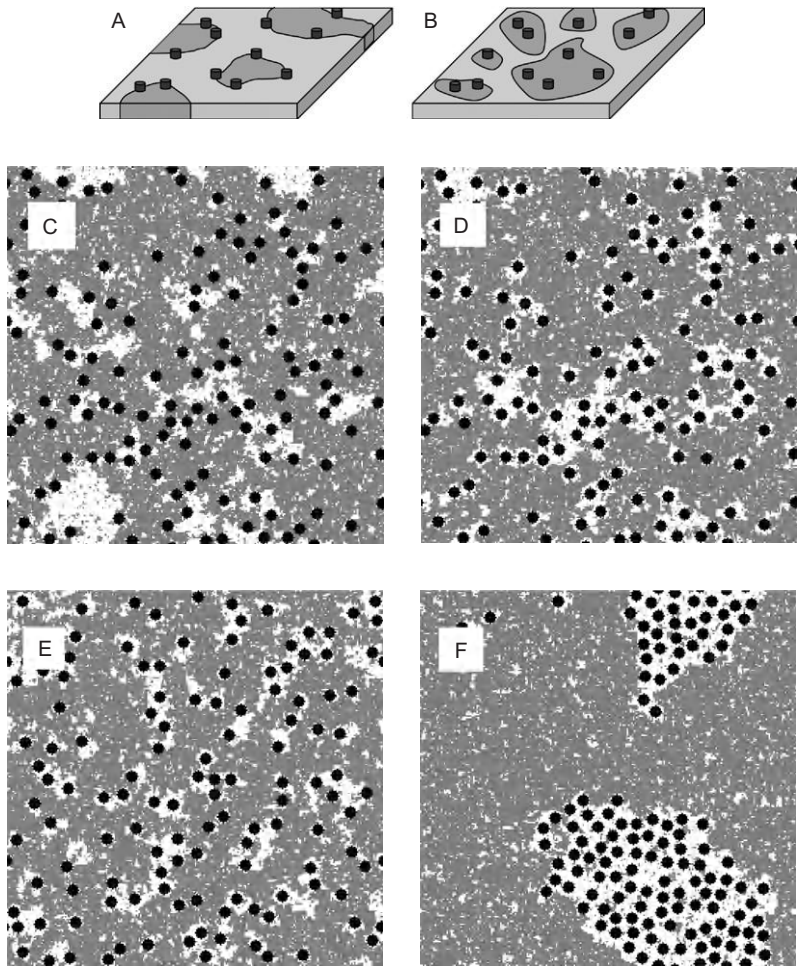

Figure 7 First row: schematic description of the two mechanisms for nanodomain stabilization. (A) Neutral proteins relax the line tension between lipid domains. (B) Interacting proteins nucleate domains of compatible lipids that are not allowed to coarsen. Second row: Monte Carlo simulations capturing the two stabilization mechanisms. (C) Corresponds to inert proteins and displays a protein–lipid organization similar to the one in (A), whereas in (D), the configuration for interacting proteins resembles (B). Third row: simulations showing the effect of mobile interacting proteins. (E) Proteins move at random, mixing the lipid matrix. (F) Proteins move seeking the free-energy minimum of the system, promoting phase separation. All the snapshots are representative of equilibrium or stationary states. In all cases, $N = 256$, $\chi = 0.25$, $\phi = 0.1$, $r = 4$, $\lambda = -0.2$ (except (C), in which $\lambda = 0$) and $T = 35\,^{\circ}\mathrm{C}$. Ordered lipids are depicted in white, disordered lipids in gray, and proteins in black.

an effect has also recently been found in continuum mean-field models of lipid–protein membrane mixtures [38].

The two mechanisms for nanodomain stabilization schematically described in Fig. 7A and B can also be captured by means of a simple Monte Carlo algorithm. We start with a fixed lipid composition of $\chi = 0.25$ and a coverage of proteins of $\phi = 0.1$ and a radius $r = 4$. We then apply a nonkinetic conserved Monte Carlo algorithm based on a completely *rough* dynamics of attempted moves whereby (any) two lipid spins may exchange places according to a Metropolis rule. Although this method does not reproduce the realistic kinetics of the system since diffusion in a real system occurs by exchange of nearest-neighbor particles, it is a mean-field approach that ensures the fastest equilibration. Representative snapshots of equilibrium systems with neutral ($\lambda = 0$) and interacting ($\lambda = -0.2$) proteins are plotted in Fig. 7C and D, respectively, showing good agreement with schematic Fig. 7A and B. Based on these simulations, a quantitative characterization of the two reported mechanisms has been performed in the following two steps. First, the spatial correlation function for the lipid spin variable is averaged over a large number of simulation configurations for the cases in Fig. 7C and D. The distance L at which the correlation is lost (i.e., the correlation function first crosses zero) provides a characteristic length of the lipid domains. For both cases, we obtain $L \approx 40$ nm, whereas for the case without proteins, L is expected to continuously grow with time since macroscopic phase separation takes place (not shown). Second, we have computed the fraction χ_p of lipids of each kind occupying the sites in contact with proteins. For the simulations with neutral proteins in Fig. 7C, we get $\chi_p \approx 0.4$. This fraction is larger than the overall lipid fraction $\chi = 0.25$ used in the simulation and approaches 50% of each kind of lipid, thus verifying the surfactant action of inert proteins. For the case of interacting proteins in Fig. 7D, we obtain $\chi_p \approx 0.8$, much larger than $\chi = 0.25$, confirming the nucleating role of the interacting inclusions.

Although both protein-induced nanodomain stabilization mechanisms reported so far correspond to the case of static proteins, some final comments on a more general scenario with mobile inclusions can be anticipated. For interacting proteins, two different situations have to be considered: completely random mobility due to external forces (nonequilibrium, for instance, due to proteins anchored to actin filaments growing and pushing the membrane), and protein diffusion seeking the free-energy minimum of the system (equilibrium). In the former case, the mobility of the interacting proteins has a "mixing" effect and acts against phase separation, so that the stabilization of the mixed phase in the phase diagram reported here for static inclusions is expected to be even further enhanced. Additionally, the nanodomain stabilization mechanism presented in Figs. 7B and D for interacting proteins still applies (see Fig. 7E for a representative snapshot), although the size and lifetime of the lipid aggregates that nucleate around

proteins would probably decrease, particularly for high protein mobilities. In the equilibrium scenario, the effect is completely different since mobile interacting proteins promote complete phase separation and increase the transition temperature from that of a protein-free system. Proteins nucleate compatible lipids around them, and protein mobility helps the coarsening process (see Fig. 7F for a representative snapshot).

4. Tuning Membrane Lipid Heterogeneity Near the Phase Boundary

While miscible systems are macroscopically homogeneous, tiny and unstable composition fluctuations are continuously formed and destroyed. For lipid bilayer mixtures, these fluctuations can even be experimentally detected when the system is near a phase boundary [18,19]. Close to a phase separation boundary, the spatiotemporal behavior of the system becomes extremely sensitive to external perturbations, and we next inspect the possibility of raft formation in this scenario.

A lipid membrane mixture that consists of saturated lipids, unsaturated lipids, and cholesterol is investigated by means of a Monte Carlo model. We address the spatiotemporal characterization of compositional heterogeneities when the lipid mixture approaches a phase boundary as a result of changes in its cholesterol content. The properties of such domains are shown to be determined by the balance of the affinities between constituent species and by their molecular fractions. We first analyze the size and lifetime of these transient aggregates when the phase boundary is approached by increasing the amount of cholesterol in the membrane. The size and stability of compositional fluctuations are found to abruptly change in the pretransition region, thus providing a switch-like mechanism that controls the generation of either small and transient domains or large and stable lipid structures [39].

Second, as suggested in the previous section, the inclusion of certain proteins in the membrane plays an active role in lipid organization by stabilizing small lipid assemblies. In this case, the characteristics of fluctuations vary more smoothly when approaching the phase boundary, providing a tuning mechanism that modulates the size and lifetime of lipid domains [39].

4.1. The Model and Spatiotemporal Characterization

Our Monte Carlo approach is based on a lattice system for the description of lipid/cholesterol membranes. Two kinds of generic lipids, saturated (A) and unsaturated (B), fully occupy a 2D triangular lattice with N^2 sites, ϕ being the molar fraction of saturated lipid on the lattice. Cholesterol (C)

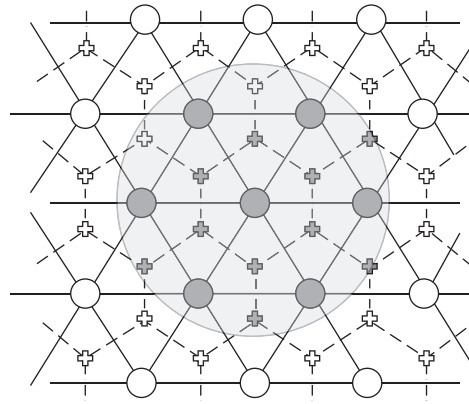

Figure 8 Lattices of our model. Saturated and unsaturated lipids fully occupy the triangular lattice of circular nodes. Cholesterols are intercalated between the lipids and occupy some of the cross nodes forming the honeycomb lattice. Gray sites correspond to a protein particle residing on the lipid/cholesterol lattices.

molecules are intercalated on a complementary honeycomb lattice of $2N^2$ sites (see Fig. 8), c being its occupancy fraction. The membrane molar fractions X_i for i = A, B, and C components are $\frac{\phi}{1+2c}$, $\frac{1-\phi}{1+2c}$ and $\frac{2c}{1+2c}$, respectively. A triangular lattice has been used in computer simulations to model lipids in membranes [16,40], and the combination with a superimposed hexagonal lattice has been also used to study the effect of cholesterol on lipid mixtures [24,41]. Moreover, this choice agrees with the experimental values for the area per molecule for each species. Common membrane lipids occupy about 0.6–0.8 nm^2/molecule (as noted earlier in Section 3.1), whereas cholesterol molecules fill up about 0.35–0.4 nm^2/molecule. The combination of the two proposed lattices follows the observed 2/1 ratio for the lipid/cholesterol area per molecule. The choice of 0.64 nm^2/lipid molecule fixes the linear site-to-site distance of the triangular lattice at 0.8 nm.

The description of the energetics of the system is performed in terms of two sets of spin variables, namely, spins $\{S_i\}$ which are fixed on the N^2 sites $\{i\}$ of the triangular lattice, and spins $\{\hat{S}_\alpha\}$ on the $2N^2$ sites $\{\alpha\}$ of the hexagonal lattice. The spins S_i take on the values $+1$ or -1 denoting the presence of an A or B particle at site i, respectively. The spin $\hat{S}_\alpha$ is equal to 1 if a C particle occupies the site α, and 0 otherwise. According to these spin variables, our Ising Hamiltonian has the form

$$\frac{\mathcal{H}}{k_B T} = -J_0 \sum_{\langle ij \rangle} S_i S_j - G_0 \sum_{\langle i\alpha \rangle} S_i \hat{S}_\alpha, \tag{8}$$

where only nearest-neighbor interactions are considered in the AB lattice (denoted by $\langle ij \rangle$) and between the two lattices (denoted by $\langle i\alpha \rangle$). J_0 again corresponds to the strength of the exchange interaction between A and B, and G_0 accounts for the interaction with the lattice containing C. $G_0 > 0$ corresponds to a preferential affinity between A and C components. In this section, the interaction parameters are again given in units of $k_B T$. The connection between interaction parameters in continuum (J, G) and discrete (J_0, G_0) models can be found in Ref. [24].

Kawasaki spin dynamics [42] is chosen to evolve the system toward the equilibrium associated with Eq. (8). The selected spin dynamics and an appropriate choice for the Monte Carlo time step in our simulations lead to the reproduction of a realistic kinetics of the system (see Ref. [39] for more details). We refer to this algorithm as kinetic Monte Carlo simulations. All our kinetic simulations are performed on lattices of size $N = 500$ ($0.4\ \mu m \times 0.4\ \mu m$) and a number of steps between 5×10^{10} and 10^{12}, depending on the lifetimes of the resulting domains (see below). The longest simulations allow the calculation of lifetimes up to 0.05 s, the upper limit of our kinetic simulations. The lattice size also fixes a limit of 150 nm for the length of emerging domains (domain sizes larger than this value are taken to correspond to complete phase separation). Periodic boundary conditions are applied to both lattices. The disordered initial configuration is obtained by randomly placing N_A and N_B particles on the triangular lattice and N_C particles on the hexagonal lattice, with $N_A + N_B = N^2$, $\phi = N_A/N^2$, and $c = N_C/2N^2$. The size and lifetime results are averaged after an equilibration period of 50% of the simulation time.

Kinetic Monte Carlo simulations become increasingly long and may lead to misleading conclusions about the phase stability of the mixture when close to the phase boundary. We again follow our earlier procedure of circumventing this problem by using a nonkinetic algorithm based on a completely *rough* dynamics of attempted moves whereby (any) two spins of a given lattice may exchange places. This algorithm does not reproduce the realistic kinetics of the system but ensures the fastest equilibration and allows us to check the phase stability of the system. For each kinetic simulation, the corresponding nonkinetic simulation is run in larger systems (1000×1000), to confirm the phase stability of the system.

The spatiotemporal behavior of the lipid mixture is studied from two perspectives: the size of the domains and their mean lifetime. Although the phenomenon is dynamic (clusters are continuously created and annihilated), fluctuations can be characterized by an equilibrium size-distribution function. Here, domain sizes are analyzed by the domain size distribution $p(n)$ of interconnected lipid A molecules. From this distribution, we compute the probability that a lipid A is at any given moment forming a cluster with n interconnected A lipids, $P(n) = np(n)/\int np(n)\mathrm{d}n$, and, from here, the mean linear domain size,

$$L = 0.8\left[\int nP(n)\mathrm{d}n\right]^{1/2} \text{nm}, \tag{9}$$

where, as stated earlier, each lipid molecule is taken to occupy an area of 0.8 nm × 0.8 nm. A domain lifetime $t_{1/2}$ is estimated as the time needed for a given domain to lose half of its lipid components. The stability of a domain depends on its size (generally, for a given simulation, larger domains are more stable), so that the computation of $t_{1/2}$ is performed for different domain sizes. The characteristic lifetime is then taken to be the lifetime associated with the mean linear size, $t_{1/2}(L)$. The estimation of the simulation time units, s.t.u., is as follows. We consider the mean square displacement of a freely diffusing A particle to be $\lambda = \sqrt{2D\Delta t} \approx 0.8\,\text{nm}$, where the membrane lipid diffusivity $D \approx 10\ \mu\text{m}^2/\text{s}$ [28] and Δt is the time interval between particle jumps. Since the diffusing lipid molecule can jump freely to six different neighboring sites, one has $\Delta t = \text{s.t.u.}/6$, and therefore $\text{s.t.u.} \approx 2 \times 10^{-7}$ s.

4.2. Crossing the Phase Boundary in the Absence of Proteins

The strategy of the simulations in this section consists in approaching the phase boundary by performing simulations at different values of a given control parameter. Temperature is a fairly unvarying system variable in living cells, so that it cannot be appealed to explain changes in the membrane lipid organization *in vivo*. Changes in the phase stability of the membrane are more likely to originate from variations in the composition of the mixture. In this context, membrane cholesterol levels are known to be precisely controlled by numerous cellular processes [43], and these levels are believed to play a fundamental role in regulating the structural and dynamical properties of cell membranes [22]. We explore this premise by performing numerical simulations with different amounts of cholesterol.

The values for the model parameters and simulation conditions are chosen as follows. The system is chosen to have a 2:1 ratio of unsaturated: saturated lipids ($\phi = 0.333$) as a reasonable lipidic proportion in cell membranes [28]. Calorimetry experiments in lipid systems with cholesterol and different saturated and unsaturated lipids [25,26] lead to a reasonable estimation $J_0 \in (0.07\text{–}0.25)$ and $G_0 \in (0.5\text{–}1)$ [39], both in $k_\text{B}T$ energy units (consistent with values quoted in Sections 2 and 3). Here, intermediate values $J_0 = 0.12$ and $G_0 = 0.75$ have been chosen for all simulations. The following set of simulations is performed. The first simulation corresponds to a system with a very small cholesterol fraction X_C that places the mixture in the one-phase region far from the phase separation boundary. The kinetic Monte Carlo protocol explained above is applied, and the average size L and lifetime $t_{1/2}$ of the equilibrium fluctuations are computed. This process is

successively repeated for increasing values of X_C, until immiscibility is detected by the nonkinetic simulations in 1000×1000 systems. This procedure is schematically represented in the inset of Fig. 9C.

The results of this set of simulations are presented in Fig. 9. Low cholesterol fractions place the mixture in the one-phase region far from the phase boundary, and the system only displays very small A/C clusters that break up quickly. When the cholesterol amount is increased, larger and more stable A/C (raft-like, liquid-ordered) domains appear in the system: domain size distributions $P(n)$ are shifted to larger sizes and domain lifetimes $t_{1/2}$ increase (see (A) and (B) of Fig. 9, respectively). A range of cholesterol compositions is found before crossing the transition value that displays biologically realistic domain sizes and lifetimes [7]. For example, the case with low cholesterol fraction, $c = 0.1$ ($X_C = 0.167$), leads to a small mean linear domain size of $L = 8.2$ nm and a very short lifetime of $t_{1/2} = 0.038$ ms. Increasing the amount of cholesterol up to $c = 0.16$ ($X_C = 0.242$) results in $L = 20.95$ nm and $t_{1/2} = 1.19$ ms. Going further, up to $c = 0.18$ ($X_C = 0.265$), simulations yield $L = 56.48$ nm and $t_{1/2} = 4.69$ ms. The closer one gets to the phase boundary, the larger and more stable are the domains. A larger amount of cholesterol, $c = 0.19$ ($X_C = 0.275$), still corresponds to the one-phase state and leads to larger mean domain sizes, $L = 131.28$ nm, although in this case, the mean lifetime exceeds the maximum that can be evaluated with our kinetic simulations. Beyond this value ($X_C > 0.275$), the phase separation boundary is crossed and a single stable A/C domain is observed. Domain size and lifetime are no longer computed in these situations since both quantities formally diverge in the immiscibility region.

The results presented here have shown how changes in the cholesterol amount may be used by the cell to regulate the size and stability of the membrane lipid fluctuations within the same length and timescales as those found experimentally for rafts [7]. Note, however, that the increase of L and $t_{1/2}$ in the pretransition region is rather sharp, that is, a narrow range of X_C leads to intermediate domain sizes and lifetimes. The characteristics of fluctuations are then extremely sensitive to cholesterol variations when the miscibility boundary is approached, and this can be understood as a switch-like mechanism that regulates the formation of either very small short-lived raft-like structures or large stable lipid platforms.

4.3. Crossing the Phase Boundary in the Presence of Proteins

A higher level of description for the cell membrane beyond its lipid composition is needed to take into account the effect of membrane proteins. We noted earlier (cf. Section 3.1) that at a first level of complexity, proteins are considered to be statically inserted in the membrane, thus acting as neutral obstacles. This picture addresses, for example, the transmembrane

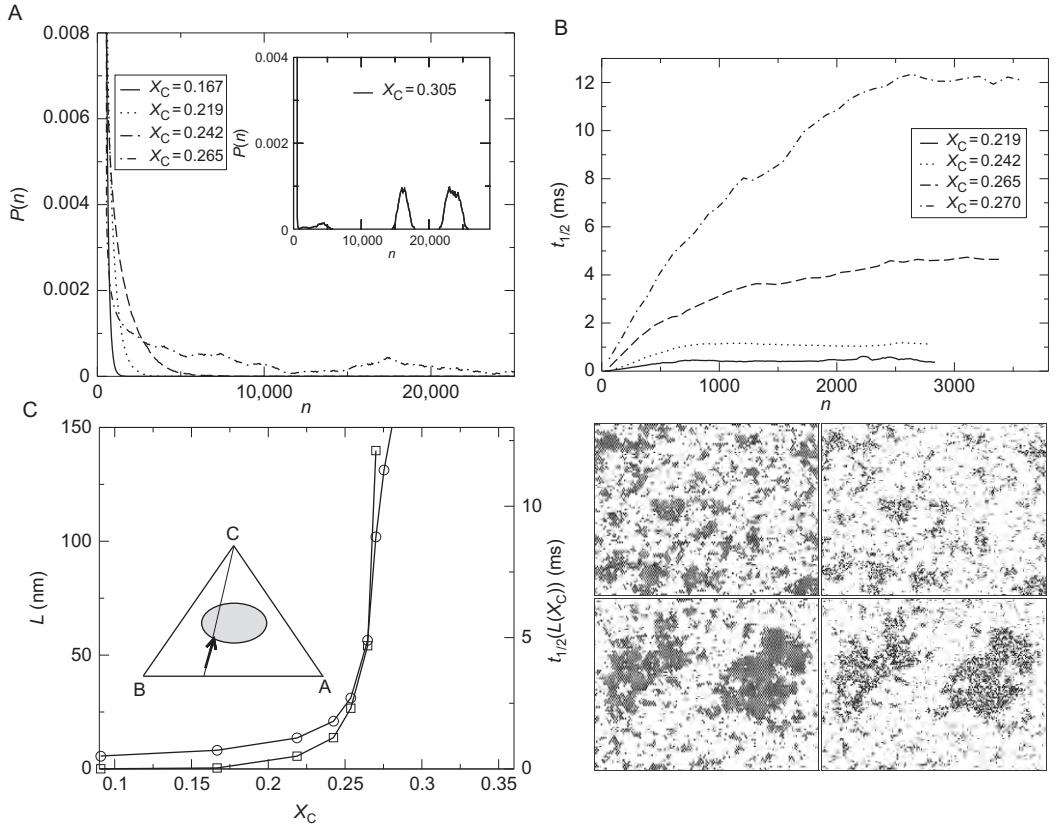

Figure 9 Domain size $P(n)$ (A) and lifetimes $t_{1/2}$ (B) distributions plotted for different cholesterol compositions c in simulations with $\phi = 0.333$, $J_0 = 0.12$, and $G_0 = 0.75$. (C) Mean linear domain size L (circles) and the corresponding characteristic domain lifetimes $t_{1/2}(L)$ (squares) as a function of cholesterol fraction. The inset corresponds to a schematic representation of the phase diagram exploration line. The arrow describes the approach to the phase boundary by increasing the amount of cholesterol while keeping the 2:1 ratio of unsaturated(B):saturated

proteins bound to the cytoskeleton and anchored to the membrane as "pickets." In this section, for simplicity, such proteins are considered to not energetically interact with the lipid mixture (i.e., we consider the case of no preferential affinity to any of the three lipid components), but they may modify the phase stability of the mixture [20,21].

In the proposed lattice model, each protein is assumed to occupy a unit of seven neighboring lipid sites and the surrounding 12C lattice nodes, covering a membrane area ≈ 4 nm^2 (see Fig. 8). The insertion of proteins does not alter the form of the Hamiltonian in Eq. (8). Since the simulated proteins are considered neutral, all protein site spins are set to zero in both lattices and the Hamiltonian can be retained as given. The spin dynamics, however, is modified to simulate proteins. Since the proteins are considered to be static, all events involving the exchange of a lipid or cholesterol particle on a protein site are ignored in the Monte Carlo algorithm. The simulations are run for different fractions of membrane area occupied by proteins, that is, for a particular number of proteins initially distributed randomly in the membrane. For a given amount of protein, averages are computed for 10 different initial configurations of randomly placed proteins. Molar fractions of lipid species stated in this section do not consider the area occupied by proteins; instead, they are only fractions of the mixture of lipid components. Protein concentration is given in percent of coverage area.

As a general outcome, the simulations show that the presence of proteins changes lipid organization in a drastic manner. Even for a small area fraction of protein, domains of a larger mean linear size than in protein-free systems are observed, even though the lipid mixture is eventually prevented from complete phase separation. The analysis of the temporal stability reveals that the generated transient domains, regardless of their size, are in general much more stable if proteins are present, with lifetimes up to several tens of milliseconds or even longer. Visual inspection of simulation snapshots unveils the mechanism that stabilizes such raft-like domains. When placed at the interface of generated domains, proteins relax nonfavorable interactions between unlike species at the domain boundaries, acting as surfactants. Such a mechanism was already reported in the previous section of this chapter for neutral proteins in binary lipid mixtures [21]. Here, a new insight has been gained, with a quantitative study of the domain size and stability.

(A) lipids. The gray region corresponds to the two-phase region. Right-bottom panel: representative snapshots for small 100 × 100 systems with cholesterol composition $c(X_C) = 0.14(0.219)$ (top) and $c(X_C) = 0.18(0.265)$ (bottom). The lipid lattice is shown in the first row (black for saturated lipids A, white for unsaturated lipids B); the second row shows the cholesterol lattice (black for cholesterol molecules C).

A new set of simulations addresses the behavior as a function of cholesterol concentration when proteins are present. In Fig. 10, the mean linear domain sizes and lifetimes are plotted as a function of cholesterol concentration for different protein coverages. Following the trend presented above, protein insertion shifts the cholesterol amount needed to promote phase separation to larger values and strongly increases the stability of fluctuations. More significantly, the *steep* behavior of L and $t_{1/2}$ when approaching phase separation (by means of cholesterol addition) is made

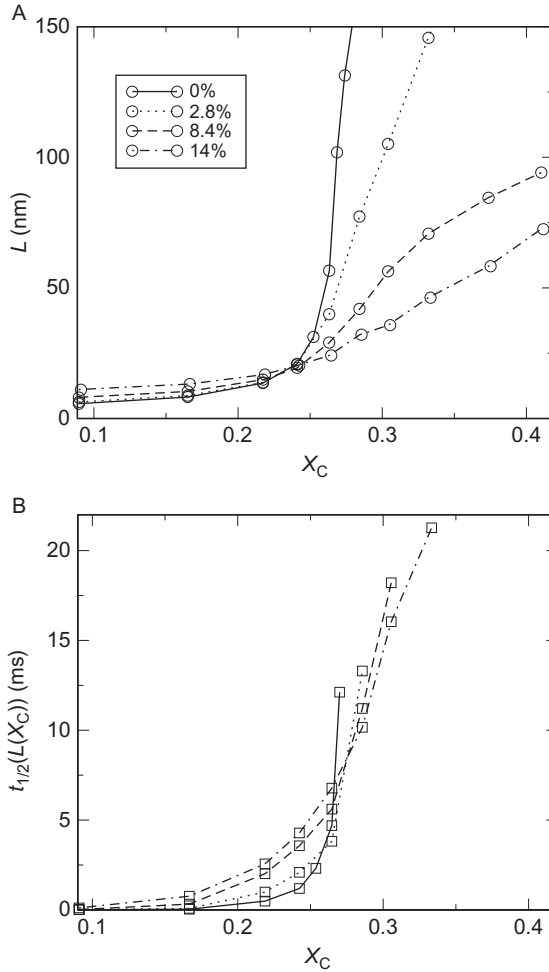

Figure 10 Mean linear domain size L (A) and the corresponding domain lifetimes $t_{1/2}(L)$ (B) as a function of cholesterol composition at different protein area fractions. The other simulation parameters are $\phi = 0.333$, $J_0 = 0.12$, and $G_0 = 0.75$, the same as those used in Fig. 9.

more *gradual* when proteins are inserted in the membrane [39]. The main conclusion is that the inclusion of proteins *smooths* the behavior of the characteristics of fluctuations in the pretransition region, thus providing a reasonably flexible and adaptable cooperative tuning mechanism to modulate the size and stability of rafts in cell membranes.

The quantification of the equilibrium spatial and temporal characteristics of composition fluctuations in a lipid mixture when approaching the phase boundary by addition of cholesterol is one of the important results reported in this section. The other important outcome is the identification of two different mechanisms for raft regulation in the latter context: a switch-like mechanism that leads to either small and unstable structures or large lipid platforms, and a more gradual tuning mechanism that modulates the size and stability of raft-like domains. The latter mechanism involves the presence of inert and static proteins that strongly stabilize nanometric domains up to lifetimes of the order of tens of milliseconds or more. The general outcome of our study is also consistent with a dynamic picture of the raft phenomenology: small and transient rafts exist in the cell membrane, and their size and stability can be dynamically modified by simply adding or removing small amounts of any of its components. Formation of macroscopic and stable raft platforms as a result of the coalescence of small ones can be explained in this picture as the displacement of the lipid mixture into the immiscibility region of the phase diagram caused by a particular signal or stimulus.

5. Conclusions

We have reviewed several mechanisms that may explain raft phenomenology in cell membranes. First, we have considered the case of a lipid mixture in the two-phase region of its phase diagram and have shown that a cholesterol exchange process counteracts the phase separation process, leading to the formation of finite-size lipid aggregates. Second, we have shown how the insertion of transmembrane proteins in a miscible lipid mixture stabilizes lipid fluctuations. Finally, the combination of the variation of cholesterol membrane contents and the insertion of proteins has been shown to provide a robust cooperative mechanism for the control of nanoscale lipid organization in cell membranes. The applicability of the results of these proposals in a biological context has been discussed.

Due to the complexity of the cell membrane, the real mechanisms that control its lipid organization are also complex. Actually, there is no single button that can be pushed to control lipid organization in the cell membrane. More likely, multiple factors act cooperatively to control such organization. Here, we have explored the effects of some of these possible contributions.

ACKNOWLEDGMENTS

Computational resources were provided by the Barcelona Supercomputing Center (MareNostrum). We would like to thank J. Gómez, F. Sagués, and J. Buceta for their contribution to different parts of this review. R. R. thanks the financial support provided by SEID through project BFU2010-21847-C02-02 and by DURSI through project 2009-SGR1055. K. L. gratefully acknowledges the NSF under Grant No. PHY-0855471.

REFERENCES

[1] S.J. Singer, G.L. Nicolson, The fluid mosaic model of the structure of cell membranes, Science 175 (1972) 720–731.
[2] G. Vereb, J. Szöllösi, J. Matkó, P. Nagy, T. Farkas, L. Vígh, et al., Dynamic, yet structured: the cell membrane three decades after the Singer-Nicolson model, Proc. Natl. Acad. Sci. USA 100 (2003) 8053–8058.
[3] K. Simons, E. Ikonen, Functional rafts in cell membranes, Nature 387 (1997) 569–572.
[4] K. Simons, D. Toomre, Lipid rafts and signal transduction, Mol. Cell. Biol. 1 (2000) 31–41.
[5] A.D. Douglass, R.D. Vale, Single-molecule microscopy reveals plasma membrane microdomains created by protein-protein networks that exclude or trap signaling molecules in T cells, Cell 121 (2005) 937–950.
[6] R.G.W. Anderson, K. Jacobson, A role for lipid shells in targeting proteins to caveolae, rafts, and other lipid domains, Science 296 (2002) 1821–1825.
[7] A. Kusumi, I. Koyama-Honda, K. Suzuki, Molecular dynamics and interactions for creation of stimulation-induced stabilized rafts from small unstable steady-state rafts, Traffic 5 (2004) 213–230.
[8] J.F. Hancock, Lipid rafts: contentious only from simplistic standpoints, Mol. Cell. Biol. 7 (2006) 456–462.
[9] J.R. Silvius, Role of cholesterol in lipid raft formation: lessons from lipid model systems, Biochim. Biophys. Acta 1610 (2003) 174–183.
[10] A. Radhakrishnan, H. McConnell, Condensed complexes in vesicles containing cholesterol and phospholipids, Proc. Natl. Acad. Sci. USA 102 (2005) 12662–12666.
[11] S.L. Veatch, S.L. Keller, Miscibility phase diagrams of giant vesicles containing sphingomyelin, Phys. Rev. Lett. 94 (2005) 148101.
[12] V.A.J. Frolov, Y.A. Chizmadzhev, F.S. Cohen, J. Zimmerberg, 'En-tropic traps' in the kinetics of phase separation in multicomponent membranes stabilize nanodomains, Biophys. J. 91 (2006) 189–205.
[13] C. Zurzolo, G. van Meer, S. Mayor, The order of rafts, EMBO Rep. 4 (2003) 1117–1121.
[14] M.S. Turner, P. Sens, N.D. Socci, Nonequilibrium raftlike membrane domains under continuous recycling, Phys. Rev. Lett. 95 (2005) 168301.
[15] L. Foret, A simple mechanism of raft formation in two-component fluid membranes, Europhys. Lett. 71 (2005) 508–514.
[16] J. Gómez, F. Sagués, R. Reigada, Actively maintained lipid nanodomains in biomembranes, Phys. Rev. E 77 (2008) 021907.
[17] J. Gómez, F. Sagués, R. Reigada, Nonequilibrium patterns in phase separating ternary membranes, Phys. Rev. E 80 (2009) 011920.
[18] G.W. Feigenson, J.T. Bulboltz, Ternary phase diagram of dipalmitoyl-PC/dilauroyl-PC/cholesterol: nanoscopic domain formation driven by cholesterol, Biophys. J. 80 (2001) 2775–2788.

[19] S.L. Veatch, O. Soubias, S.L. Keller, K. Gawrisch, Critical fluctuations in domain-forming lipid mixtures, Proc. Natl. Acad. Sci. USA 104 (2007) 17650–17655.
[20] A. Yethiraj, J.C. Weisshaar, Why are lipid rafts not observed in vivo? Biophys. J. 93 (2007) 3113–3119.
[21] J. Gómez, F. Sagués, R. Reigada, Effect of integral proteins in the phase stability of a lipid bilayer: application to raft formation in cell membranes, J. Chem. Phys. 132 (2010) 135104.
[22] S. Mayor, M. Rao, Rafts: scale-dependent, active lipid organization at the cell surface, Traffic 5 (2004) 231–240.
[23] P. Sharma, R. Varma, R.C. Sarasij, K. Gousset, G. Krishnamoorthy, M. Rao, et al., Nanoscale organization of multiple GPI-anchored proteins in living cell membranes, Cell 116 (2004) 577–589.
[24] R. Reigada, J. Buceta, J. Gómez, F. Sagués, K. Lindenberg, Phase separation in three-component lipid membranes: from Monte Carlo simulations to Ginzburg-Landau equations, J. Chem. Phys. 128 (2008) 025102.
[25] P.F.F. Almeida, A. Pokorny, A. Hinderliter, Thermodynamics of membrane domains, Biochim. Biophys. Acta 1720 (2005) 1–13.
[26] M.L. Frazier, J.R. Wright, A. Pokorny, P.F.F. Almeida, Investigations of domains formation in sphingomyelin/cholesterol/POPC mixtures by fluorescence resonance energy transfer and Monte Carlo simulations, Biophys. J. 92 (2007) 2422–2433.
[27] J.W. Cahn, J.E. Hilliard, Free energy of a nonuniform system. I. Inter-facial free energy, J. Chem. Phys. 28 (1958) 258–267.
[28] M.D. Houslay, K.K. Stanley, Dynamics of Biological Membranes, John Wiley & Sons, Chischester, 1982.
[29] T.L. Steck, J. Ye, Y. Lange, Probing red cell membrane cholesterol movement with cyclodextrin, Biophys. J. 83 (2002) 2118–2125.
[30] See, for example, the "Orientation of Proteins in Membranes" (OPM) data base in http://www.opm.phar.umich.edu/.
[31] R.H. Swendsen, J.S. Wang, Nonuniversal critical dynamics in Monte Carlo simulations, Phys. Rev. Lett. 58 (1987) 86–88.
[32] E. Luijten, Introduction to cluster Monte Carlo algorithms, Lect. Notes Phys. 703 (2006) 13–38.
[33] M.M. Sperotto, S. May, A. Baumgaertner, Modelling of proteins in membranes, Chem. Phys. Lipids 141 (2006) 2–29.
[34] M.M. Sperotto, O.G. Mouritsen, Monte Carlo simulation studies of lipid order parameter profiles near integral membrane proteins, Biophys. J. 59 (1991) 261–270.
[35] D. Marsh, Energetics of hydrophobic matching in lipid-protein interactions, Biophys. J. 94 (2008) 3996–4013.
[36] S. Chianta, N. Kahya, P. Schwille, Raft domain reorganization driven by short- and long-chain ceramide: a combined AFM and FCS study, Langmuir 23 (2007) 7659–7665.
[37] S. Dukovsky, J. Machta, C. Saravanan, S.M. Auerbach, Cluster Monte Carlo simulations of phase transitions and critical phenomena in zeolites, J. Chem. Phys. 113 (2000) 3697–3703.
[38] J. Fan, M. Sammalkorpi, M. Haataja, Influence of nonequilibrium lipid transport, membrane compartmentalization, and membrane proteins on the lateral organization of the plasma membrane, Phys. Rev. E 81 (2010) 011908.
[39] R. Reigada, Monte Carlo study of lipid nanoscale organization in cell membranes: tuning domain size and stability near the phase boundary, Biophys. Rev. Lett. 4 (2010) 245–263.

[40] J.H. Ipsen, O.G. Mouritsen, Modelling the phase equilibria in two-component membranes of phospholipids with different acyl-chain lengths, Biochim. Biophys. Acta 944 (1988) 121–134.
[41] S. Banerjee, J. Saha, A simulation study on multicomponent lipid bi-layer, Physica A 362 (2006) 423–432.
[42] K. Kawasaki, in: C. Domb, J.L. Lebowitz (Eds.), Phase Transitions and Critical Phenomena, Academic Press, London, 1983, vol. 2.
[43] K. Simons, E. Ikonen, How cells handle cholesterol, Science 290 (2000) 1721–1726.

CHAPTER FIVE

Statistical Thermodynamics of Adhesion Points in Supported Membranes

Oded Farago*

Contents

Abstract

Supported lipid membranes are useful and important model systems for studying cell membrane properties and membrane-mediated processes. One attractive application of supported membranes is the design of phantom cells exhibiting well-defined adhesive properties and receptor densities. Adhesion of membranes may be achieved by specific and nonspecific interactions and typically requires the clustering of many adhesion bonds into "adhesion domains." One potential mediator of the early stages of the aggregation process is the Casimir-type forces between adhesion sites induced by the membrane thermal fluctuations. In this review, I will present a theoretical analysis of fluctuation-induced aggregation of adhesion sites in supported membranes. I will first discuss the influence of a single attachment point on the spectrum of

* Corresponding author. Tel.: +972-8-6479830; Fax: +972-8-6479445.
E-mail address: ofarago@bgu.ac.il

Department of Biomedical Engineering and Ilse Katz Institute for Nanoscale Science and Technology, Ben-Gurion University of the Negev, Be'er Sheva, Israel

Advances in Planar Lipid Bilayers and Liposomes, Volume 14
ISSN 1554-4516, DOI: 10.1016/B978-0-12-387720-8.00005-4

membrane thermal fluctuations, from which the free energy cost of the attachment point will be deduced. I will then analyze the problem of a supported membrane with two adhesion points. Using scaling arguments and Monte Carlo simulations, I will demonstrate that two adhesion points attract each other via an infinitely long range effective potential that grows logarithmically with the pair distance. Finally, I will discuss the many-body nature of the fluctuation-induced interactions. I will show that while these interactions alone are not sufficient to allow the formation of aggregation clusters, they greatly reduce the strength of the residual interactions required to facilitate cluster formation. Specifically, for adhesion molecules interacting via a short-range attractive potential, the strength of the direct interactions required for aggregation is reduced by about a factor of two to below the thermal energy k_BT.

1. Introduction

Fatty acids and other lipids are essential to every living organism. Because of their amphiphilic nature, they spontaneously self-assemble into bilayer membranes that define the limits of cells and serve as permeability barrier to prevent proteins, ions, and metabolites from leaking out of the cell and unwanted toxins leaking in [1]. In eukaryotic cells, membranes also surround the organelles allowing for organization of biological processes through compartmentalization. In addition, biological membranes host numerous proteins that are crucial for the mechanical stability of the cell, and which carry out a variety of functions such as energy and signal transduction, communication, and cellular homeostasis [2].

An important aspect of biological membranes is that they are typically not free but rather confined by other surrounding membranes, adhere to other membranes, and attach to elastic networks like the cytoskeleton and the extracellular matrix. Several model systems with reduced compositional complexity have been designed to mimic biological membranes. These biomimetic systems include phospholipid bilayers deposited onto solid substrates (solid-supported membranes) [3], or on ultrathin polymer supports (polymer-supported membranes) [4]. Placing a membrane on a flat substrate allows for the application of several different surface sensitive techniques, including atomic force microscopy, X-ray and neutron diffraction, ellipsometry, nuclear magnetic resonance, and others [5]. With the aid of biochemical tools and generic engineering, supported membranes can be functionalized with various membrane-associated proteins [6]. Synthetic supported membranes with reconstituted proteins are increasingly used as controlled idealized models for studying key properties of cellular membranes [7]. They provide a natural environment for the immobilization of proteins under nondenaturating conditions and in well-defined orientations [8]. Another attractive application of supported membranes is the design of

phantom cells exhibiting well-defined adhesive properties and receptor densities [9]. Using advanced imaging techniques, detailed information can be obtained about the structure of the adhesion zone between the receptor-functionalized supported membrane and ligand-containing vesicles that can bind to the supported membrane [10,11]. These studies provide insight into the dynamics of adhesion processes and the molecular interactions involved in cell adhesion [12,13]. Understanding these interactions is crucial for the development of drug delivery systems that depend on efficient adhesion between a liposome and the plasma membrane of the target cell.

Adhesion between two membranes or between a membrane and another surface can, in principle, be facilitated by nonspecific attractive interactions (e.g., Coulomb and van der Waals interactions) [14–17]. Cell adhesion, however, is usually caused by highly specific receptor molecules located at the outside of the plasma membrane of the cell that can bind to specific ligands on the opposite surface [18,19]. Typically, the area density of the receptor molecules located at the outside of the plasma membrane is rather low which does not lead to efficient adhesion. However, when facing a surface with enough ligands, the receptors may cluster into highly concentrated adhesion domains to establish much stronger binding [20,21]. Formation of adhesion clusters occurs in many biological processes [22], including the binding of white blood cells to pathogens [23], cadherin-mediated adhesion of neighboring cells [24], and focal adhesion of cells to the extracellular matrix [25]. Many biophysical aspects of specific adhesion processes, ranging from the cooperativity in adhesion cluster formation to the influence of stochastic processes such as the ligand–receptor reaction kinetics, have been and continue to be studied theoretically using various models [26–37].

Adhesion-induced domain formation requires some attractive intermolecular interactions between the receptor–ligand pairs. These interactions include both *direct* and *membrane-mediated* contributions. The former are typically described by pairwise potentials which are infinitely repulsive at very small molecular separations and attractive at somewhat longer (but still finite) distances [38]. Their effect can, therefore, be studied in the framework of the thoroughly researched lattice-gas model [39]. In contrast, much less is known about the membrane-mediated mechanism, which has been proposed by Braun *et al.* to explain the formation of gap junctional plaque at cell–cell interfaces [40], and whose origin can be understood as follows: Consider two adhesion bonds between two membranes or between a membrane and a surface (Fig. 1A). The adhesion points restrict the thermal height fluctuations of the membrane in their vicinity. This entropy loss can be minimized if the two adhesion bonds are brought to the same place (Fig. 1B), in which case the membrane becomes pinned at only one place rather than two. The membrane fluctuations, thus, induce an attractive potential of mean force between the adhesion bonds. This effect is often

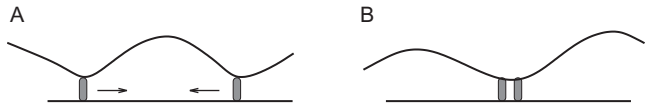

Figure 1 (A) Schematic of a membrane attached by two distant adhesion bonds to an underlying surface. There is an entropy penalty associated with each adhesion bonds due to the restrictions imposed on the membrane thermal fluctuations in their vicinity. (B) The entropy cost can be minimized by bringing the adhesion bonds close to each other, in which case the thermal fluctuations become limited at only one location. The increase in the entropy in (B) compared to (A) is the origin of the attractive fluctuation-induced interactions between the adhesion bonds.

named after Casimir who predicted the existence of an attractive force between two conducting plates, due to quantum fluctuations of the electromagnetic field in the intervening space [41]. Later, Fisher and de Gennes generalized this concept to classical interactions induced by thermal fluctuations in soft matter systems [42]. For bilayer membranes, there is a great body of theoretical work on the Casimir effect between transmembrane proteins (see review in Ref. [43], and references therein). Just like adhesion bonds, membrane inclusions represent a "constraint" on the shape of the membrane, and therefore, one should expect that they also interact with each other through Casimir-like interactions. In addition to the fluctuation-induced forces, the inclusions also experience other membrane-mediated interactions which arise from the membrane curvature elasticity and from the packing of the lipids near the inclusions' surfaces (see review in Ref. [44], and references therein). These other types of membrane-mediated interactions are also expected to exist between membrane adhesion bonds.

The fundamental difficulty in attempting to provide a statistical–mechanical analysis of the aggregation behavior of the adhesion bonds is the need to integrate out the membrane degrees of freedom and write down the potential of mean force as a function of the coordinates of the adhesion sites $\phi(\vec{r}_1, \vec{r}_2, \vec{r}_3, \ldots, \vec{r}_N)$. This is a nontrivial problem since the membrane-mediated potential $\phi(\vec{r}_1, \vec{r}_2, \vec{r}_3, \ldots, \vec{r}_N)$ is a many-body potential which cannot be expressed as the sum of two-body terms. The many-body nature of $\phi(\vec{r}_1, \vec{r}_2, \vec{r}_3, \ldots, \vec{r}_N)$ is best illustrated by the following example: Consider the configuration shown in Fig. 2A with two adhesion bonds at located at $\vec{r}_1$ and $\vec{r}_2$ and, in comparison, the one shown in Fig. 2B with a single bond at $\vec{r}_1$ and a cluster of three bonds around $\vec{r}_2$. Clearly, the spectrum of membrane thermal fluctuations in both cases is quite the same, and therefore, the adhesion bond located at $\vec{r}_1$ is attracted to the three-point cluster in 2(B) by the same force to which it is attracted to the single adhesion point in 2(A). If $\phi(\vec{r}_1, \vec{r}_2, \vec{r}_3, \ldots, \vec{r}_N)$ was the sum of pair interactions, the force in Fig. 2B would be three times larger than the force in 2(A).

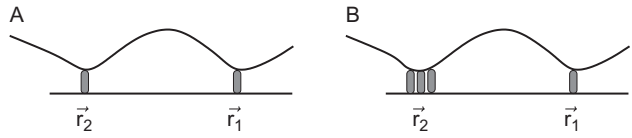

Figure 2 (A) Schematic of a supported membrane with two adhesion located at $\vec{r_1}$ and $\vec{r_2}$. (B) Similar to (A), but with a three-bond cluster instead of a single adhesion bond in $\vec{r_2}$. The adhesion bond in $\vec{r_1}$ is equally attracted (by a Casimir-like force) to the adhesion bond located in $\vec{r_2}$ in (A) and to the cluster of three adhesion bonds shown in (B).

2. Lattice-Gas Model for Adhesion Bonds in Supported Membranes

What is the difference between the aggregation of adhesion bonds in supported membranes and the traditional process of gas to liquid condensation? Condensation phase transitions are usually associated with a competition between the mixing entropy S which is higher in the dilute gas phase and the interaction energy U which is lower in the condensed liquid state. The equilibrium phase corresponds to the minimum of the free energy $F = U - TS$, where T is the temperature of the system. At high T, the free energy F is "entropy-dominated" and equilibrium is attained in the gas phase. Conversely, at low T, the free energy is "energy-dominated," and therefore, the condensed phase becomes thermodynamically more favorable. The liquid–gas phase transition can be analyzed in the framework of an Ising-like model of identical particles that populate a lattice. Excluded volume interactions between the particles are represented by the fact that each lattice site can be occupied by no more than one particle. When two particles occupy nearest-neighbor sites, they interact in a pairwise fashion with an attractive energy $-\varepsilon$. Denoting the occupancy of a lattice site by s_i, with $s_i = 0$ for an empty site and $s_i = 1$ for an occupied site, the Hamiltonian of the lattice-gas model is given by

$$\mathcal{H}_{LG} = -\varepsilon \sum_{ij} s_i s_j, \tag{1}$$

where the sum runs over all the pairs of lattice nearest-neighbor sites. The phase diagram of the lattice-gas model is well known. There exists a critical value α_c such that if the interaction energy $\varepsilon < \alpha_c k_B T$, the particles will be distributed uniformly within the lattice. Above this critical value, $\varepsilon > \alpha_c k_B T$, a uniform distribution of the particles is observed only at low concentrations of particles (gas phase), but upon increasing the concentration of particles, the system undergoes a first-order phase transition and a

second coexisting phase appears with a considerably larger concentration (condensed phase).

As discussed in the previous section, the aggregation process of adhesion domains involves an additional attractive potential of mean force resulting from the membrane thermal fluctuations. A lattice model where each lattice particle represents an adhesion bond in a supported membrane can, therefore, be introduced by supplementing Eq. (1) with an energy term corresponding to the fluctuation-induced interactions. Since the functional form of this many-body potential is yet unknown, we would, at this moment, introduce it via a general potential function ϕ that depends on the coordinates of the lattice particles:

$$\mathcal{H} = -\varepsilon \sum_{ij} s_i s_j + \phi(\{s_i\}). \tag{2}$$

Our first task must be to derive an expression for $\phi(\{s_i\})$. Once this is accomplished, one can attempt to analyze the statistical mechanical properties of the model and address the question appearing at the beginning of Section 2. One particular issue that we would like to address is whether the fluctuation-induced attractive potential (which is of entropic origin) can win the competition against the repulsive force originating from the mixing entropy? In other words, can adhesion clusters form for purely entropic grounds, that is, for $\varepsilon = 0$ in Eq. (2)? Gas to liquid condensation transitions are generally believed to involve energy versus entropy competition [45], but purely entropic phase transitions from a fluid (disordered) phase into a crystalline (ordered) phase are known to exist. Hard sphere systems, for instance, undergo a first-order phase transition from a low-density fluid phase into a high-density solid phase [46]. This transition results from the competition between two entropies—the configurational mixing entropy which is higher in the disordered phase and the entropy associated with the free volume available for each sphere, which is higher in the ordered crystal.

3. Statistical Mechanics of a Membrane with One Adhesion Point

We start our analysis by considering the system shown schematically in Fig. 3, consisting of a membrane with bending rigidity κ that fluctuates above a flat impenetrable surface [47]. Let $h(\vec{r}) \geq 0$ be the height of the membrane with respect to the surface, and assume that the membrane is pinned to the surface at one fixed point located at $\vec{r}_0$ ($h(\vec{r}_0) = 0$). The elastic curvature energy of the membrane is given by the Helfrich effective Hamiltonian [48]

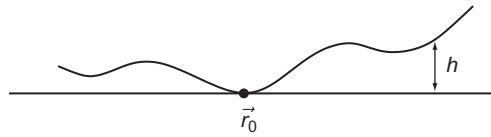

Figure 3 (A) Schematic picture of the model system consisting of a membrane that fluctuates above a flat impenetrable surface to which it is pinned at a single point.

$$\mathcal{H}_{\text{hel}} = \int \left[\frac{\kappa}{2}\left(\nabla^2 h\right)^2\right] \Phi(h)\delta[h(\overrightarrow{r_0})]\mathrm{d}^2\overrightarrow{r}, \tag{3}$$

where Φ represents the hard wall constraint due to the surface ($\Phi = 1$ for $h \geq 0$, and $\Phi = +\infty$ for $h < 0$), δ is the Dirac delta-function, and the integration is taken over the cross-sectional (projected) area of the membranes of size L^2.One can calculate the partition function Z corresponding to Hamiltonian (3), by considering the Helfrich effective Hamiltonian of a *freely fluctuating* membrane

$$\mathcal{H}^0_{\text{hel}} = \int \left[\frac{\kappa}{2}\left(\nabla^2 h\right)^2\right] \mathrm{d}^2\overrightarrow{r}. \tag{4}$$

In this case, the associated partition function Z_{free} is readily calculated by introducing the Fourier transformation of $h(\overrightarrow{r}) : h_q = (1/L^2)\int h(\overrightarrow{r})$ $\exp(i\overrightarrow{q}\cdot\overrightarrow{r})$, which decompose Hamiltonian (4) into the sum of independent harmonic oscillators

$$\mathcal{H}^0_{\text{hel}} = \frac{l^4}{L^2}\sum_{\overrightarrow{q}} \frac{\kappa}{2} q^4 |h_q|^2, \tag{5}$$

where l is a microscopic length scale of the order of the bilayer thickness. Hamiltonian (3) which also includes the functions Φ and δ cannot be diagonalized in the same manner. However, one can relate the partition function Z of Hamiltonian (3) with the partition Z_{free} of the free membrane Hamiltonian (4), by using the following simple argument. The energy of a freely fluctuating membrane is invariant with respect to rigid-body transformations such as a vertical translation $(h(\overrightarrow{r}) \rightarrow h(\overrightarrow{r}) - h_0)$ of the membrane's center of mass. Therefore, one can draw a flat surface and translate the free membrane such that the global minimum of its height function coincides with the surface (see Fig. 4A). The vertically translated free membrane looks very similar to the pinned membrane shown in Fig. 3A. The only difference between them is that the former can also glide over the surface (see Fig. 4B), while the latter is pinned at a fixed position on the

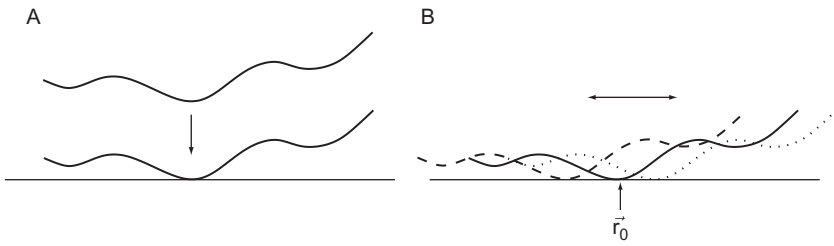

Figure 4 (A) A freely fluctuating membrane can be always translated vertically such that the point at which its height function $h(\vec{r})$ attains its global minimum is on a flat surface and the rest of the membrane is above the surface. (B) A freely fluctuating membrane can be also translated horizontally. All the membrane configurations generated in this way are similar to each other, and the one for which the point of absolute minimum is at $\vec{r}_0$ (represented by the solid line) is identical to the pinned membrane configuration shown in Fig. 3.

surface. This suggests that the pinning point effectively eliminates the membrane horizontal translational degree of freedom. In a statistical mechanical language, the configurational phase space of the pinned membranes is smaller than, yet *similar* to, the phase space of a free membrane. Each subspace of identical free membrane configurations, like the ones shown in Fig. 4B, includes one pinned membrane configuration—the configuration where the minimum of $h(\vec{r})$ is at the pinning point $\vec{r}_0$ (or, more precisely, within a microscopic area of size l^2 around the pinning point, where l is the spatial resolution of the continuum model). This pinned membrane configuration occupies a fraction $(l/L)^2$ of the corresponding larger free membrane configurational subspace, which implies that the partition functions of the two systems are related by $Z = (l/L)^2 Z_{\text{free}}$. The free energy is obtained from

$$F = -k_{\text{B}}T\ln(Z) = -k_{\text{B}}T\ln(Z_{\text{free}}) + 2k_{\text{B}}T\ln\left(\frac{L}{l}\right) \tag{6}$$

The first term on the right hand side is the free energy of the free membrane whose elastic energy is given by Helfrich Hamiltonian (3). The second term,

$$F_{\text{attachment},1} = 2k_{\text{B}}T\ln\left(\frac{L}{l}\right), \tag{7}$$

is the free energy cost of attaching the membrane to the surface at one point.

Following the above argument leads to a very interesting conclusion. Because of the similarity mapping that exists between the configurational

phase spaces of the two problems, the statistical properties of the pinned and the free membrane must be identical to each other. This surprising result can be demonstrated by using an implicit-solvent coarse-grained (ISCG) bilayer model which enables molecular simulations of mesoscopically large bilayer membranes over relatively large time-scales [49–51]. Toward this end, we ran two independent Monte Carlo (MC) simulations—one of a free membrane (without a surface) and one of a membrane supported by a flat impenetrable surface. A snapshot from the supported membrane simulations is shown in Fig. 5. Each lipid molecule is represented in the model by a short string of three spherical beads, where one of the beads (depicted as a dark gray sphere in Fig. 5) represents the hydrophilic head group and two beads (light gray spheres in Fig. 5) represent the hydrophobic tail of the lipid. In the supported membrane simulations, the head bead of one of the lipids (appearing in the corner at the front of the figure and indicated by an arrow) was fixed to a flat surface which the lipids were not allowed to cross. We measured the Fourier spectrum of the membrane height function. For the free membrane, the application of the equipartition theorem to the Fourier-space representation of the Helfrich Hamiltonian (5) yields the following relationship between the mean squared amplitude of the Fourier modes (spectral intensity) and the wave-vector q:

$$\left\langle |h_q|^2 \right\rangle = \frac{k_B T L^2}{\kappa l^4 q^4}. \tag{8}$$

Figure 6 depicts the results of our MC simulations for the spectral intensity versus the wavenumber $n = qL/(2\pi)$. The figure shows that, in

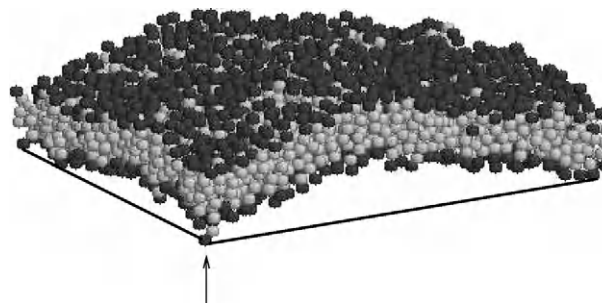

Figure 5 Equilibrium configuration of a membrane consisting of 2000 lipids. Each lipid is represented by a trimer of one "hydrophilic" bead (dark gray sphere) and two "hydrophobic" beads (light gray spheres). The membrane is fluctuating above a plane surface (frame indicated by a thick black line), while one of the hydrophilic beads (the black sphere appearing at the front of the figure and indicated by an arrow) is held on the surface at a fixed position.

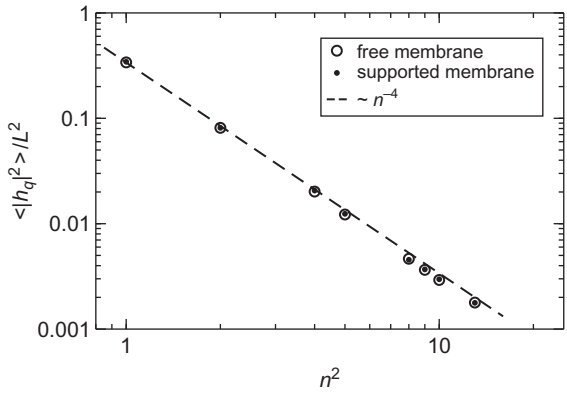

Figure 6 The mean square amplitude of the thermal height fluctuations as a function of the wavenumber n. The results from the supported membrane simulations are shown by small solid circles. These results are essentially identical to those obtained from simulations of a free membrane which are represented by larger open circles. The dashed line indicates the asymptotic $\langle |h_q|^2 \rangle \sim n^{-4}$ power law for small n (adapted from Ref. [47]).

agreement with our predictions, (i) the free (open circles) and pinned (solid circles) membranes exhibit the same statistics of thermal height fluctuations and (ii) the spectral intensities of both membranes follow the n^{-4} power-law dependence anticipated by Eq. (8) (dashed line).

One can reverse the argument and derive Eq. (7) starting from the assumption that the spectral intensity of the supported membrane is identical to that of a free membrane and, therefore, can be described by Eq. (8). The derivation proceeds as follows: First, from Eq. (8), one can straightforwardly show that the typical height at which the membrane undulates above the surface at a distance r away from the pinning point scales linearly with r [47,52] (see Fig. 7):

$$u(r) \equiv \langle h(r) \rangle \sim r \sqrt{\frac{k_B T}{\kappa}}. \tag{9}$$

There is a repulsive force acting between the fluctuating membrane and the underlying surface, caused by their mutual steric hindrance. Helfrich [53] showed that the associated repulsive interaction free energy density (per unit area) has the following scaling behavior $V(r) \sim (k_B T)^2/\kappa u(r)^2$ which, together with Eq. (9), yields

$$V(r) \sim \frac{k_B T}{r^2}. \tag{10}$$

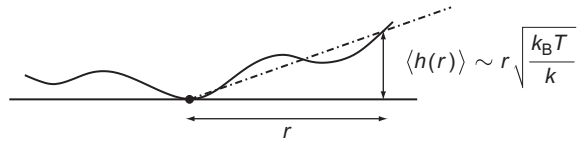

Figure 7 The fact that the statistics of thermal height fluctuations is not affected by the single pinning point implies that the typical height of the fluctuations scales linearly with the distance from the pinning site.

By integrating this energy density over the projected area of the membrane, one derives Eq. (7) up to a numerical prefactor

$$F_{\text{attachment},1} = \int V(r) \mathrm{d}^2 \overrightarrow{r} \sim \int_l^L 2\pi r \frac{k_B T}{r^2} \mathrm{d}r = C k_B T \ln\left(\frac{L}{l}\right). \tag{11}$$

To set $C = 2$, as in Eq. (7), one needs to replace the scaling relation Eq. (10) with the equality

$$V(r) = \frac{1}{\pi} \frac{k_B T}{r^2}. \tag{12}$$

4. Fluctuation-Induced Attraction Between Two Adhesion Points

As noted by Helfrich [53], the free energy density Eq. (12) due to the steric hindrance between the two surfaces (i.e., the fluctuating membrane and the underlying supporting surface) is directly related to the rate of collisions between them. In other words, the probability density that the membrane hits the supporting surface at a distance r from the pinning point exhibit the same dependence on r as $V(r)$:

$$p[h(\overrightarrow{r}) = 0] \sim \frac{1}{r^2}. \tag{13}$$

This relationship provides the information needed for calculating the fluctuation-induced attractive potential between two adhesion points. This is done by regarding the point of collision between the membrane and the surface as a second pinning point which can diffuse across the surface. In this context, the probability density $p[h(\overrightarrow{r}) = 0]$ is identified with the pair correlation function between the adhesion points which, therefore, also follows the scaling form

$$g(\vec{r}) \sim \frac{1}{r^2}. \tag{14}$$

By definition, the pair potential of mean force is given by

$$\phi(\vec{r}) \equiv -k_B T \ln[g(\vec{r})] = 2k_B T \ln(r), \tag{15}$$

which is an infinitely long range attractive potential that does not depend of the bending rigidity of the membrane, κ. The validity of Eq. (14) can be tested by using MC simulations of the ISCG model shown in Fig. 5 with two lipid heads attached to surface—one fixed at the origin and the other allowed to diffuse on the flat surface. The pair correlation function is then directly computed by sampling the position of the mobile adhesion point. Our results [54], which are shown in Fig. 8, agree very well with Eq. (14). The slope of the straight line on the log–log plot is equal to -2. The deviations from the power-law behavior $g(\vec{r}) \sim 1/r^2$ at small values of $r\,(r/L < 0.05)$ are related to the breakdown of the continuum description of the Helfrich Hamiltonian at small spatial scales. At small separations, the molecular nature of the lipids becomes important and the radial pair distribution function is dominated by the depletion shells around the lipids.

What if, in addition to the excluded volume repulsion, the membrane and the surface also interact via an attractive potential of somewhat longer range? Let us consider, for instance, the case when a harmonic confining potential is added to the Helfrich Hamiltonian:

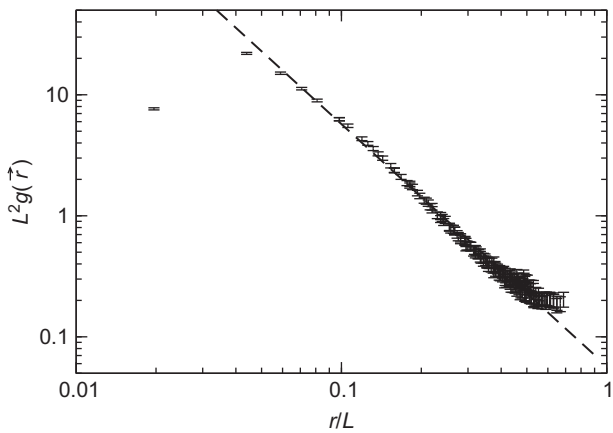

Figure 8 The pair correlation function, $g(\vec{r})$, of a nonstressed membrane versus the pair distance r. The slope of the dashed straight line is -2 (adapted from Ref. [54]).

$$\mathcal{H} = \int \left[\frac{\kappa}{2} \left(\nabla^2 h \right)^2 + \frac{\gamma}{2} h^2 \right] \mathrm{d}^2 \vec{r}. \tag{16}$$

For the harmonically confined membrane, one can define the length scale $\xi_\gamma \sim (\kappa/\gamma)^{1/4}$ which marks the transition between two scaling regimes. For $r \ll \xi_\gamma$, the thermal fluctuations are governed by the bending rigidity term in Hamiltonian (16), while for $r \gg \xi_\gamma$ the harmonic confinement term becomes dominant. The latter term is a local one, which implies that the influence of the adhesion point becomes screened at large distances. In the case of a single adhesion point, the height of the fluctuations is now given by (compare with Eq. (9))

$$\langle h(r) \rangle \sim \begin{cases} r \sqrt{\dfrac{k_\mathrm{B} T}{\kappa}} & \text{for } r \ll \xi_\gamma \\ \xi_\gamma \sqrt{\dfrac{k_\mathrm{B} T}{\kappa}} & \text{for } r \gg \xi_\gamma \end{cases}, \tag{17}$$

as illustrated schematically in Fig. 9A. The correlation function of a pair of adhesion points is given by (compare with Eq. (14))

$$g(\vec{r}) \sim \begin{cases} r^{-2} & \text{for } r \ll \xi_\gamma \\ r^0 & \text{for } r \gg \xi_\gamma \end{cases}. \tag{18}$$

The results of MC simulations of an ISCG molecular model of a harmonically confined membrane verify this crossover between the two scaling regimes of $g(\vec{r})$ (see Fig. 9B).

The energy of a membrane subjected to lateral surface tension $\sigma > 0$ is given by the following Hamiltonian

$$\mathcal{H} = \int \left[\frac{\kappa}{2} \left(\nabla^2 h \right)^2 + \frac{\sigma}{2} \left(\vec{\nabla} h \right)^2 \right] \mathrm{d}^2 \vec{r}. \tag{19}$$

Scaling arguments [54] show that, in this case, the pair correlation function exhibits behavior intermediate between Eqs. (14) and (18):

$$g(\vec{r}) \sim \begin{cases} r^{-2} & \text{for } r \ll \xi_\sigma \\ r^{-1} & \text{for } r \gg \xi_\sigma \end{cases}, \tag{20}$$

where the crossover length $\xi_\sigma \sim (\kappa/\sigma)^{1/2}$. This scaling form is also confirmed by MC simulations (see Fig. 10).

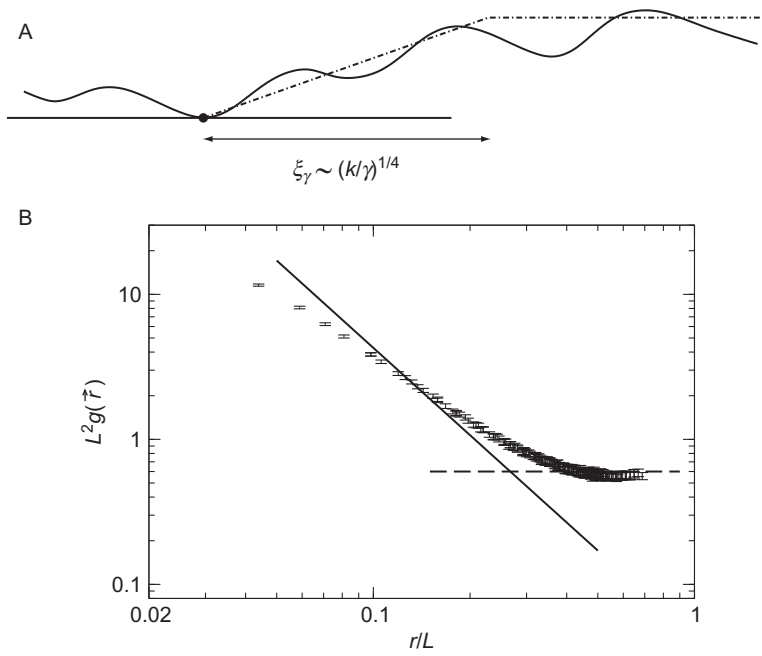

Figure 9 (A) The typical height of the fluctuations of a supported membrane experiencing a harmonic confining surface potential grows linearly close to the pinning point and saturates at large distances. (B) The pair correlation function, $g(\vec{r})$, of such a membrane versus the pair distance r. The slopes of the solid and dashed straight lines are -2 and 0, respectively. ((B) is adapted from Ref. [54].)

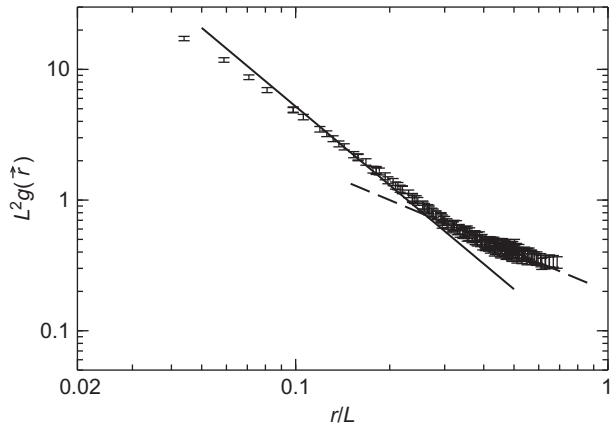

Figure 10 The pair correlation function, $g(\vec{r})$, of a supported membrane under tension versus the pair distance r. The slopes of the solid and dashed straight lines are -2 and -1, respectively. (adapted from Ref. [54])

5. The Strength of the Fluctuation-Induced Attraction

One of the main questions we aim to explore is whether the fluctuation-induced interactions are sufficiently strong to allow the formation of adhesion clusters. In the case of two adhesion points, the answer is no. Despite of the attractive force between the adhesion points, they remain unbound and their mean pair separation grows linearly with the system size L. More generally, if the pair correlation function decays algebraically at large distance, $g(\overrightarrow{r}) \sim r^{-c}$, the mean pair separation is given by

$$\langle r \rangle \sim \frac{\int_l^L r^2 g(\overrightarrow{r})\mathrm{d}r}{\int_l^L r g(\overrightarrow{r})\mathrm{d}r} \sim \begin{cases} L & \text{for } c < 2 \\ L/\ln L & \text{for } c = 2 \\ L^{3-c} & \text{for } 2 < c < 3 \\ \ln L & \text{for } c = 3 \\ l & \text{for } c > 3 \end{cases}. \tag{21}$$

The physically relevant cases in Eq. (21) are $c = 2{,}1$, and 0 which, respectively, correspond to pinned, pinned-stressed, and pinned-confined membranes. In all of these cases, $\langle r \rangle$ grows with the size of the system.

Another quantity of interest is the mean number $\langle C \rangle$ of contacts between the surface and a membrane with one adhesion point. As discussed in Section 4, the probability density that membrane comes into contact with the surface at a distance r from the pinning point has the same scaling form as the pair correlation function $g(\overrightarrow{r})$. Thus,

$$\langle C \rangle \sim \int_l^L g(\overrightarrow{r}) r \mathrm{d}r \sim \begin{cases} \left(L/\xi_\gamma\right)^2 & \text{for } c = 0 \\ L/\xi_\sigma & \text{for } c = 1 \\ \ln(L/l) & \text{for } c = 2 \end{cases}. \tag{22}$$

We can use this last result to generalize and recalculate the attachment free energy of one adhesion point, Eq. (7). Our original derivation of Eq. (7) was based on the argument that the configuration phase space of a pinned membrane comprises a small subspace within the configuration phase space of a free membrane. More precisely, we argued that this subspace includes the free membrane configurations in which the global minimum of the height function occurs at the pinning point of the corresponding supported membrane. We further argued that the relative size of the subspace is $(l/L)^2$, which was based on the assumption that typically there is only one contact point with the surface, and therefore, this contact point must be the adhesion site. However, as we see from Eq. (22), a typical configuration makes $\langle C \rangle$ contacts with the surface. Therefore, the partition

functions of the two problems (free vs. pinned membranes) are actually related by $Z = [\langle C \rangle \, (l/L)^2] \, Z_{\text{free}}$. The attachment free energy is given by

$$F_{\text{attachment},1} = -k_{\text{B}} T \ln\left(\frac{\langle C \rangle l^2}{L^2}\right)$$

$$= \begin{cases} 2k_{\text{B}} T \ln\left(\xi_\gamma / l\right) & \text{for } c = 0 \\ k_{\text{B}} T \ln(L/l) + k_{\text{B}} T \ln(\xi_\sigma / l) & \text{for } c = 1 \\ 2k_{\text{B}} T \ln(L/l) - k_{\text{B}} T \ln[\ln(L/l)] & \text{for } c = 2 \end{cases}. \tag{23}$$

Notice that for sufficiently large L, $F_{\text{attachment},1}(c = 2) > F_{\text{attachment},1}(c = 1) > F_{\text{attachment},1}(c = 0)$. Indeed, the attachment of a free membrane to a surface is likely to be more costly than the attachment of stressed and harmonically confined membranes that exhibit reduced fluctuations and, thus, remain close to the surface anyway.

6. The Many-Body Problem

Let us look back at Fig. 8 which shows the pair correlation function between two adhesion points. The figure demonstrates that the scaling form Eq. (14) holds over almost the entire range of pair separations considered $\left(l < r < L/\sqrt{2}\right)$. The deviations from the power law at small pair distances arising from the short-range depletion forces between lipids have already been discussed in Section 4. What is quite surprising, though, is the pretty good agreement between the MC results and Eq. (14) at large pair distances. Equation (14) has been derived for two adhesion points in a very large membrane, neglecting boundary effects. In the simulations, the conditions are different—the membrane has a finite size and periodic boundary conditions are employed to reduce the finite size effects. Thus, each adhesion point interacts not only with the other adhesion point but also with its infinite array of periodic images. Nevertheless, the existence of periodic images seems to have a very small impact on the results. This observation is particularly unexpected for $r > L/2$ corresponding to situations where one of the adhesion points is equally close to two images of the other adhesion point. The only possible way to explain this surprising observation is to assume that the periodic images of the adhesion points are largely screened. This assumption is consistent with the following physical picture: The membrane-mediated interactions originate from the entropic cost due to the suppression of the membrane thermal undulations. Thus, the presence of each adhesion point is felt only in the region where it affects the fluctuations and cause their reduction, while outside of this region, the adhesion point is effectively screened. In this perspective, the idea that distant

adhesion points are screened seems logical. The fluctuations vanish at each adhesion point, irrespective of the distribution of the others. Moreover, in the immediate vicinity of each adhesion point, one expects the amplitude of the fluctuations to depend only on the distance from that adhesion point. If the membrane is neither stressed nor experiencing a confining surface potential, the amplitude of the fluctuations in this region grows linearly with the distance r from the adhesion point, as given by Eq. (9). We now wish to introduce a more general expression that holds over the entire area of the membrane and coincides with Eq. (9) close to every adhesion point. Our suggestion is as follows [55]: In each unit area of the membrane, the mean height of the membrane above the surface is given by (compare with Eq. (9))

$$\langle h(r) \rangle \sim d_{min} \sqrt{\frac{k_B T}{\kappa}}, \tag{24}$$

where $d_{\min}$ is the distance of the unit area from the *nearest* adhesion point. We also replace r with $d_{\min}$ in Eq. (12) for the attachment free energy density, which now reads

$$V(r) = \frac{1}{\pi} \frac{k_B T}{d^2_{\min}}. \tag{25}$$

The total attachment free energy of a given distribution of adhesion points is obtained by integrating the attachment free energy density Eq. (25) over the entire membrane area. This calculation is done by constructing the Voronoi diagram of the distribution of adhesion points, integrating the free energy density with each cell (where in each cell the distance is measured from the adhesion point located in the cell, and a small region of microscopic size l around the point is excluded from the integral), and summing the contributions of the different cells:

$$F_{\text{attachment}} = \sum_{i=1}^{N_{\text{cell}}} \int \frac{k_B T}{\pi r^2} \mathrm{d}^2 \vec{r}. \tag{26}$$

In a lattice-gas model, the discrete analog of this expression applies

$$F_{\text{attachment}} = \sum_i \frac{k_B T}{\pi} \left(\frac{l}{d_{\min}} \right)^2 (1 - s_i), \tag{27}$$

where the sum run over all the empty lattice sites ($s_i = 0$) and l^2 is the area per lattice site.

As discussed in Section 2, our main goal is to develop and use a lattice-gas model for the aggregation problem of adhesion points. In the model,

each lattice point represents an adhesion point between the membrane and surface. The energy of a given configuration of lattice points is given by Eq. (2), where the first term represents the short-range attraction between adhesion points and the second term is a many-body fluctuation-induced potential $\phi(\{s_i\})$. Our journey to derive an expression for $\phi(\{s_i\})$ started in Section 3, and has finally reached the end. $\phi(\{s_i\})$ is a potential of mean force which, for a given distribution of adhesion points, is determined by tracing over all the relevant membrane configurations and calculating the free energy penalty associated with the reduced thermal fluctuations. Equation (27) provides this expression by assigning a free energy cost with each empty lattice site that represents a fluctuating unit area of the supported membrane. Introducing Eq. (27) into Eq. (2), yields the energy function of our lattice model of adhesion points

$$\mathcal{H} = -\varepsilon \sum_{ij} s_i s_j + \sum_i \frac{k_B T}{\pi} \left(\frac{l}{d_{\min}} \right)^2 (1 - s_i). \tag{28}$$

6.1. The Two-Body Problem Revisited

Let us see how one can rederive Eq. (15) for the pair potential of mean force by calculating the attachment free energy Eq. (26). Toward this end, consider the membrane shown schematically in Fig. 11 with two adhesion points, each of which located a distance $r/2$ from the center of the membrane. The dashed line shows the border between the Voronoi cells of the adhesion points, where each cell extends over half of the area of the membrane. For the configuration shown in Fig. 11, the attachment free energy Eq. (26) reads:

$$\begin{aligned} F_{\text{attachment},2} = 4 \int_0^{L/2} \mathrm{d}y \Bigg[\int_0^{(r-l)/2} \mathrm{d}x \frac{k_B T}{\pi \left[y^2 + (x - r/2)^2 \right]} \\ + \int_{(r+l)/2}^{L/2} \mathrm{d}x \frac{k_B T}{\pi \left[y^2 + (x - r/2)^2 \right]} \Bigg]. \end{aligned} \tag{29}$$

Integrating over y yields,

$$\begin{aligned} F_{\text{attachment},2} = \frac{4 k_B T}{\pi} \Bigg[\int_0^{(r-l)/2} \frac{\mathrm{d}x}{\mid x - r/2 \mid} \tan^{-1} \left(\frac{L}{2 \mid x - r/2 \mid} \right) \\ + \int_{(r+l)/2}^{L/2} \frac{\mathrm{d}x}{\mid x - r/2 \mid} \tan^{-1} \left(\frac{L}{2 \mid x - r/2 \mid} \right) \Bigg]. \end{aligned} \tag{30}$$

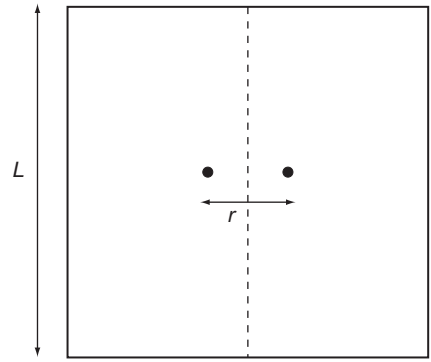

Figure 11 Schematic of a square membrane of linear size L with two adhesion points located at $(x, y) = (\pm r/2, 0)$. The dashed line shows the border between the Voronoi cells of the adhesion points.

Assuming that $l < r \ll L$, the inverse tangent function in Eq. (30) can be approximated by the constant value of $\pi/2$ over most of the integration range. With this approximation, one gets

$$F_{\text{attachment},2}(r, L) \simeq 2k_{\text{B}}T \ln\left(\frac{L}{l}\right) + 2k_{\text{B}}T \ln\left(\frac{r}{l}\right) = F_{\text{attachment},1}(L) + \phi(r). \tag{31}$$

The first term in Eq. (31) is the free energy cost of a single adhesion site (Eq. (7)), which is the expected value when the two adhesion points coincide ($r \simeq l$) to form a single cluster. The second term, which represents the additional free energy cost associated with the separation of the adhesion points, is identified as the fluctuation-induced pair potential, in agreement with Eq. (15).

6.2. Mean Field Theory

We now come back to the many-body problem and start with a mean field analysis of our lattice model Hamiltonian (28). Let us consider a lattice of N_{s} sites of which $N \leq N_{\text{s}}$ sites are occupied by adhesion points. Let us further assume that the adhesion points form $N_{\text{c}} \leq N$ adhesion clusters. The free energy of system includes three contributions: (i) the mixing entropy of the adhesion clusters, F_{mix}; (ii) the lattice-gas energy, E_{LG}, of the direct interactions between the adhesion points [first term in Eq. (28)]; and (iii) the attachment free energy, F_N [second term in Eq. (28)]. The first free energy contribution is given by

$$\frac{F_{\mathrm{mix}}}{k_{\mathrm{B}}T} = N_{\mathrm{c}}\left[\ln\left(\frac{N_{\mathrm{c}}}{N_{\mathrm{s}}}\right) - 1\right] + \frac{1}{2}c\left(\frac{N_{\mathrm{c}}^2}{N_{\mathrm{s}}}\right), \tag{32}$$

where c is the second virial coefficient. On average, each cluster consists of (N/N_{c}) adhesion points; and if we assume that it has a roughly circular shape than $c \simeq 4(N/N_{\mathrm{c}})$. Denoting the number densities of the adhesion points by $\rho = N/N_{\mathrm{s}}$, and of the clusters by $\rho^* = N_{\mathrm{c}}/N_{\mathrm{s}} \leq \rho$, the free energy of mixing per lattice site is given by

$$\frac{F_{\mathrm{mix}}}{N_{\mathrm{s}}k_{\mathrm{B}}T} = \rho^*[\ln(\rho^*) - 1] + 2\rho\rho^*. \tag{33}$$

The second contribution to the free energy is due to the direct interactions between the adhesion points. The ground state of the interaction energy E_{LG} is achieved when a single circular adhesion domain with minimal surface is formed. If we set the ground state as the reference energy, the energy of an ensemble of clusters can be estimated as being proportional to the total length of the domain boundaries. For N_{c} circular clusters of size (N/N_{c}) we have

$$\frac{E_{\mathrm{LG}}}{N_{\mathrm{s}}k_{\mathrm{B}}T} = \lambda\frac{N_{\mathrm{c}}}{N_{\mathrm{s}}}\sqrt{\frac{N}{N_{\mathrm{c}}}} = \lambda\sqrt{\rho\rho^*}, \tag{34}$$

where λ, the associated dimensionless line tension, is proportional to the interaction energy ε

$$\lambda = 2\sqrt{\pi}B\varepsilon, \tag{35}$$

and B is the mean number of nearest-neighbor vacant sites per occupied site on the boundary of a cluster ($B \to 1$ for very large clusters). The sum of free energy contributions (33) and (34) constitutes the total free energy density (per lattice site) of a 2D lattice gas of clusters:

$$\frac{F_{\mathrm{LG}}}{N_{\mathrm{s}}k_{\mathrm{B}}T} = \rho^*\ln(\rho^*) - \rho^* + 2\rho\rho^* + \lambda\sqrt{\rho\rho^*}. \tag{36}$$

The third contribution to the attachment free energy can be estimated as follows. The clusters form N_{c} Voronoi cells, each of which has on average an area of $A_{\mathrm{vor}} = (N_{\mathrm{s}}/N_{\mathrm{c}})l^2$. The attachment free energy of each Voronoi cell is given by an equation similar to Eq. (7) for the

attachment free energy of one adhesion point, but with A_{vor} instead of the total membrane area L^2. Thus

$$F_N = N_{\mathrm{c}}\left[k_{\mathrm{B}}T\ln\left(\frac{N_{\mathrm{s}}}{N_{\mathrm{c}}}\right)\right], \tag{37}$$

and the attachment free energy density is given by

$$\frac{F_N}{N_{\mathrm{s}}k_{\mathrm{B}}T} = -\rho^*\ln(\rho^*), \tag{38}$$

which eliminates the first term in the lattice-gas free energy density (Eq. (36)), yielding

$$\frac{F}{N_{\mathrm{s}}k_{\mathrm{B}}T} = \frac{F_{\mathrm{LG}}}{N_{\mathrm{s}}k_{\mathrm{B}}T} + \frac{F_N}{N_{\mathrm{s}}k_{\mathrm{B}}T} = -\rho^* + 2\rho\rho^* + \lambda\sqrt{\rho\rho^*}. \tag{39}$$

We consider a low density of adhesion sites $\rho \ll 1$, which also implies a low number density of adhesion clusters since $\rho^* \leq \rho$. By minimizing the free energy density, we obtain the equilibrium value of the ρ^* for the standard lattice-gas model (Eq. (36)) and for the adhesion points of a fluctuating supported membrane (Eq. (39)). In both cases, the system undergoes a first-order phase transition at $\lambda_1(\rho)$ from the gas phase ($\rho^* = \rho$) to a condensed phase consisting of only a few clusters ($\rho^* \sim 0$). Also, in both cases, the free energy reaches a maximum at intermediate densities ($0 < \rho^* < \rho$). This free energy barrier for condensation disappears at the spinodal point $\lambda_2(\rho) > \lambda_1(\rho)$. For the lattice-gas problem, we find

$$\begin{aligned}\lambda_1^{\mathrm{LG}} &= 1 - 2\rho - \ln(\rho)\\ \lambda_2^{\mathrm{LG}} &= -4\rho - 2\ln(\rho),\end{aligned} \tag{40}$$

while for the adhesion points of fluctuating membranes, we have

$$\begin{aligned}\lambda_1 &= 1 - 2\rho\\ \lambda_2 &= 2 - 4\rho = 2\lambda_1.\end{aligned} \tag{41}$$

The results of Eqs. (40) and (41) are summarized in Fig. 12A and B, respectively. The important points in the results are that (i) $\lambda_1 > 0$, which means that the fluctuation-induced interactions alone are *not* sufficient to induce aggregation of adhesion domains, but (ii) they greatly reduce the strength of the direct interactions required to facilitate cluster formation since $\lambda_1 < \lambda_1^{\mathrm{LG}}$ (and also $\lambda_2 < \lambda_2^{\mathrm{LG}}$). Below, we support these conclusions with MC simulations and show that for adhesion points of fluctuating

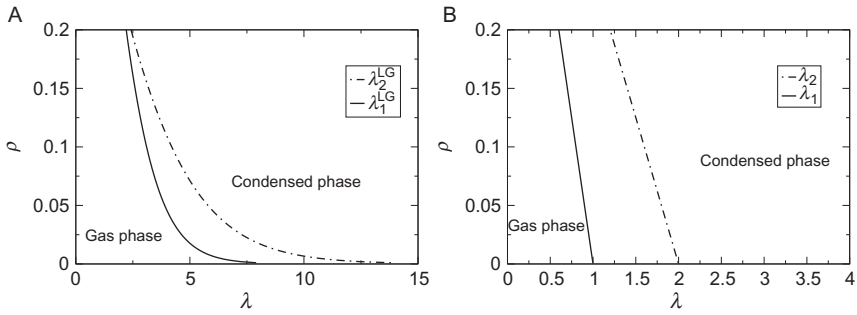

Figure 12 The phase diagram of the adhesion sites calculated within the mean field approximation. (A) Equation (40) for the standard 2D lattice-gas model. (B) Equation (41) for adhesion points of fluctuating membranes. λ_1 and λ_2 represent the first-order transition and spinodal lines, respectively. (adapted from Ref. [55])

membranes, the site–site cohesive energy ε for the onset of aggregation falls below the thermal energy $k_B T$.

6.3. Monte Carlo Simulation

To further investigate the aggregation behavior in supported membranes, we performed MC simulations of both our lattice model of adhesion points and of the standard 2D lattice-gas model [55]. We simulated the system at two different densities $\rho = N/N_s = 0.05$ and $\rho = 0.1$, and for various values of ε ranging from 0 to 3 $k_B T$. Snapshots taken from simulations for $\varepsilon = 1 k_B T$ and $\rho = 0.1$ are shown in Fig. 13. Figure 13A shows the initial configuration where the points are randomly distributed on the lattice. Figure 13B and C shows, respectively, typical equilibrium configurations of the standard lattice-gas model and of our model of adhesion points. One clearly sees that for the same strength of the interaction energy $\varepsilon = 1 k_B T$, the standard lattice-gas model remains in the gas phase, while the adhesion points (that, in addition to the direct interactions, also attract each other via the fluctuation-induced mechanism) condense into a large cluster containing almost all the adhesion points.

In order to determine the onset of the gas to liquid transition, we measured the average number of clusters in the system (where a cluster is defined as a set of neighboring occupied sites), and the mean value of the energy of direct interactions between sites, $\langle E_{LG} \rangle$ [first term in Eq. (28)]. Our results are summarized in Fig. 14A (for $\rho = 0.05$) and 14B (for $\rho = 0.1$). For each ρ, we measured these quantities both for the standard lattice-gas model (open symbols and dash-dotted lines in Fig. 14) and for the adhesion points model (solid symbols and solid lines in Fig. 14). The number of clusters is denoted by squares (values on the right y-axis of

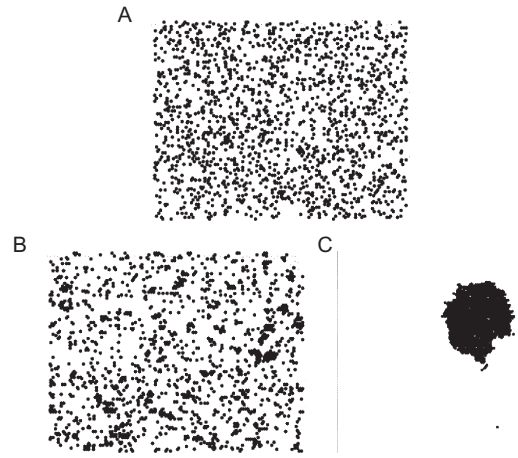

Figure 13 (A) Initial configurations of the simulations in which the points are randomly distributed on the lattice. (B) Representative equilibrium configurations of the standard lattice-gas model for $\rho = 0.1$ and $\varepsilon = 1k_BT$. (C) Representative equilibrium configurations of our lattice model of adhesion points for the same values of ρ and ε as in (B).

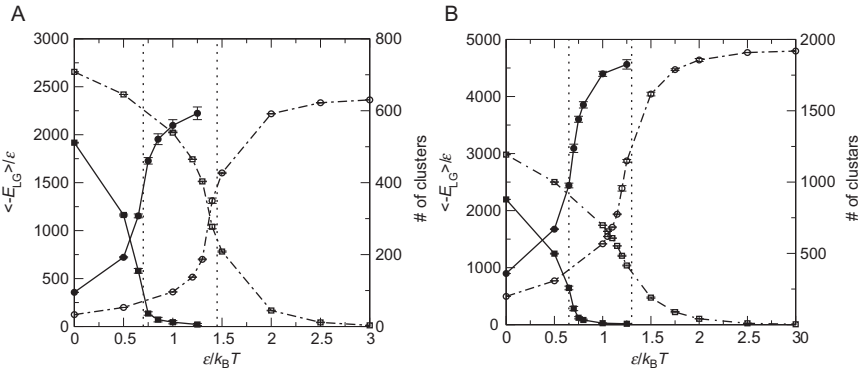

Figure 14 Left y-axis: The energy of direct interactions between sites, $\langle E_{LG} \rangle$, as a function of ε, for $\phi = 0.05$ (A) and $\phi = 0.1$ (B). *Solid circles*: results for our model for adhesion points. *Open circles*: results for the standard lattice-gas model. Right y-axis: The number of clusters as a function of ε, for $\phi = 0.05$ (A) and $\phi = 0.1$ (B). *Solid squares*: results for our model for adhesion points. *Open squares*: results for the standard lattice-gas model. (adapted from Ref. [55])

the figures), while $\langle E_{LG} \rangle$ is represented by circles (values on the left y-axis). The gas phase is characterized by a large number of small clusters, some of which may be of the size of a single site. Furthermore, since each occupied site has a relatively small number of neighboring occupied sites, the mean

configurational energy $\langle -E_{\rm LG} \rangle$ is relatively low. Conversely, when the sites form large clusters in the condensed phase, $\langle -E_{\rm LG} \rangle$ is high, and the total number of clusters decreases (and in many cases, especially for large values of ε, we simply observe only a single cluster in our system). Figure 14 exhibits an abrupt, clearly first-order, transition from a gas phase with a large number of clusters and small $\langle -E_{\rm LG} \rangle$ to a condensed state with a small number of clusters and large $\langle -E_{\rm LG} \rangle$. The estimated values of ε at the transition are (see vertical lines in Fig. 14): $\varepsilon_t \simeq 0.7 k_{\rm B}T$ ($\rho = 0.05$) and $\varepsilon_t \simeq 0.65 k_{\rm B}T$ ($\rho = 0.1$). In comparison (see also Fig. 14), for the standard lattice-gas model, the transition values are roughly twice larger than these values: $\varepsilon_t^{\rm LG} \simeq 1.45 k_{\rm B}T$ ($\rho = 0.05$) and $\varepsilon_t^{\rm LG} \sim 1.3 k_{\rm B}T (\rho = 0.1)$.

Our computational results which show that the fluctuation-mediated interactions reduce the strength of ε_t, are in a qualitative agreement with the mean field theory prediction. To make a quantitative comparison between the theory and the simulations, one needs to estimate the parameter B appearing in Eq. (35). Several reasons make such an estimation difficult and inaccurate: First, our nonstandard mean field theory is based on the assumption that the clusters are circular and roughly have the same size, which is quite a crude approximation. Second, tracing the precise location of ε_t in Fig. 14 is largely inaccurate because of the finite size of the system that makes the transitions look like crossovers. To reduce the large uncertainties associated with the determination of ε_t, one can look at the difference between the value of this quantity in our model of adhesion points and for the standard lattice-gas model. Using

$$\lambda_1^{\rm LG} - \lambda_1 = 2\sqrt{\pi} B \left(\varepsilon_t^{\rm LG} - \varepsilon_t \right), \tag{42}$$

for $\rho = 0.1$, we find $B \simeq 1$, as indeed expected for large clusters.

7. Conclusions

In this review, we presented a statistical thermodynamics analysis of the aggregation behavior of adhesion points between a fluctuating membrane and a supporting surface. Our analysis focused on the contribution of the membrane thermal fluctuations to this process, via the attractive interactions that they mediate between the adhesion points. The origin of the fluctuation-induced (Casimir-like) interactions are the restrictions imposed on the membrane thermal fluctuations by the adhesion points, and the associated free energy cost which is minimized when the adhesion points localize in a cluster. We investigated both the two- and many-body fluctuation-induced interactions. For the two-body problem, our analysis reveals that the fluctuation-induced pair potential is infinitely long range with a

logarithmic dependence on the pair distance. If, in addition to the excluded volume interactions, the membrane and the surface also interact via an attractive confining potential, the fluctuation-induced pair potential becomes screened at large distances. The screening of the pair potential is due to the fact that far away from each adhesion point, the amplitude of the fluctuations is governed by the strength of the external potential rather than by the presence of the other adhesion point.

In the many-body problem, the fluctuation-induced interactions are self-screened. The amplitude of the thermal fluctuations at each unit area of the membrane is governed by the distance to the closest adhesion points, which implies that each point interacts only with a few nearby points. This justifies our mapping of the problem into the 2D lattice-gas model with an effectively larger (renormalized) interaction energy. Depending on the strength of the renormalized interactions, the system may be either in a "gas" (uniform distribution) or a "condensed" (adhesion cluster) phase. The interesting question which arises is whether the fluctuation-induced contribution to the attraction is sufficiently strong to allow cluster formation. Our analysis finds that the answer to this question is no. The fluctuation-induced interactions alone are too weak to induce the condensation transition. They do, however, greatly reduce (to below the thermal energy $k_B T$) the strength of the direct interactions at which the transition takes place.

ACKNOWLEDGMENT

I wish to express my deep gratitude to Prof. Phil Pincus for inspiring me to work on this fascinating problem. I have benefited enormously from many insightful discussions with him. I also wish to thank my student, Noam Weil, who participated in the final part of the research with such enthusiasm and creativity. The work was supported by the Israel Science Foundation (Grant Number 946/08).

REFERENCES

[1] R. Lipowsky, E. Sackmann (Eds.), Handbook of Biological Physics: Structure and Dynamics of Membranes, Elsevier, Amsterdam, 1995.
[2] B. Alberts, D. Bray, J. Lewis, M. Raff, K. Roberts, J.D. Watson, Molecular Biology of the Cell, Garland, New York, 1994.
[3] T. Salditt, Thermal fluctuations and stability of solid-supported lipid membranes, J. Phys. Condens. Mat. 17 (2005) R287–R314.
[4] M. Tanaka, E. Sackmann, Polymer-supported membranes as models of the cell surface, Nature 437 (2005) 656–663.
[5] H.A. Rinia, G.W.H. Wurpel, M. Müller, Visualization and characterization of domains in model membranes, in: A. Ottova-Tien (Ed.), Advances in Planar Lipid Bilayers and Liposomes, Vol. 3 Elsevier, Amsterdam, 2006, pp. 85–123.
[6] M. Tanaka, E. Sackmann, Supported membranes as biofunctional interfaces and smart biosensor platforms, Phys. Stat. Sol. (a) 203 (2006) 3452–3462.

[7] P.P. Girard, E.A. Cavalcanti-Adam, R. Kemkemer, J.P. Spatz, Cellular chemomechanics at interfaces: sensing, integration and response, Soft Matter 3 (2007) 307–326.
[8] J. Salafsky, J.T. Groves, S.G. Boxer, Architecture and function of membrane proteins in planar supported bilayers: a study with photosynthetic reaction centers, Biochemistry 35 (1996) 14773–14781.
[9] E. Sackmann, Supported membranes: scientific and practical applications, Science 271 (1996) 43–48.
[10] A. Kloboucek, A. Behirsch, J. Faix, E. Sackmann, Adhesion-induced receptor segregation and adhesion plaque formation: a model membrane study, Biophys. J. 77 (1999) 2311–2328.
[11] Y. Kaizuka, T.J. Groves, Structure and dynamics of supported intermembrane junctions, Biophys. J. 86 (2004) 905–912.
[12] A.-S. Smith, B.G. Lorz, U. Seifert, E. Sackmann, Antagonist-induced deadhesion of specially adhered vesicles, Biophys. J. 90 (2006) 1064–1080.
[13] A. Ananthakrishnan, A. Ehrlicher, The forces behind cell movement, Int. J. Biol. Sci. 3 (2007) 303–317.
[14] P.S. Swain, D. Andelman, The influence of substrate structure on membrane adhesion, Langmuir 15 (1999) 8902–8914.
[15] S. Komura, D. Andelman, The unbinding transition of mixed fluid membranes, Europhys. Lett. 64 (2003) 844–850.
[16] K.R. Mecke, T. Charitat, F. Graner, Fluctuating lipid bilayer in an arbitrary potential: theory and experimental determination of bending rigidity, Langmuir 19 (2003) 2080–2087.
[17] M.I. Hoopes, M. Deserno, M.L. Longo, R. Faller, Coarse-grained modeling of interactions of lipid bilayers with supports, J. Chem. Phys. 129 (2008) 175102-1–175102-7.
[18] M.C. Beckerle (Ed.), Cell Adhesion, Oxford University Press, Oxford, 2001.
[19] D.A. Lauffenburger, J. Linderman, Receptors: Models for Binding, Trafficking, and Signaling, Oxford University Press, Oxford, 1995.
[20] A.-S. Smith, U. Seifert, Vesicles as a model for controlled (de-) adhesion of cells: a thermo-dynamic approach, Soft Matter 3 (2007) 275–289.
[21] T.R. Weikl, M. Asfaw, H. Krobath, B. Różycki, R. Lipowsky, Adhesion of membranes via receptor–ligand complexes: domain formation, binding cooperativity, and active processes, Soft Matter 5 (2009) 3213–3224.
[22] P.F. Lenne, A. Nicolas, Physics puzzles on membrane domains posed by cell biology, Soft Matter 5 (2009) 2841–2848.
[23] V. Niggli, Signaling to migration of neutrophils: importance of localized pathways, Int. J. Biochem. Cell Biol. 35 (2003) 1619–1638.
[24] K. Giehl, A. Menke, Microenvironmental regulation of E-cadherin-mediated adherens junctions, Front. Biosci. 13 (2008) 3975–3985.
[25] B. Geiger, A. Bershadsky, R. Pankov, K.M. Yamada, Transmembrane extracellular between the matrix-cytoskeleton crosstalk, Nat. Rev. Mol. Cell Biol. 2 (2001) 793–805.
[26] A.G. Moreira, C. Jeppesen, F. Tanaka, C.M. Marques, Irreversible vs. reversible bridging: when is kinetics relevant for adhesion? Europhys. Lett. 62 (2003) 876–882.
[27] X. Zhang, V.T. Moy, Cooperative adhesion of ligand–receptor bonds, Biophys. Chem. 104 (2003) 271–278.
[28] N. Gov, S.A. Safran, Pinning of fluid membranes by periodic harmonic potentials, Phys. Rev. E 69 (2004) 011101-1–011101-10.
[29] T. Gruhn, R. Lipowsky, Temperature dependence of vesicle adhesion, Phys. Rev. E 71 (2005) 011903-1–011903-10.
[30] G. Lomgo, I. Szleifer, Ligand–receptor interactions in tethered polymer layers, Langmuir 21 (2005) 11342–11351.

[31] N.W. Moore, T.L. Kuhl, The role of flexible tethers in multiple ligand–receptor bond formation between curved surfaces, Biophys. J. 91 (2006) 1675–1687.
[32] L.C.-L. Lin, J.T. Groves, F.L.H. Brown, Analysis of shape, fluctuations, and dynamics in intermembrane junctions, Biophys. J. 91 (2006) 3600–3606.
[33] H. Krobath, G.J. Schütz, R. Lipowsky, T.R. Weikl, Lateral diffusion of receptor–ligand bonds in membrane adhesion zones: effect of thermal membrane roughness, Europhys. Lett. 78 (2007) 38003-1–38003-6.
[34] R.-J. Merath, U. Seifert, Fluctuation spectra of free and supported membrane pairs, Eur. Phys. J. E 23 (2007) 103–116.
[35] M. Lamblet, B. Delord, L. Johannes, D. van Effenterre, P. Bassereau, Key role of receptor density in colloid/cell specific interaction: a quantitative biomimetic study on giant vesicles, Eur. Phys. J. E 26 (2008) 205–216.
[36] E. Reister-Gottfried, K. Sengupta, B. Lorz, E. Sackmann, U. Seifert, A. Suncăna Smith, Dynamics of specific vesicle–substrate adhesion: from local events to global dynamics, Phys. Rev. Lett. 101 (2008) 208103-1–208103-4.
[37] C. Selhuber-Unkel, M. Lopez-Garcia, H. Kessler, J.P. Spatz, Cooperativity in adhesion cluster formation during initial cell adhesion, Biophys. J. 95 (2008) 5424–5431.
[38] J. Israelachvili, Intermolecular and Surface Forces, Academic Press, London, 1985.
[39] B. Simon, The Statistical Mechanics of Lattice Gases, Vol. I Princeton University Press, Princeton, 1993.
[40] J. Braun, J.R. Abney, J.C. Owicki, How gap junction maintains its structure, Nature 310 (1984) 316–318.
[41] H.B.G. Casimir, On the attraction between two perfectly conducting plates, Proc. K. Ned. Akad. Wet. B51 (1948) 793–796.
[42] M.E. Fisher, P.G. de Gennes, Wall phenomena in a critical binary mixture, C. R. Seances Acad. Sci. Ser. B 287 (1978) 207–209.
[43] M. Kardar, R. Golestanian, The "friction" of vacuum, and other fluctuation-induced forces, Rev. Mod. Phys. 71 (1999) 1233–1245.
[44] M. Deserno, Mesoscopic membrane physics: concepts, simulations, and selected applications, Macromol. Rapid Commun. 30 (2009) 752–771.
[45] D. Frenkel, Introduction to colloidal systems, in: W.C.K. Poon, D. Andelman (Eds.), Soft Condensed Matter Physics in Molecular and Cell Biology, Taylor and Francis, New York, 2006, pp. 19–47.
[46] A.P. Gast, W.B. Russel, Simple ordering in complex fluids, Phys. Today 51 (1998) 24–30.
[47] O. Farago, Membrane fluctuations near a plane rigid surface, Phys. Rev. E 78 (2008) 051919-1–051919-9.
[48] W. Helfrich, Elastic properties of lipid bilayers: theory and possible experiments, Z. Naturforsch C 28 (1973) 693–703.
[49] O. Farago, "Water-free" computer model for fluid bilayer membranes, J. Chem. Phys. 119 (2003) 596–605.
[50] I.R. Cooke, K. Kremer, M. Deserno, Efficient tunable generic model for fluid bilayer membranes, Phys. Rev. E 72 (2005) 011506-1–011506-4.
[51] G. Brannigan, L.C.-L. Lin, F.L.H. Brown, Implicit solvent simulation models for biomembranes, Eur. Biophys. J. 35 (2006) 104–124.
[52] R. Bruinsma, M. Goulian, P. Pincus, Self-assembly of membrane junctions, Biophys. J. 67 (1994) 746–750.
[53] W. Helfrich, Steric interaction of fluid membranes in multilayer systems, Z. Naturforsch. C 33A (1978) 305–315.
[54] O. Farago, Fluctuation-induced attraction between adhesion sites of supported membranes, Phys. Rev. E 81 (2010) 050902(R)-1–050902(R)-4.
[55] N. Weil, O. Farago, Entropy driven aggregation of adhesion sites of supported membranes, Eur. Phys. J. E 33 (2010) 81–87.

CHAPTER SIX

Monte Carlo Simulations of Lipid Bilayers and Liposomes Using Coarse-Grained Models

M. Wahab,* H.-J. Mögel, *and* P. Schiller

Contents

Abstract

Monte Carlo simulations provide some insight into self-assembled aggregates of amphiphiles in aqueous environment. A rather simple solvent-free model, where a molecule is formed by a hydrophilic head segment and some hydrophobic chain segments, is suitable for describing the formation of micelles, stable membranes, and spherical vesicles. Characteristic features of the self-assembled aggregates, such as the elastic properties of bilayers, can be

* Corresponding author. Tel.: +49-3731-393424 or +49-3731-394013; Fax: +49-3731-393588.
E-mail address: mirco.wahab@chemie.tu-freiberg.de

TU-Freiberg, Institute of Physical Chemistry, Freiberg, Germany

Advances in Planar Lipid Bilayers and Liposomes, Volume 14
ISSN 1554-4516, DOI: 10.1016/B978-0-12-387720-8.00006-6

obtained from simulated data. The capability of this simple approach was demonstrated for a surfactant model with three spherical segments. Analyzing vesicle fluctuations by Monte Carlo simulations, the surface tension and the curvature elastic constant of bilayers that form vesicles can be evaluated. If the vesicles contain hydrophilic solute molecules, thermal fluctuations of spherical vesicles depend on their osmotic pressure. Already at relatively low solute concentrations, the appearance of an osmotic pressure leads to a strong depression of vesicle fluctuations.

The adsorption of colloidal particles on surfaces of soft materials causes elastic distortions. Biological membranes contain a large amount of embedded and adsorbed macromolecules, especially transmembrane and peripheral proteins consisting of large polypeptide chains folded in compact particles. Membrane distortions spread around each protein can superimpose and produce indirect forces between them. Similar effects are based on concentration fluctuations of the lipid components forming the membrane. Proteins as well as smaller peptides disturb the homogeneous distribution of the lipid mixture, facilitating a phase separation of the lipid components. Disturbances of the spatial lipid distribution can also be accompanied by an enhanced adsorption of water soluble peptides. This effect is amplified for nonideal mixtures, when the correlation length of concentration fluctuations is enlarged. Concentration fluctuations also produce forces between membrane proteins, which can enforce the aggregation of membrane bound proteins. Monte Carlo simulations are suitable for testing general concepts and theories on protein-membrane interactions.

1. Introduction

Amphiphilic molecules are capable of self-assembling in aqueous environment, forming micelles, bilayers, or even more complex liquid crystalline phases in dependence on their molecular structure [1]. Because of their biological relevance, lipid bilayer membranes are of special interest. According to the well-established model of Singer and Nicolson [2], biological membranes consist of a lipid bilayer with embedded and adsorbed amphiphatic macromolecules such as proteins and smaller peptides. The lipid molecules and many of the proteins can move freely in the membrane plane. Most lipid molecules in a biological membrane consist of a hydrophilic headgroup and two hydrocarbon chains, but also single-chain lipids and lipids with more than two chains exist. A native membrane contains a large variety of lipid components, which differ in their hydrophilic heads and hydrophobic tails. The very complex interactions of lipids and intrinsic or associated membrane proteins is a topic of intense biological research [3–6]. After establishing the generally accepted membrane model, biologists have elucidated a large number of phenomena that are based on the interplay of lipids and proteins associated with the bilayer. Subtle and

specific biological effects cannot be described by common physical methods such as molecular simulations and statistical mechanics. However, there are also some general basic properties which may be suitable for the application of statistical mechanics. Some interesting membrane processes are believed to have a simple physical origin, resulting from membrane elasticity, fluidity, and nonideal mixing of membrane lipids [7,8].

In these cases, where collective effects take place in lipid bilayers, Monte Carlo (MC) simulations [9] provide a theoretical framework suitable to elucidate a variety of physical properties. Apart from Monte Carlo simulations, there are also other simulation techniques which can be used to investigate systems with many degrees of freedom. A large number of studies on amphiphiles have been done by using molecular dynamics [10], Brownian dynamics [11], and dissipative particle dynamics simulations [12,13]. These techniques have the advantage that they account for true physical processes, whereas the pathway of successive states in Monte Carlo simulations usually does not reflect the system evolution. Monte Carlo simulations are suitable for studying final states, where the thermodynamic equilibrium appears, but not the detailed kinetic process from an equilibrium state to another one after changing external conditions. Unfortunately, many interesting problems concerning the pathway of specific processes, for example, self-assembly of bilayers, membrane fusion [14], endocytosis, and exocytosis [15], can hardly be elucidated by standard MC simulations. A remedy could be kinetic MC [16], but in most cases other methods are favored to simulate the evolution of thermodynamic systems.

On the other side, MC simulations have the advantage that nonphysical MC moves frequently drive a system faster toward the equilibrium state than physical moves of other simulation methods. If equilibrium properties are studied, MC simulations are suitable to gain insight into thermodynamical and mechanical equilibrium properties of bilayers. A classical problem is to find out how macroscopic membrane properties emerge from microscopic interactions between amphiphilic molecules. It has been demonstrated that bilayers possessing the essential experimentally observed properties are formed by simulating systems that contain very simple model molecules [11,17,18]. Analyzing self-assembled model bilayers may also help to formulate macroscopic theories more precisely. Several slightly different versions of the macroscopic elasticity theory for bilayer deformations are known, which have been used to predict a large variety of possible vesicle shapes [19].

MC and other simulation techniques can help to decide which version of the elasticity theory is the most realistic one for a reliable macroscopic description of bilayer membranes. Another problem under debate is the disturbance of the lipid bilayer by peripheral and transmembrane proteins [3,6,20–22]. Lipid–protein interactions are accompanied by redistributions of lipid mixture constituents and elastic deformations. In this chapter, we

discuss the application of Monte Carlo simulations to some problems arising in membrane physics:

- Fluctuations and elastic properties of self-assembled vesicles
- Peptide adsorption enhanced by demixing and concentration fluctuations of membrane lipids
- Membrane-mediated interactions between peripheral and transmembrane proteins due to concentration fluctuations and elastic deformations
- Short-range membrane-mediated elastic interactions between adsorbate particles on supported membranes

It will be demonstrated that simulations of ensembles with very simple molecular models are capable of reproducing characteristic physical properties of membranes. This approach is not appropriate for investigating special properties of lipid compounds or peptides, but it can yield some insight into several collective properties of bilayers. When simple coarse-grained molecular models are used, it is more promising to draw general conclusions on the strength and importance of membrane-mediated effects [23]. In particular, Monte Carlo simulations are useful to test concepts and recent ideas concerning the mechanisms of indirect interactions between membrane-associated proteins.

MC simulations may also be helpful to tackle more specific problems related to liposomes. In these cases, it would be necessary to introduce more detailed molecular models mapping more features of the real architecture of lipids. As an example, we consider the solubilization of a liposome by bile salts, which is an important step of the digestion of lipids [24]. If only small displacements and rotations of molecular segments between successive system configurations are generated, the system evolution is similar to a Brownian motion. This approach works well for describing disordered systems. Thus, the kinetic MC method is supposed to provide a fairly good representation of possible intermediate structures arising when a system transforms into an equilibrium state. We have used kinetic MC for elucidating the transformation of a liposome into micelles. In a similar way, adding more characteristic features to molecular models, MC procedures may offer appropriate tools to simulate equilibrium states of specific bilayer membranes, or even the evolution of a strongly fluctuating system from a nonequilibrium toward an equilibrium state.

2. Self-assembled Vesicles

The amphiphilic character of surfactants leads to the formation of various aggregates in water. Surfactant molecules consist of a polar head group and one or more hydrocarbon chains. The polar heads promote

dissolution in water, whereas hydrocarbon chains are hydrophobic and thus nearly insoluble. The insolubility is based on unfavorable orientations of water molecules, which are highly ordered in the vicinity of hydrocarbon chains [25].

Already at low or moderate concentrations, surfactant molecules organize themselves into aggregated structures to shield their hydrocarbon chains from water. In contrast, solvent-mediated attraction forces between polar groups should be small, since water is a good solvent for the heads of amphiphilic molecules. Hence, the aggregation of amphiphilic molecules is driven by a strong effective attraction between chain segments, which tends to minimize the unfavorable contacts between polar solvent and apolar parts of solute molecules (hydrocarbon chains). This indirect force, usually denoted as hydrophobic interaction, is known to be several times stronger than the familiar van der Waals force between hydrocarbon chains [26]. Changing the number of water-like and oil-like segments in surfactant molecules leads to a strong alteration of the effective interaction. In many cases, the amphiphilic molecules aggregate into spherical micelles. But there exist various different aggregated structures, for example, disk-like or cylindrical micelles. At higher surfactant concentrations, the hexagonal phase, membranes, cubic phases, or even more complex morphologies can appear [1].

Lipid vesicles made of flexible bilayers of amphiphilic molecules in aqueous solutions have various different shapes [27]. They may serve as carriers for biomolecules into (endocytosis) and out of cells (exocytosis) [15]. In pharmaceutical applications, filled vesicles are useful for drug delivery [28]. Very large vesicles with radii in the micrometer range, called giant vesicles, have found much attention both from experimental and theoretical point of view [29]. In dependence on constraints, such as bilayer area and enclosed volume, a large variety of vesicle shapes has been predicted [30]. An important material parameter is the curvature elastic modulus. A conventional method to determine this modulus is based on the thermal shape fluctuations of spherical vesicles [31,32]. Giant vesicles are very fragile elastic objects, their strong thermal fluctuations can be observed under an optical microscope. Analyzing many snapshots of these fluctuations yields the curvature elastic modulus. Although small vesicles are invisible by optical microscopy, the investigation of their physical properties can lead to relevant biological results, for example, for elucidating endocytosis and exocytosis.

2.1. Simple Model for Monte Carlo Simulations of Self-assembled Amphiphilic Aggregates

Apart from Monte Carlo simulations for lattice models [33,34], most current investigations are focused on off-lattice systems [35,36] utilizing the considerable progress in computing performance. If atomic resolution is used for

off-lattice molecular simulations, the complete configuration space of a surfactant-water system, even when small systems of surfactant molecules are considered, comprises a vast number of coordinates. A detailed model may be utilized to simulate small systems, for example, single micelles or bilayer membrane patches. For describing the self-assembly of larger systems, however, much simpler concepts are needed to avoid exceptionally long simulation times. Simplified coarse-grained models are not suitable to allow for molecular details, but they can help to understand the underlying physics of self-assembly processes in surfactant systems. For this purpose, the molecules are divided into segments, each of them contains some atoms or functional groups.

A further essential reduction of computational effort is possible by using solvent-free effective interaction models. In a formal way, the effective interaction potential is generated by an integration of the complete many-particle distribution function over the complete set of solvent coordinates. The resulting reduced distribution function depends only on the solute coordinates and its logarithm is related to the effective potential [37]. Furthermore, neglecting many-body contributions, it is usually assumed that the effective potential can be expressed as a sum of effective pair potentials for the interaction between molecular segments. For surfactant molecules at least two segment types, namely hydrophilic and hydrophobic segments, have to be considered. We use the simplest model capable of accounting for the combined hydrophilic and hydrophobic character of flexible surfactant molecules [18].

Water can be chosen as a reference for introducing the interaction energies between different molecular segments. Thus, we distinguish between water-like heads and oil-like (hydrocarbon) chain segments. Self-assembled surfactant structures such as micelles or membranes are not fixed aggregates, but they change size and shape as a consequence of very strong thermal fluctuations. In this case, predictions of simulations by coarse-grained models depend on the interaction range, but they are not very sensitive to details of the chosen pair potential [17]. All segments are considered as hard spheres with the same diameter, which defines the range of the excluded volume interaction.

The first segment, the hydrophilic head, comprises the surfactant head group atoms with tightly bound water, while further segments represent the hydrocarbon chains. A few CH_2-segments are joined to form an oil-like chain segment similar to chain models in polymer physics. Except for the restrictions resulting from the excluded volume interaction, the angle enclosed by adjacent bonds between spherical segments can vary arbitrarily. Let us consider a model with amphiphilic molecules consisting of a head and two oil-like chain segments (Fig. 1). Neglecting other attractive forces, we only consider the hydrophobic interaction as the main attractive force between surfactant molecules. Defining central forces between the spherical segments, the effective interaction may be expressed as a square-well potential

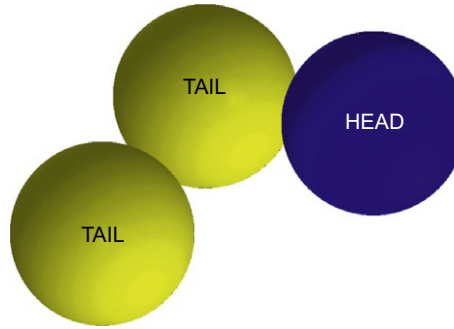

Figure 1 Model of an amphiphilic molecule consisting of a water-like head segment and two oil-like tail segments.

$$u(r) = \begin{cases} \infty & \text{for } r \leq \sigma, \\ -\varepsilon & \text{for } \sigma < r \leq \sigma + d, \\ 0 & \text{for } r > \sigma + d, \end{cases} \tag{1}$$

where r is the distance between the centers of interacting spheres, σ is their diameter, and d is the width of the well. For head–head and head–tail interactions the interaction parameter ε is assumed to be equal to zero, for the tail–tail interaction the hydrophobic attraction ε is larger than zero. This choice of the effective pair potential implies the generally accepted realization that the hydrophobic interaction should be much stronger than other attractive forces between surfactant segments.

It should be noted that other studies [17,35,38,39] have used a similar simple water-free effective interaction model with a lipid model consisting of three beads for simulating bilayer membranes. In comparison to our version [18], these models introduce an intramolecular potential, which prefers the beads to lie on a straight line. The simulations of Farago *et al.* [38,39] are focused on thermal undulation fluctuations of planar preassembled bilayer membranes.

As starting point for our Monte Carlo simulations, $N_0 = 2000$ or more surfactant molecules were randomly placed in a cubic box with edge length $L = 48\sigma$. Periodic boundary conditions were applied to minimize finite size effects. Using the Metropolis algorithm, at least 5×10^6 attempted Monte Carlo steps were carried out to achieve thermodynamic equilibrium. In some cases, the model molecules have formed spherical vesicles. For studying vesicle fluctuations, further 10^8 Monte Carlo steps have been accumulated to analyze deviations from the spherical shape.

2.2. Phase Diagram of the Three-Segment Model

The model containing particles composed of a few beads is very simple. Distances can be scaled by the bead diameter σ and energies should be expressed in terms of the mean thermal energy kT. Hence, there are only two essential parameters which are needed to scale physical results for this simple model, namely the reduced well depth ε/kT characterizing the strength of the hydrophobic interaction between two tail beads and the reduced range of this interaction d/σ. Quantitative results could be expressed in terms of theses two parameters. Both parameters are useful to construct a phase diagram for the observed aggregates. Micelles, curved bilayer membranes, and system configurations without aggregation have been found.

Snapshots of some aggregates are depicted in Fig. 2. Plotting ε/kT versus d/σ, Fig. 3 shows a phase diagram of the self-assembled structures for the three-segment model [18]. As the interaction range of the hydrophobic

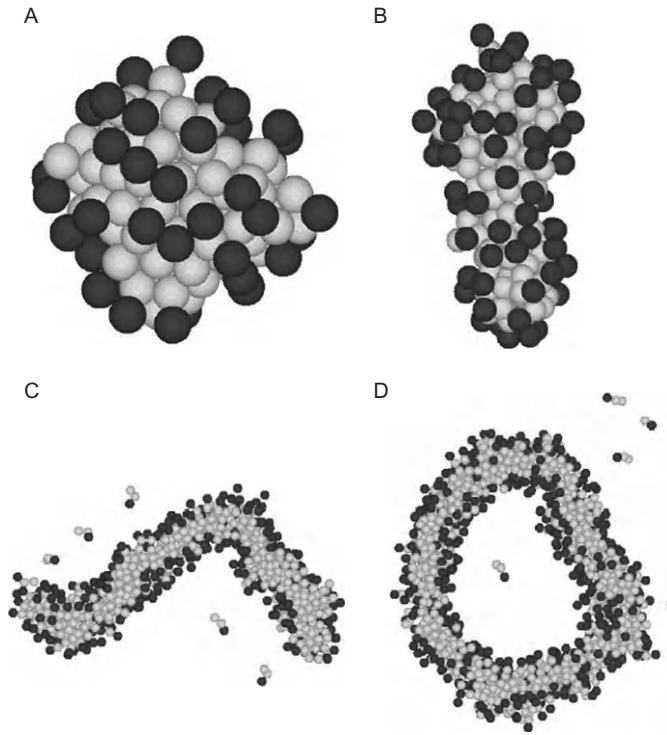

Figure 2 Snapshots obtained from Monte Carlo simulations illustrate the shapes of surfactant aggregates. (A) Spherical micelle; (B) cylindrical micelle; (C) cross-section of curved membranes; (D) cross-section of a vesicle. (adapted from Ref. [18])

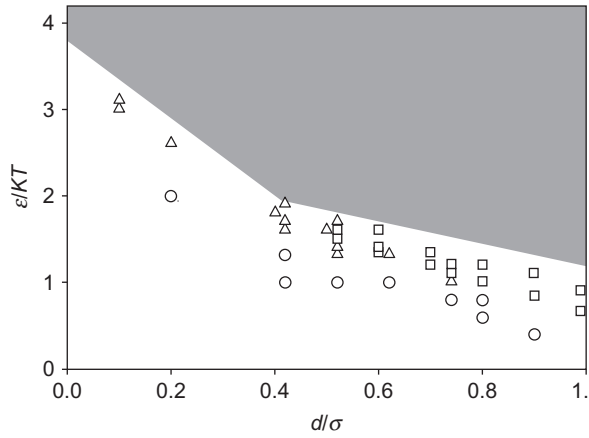

Figure 3 Stability regions for self-assembled aggregates with particles consisting of three segments. In the gray region of the diagram an unambiguous allocation of stable structures was not possible, because the simulation time required to achieve the final state of system evolution was too large. ○, Surfactant solution without large clusters; Δ, micellar aggregates; □, curved membranes. (adapted from Ref. [18])

effect is generally supposed to be relatively large, d/σ is varied in the limits between 0.1 and 1. The diagram refers to $N_0 = 2000$ surfactant molecules distributed in a cubic simulation box with edge length $L = 48\sigma$. Due to the hard core potentials and the sequential single-molecule moves in the Monte Carlo simulations, the ordered chain packing of gel phases is not easily accessible. The chain insertion probability in dense aggregates is prohibitively low, leading to inadequate configuration statistics. Therefore, only fluid phase regions can be simulated. These regions are shown in the phase diagram (Fig. 3).

Completely stable and self-assembled curved bilayers can be observed if the reduced interaction range d/σ is relatively large, exceeding a certain value $(d/\sigma > 0.5)$. It should be mentioned, however, that membranes can occur also outside the phase boundaries shown in Fig. 3, because bilayers may remain stable after preassembling the surfactant molecules by appropriately adjusting the start configuration for the simulation.

Thus, the simple surfactant model is suitable for simulations of bilayer membranes even if the parameters d/σ and ε/kT are located outside the bilayer region indicated in the phase diagram. However, we have considered only structures which are self-assembled from random initial configurations. Cooke *et al.* [17] localized the bilayer membrane existence region at large values of d/σ quite similar to our results. Their surfactant model has the same topology as that used in this chapter, although the chosen interaction potential is more complicated and supplemented with an angle dependent bending potential for the three-segment molecules.

In most cases, our membranes consist of randomly curved patches (Fig. 2C). However, a spherical vesicle was occasionally formed after starting the simulation from a random initial configuration. Clearly, the self-assembly of a closed vesicle from random initial configurations is considerably less probable than the formation of a randomly curved surface. Nevertheless, accidentally formed spherical vesicles remain stable, although strong shape fluctuations may occur. For example, the fluctuating vesicle shown in Fig. 2D did not decay, even after 10^8 Monte Carlo steps. It can be speculated that these small vesicles are metastable and their free energy has a local minimum, whereas the more frequently observed randomly curved bilayers are absolutely stable.

2.3. Curvature Elasticity and Vesicle Fluctuations

Bilayer membranes fluctuate strongly, because their surface tension and bending energies are rather low. It is interesting to compare MC simulation data for vesicles with typical experimental results. Analyzing the shape fluctuations of spherical vesicles, it is possible to determine both the interface tension γ and the bending rigidity κ of the membrane. The macroscopic approach to study vesicle shapes is based on the free energy [32]

$$F = \gamma A + 2\kappa \int_A dA H^2 \tag{2}$$

where A is the vesicle surface area and $H = (R_1^{-1} + R_2^{-1})/2$ is the mean curvature of the vesicle surface (R_1, R_2—main curvature radii). Fluctuations produce deviations from a perfect sphere with radius r_0. Using such a reference sphere, a spherical coordinate system with polar angle θ and azimuthal angle ϕ is introduced. The position of the deformed almost spherical membrane surface can be expressed as

$$r = r_0[1 + u(\theta, \phi)]\mathbf{e}_r(\theta, \phi), \tag{3}$$

where $\mathbf{e}_r(\theta, \phi)$ is the sphere normal and $u(\theta, \phi)$ characterizes the small deformations. Expansion of the field $u(\theta, \phi)$ in terms of spherical harmonics yields

$$u(\theta, \phi) = \sum_{n,m} u_{nm} Y_n^m(\theta, \phi). \tag{4}$$

The coefficients in expansion (4) are evaluated by

$$u_{nm} = \int_\Omega u(\theta, \phi) Y_n^{m*}(\theta, \phi) d\Omega, \tag{5}$$

where Ω symbolizes the unit sphere. The integral [Eq. (5)] should be replaced by a sum for using the discrete data from Monte Carlo simulations. We assume that the heads of the amphiphiles in the outer shell of the vesicle membrane form a randomly distributed net, the coordinates of which define the position of the vesicle surface. Let r_0 be the radius of the reference sphere [40]. The field $u(\theta, \phi)$ is replaced by $u(\theta_j, \phi_j) = (r_j - r_0)/r_0$, where r_j is the distance between a single head $j(j = 1, 2, \ldots, M)$ and the gravity center of the surface net formed by all surfactant heads in the outer vesicle shell. Thus, the integral [Eq. (5)] is replaced by a sum

$$u_{nm} = \frac{4\pi}{M} \sum_{j=1}^{M} \left(\frac{r_j - r_0}{r_0} \right) Y_n^{m*}\left(\theta_j, \phi_j\right). \tag{6}$$

The zenith axis of the spherical coordinate system (z-axis) can be parallel to any space direction. We have obtained almost identical results for different choices of the z-axis. Fluctuations of the quasispherical vesicle surface can be analyzed by considering a suitable statistical ensemble of vesicles. Milner and Safran [31] found that the mean squares of the fluctuation amplitudes are

$$\left\langle |u_{nm}|^2 \right\rangle = \left(\frac{kT}{\kappa} \right) \frac{1}{(n+2)(n-1)[n(n+1) + \Lambda]}, \tag{7}$$

where kT is the mean thermal energy and $\Lambda = \gamma r_0^2/\kappa$. Using Eq. (7), the bending constant κ and the interface tension γ can be evaluated. Figure 4 shows the decrease of the mean square of the fluctuation amplitude $\langle |u_{n0}|^2 \rangle$ with increasing values of n for $\varepsilon = 0.7kT$. The curve in Fig. 4 results from fitting κ and Λ in Eq. (7). In the case of small vesicles, the finite bilayer thickness can produce deviations from the fluctuation amplitudes evaluated by the curvature model. Figure 4 indicates that errors, which may result from limitations in simulation time and the use of a macroscopic bilayer elasticity model for a small vesicle, are relatively low. If $d/\sigma = 0.99$ and $\varepsilon/kT = 0.7$, the value of the bending coefficient $\kappa = 0.74kT$ is very small, because we have chosen rather short particles consisting of three segments. The interface tension γ can be evaluated additionally. For $r_0 = 5.3$ nm, we obtain $\gamma \simeq 1.87 \times 10^{-3}$ N/m if $\varepsilon/kT = 0.7$. This value of γ is approximately 40 times smaller than the surface tension of the air–water interface, but has a nonzero value. Probably, a remarkable nonzero tension of the bilayer membrane is caused by the large curvature of small vesicles. Giant vesicles are supposed to have a lower tension (effective surface tension), because the hydrophobic parts of the flat membrane are more densely packed, and thus they have a better protection against water. At somewhat

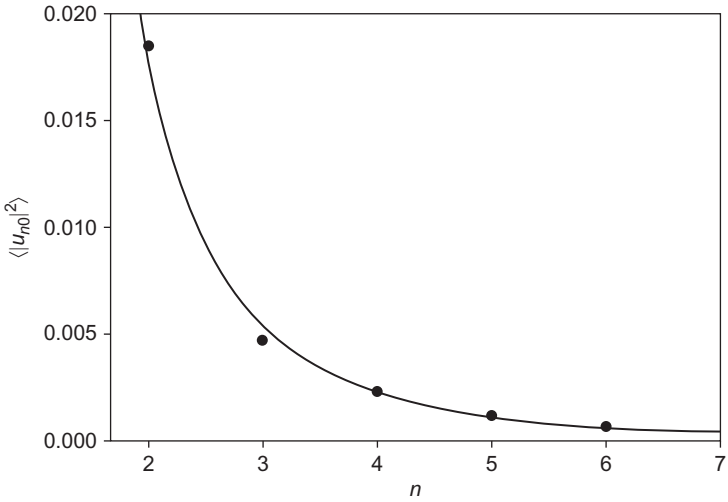

Figure 4 Amplitudes $\langle |u_{n0}|^2 \rangle$ of vesicle fluctuations for $n = 2, 3, 4, 5$, and 6. (adapted from Ref. [18]).

lower temperature, if $T = 1.14\varepsilon/k$ or $\varepsilon/kT = 0.875$, the value $\kappa = 8.3kT$ was found for a vesicle consisting of $N_0 = 2500$ molecules [40]. Obviously, the bending modulus κ increases with decreasing temperature. It can also be checked if an osmotic pressure, generated by hydrophobic spherical particles placed into the vesicle, quenches the fluctuations (Fig. 5). In this case, the free energy Eq. (2) is supplemented with a term that accounts for the work resulting from vesicle volume changes. Thus, denoting the osmotic pressure by Π, the free energy is [27]

$$F = \gamma A + 2\kappa \int_A dA H^2 - \Pi \Delta V, \tag{8}$$

where ΔV is the change of the vesicle volume due to a fluctuation. If ΔV changes, water must be exchanged between the interior of the vesicle and the region outside. It is usually assumed that fluctuations of very large (giant) vesicles with sizes in the micrometer range do not change the surface area. Furthermore, the enclosed vesicle volume is assumed to be constant, because the hydrophobic part of the bilayer hinders permeation of water and solute molecules. Thus, if the observation time is sufficiently short, both the vesicle surface area and the enclosed volume have fixed values. However, in the case of small vesicles, which can have diameters smaller than 20 nm [41], the water permeability of the bilayer shell can lead to a change of the vesicle volume within a short observation time, since the area to volume ratio for such small vesicles is much larger than for giant vesicles.

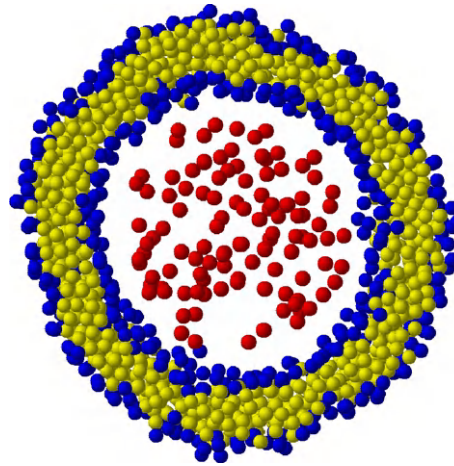

Figure 5 Snapshot of a vesicle (cross section) containing $N = 100$ hydrophilic solute molecules. (adapted from Ref. [40]).

Fluctuations of small vesicles should strongly be influenced by the osmotic pressure. Water can permeate through the membrane in a time scale beneath the observation time of vesicle fluctuations, whereas the amphiphilic bilayer is impermeable for large solute molecules.

For a nonzero osmotic pressure, free energy Eq. (8) leads to the same relation as Eq. (7), except for a different meaning of parameter Λ. This parameter is found to be $\Lambda = \Pi r_0^3/(2\kappa)$, where r_0 denotes the vesicle radius. The osmotic pressure can be evaluated by van't Hoff's equation of state $\Pi V_i = NkT$, where V_i is the volume of the interior of the vesicle. Equation (7) with relation $\Lambda = \Pi r_0^3/(2\kappa)$ has been tested for different numbers N of particles put in the vesicle. Figure 6 depicts the comparison between the case $N = 0$ (i.e., $\Pi = 0$) and $N = 300$. Obviously, an osmotic pressure can considerably quench vesicle fluctuations. However, if the added particles are placed outside the vesicle, the osmotic pressure difference Π is negative and shape fluctuations are amplified, which is accompanied by a destabilization of the spherical vesicle shape. There is a transcritical bifurcation at the critical particle density $c_t = 12\kappa/(r_0^3 kT)$, above which the spherical vesicle shape changes. If $c > c_t$, an oblate or a prolate vesicle can evolve from the spherical shape. The free energies for both routes do not differ much [42], so that the observed evolution of an originally spherical vesicle depends on small initial fluctuations. For the case $\varepsilon/kT = 0.875$, we obtain the bifurcation threshold $c_t = 3.9 \times 10^{-2}\sigma^{-3}$ for $\kappa = 8.3kT$ and $r_0 = 13.7\sigma$. Actually, for $c > c_t$ the simulations have indicated that a shape transformation away from the initial spherical shape occurs [40].

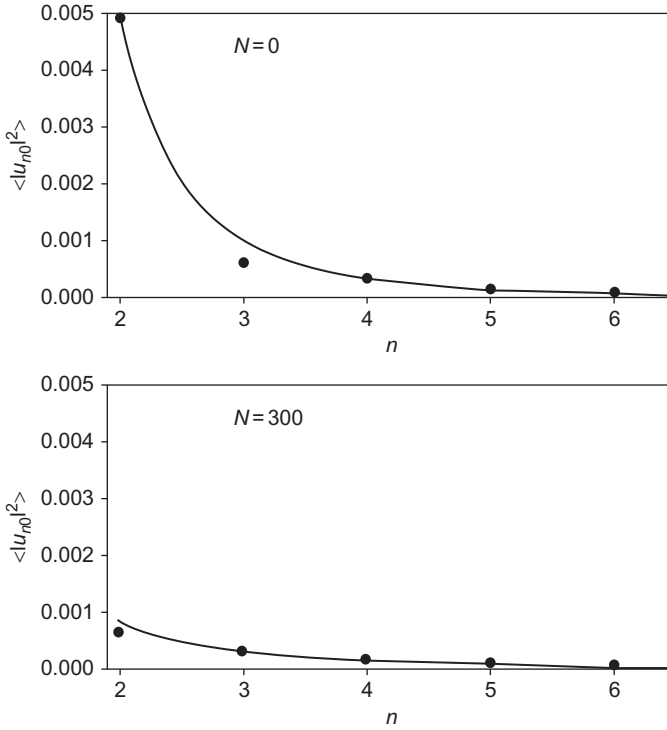

Figure 6 Fluctuation amplitudes $\langle |u_{n0}|^2 \rangle$ for $n = 2, 3, 4, 5$, and 6. The simulated data are fitted by using Eq. (25). The only fit parameter is κ, which is chosen as $\kappa = 8.3kT$ for both depicted diagrams with different numbers of solute molecules ($N = 0$ and 300) inside the vesicle. (adapted from Ref. [40])

2.4. Conclusions

In accord with the reasoning of Israelachvili [26], amphiphiles with almost equal cross-sectional area of head group and tail region are prone to the formation of membranes instead of strongly curved aggregates such as micelles. The phase diagram (Fig. 3) suggests that a relatively long range hydrophobic interaction is a further prerequisite for the stability of bilayer membranes. Actually, experimental investigations suggest that the range of this interaction is relatively large [26], its decay length is estimated to be about 1 nm. The very simple pair potentials for the hydrophobic and hydrophilic beads of the model are sufficient to account for the essential driving forces that lead to the formation of membranes and vesicles.

The macroscopic elastic bend modulus of self-assembled bilayer membranes can be adjusted to experimental data by a proper choice of the ratio ε/kT, where ε is defined by Eq. (1). Apart from shape fluctuations, the coarse-grained model should also be suitable to study more subtle topics of membrane

physics, as long as specific material properties of lipid species can be disregarded. The bead model with only two essential physical parameters should be reasonable to elucidate some general properties of bilayer membranes accompanied by cooperative phenomena. Examples for such phenomena are demixing in mixed membranes, fluctuations, long range elastic interactions, and budding.

3. Particular Physical Effects Resulting from Fluidity, Elasticity, and Concentration Fluctuations of Mixed Membranes

Compared to solid substrates, there are many possibilities for bilayer membranes to respond to external disturbances. For example, the lipids may easily be rearranged in the membrane plane as in a two-dimensional liquid. On the other hand, the membrane behaves as an elastic sheet if forces bend the bilayer midplane. Furthermore, although membranes withstand compression forces to some extend, the effective compression modulus of the soft bilayer is not very high, and thus adsorbed or embedded proteins can locally change the bilayer thickness. It is generally appreciated that lipid membranes have a distinct effect on the interaction and arrangement of membrane associated peptides and proteins [8].

Various models for membrane-mediated interactions have been proposed. In particular, there are many basically simple physical theories that account for mechanisms of membrane-mediated attractive or repulsive forces between embedded and transmembrane proteins. However, most analytically solvable models are restricted to linearized equations, which do not allow reliable conclusions on the strength and importance of membrane-mediated effects. Additional difficulties appear, if reasonable boundary conditions of higher order differential equations, which are typically for the elasticity theory of membranes, cannot be imposed unambiguously. Nevertheless, solvable models based on linearized equations are necessary to outline the essential physics. In this case, Monte Carlo simulations can help to estimate whether basic physical concepts are justified. Unfortunately, there are only a few simulations which are suitable for testing analytical theories describing membrane-mediated interactions. In this section, we display some theoretical approaches and compare them with simulations provided that they are available.

3.1. Enhanced Adsorption of Peptides and Membrane-Mediated Force

Adsorption of proteins and peptides onto lipid membranes is an ubiquitous phenomenon in cell biology. Usually, native bilayers contain a large variety of anionic, neutral, and zwitterionic lipids. Apart from other interaction

forces, peripheral polypeptides and proteins are often bound to lipid membranes by screened electrostatic attraction forces [43]. In many cases, adsorption equilibria, for example, when peptides such as antimicrobials adsorb on bacteria cells, have biological relevance [44]. There is experimental evidence that the adsorption of peptides causes redistributions of lipid compounds in mixed membranes [3,45,46]. Compounds which lower peptide-lipid interaction energy migrate toward the region where the peptides touch the membrane surface, whereas other compounds move away from this region (Fig. 7).

Although this migration increases somewhat the mixing entropy, the change of adsorption energy is more relevant. Thus, the redistribution of the lipid compounds reduces the total free energy of the combined system consisting of the bilayer and adsorbed peptides. Consequently, the adsorbate density is higher than the adsorbate density for a frozen membrane without lipid migration. If the lipid mixture is nonideal, the domains of the favored lipids may be even considerably larger than the cross-sectional areas of peptides. In this case, a halo of preferred lipids is stable around each adsorbed peptide. A sufficiently dense adsorbate may even cause a macroscopic

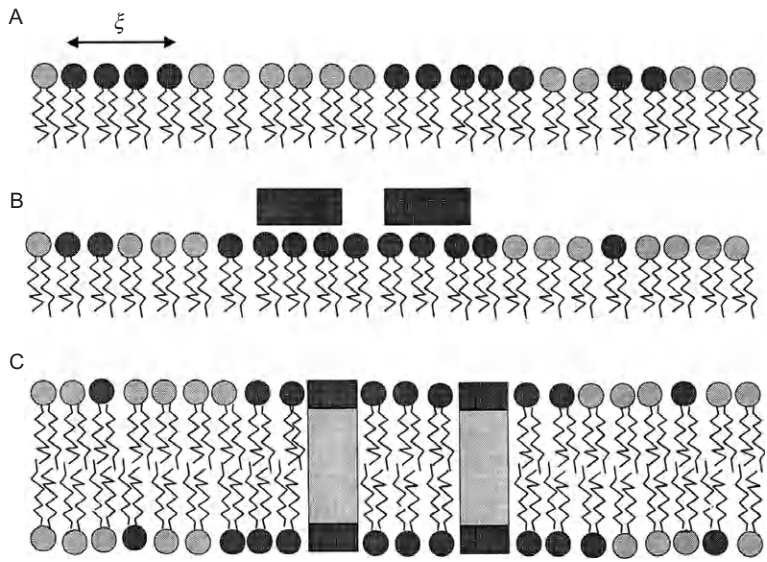

Figure 7 Rearrangements of the lipid molecules take place if the polypeptides have different affinities to the lipid components (after Fig. 1 in [45]). (A) Lipid mixture with spontaneous thermal concentration fluctuations characterized by a correlation length ξ. Adsorbed polypeptides (B) and inclusions (C) can enforce a partial demixing into domains with different lipid composition and substrate densities. (adapted from Ref. [47]).

demixing, which leads to rather large lipid domains. Domain formation is also facilitated by membrane-mediated attraction forces acting between adsorbed peptides. A peculiar membrane-mediated attraction force, which results from lipid redistributions, adds to the direct peptide–peptide interaction. If the halos or domains with enlarged concentration of preferred lipids around two adjacent peptides or proteins overlap, the free energy is smaller than the sum of the free energies of two separate domains [47,48]. This free energy reduction is accompanied by a membrane-mediated attractive force between adsorbate molecules, which supports the aggregation of peptides.

In lipid mixtures imperfect behavior is frequently observed, especially if mixtures contain cholesterol [7,8]. Imperfect mixing of lipids may result from differences in the interaction strength of lipid head groups or from an incompatibility due to different lengths of the hydrocarbon chains. In most cases, a decay into macroscopic lipid domains with different composition of lipid compounds is not observed. However, concentration fluctuations amplified by imperfect mixing are associated with the permanent formation and decay of small temporary domains. The size of these temporary domains can be estimated by a coherence length ξ for concentration fluctuations. For an ideal mixture, the length ξ is not larger than a cross-sectional radius of a lipid molecule, whereas in the nonideal case ξ can be rather large or even diverge close to the spinodal or the critical demixing point. In classical thermodynamics, imperfect mixtures are frequently described by the regular solution model [49]. The free energy of a homogeneous regular solution is written as

$$F_{\mathrm{m}} = MkT[X_{\mathrm{A}} \ln(X_{\mathrm{A}}) + X_{\mathrm{B}} \ln(X_{\mathrm{B}})] - \frac{1}{2} MwzX_{\mathrm{A}}X_{\mathrm{B}}, \tag{9}$$

where $X_{\mathrm{A}} = M_{\mathrm{A}}/M$ and $X_{\mathrm{B}} = M_{\mathrm{B}}/M$ are the particle number fractions of a binary mixture consisting of $M = M_{\mathrm{A}} + M_{\mathrm{B}}$ lipids, $z = 6$ is the number of the nearest neighbors of a lipid molecule, and energy parameter w accounts for nonideal mixing. In simple molecular statistical lattice models for mixtures, w is evaluated by $w = \varepsilon_{\mathrm{AA}} + \varepsilon_{\mathrm{BB}} - 2\varepsilon_{\mathrm{AB}}$, where ε_{ij} denotes the mean interaction energy between lipid species i and j (i, $j = A$, B). Spatial concentration fluctuations are taken into account by introducing local particle number densities $\rho_{\mathrm{A}}(x)$ and $\rho_{\mathrm{B}}(x)$, which may depend on the coordinates x defined for the membrane plane. For a homogeneous membrane, these number densities can be expressed as $\rho_{\mathrm{A}}^{0} = M_{\mathrm{A}}/S$ and $\rho_{\mathrm{B}}^{0} = M_{\mathrm{B}}/S$, where S denotes the membrane area. If fluctuations of the total lipid density $\rho = \rho_{\mathrm{A}}(x) + \rho_{\mathrm{B}}(x)$ are neglected, the concentration field $\psi(x) = \rho_{\mathrm{B}}(x) - \rho_{\mathrm{B}}^{0} = \rho_{\mathrm{A}}(x) - \rho_{\mathrm{A}}^{0}$ characterizes local deviations from the equilibrium surface density. Fluctuations should rise the free energy of the membrane. According to the linearized version of the Cahn–Hilliard

theory, the increase of the free energy due to concentration fluctuations is expressed as [50]

$$\hat{H}_{\mathrm{m}}[\psi] = \frac{1}{2}\int_S \left[A(\nabla\psi(x))^2 + B\psi^2(x)\right] d^2x, \tag{10}$$

where the coefficients $A > 0$ and $B > 0$ do not depend on the coordinate x, and the integration region S is extended over the whole membrane plane. Particle number preservation leads to the condition

$$\int_S \psi(x) d^2x = 0. \tag{11}$$

Coefficient B is obtained from an expansion of Eq. (9):

$$B = \left(\frac{1}{X_{\mathrm{A}}X_{\mathrm{B}}} - \frac{wz}{kT}\right)\frac{kT}{\rho} \tag{12}$$

It can easily be shown that the relation $\xi = \sqrt{A/B}$ defines the correlation length of spontaneous thermal concentration fluctuations. In the vicinity of the spinodal or the critical point of demixing, coefficient B tends to zero. Then the correlation length ξ diverges, whereas coefficient A remains regular. Hence, as a reasonable approximation, the product $B\xi^2 = A$ can be considered as constant. Sufficiently far away from the spinodal, the lipid mixture should be nearly ideal, the correlation length is short ranged, and coefficient B is approximated by its value for an ideal mixture $B_{\mathrm{id}} = kT/(\rho X_{\mathrm{A}}X_{\mathrm{B}})$. Hence, coefficient A can be estimated as $A = \xi_0^2 kT/(\rho X_{\mathrm{A}}X_{\mathrm{B}})$, where the correlation length ξ_0 for an ideal mixture should be comparable with the cross-sectional radius of a lipid molecule ($\xi_0 \simeq 0.3$ nm). Apart from spontaneous thermal fluctuations, the homogeneity of the membrane mixture is disturbed by adsorbed polypeptides. Let ε_{A} and ε_{B} be the adsorption energies which refer to a protein bound to membranes consisting of the pure lipid components A and B, respectively. Assuming short-range interactions between molecules, the protein–lipid coupling is restricted to the lipids which are in direct contact with the adsorbed peptide. Each adsorbed protein is assumed to cover a circular membrane region with area $s_{\mathrm{p}} = \pi R^2$ (R, protein radius) which contains $n = \rho s_{\mathrm{p}}$ lipid molecules.Thus, the free energy, supplemented with a lipid–protein coupling term, can be written as [47,51]

$$\hat{H}_{\mathrm{mp}}[\psi] = \hat{H}_{\mathrm{m}}[\psi] + N\varepsilon_{\mathrm{X}} + \frac{\varepsilon_{\mathrm{B}} - \varepsilon_{\mathrm{A}}}{n}\sum_{i=1}^{N}\int_{s_{\mathrm{p}}(i)} \psi(x) d^2x, \tag{13}$$

where $\varepsilon_X = X_A\varepsilon_A + X_B\varepsilon_B < 0$ defines the mean adsorption energy of a protein for a bilayer with randomly distributed lipid compounds. The last term in Eq. (13) accounts for local fluctuations of the concentration produced by the proteins. $s_p(i)$ is the area of the membrane surface patch, where the interaction energy between peptide i ($i = 1, 2, \ldots, N$) and the membrane lipids is nonzero. This region can be identified with the cross-sectional area of a peptide. However, it should be taken into account that the number of lipid molecules is fixed for each mixture component. This restriction leads to a Lagrange multiplier λ associated to condition (11). Hence, the corresponding modified Hamiltonian may be expressed as

$$\hat{H}[\psi] = \hat{H}_{\mathrm{mp}}[\psi] - \lambda \int_S \psi(x) d^2x. \tag{14}$$

Finally, the change of the free energy of the combined substrate–adsorbate system due to lipid redistribution is expressed in terms of the canonical partition function

$$F - F_0 = -kT \ln \int D\psi \exp\left(-\frac{\hat{H}[\psi]}{kT}\right). \tag{15}$$

The functional integration can be done in a simple way, since $\hat{H}[\psi]$ contains only linear and quadratic terms of ψ [52]. The neglect of cubic and higher order terms in the expansion of $\hat{H}[\psi]$ is a disadvantage of the theoretical approach, since large amplitude fluctuations cannot be described. This disadvantage is avoided in recent papers [48,53], which use the complete nonlinear mixing entropy. However, the free energy contributions of domain walls that are formed in the vicinity of adsorbed peptides have been introduced rather intuitively, so that a comparison with simulated data seems to be impossible.

3.1.1. Frozen membranes

From a general point of view, it is interesting to elucidate how the adsorption on a membrane surface is amplified due to the mobility of the lipid compounds. For this purpose, we first consider the adsorption on a membrane with immobile lipids ($\psi(x) = 0$), for example, if the temperature of the bilayer is well below the main transition temperature. Furthermore, let us first consider the Henry regime, where the adsorbate density is low and the interaction between adsorbate molecules is negligibly small. In this case, the surface density of adsorbed peptides $\Gamma = N/S$ is proportional to the concentration c of the peptides in the aqueous solution and we obtain the Boltzmann distribution [51]

$$\frac{\Gamma}{\Gamma_0(T)} = \frac{c}{c_0(T)} \exp\left(-\frac{\varepsilon_X}{kT}\right), \tag{16}$$

where Γ_0 (T) and c_0 (T) are temperature functions.

3.1.2. Adsorption on liquid bilayers consisting of an ideal mixture: Redistribution of lipid components

In the next step, the redistribution of the lipid mixture is considered additionally. For an ideal mixture, both the correlation length ξ of concentration fluctuations and the coefficient A are small ($A \to 0$, $\xi \to 0$ with $B = \mathrm{A}\xi^{-2}$), and coefficient B is defined by the relation $B = (X_\mathrm{A} X_\mathrm{B} p)^{-1} kT$. In the Henry regime of adsorption, the spatial nonhomogenous concentration distribution, which is taken into account by free energy Eq. (15), leads to a modification of Eq. (16). The lipid redistribution due to the lipid–protein interaction produces an amplification of the adsorption, and Eq. (16) is replaced by

$$\frac{\Gamma}{\Gamma_0(T)} = \frac{c}{c_0(T)} \gamma_\mathrm{a} \exp\left(-\frac{\varepsilon_\mathrm{X}}{kT}\right), \tag{17}$$

where the amplification factor γ_a has the representation

$$\gamma_\mathrm{a} = \exp\left[\frac{n X_\mathrm{a} X_\mathrm{b}}{2(kT)^2}\left(\frac{\varepsilon_\mathrm{B} - \varepsilon_\mathrm{A}}{n}\right)^2\right]. \tag{18}$$

If the adsorption energy per lipid–protein contact $(\varepsilon_\mathrm{B} - \varepsilon_\mathrm{A})/n$ is about kT and if $X_\mathrm{A} = X_\mathrm{B} = 0.5$, the amplification factor for adsorption turns out to be remarkably large, for example, $\gamma_\mathrm{a} \simeq 6.5$ for $n \simeq 15$ and $\gamma_\mathrm{a} \simeq 12$ for $n \simeq 20$. At large peptide concentrations, beyond the Henry regime, the bilayer membrane does not contain enough lipids of the components which are attracted from the adsorbed peptides. Furthermore, the excluded volume interaction between adsorbate molecules restricts their surface density. This interaction may be taken into account by assuming that the adsorbed peptides form a hard disk fluid on the bilayer surface. The relation $\theta = \Gamma \pi R^2$ defines a surface density that corresponds to the fraction of the bilayer membrane surface covered with peptides. The free energy F_0 in Eq. (15) is equal to the free energy of the substrate without considering membrane-mediated interactions. For simplicity, the adsorbate can be modeled as hard disk fluid. In this case, an appropriate expression for $F_0 = Nf_\mathrm{P}$ (T, θ) can be derived from scaled particle theory [51]. Then Eq. (15) yields

$$F = N\varepsilon_\mathrm{X} - N(1-\theta)\ln\gamma_\mathrm{a} + Nf_\mathrm{P}(T,\theta) \tag{19}$$

for the free energy of the combined system that comprises the bilayer membrane and the adsorbate. Obviously, an amplification of adsorption due to concentration fluctuations disappears if the membrane surface is completely covered with peptides ($\theta = 1$), since preferred places toward that lipids can migrate are lacking. The equilibrium between the peptides solved in water and peptides adsorbed on the bilayer surface is evaluated by equating the corresponding chemical potentials $\mu_p^w = kT \ln(c/c_0(T))$ and $\mu_p^a = \partial F/\partial N$. Figure 8 depicts the resulting adsorption isotherm for a relatively low adsorption energy [51]. Even in this case, there is a substantial increase of the adsorbate density in comparison to a frozen membrane without lipid migration.

3.1.3. Nonideal mixtures of membrane lipids: Concentration fluctuations, enhanced adsorption, and membrane-mediated interaction

For the general case of a nonideal lipid mixture, only a few theoretical results are known. Membranes containing cholesterol frequently behave like a nonideal mixture with a tendency toward demixing. If the mixture of the lipid bilayer is nonideal, spatial correlations of concentration fluctuations can further enhance the adsorption of peptides. An increased coherence length ξ produces small regions or temporary islands where lipid concentrations may considerably deviate from average values. Peptides can easier

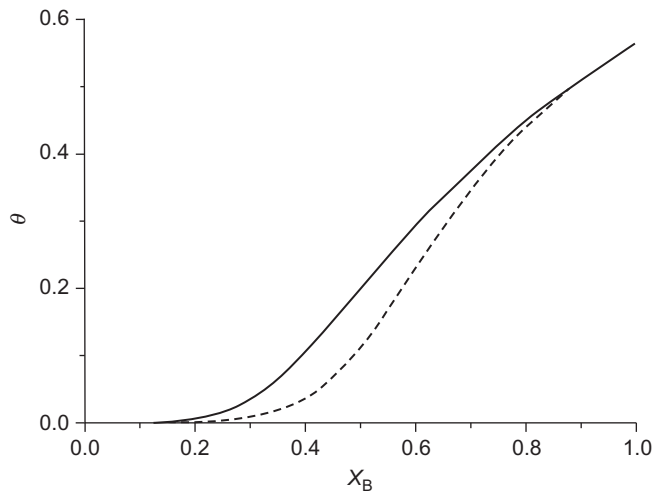

Figure 8 Plot of the polypeptide surface density θ versus the particle number fraction X_B of the lipid mixture. The continuous curve is evaluated for a fluid substrate assuming that $\varepsilon_A = 0$, $\varepsilon_B = -nkT$, $n = 15$ ($n = \rho\pi R^2$) [51]. For a frozen substrate with fixed lipid molecules the surface density (dashed curve) is lower. (adapted from Ref. [51]).

adsorb on those islands which contain favored lipids that cause the largest free energy reduction of the lipid–peptide system. Hence, spontaneous concentration fluctuations facilitate the migration and accumulation of favored lipid components in small domains around the peptides. In the Henry regime of adsorption, where enough favored lipids for a migration are available, the amplification factor γ_a should be larger than the value obtained from Eq. (18) for an ideal mixture. Utilizing free energy Eq. (15), a straightforward evaluation leads to

$$\gamma_a = \exp\left[\frac{1}{AkT}\left(\frac{\varepsilon_B - \varepsilon_A}{n}\right)^2 \xi^4 J(R/\xi)\right]. \tag{20}$$

where

$$J(R/\xi) = 2\pi \int_0^{R/\xi} \left[K_1(x)x - K_1\left(\frac{R}{\xi}\right)\frac{R}{\xi}\right] I_0(x)x\mathrm{d}x$$

is expressed in terms of the modified Bessel functions $I_0(x)$ and $K_1(x)$ [54]. Equation (20) implies that the amplification factor γ_a strongly increases with increasing coherence length ξ. Taking into account the relation $n = \rho\pi R^2$, γ_a [Eq. (20)] is expressed as a function of the reduced correlation length ξ/R:

$$\gamma_a(\xi/R) = \exp\left[\frac{(\varepsilon_B - \varepsilon_A)^2}{\pi^2 A\rho^2 kT}\left(\frac{\xi}{R}\right)^4 J(R/\xi)\right]. \tag{21}$$

Figure 9 illustrates the dependence of γ_a on the ratio ξ/R [55]. There is a considerable amplification of adsorption, even if the adsorption energies per lipid–protein contact $(\varepsilon_B - \varepsilon_A)/n$ have moderate values. If the condition for the Henry regime ($\theta \ll 1$) is violated, the amplification should be less effective.

On the other hand, when the mean distances between adsorbed peptides become shorter at higher adsorbate densities, another effect that influences adsorption isotherms appears. The halos with enlarged concentration of preferred lipid components around adsorbed peptides overlap and cause a membrane-mediated attraction force. The potential of this force can be written as

$$u(r_{12}) = -2\pi\left(\frac{\varepsilon_B - \varepsilon_A}{n}\right)^2 \frac{\xi^2 R^2}{A}\left(I_1\left(\frac{R}{\xi}\right)\right)^2 K_0\left(\frac{r_{12}}{\xi}\right), \tag{22}$$

where r_{12} is the distance between the gravity centre of two peptides with circular cross-sections, and $I_1(R/\xi)$, $K_0(r_{12}/\xi)$ are modified Bessel functions

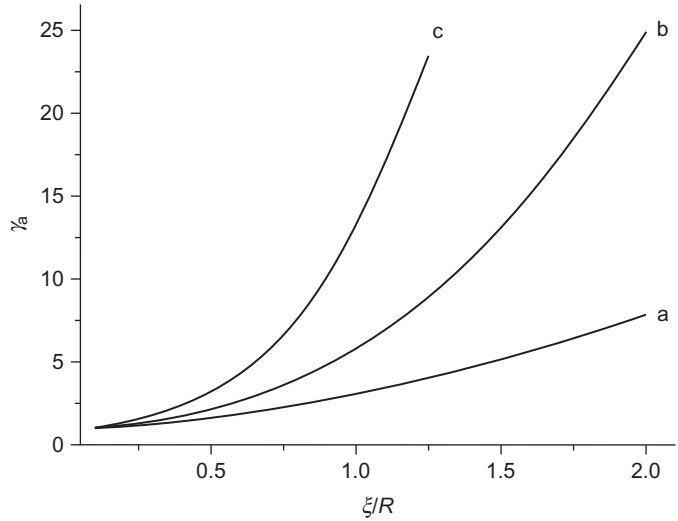

Figure 9 Amplification factor γ_a for the adsorption versus reduced correlation length ξ/R of spontaneous concentration fluctuations for (A) $|\varepsilon_A - \varepsilon_B|/n = 0.2kT$, (B) $|\varepsilon_A - \varepsilon_B|/n = 0.25kT$, (C) $|\varepsilon_A - \varepsilon_B|/n = 0.3kT$, $n = 20$, $\rho = 2$ nm^{-2} and $X_A - X_B = 0.5$. (adapted from Ref. [55]).

[54]. Except for the prefactor, Eq. (22) is formally equivalent to a pair potential derived for elastic membrane-mediated interactions [56]. In the special case, when the peptide radius R is distinctly larger than the interaction range ($R \gg \xi$), an expansion of Eq. (22) yields

$$u(H) = -\frac{1}{2}\left(\frac{\varepsilon_B - \varepsilon_A}{n}\right)^2 \frac{\xi^4}{A}\sqrt{\frac{\pi R}{\xi}}\exp\left(-\frac{H}{\xi}\right), \tag{23}$$

where $H = r_{12} - 2R$ is the gap between two adjacent peptides. This simple result can also be obtained by using Derjaguin's approximation [47,51]. Let us evaluate the interaction energy for two peptides in contact ($H = 0$). If we assume $|\varepsilon_B - \varepsilon_A|/n = 0.5kT$, $\xi = 1$ nm, $R = 3$ nm and $A = 0.74 \times 10^{-12}$ N nm^5 (Table 1), the value of $|u(H = 0)|$ is approximately equal to $2kT$. However, the pair potentials Eq. (22) and Eq. (23) strongly increase with increasing coherence length ξ, and thus the strength of the interaction could be substantially larger.

Recently, Reynwar and Deserno [57] studied composition-mediated interactions between proteins adsorbed onto a two-component liquid bilayer using molecular dynamics (MD) simulations. Lipids have been built up of three-segment molecules with one hydrophilic bead and two hydrophobic beads [17]. The nonideal behavior of the lipid mixture results

Table 1 Parameter values for estimations of membrane-mediated interactions

Symbol	Meaning	Values for estimations
R	Cross-sectional radius of a polypeptide	$1 - 5$ nm
ρ	Surface density of the lipids in a membrane	$2\ \mathrm{nm}^{-2}$
B	Coefficient in Eq. (10) for $X_A = X_B = 0.5$	$(0.0 - 4)\ \rho^{-1}\ kT$
ξ	Correlation length of concentration fluctuations	$0.3 - 10$ nm ($\xi = (A/B)^{1/2}$)
A	Coefficient in Eq. (10) for $X_A = X_B = 0.5$	$A = B_{id}\xi_0^2 \simeq 0.74 \times 10^{-12}$ Nn m^5
n	Number of protein–lipid contact sites	$n = \rho s_P$ with $s_P = \pi R^2$
$\varepsilon_B - \varepsilon_A$	Difference between adsorption energies	$\lvert\varepsilon_B - \varepsilon_A\rvert \simeq (0.2 - 2) \times n \times kT$
kT	Thermal energy (for $T \simeq 300\ K$)	4.1×10^{-12} N nm
K	Splay-distortion modulus	2×10^{-10} N nm
B_m	Compression modulus	3×10^{-11} N nm^{-3}
ξ_m	Length scale for elastic deformations	$1 - 4$ nm [$\xi_m = (K/B_m)^{1/4}$]

from choosing different interaction ranges for the hydrophobic beads of the components. The plate-like proteins were assumed to adsorb onto the membrane by binding preferentially to one of the two lipid species of the binary membrane mixture. In accordance with Eq. (22), the membrane-mediated interaction energy between two proteins increases with increasing coherence length ξ. In a region not far away from the critical demixing point, the minimum value of this attractive pair potential has been found to be $-4kT$. A shallow minimum of the pair potential, which may result from the depletion force between the protein models, was detected even for an ideal mixture [57].

3.2. Attraction Force Between Transmembrane Proteins in Mixed Membranes

A simple intuitive model of membrane spanning proteins (inclusions) consists of a hydrophobic cylinder which is terminated by two hydrophilic caps on both cylinder faces. If the length of the hydrophobic part matches with the hydrophobic region of the bilayer membrane, the proteins span the whole bilayer membrane. The hydrophilic end caps of transmembrane

proteins may have different affinities to the components of the lipid mixture. In a way similar to the case of peripheral proteins, the resulting redistribution of the lipid mixture may cause a membrane-mediated attraction force. This attraction can be estimated by minimizing free energy Eq. (10). For simplicity, let us neglect the balance Eq. (11), which would be important if the proteins were densely distributed in the bilayer membrane. Thus, we arrive at the Helmholtz equation $A\Delta\psi - B\psi = 0$ with the boundary condition $\psi(R) = \psi_0$ on the circular rim of a protein. Even in the simple case of two proteins with fixed distance r_{12}, an exact analytical formula for the pair interaction potential does not exist. However, in some cases simple approximations are possible. If the coherence length ξ of concentration fluctuations is large ($\xi \gg r_{12}$, R) close to the critical demixing point or the spinodal, the pair potential of the protein–protein attraction is [58]

$$u(r_{12}) = -\frac{2\pi A_\rho^2 (\Delta X)^2}{[\ln(R/\xi)]^2}\sqrt{\frac{\pi\xi}{2r_{12}}}\exp(-r_{12}/\xi), \tag{24}$$

where $\Delta X = \psi_0/\rho$ denotes the difference between the particle number fractions at the rim and far away from a protein. If the coherence length ξ is shorter than the protein radius R, Derjaguin's approximation leads to [58]

$$u(H) = -4A\rho^2(\Delta X)^2\sqrt{\frac{R}{\xi}}\int_0^\infty dq\,\frac{\exp\left(-H\xi^{-1} - q^2\right)}{1 + \exp\left(-H\xi^{-1} - q^2\right)}, \tag{25}$$

where H again denotes the gap between adjacent proteins. If they are in touch ($H = 0$), Eq. (25) can be simplified to

$$u(H = 0) \simeq -2A\rho^2(\Delta X)^2\sqrt{R/\xi}. \tag{26}$$

Equation (25) predicts a roughly exponential decay of the interaction potential with a decay length somewhat different from ξ. Assuming $(\Delta X)^2 = 0.1$ and using data listed in Table 1, we arrive at $u(H = 0)/kT \simeq -\sqrt{R/\xi}$ for two inclusions in contact. If $R = 4$ nm and $\xi = 1$ nm, the interaction energy $|u(H = 0)| = 2kT$ results.

Using MC simulations, Wahab *et al.* [58] studied the interaction between inclusions embedded in a bilayer membrane consisting of an 1:1 mixture. Figure 10 illustrates the models for the liquid components and the proteins. In Fig. 11, a start and an equilibrium configuration of the amphiphiles in the simulation box are shown. The redistribution of the lipid components in bilayer membranes is caused by different interaction energies between the lipid heads and the hydrophilic protein caps. Concentration

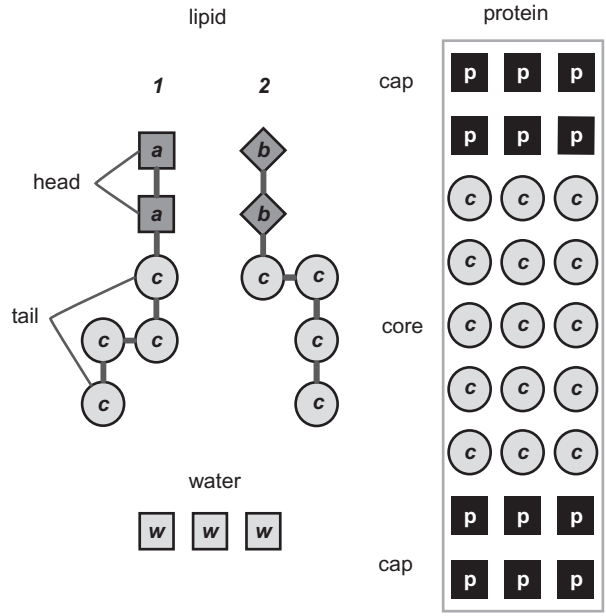

Figure 10 Structure of the lipid species and front view of the protein model. The symbol *w* refers to an unoccupied lattice site which is considered as a water molecule. (adapted from Ref. [58]).

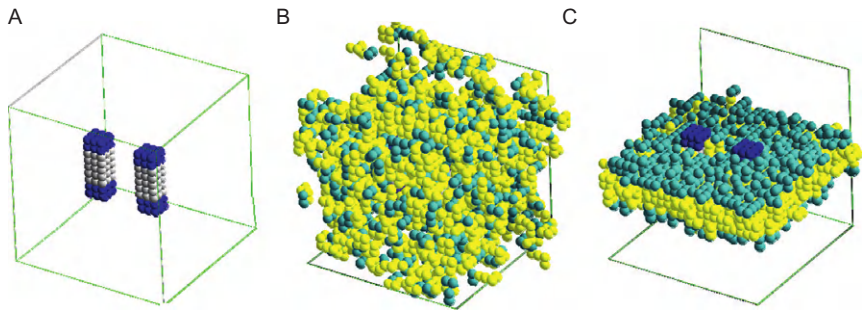

Figure 11 View into the simulation box. (A) Two protein models, which are fixed in each simulation run, are inserted into the lattice. (B) Disordered start configuration. (C) After 10^7 Monte Carlo steps the equilibrium configuration is a bilayer arranged around the protein models. (adapted from Ref. [58]).

profiles for several distances H between the inclusions are illustrated in Fig. 12. In a surprisingly large membrane region around the inclusion, remarkable disturbances of the concentration distribution have been found. This effect is accompanied by an attraction force between the inclusions. We suggest that the protein–protein attraction is further

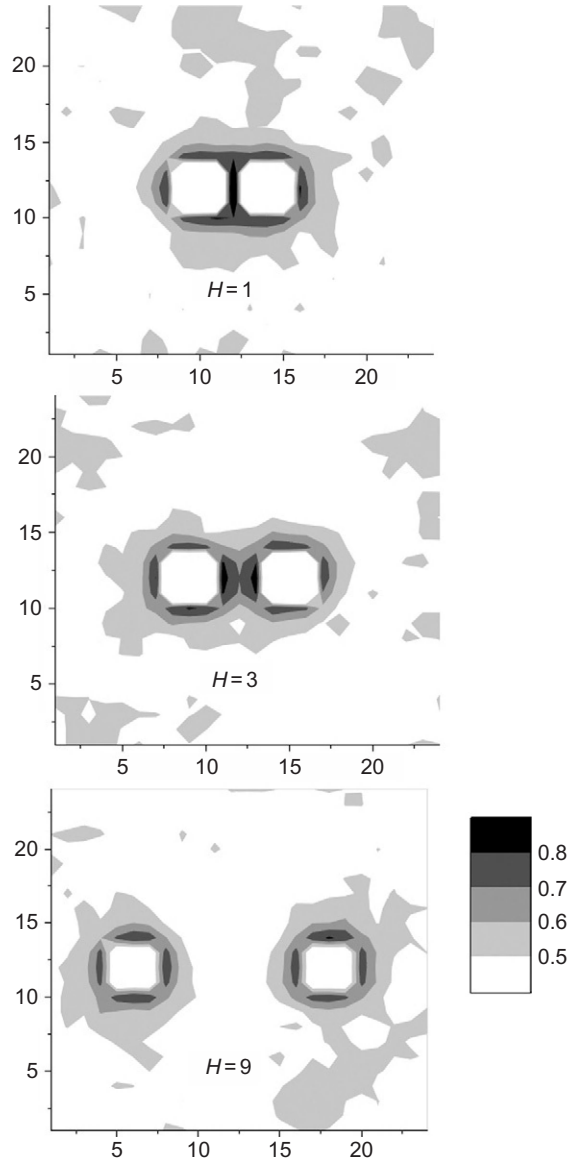

Figure 12 Concentration distribution (X_A) of a lipid component in the simulation box for different gaps between the proteins. (adapted from Ref. [58]).

enhanced by elastic membrane-mediated forces, since a thickness difference between the hydrophobic bilayer region and the hydrophobic part of the inclusions produces elastic distortions.

A direct comparison of analytical expressions for the pair potential of inclusions and simulated data was not possible, as the simulation of the lattice model did not allow to evaluate the entropic contribution to membrane-mediated interactions [58]. Energy differences between configurations with different protein–protein distance were found to be relatively large ($\sim 15kT$). However, due to the entropic contribution, the variation of the effective pair potential should be considerably smaller than $15kT$.

3.3. Elastic Deformations and Membrane-Mediated Interactions

Apart from lipid sorting, elastic deformations are also supposed to contribute to the interaction of membrane associated particles. Adsorbed peripheral proteins can produce a curvature of an originally flat bilayer membrane. The same effect is caused by membrane spanning proteins if they have not a cylindrical but a conical shape. Since there is no length scale for bending deformations, the corresponding indirect forces between membrane associated particles are long range [22,59]. A theoretical description of this interaction and other membrane induced forces has been reviewed by Goulian [21].

The bending mode of membrane deformations is suppressed, when the membrane rests on a plane solid support. Furthermore, if adsorbed molecules locally reduce or increase the bilayer thickness, resulting elastic distortions heal out over distances not longer than a few nanometers. In these cases, the decay length of elastic deformations is approximately equal to the bilayer thickness. For example, small adsorbed amphiphatic peptides, which are known as antimicrobials, can locally reduce the membrane thickness [44,60]. If the distance between two adsorbed molecules is comparable to or smaller than the bilayer thickness, a membrane-mediated force arises between both particles. This relatively strong short-range force influences the lateral organization and can cause a phase transition from a low-density to an aggregated state, of the adsorbate. In the aggregated state, the biological activity of peptides could be enhanced. For example, aggregation of many antimicrobials promotes the formation of ion channels which kill bacteria [44]. Transmembrane proteins can also locally change the membrane thickness. A reasonable theoretical concept is based on the hydrophobic mismatch [20,61,62]. If the length of the hydrophobic protein part and the thickness of the alkyl chain region in the lipid bilayer are different, elastic deformations around the proteins are produced.

3.3.1. Membrane-mediated interactions based on curvature effects

If the bilayer midplane of a membrane becomes curved, the resulting increase of free energy can be evaluated by Eq. (2). Small deviations u from a flat membrane configuration are usually expressed in the Monge representation [63] of surfaces. In this case, the Eulerian equation related to the free energy Eq. (2), $\Delta\Delta u = 0$ for a tensionless membrane ($\gamma = 0$), has no intrinsic length scale. Hence, in this case membrane-mediated interactions should be long range. Goulian *et al.* [21,22] considered conical membrane inclusions. If the surface normals of two cones and the bilayer midplanes enclose a fixed contact angle α, where α is assumed to be small ($\alpha << 1$), the pair potential $u(r_{12}) = 8\pi\kappa\alpha^2R^4/r_{12}^4$ results for $r_{12} \gg R$ (R, cone radius at the membrane midplane). This potential is related to a repulsion force between inclusions. The theory has been extended by Weikl *et al.* [59] for describing membranes with a nonzero tension ($\gamma \neq 0$). In this case, the Eulerian equation can be written as $\Delta\Delta u = \xi_\gamma^{-2}\Delta u$, where $\xi_\gamma = \sqrt{\kappa/\gamma}$ is a decay length for elastic deformations. If $\xi_\gamma \neq 0$, the interaction energy $u(r_{12}) \propto \exp(-r_{12}/\xi_\gamma)$ decays roughly exponentially. The force between two inclusions depends on their mutual orientation. For parallel cones the force is repulsive, whereas cones with opposite orientations repel each other at short distances and attract at long distances. Averaged energies for the attractive forces have values not larger than kT. Hence, mechanisms associated with a bending of the bilayer midplane seem to be insufficient to explain aggregations of membrane bound proteins, at least for the initial stage, where the distances between proteins are long.

When the surface tension γ is nonzero, peripheral proteins should behave similarly as transmembrane proteins [56]. In the tensionless state $\gamma = 0$, the repulsion vanishes completely. However, in a special case, if two adjacent proteins touch each other, a nonzero attractive contact force appears between them. If $\gamma \neq 0$, a weak repulsion force between peripheral proteins appears. The range $\xi_\gamma = \sqrt{\kappa/\gamma}$ of the repulsion force is relatively large compared to direct protein–protein interactions. Short-range direct protein–protein attractive forces compete with the weak relatively long range membrane-mediated repulsion force. As a consequence of this competition, membrane bending peripheral proteins can aggregate into a stripe-like pattern at concentrations above a critical value [56,64]. Such periodic arrays of proteins have been observed experimentally on the cytoplasmic side of the caveolae membrane [65].

Although in most cases theoretical models predict a membrane-mediated repulsion, aggregation of proteins is an ubiquitous phenomenon. It is possible that qualitative theoretical results, which have been obtained from the analytical theory for small elastic deformations, are not valid for large membrane curvatures. Simulations could be helpful to clarify this point. Using a three-bead model for the lipids and the ESPResSo package

(MD), Reynwar *et al.* [66] have performed a simulation of a bilayer membrane decorated with many adhered peripheral proteins. They have found a transformation of the planar tensionless membrane into highly curved structures with pockets that contain clusters of the protein models. Furthermore, simulated data suggest that there exists an attractive force between adhered strong membrane deformers.

3.3.2. Forces resulting from bilayer thickness alterations

3.3.2.1. Adsorbed molecules Apart from a curvature of the bilayer midplane, membranes can also deform by changing their thickness (Fig. 13). This deformation is associated with relatively strong short-range forces. Local deviations from the equilibrium thickness heal out over distances comparable with the bilayer thickness. In supported bilayers, such elastic deformations may be relevant, since a plane support suppresses a curvature of the bilayer midplane. An adsorbed particle affects the bilayer membrane by imposing a force in the region where this particle touches the bilayer surface. Adsorbed peptides on bilayer membranes, which are not supported from below, can also locally change the membrane thickness [44,60]. When the elasticity theory is applied, such a local thickness change can be modeled as the response to a force that compresses or dilates the bilayer in a small region just below the adsorbed peptide. Hence, from a formal point of view, the theoretical descriptions of adsorbates on supported bilayer membranes and peptides which locally change the membrane thickness are quite similar.

For simplicity, we consider a fluid bilayer membrane which is supported from below by a firm solid plane. This geometry is often used in atomic force microscopy investigations [67]. Adsorbed small peptides such as antibiotics or antimicrobials have an effective radius comparable to or smaller than the membrane thickness. Experimental observations [44] revealed that these amphipathic peptides produce a local thickness reduction of lipid bilayers (Fig. 13A). In a small region around the adsorption region, the membrane is supposed to be a few tenth of a nanometer thinner than the average membrane thickness. In the framework of a theoretical model, this local thickness reduction can be produced by a normal force $Q(x)$ exerted onto the membrane in the region where the polypeptide touches the membrane interface. Then the deformation free energy reads [68]

$$F = \frac{1}{2}\int_S \left[K\left(\nabla^2 u\right)^2 + B_{\mathrm{m}} u^2 - Q(x)u\right] \mathrm{d}^2 x, \tag{27}$$

where u denotes the local thickness change of the membrane, B_{m} is the compressibility modulus and K is the splay-distortion modulus of the bilayer membrane. Some bilayer models [60] suggest a simple relation between the splay-distortion modulus K in Eq. (27) and the bending modulus κ defined

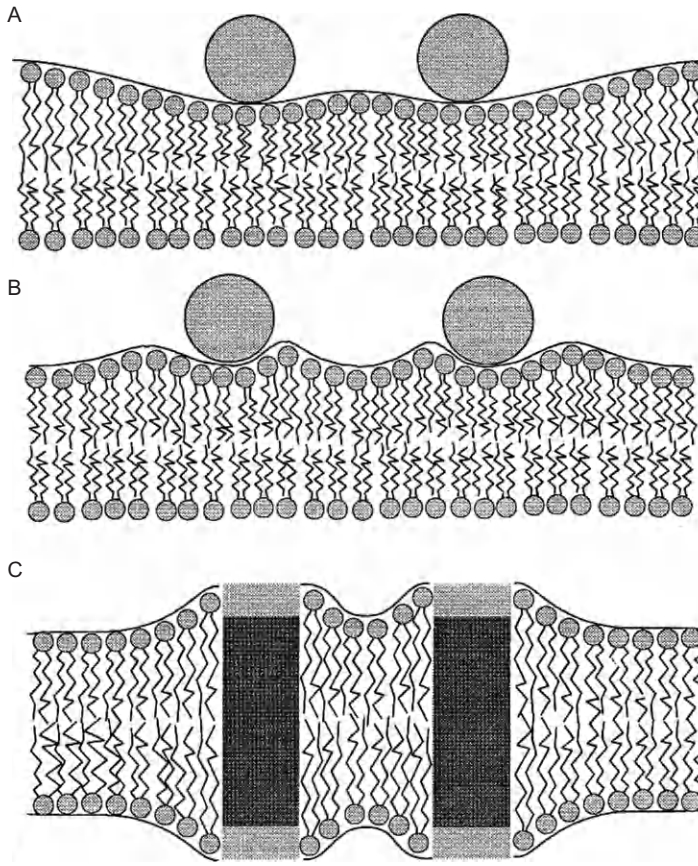

Figure 13 A polypeptide adsorbed on the membrane surface produces a depression if the adsorption force q_0 is nonzero (A). Otherwise, if $q_0 = 0$, the interface moulds around the particle without changing the average membrane thickness (B). Inclusions can produce elastic deformations if there is a mismatch between the hydrophobic protein region and alkyl chain region (C) of the lipid bilayers. (adapted from Ref. [47]).

by the Helfrich free energy [Eq. (8)]. From a macroscopic point of view, such a relation is not obvious, since a curvature of the bilayer midplane and the change of the bilayer thickness are completely different membrane deformations.

The relation $\xi_m = (K/B_m)^{1/4}$ defines a length scale, which is approximately equal to the decay length of elastic deformations. The value of ξ_m is comparable to the bilayer thickness, that is, a few nanometers. It should be mentioned that the more general case, where the surface tension is not negligible small and a term $-\gamma\ (\nabla u)^2$ arises in free energy Eq. (27), has also been considered [69]. Let the normal stress $Q(x)$ be exerted by two

circularly symmetric peptides with centers of gravity localized at the points x_1 and x_2. This stress can be written as $Q(x) = q(x - x_1) + q(x - x_2)$, where $q(x - x_i)$ is zero if the distance $|x - x_i|$ markedly exceeds the polypeptide radius R. Variation of the free energy [Eq. (27)] leads to the Eulerian equation $K\Delta\Delta u + B_m u = Q(x)$. The Green's function related to this equation is obtained from $K\Delta\Delta G(x - \bar{x}) + B_m G(x - \bar{x}) = \delta(x - \bar{x})$ ($\delta(x)$, Dirac's function) with the boundary conditions $G(x - \bar{x}) \to 0$ and $\partial_x G(x - \bar{x}) \to 0$ for $|x - \bar{x}| \to \infty$. A straightforward evaluation yields [69,70]

$$G(x - \bar{x}) = \frac{K_0(k_2|x - \bar{x}|) - K_0(k_1|x - \bar{x}|)}{2\pi K\left(k_2^2 - k_1^2\right)}, \tag{28}$$

where $k_1 = (1 + i)/(\sqrt{2}\xi_m)$ and $k_2 = (1 - i)/(\sqrt{2}\xi_m)$. The Green's function allows us to express the interaction potential attributed to the force between two adsorbed particles:

$$w(x_1, x_2) = -\int\int q(x - x_1)G(x - \bar{x})q(\bar{x} - x_2)\mathrm{d}^2x\,\mathrm{d}^2\bar{x}. \tag{29}$$

Assuming that the distance between the peptides $|x_1 - x_2| = r_{12}$ is not too short, a multipole expansion can be applied to Eq. (29). If the adsorption force $q_0 = \int q(s)\ \mathrm{d}^2s$ is nonzero, the leading term of the multipole expansion is [70]

$$w(r_{12}) = \frac{q_0^2}{2\pi B_m \xi_m^2}\mathrm{Im}K_0\left(\frac{\beta r_{12}}{\xi_m}\right), \tag{30}$$

where $\beta = (1 + \mathrm{i})/\sqrt{2}$. Except for long distances $r_{12} > 4\xi$, potential [Eq. (30)] is attributed to an attraction force. For $q_0 \neq 0$, the membrane interface has a depression around each adsorbed molecule. Assuming that the small particle exerts the normal stress $Q(x) = -q_0\delta(x)$ onto the membrane-water interface, the maximal bilayer thickness alteration just below an adsorbed convex particle can be expressed as $\mathrm{u}(0) = -q_0G(0)$ [69]. This equation allows us to estimate the effective adsorption force q_0 from measurements of the membrane thickness. X-ray measurements revealed that small antimicrobial peptides reduce the membrane thickness by a few tenth of a nanometer [44,60]. The value $-u\ (0) \simeq 0.2$ nm is consistent with the published experimental data for the average thickness reduction. Combining this value with reasonable values for the elastic material constants $K = 2 \times 10^{-10}$ N nm and $B_m = 3 \times 10^{-10}$ N nm^{-3} [69], the relations Eq. (28) and $\mathrm{u}(0) = -q_0G(0)$ yield the effective adsorption force

$q_0 = 10^{-10}$ N. Inserting this value for q_0 into Eq. (30) and assuming that $r_{12} = \xi_m$, we obtain the interaction energy $3kT$. From a theoretical point of view, it is possible that $q_0 = 0$ and $q_2 = \int s^2 q(s)\, d^2 s \neq 0$, if adsorbate particles mold around the membrane surface without changing the average thickness (Fig. 13B). Then a multipole expansion for the pair potential starts with [70]

$$w(r_{12}) = -\frac{q_2^2}{32\pi B_m \xi_m^6} \mathrm{Im} K_0\left(\frac{\beta r_{12}}{\xi_m}\right) \tag{31}$$

This pair potential is attributed to a repulsion force. However, the repulsion is expected to be rather weak for reasonable values of the second moment q_2 of the adsorption force. Apart from analytical approaches, simulations concerning the interaction between adsorbates on supported bilayer membranes or multilayer stacks of them do not seem to be available yet.

3.3.2.2. Inclusions Inclusions such as transmembrane proteins can strongly deform bilayer membranes (Fig. 13C). There are many theoretical studies focused on deformations which are accompanied by a thickness alteration of the membrane and the related membrane-mediated interactions between the inclusions [20,61,71,72]. Forces are applied to the bilayer, if the length of the hydrophobic part of a protein does not coincide with the thickness of the alkyl chain region of the membrane. Such a thickness mismatch produces a dilatation or a compression of the bilayer in a vicinity of the lipid–protein interface. The perturbation of the bilayer is described by the homogeneous differential equation $K\Delta\Delta u + B_m u = 0$ with appropriate boundary conditions for the protein–lipid boundary. This equation may be supplemented with a surface tension term $-\gamma\Delta u$, if γ is not negligibly small. Boundary conditions for a circularly symmetric inclusion with radius R can be formulated as $u(R) = u_0$ and $(\partial u/\partial r)_R = 0$, but there are many other possibilities [71]. Furthermore, a spontaneous curvature term in the free energy can strongly modify the results [20,72]. In this case, unambiguous predictions on membrane-mediated interactions between inclusions are more difficult. Frequently, reasonable boundary conditions lead to an attraction force between inclusions. The short-range attraction or repulsion forces decay exponentially with a decay length $\xi_m = (K/B_m)^{1/4}$, which is roughly a few nanometers. The magnitude of the interaction energy for two proteins in contact can exceed the mean thermal energy kT [20]. However, the ambiguity due to the unknown boundary conditions makes it difficult to draw final conclusions on the sign and the strength of the interaction potential. Computer simulations can be very helpful to select the appropriate variant of the elasticity theory. Brannigan and Brown [73,74] have

favored a model with two separate leaflets that form the bilayer membrane. Using this model, they evaluated membrane deformations produced around a single cylindrical protein with hydrophobic mismatch. The evaluated analytical result fitted well to MD simulation data for a coarse-grained model. However, the analytical approach was less successful to evaluate the pair potential for two inclusions. In this case, West *et al.* [75] found deviations between the analytical approach based on the model of Brannigan *et al.* [74] and MC simulation data for a coarse-grained model with lipids consisting of a sequence of beads. Further simulations are needed to clarify this point.

4. Models for Simulating More Complex Problems

Monte Carlo simulations can also be used to get some insight into particular aspects of more complex biologically relevant phenomena. As an example let us consider the digestion of lipids in vertebrates. An important step in the digestion mechanism is the transition of dietary membrane material into micelles in the gastrointestinal tract. This step is required for transferring the lipids into a phase state which is appropriate for further enzymatic degradation of lipid molecules during the metabolism [76]. The solubilization process is induced by particular detergents called bile salts which are able to solubilize membrane lipids including cholesterol and to form mixed bile-lipid micelles ready for further digestion [77]. Aside from their role in digestion, bile salts are used to modify the stability and resistance of vesicles used as drug carriers [78]. A huge amount of experimental data characterizing the interaction between liposomes and bile salts has been published. The solubilization mechanism can be divided into the following steps:

1. Adhesion of bile salts on the outer surface of the liposomes
2. Insertion of bile salts into the lipid membrane
3. Partition of bile salts in the membrane
4. Formation of mixed micelles

Physicochemical studies revealed the considerable role of kinetics in solubilization processes of model vesicles by bile salts [79]. After insertion of bile salts into the membrane, equilibrium states are reached relatively slowly. Depending on the rate of bile salt addition to the vesicle solution, different diffusion controlled thermodynamic and structural states can be obtained. In particular, inserted bile salts reduce the main transition temperature and, in this way, the lateral lipid diffusion is increased. For this reason, computer simulations of thermodynamic equilibrium structures as

well as kinetic relaxation effects for different steps involved in membrane solubilization are of special interest.

Based on experimental data for model systems, for example, isothermal titration calorimetry [80], turbidity measurement [79], dynamic light scattering [81,82], and cryo-transmission electron microscopy [83], a schematic phase diagram for the system lipid-bile salt (Fig. 14) has been proposed [24]. It is remarkable that several steps leading to vesicle solubilization are initiated at bile salt concentrations below the critical micelle concentration. The insertion of bile salts into the vesicle membrane and the formation of pure bile salt micelles are found to be competitive processes. For allowing both processes to happen, the chosen system size for computer simulation needs to be sufficiently large. For performing kinetic Monte Carlo simulations of the vesicle solubilization by bile salts the coarse-grained lipid model described in Section 2.1 must be extended [84]. The molecular topology of the lipid model has been refined for a better representation of double-chain lipids such as DPPC [85] (Fig. 15A) and an additional segment type (NEUT) [86] has been introduced as a linker between the head group and the hydrophobic chains in order to obtain a more realistic bilayer structure in our solvent-free model (Fig. 2B).

Furthermore, based on the cholesterol model from [87] (Fig. 15B), we have developed models for the bile salts sodium cholate and sodium deoxycholate (Fig. 15C and D). These models account for the typical structure of facial amphiphiles such as bile salts, which have a predominantly hydrophilic and a hydrophobic face instead of the head–tail-structure of double-chain lipids. The difference in the hydrophilicity of cholate and deoxycholate is taken into account by a different size of the hydrophilic segments connected to the steroid skeleton. The interaction potentials have the same form as

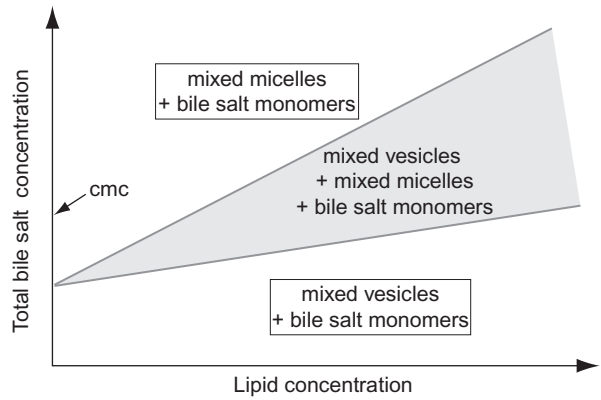

Figure 14 Schematic isothermal phase diagram of bile salt concentration versus lipid concentration. (adapted from Ref. [24]).

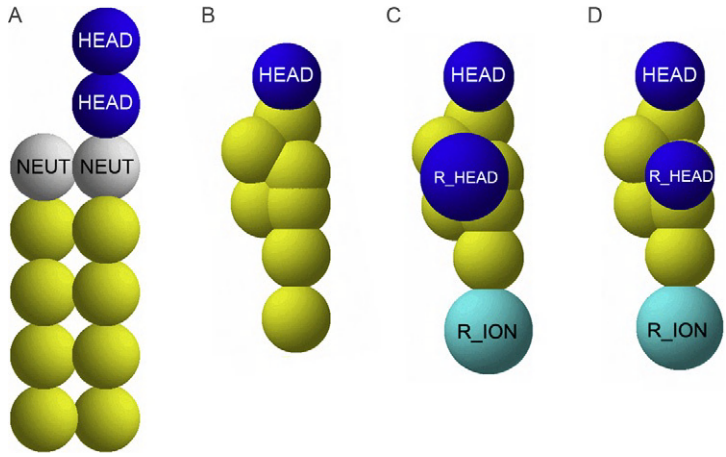

Figure 15 Coarse-grained models for (A) DPPC, (B) cholesterol, (C) sodium cholate, and (D) sodium deoxycholate.

described in Section 2.1. However, the chain flexibility is slightly restricted. The cubic simulation box has an edge length of 225σ, where σ is the diameter of one lipid tail segment.

In order to study the solubilization of liposomes, we used a preequilibrated vesicle containing 3650 DPPC molecules. The lipid concentration is roughly 5 mmol/l. After equilibration, sodium cholate molecules have been distributed randomly in the box outside the vesicle. The simulation steps only comprise physically possible movements such as small random molecular displacements, angle changes and cluster displacements. In this way, the number of Monte Carlo moves (MCS) corresponds to an arbitrary time scale.

During the first step, bile salt molecules adhere on the vesicle surface. The rate of this process increases with increasing bile salt concentration. This corresponds to the first nearly linear part of the curves in Fig. 16. The adhesion is followed by incorporation of cholate into the lipid membrane. The inserted cholate molecules induce restructuring of the membrane lipids. This process is indicated by the horizontal part of the graphs (Fig. 16). The structural change of the membrane culminates in pore formation which is accompanied by a further uptake of bile salts into the vesicle membrane. This uptake takes place predominantly at the rim of the pores. The formation of worm-like mixed micelles which contain cholate and DPPC already starts during the restructuring of the vesicle membrane at bile salt concentrations above the CMC. The mixed micelles detach from the vesicle which leads to a reduced DPPC content in the vesicle (Fig. 17). A snapshot of a vesicle with mixed worm-like micelles still connected with the vesicle is shown in Fig. 18. After complete detachment of worm-like

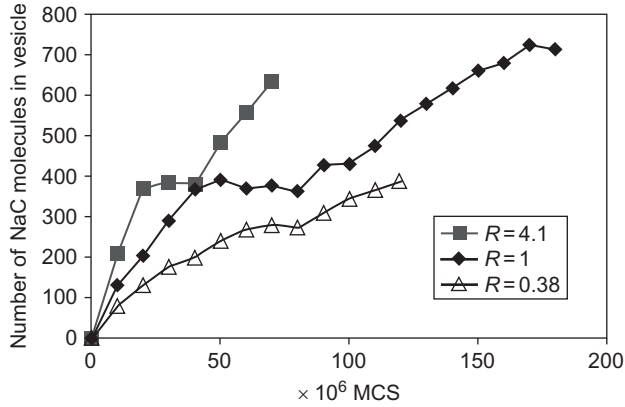

Figure 16 Number of membrane-bound bile salt molecules versus time in Monte Carlo Steps (MCS) at several bile salt (NaC) to lipid concentration ratios R.

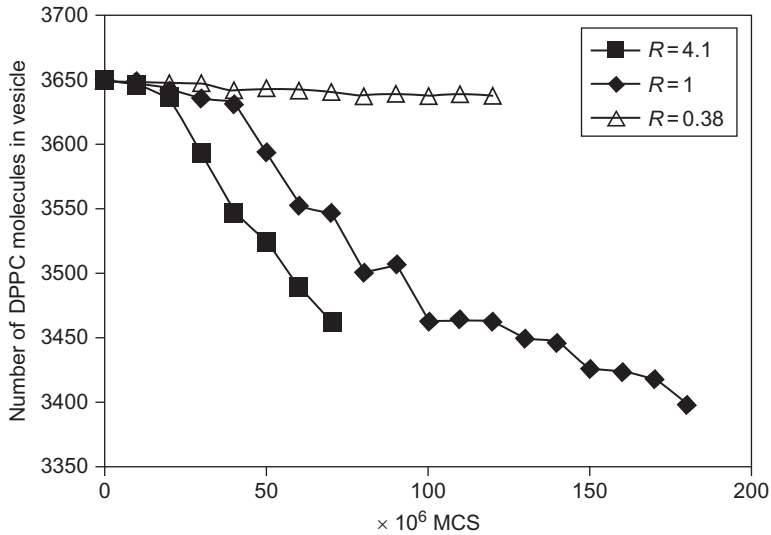

Figure 17 Number of DPPC molecules in the vesicle membrane versus time in Monte Carlo Steps (MCS) at several bile salt to lipid (DPPC) concentration ratios R.

mixed micelles, the vesicle with decreased DPPC content crumbles up and eventually collapses completely as it is shown in Fig. 19. In case of liposomes containing cholesterol, the solubilization requires a higher bile salt concentration, and the process occurs at considerably lower rate. Simulations confirm the experimental observation of cholesterol stabilizing the liposomes against solubilization by bile salts.

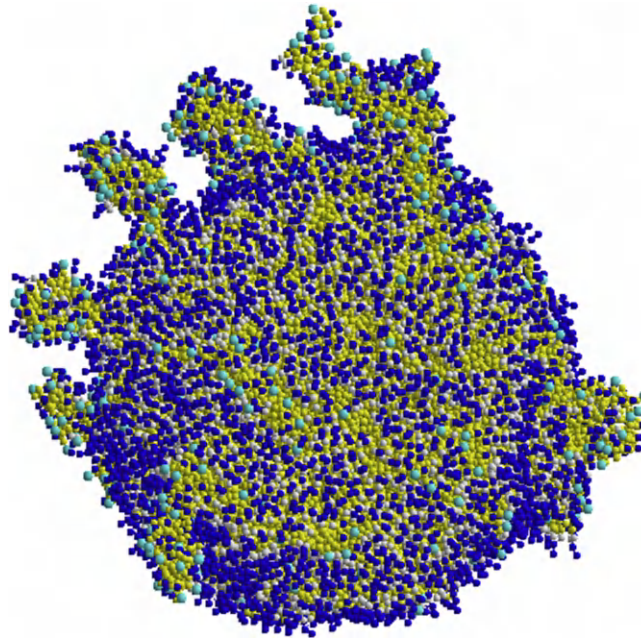

Figure 18 Snapshot of a DPPC vesicle containing sodium cholate with separating worm-like mixed micelles.

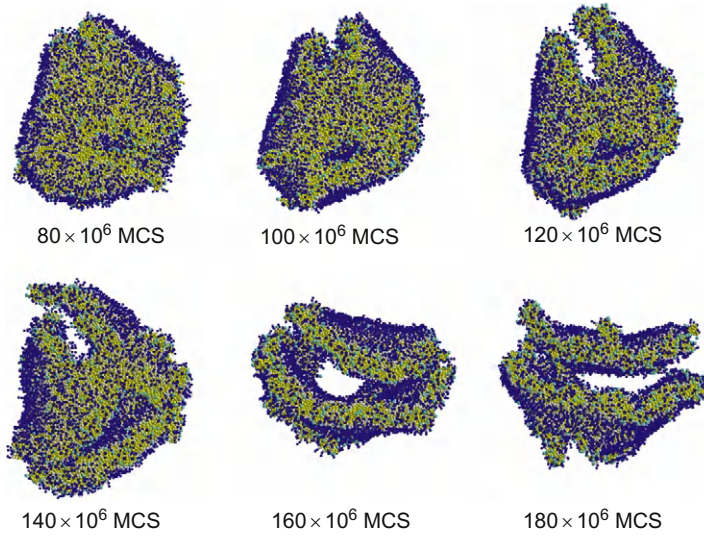

Figure 19 Shape fluctuations and crumbling of a DPPC vesicle during its solubilization by sodium cholate between 80×10^6 and 180×10^6 Monte Carlo steps (MCS). In the case of sodium deoxycholate the same mechanism is observed, although the solubilization process is faster as deoxycholate has a higher hydrophobicity than sodium cholate.

5. Summary and Outlook

Monte Carlo simulations of appropriate coarse-grained models are useful tools to gain some insight into basic properties of membranes and membrane-mediated interactions. There are several feasible ways to apply MC simulations to complex lipid bilayers that form in an aqueous solution. Dispensing with the explicit use of solvent models, a simple effective interaction model for mimicking the hydrophobic interaction can already be suitable for simulating important membrane properties. Unknown parameters entering into effective pair interactions for lipid molecules could be adjusted in such a way that phase diagrams as well as essential thermodynamic and elastic properties of experimental systems can be reproduced by the model. Such a simple approach is useful to study important physical problems of membrane physics such as fluctuations, vesicle stability and their shape transformations, membrane adhesion, lipid redistributions, adsorption, budding, exo- and endocytosis etc., which are also interesting in a biological context.

On a physical level, a topic of special interest is the interaction between the lipid matrix and membrane associated proteins. In many cases, it seems to be hardly possible to estimate the strength and importance of forces associated with the peptide-membrane interaction. For example, no satisfying theory exists which includes all important aspects accompanied by the adsorption of water soluble macromolecules on fluid membrane surfaces. In comparison to common substrates, a lipid bilayer responds to adsorbed molecules in various ways. The fluidity of bilayer membranes allows a local redistribution of lipid components, which influences the adsorption equilibrium. Furthermore, both the lipid redistribution of nonideal lipid mixtures and the particular elasticity of the bilayer membrane are the origin of membrane-mediated interactions, which should have an effect on the adsorption equilibrium and the arrangement of adsorbate molecules. Many recent experimental and theoretical studies are focused on indirect membrane-mediated interactions between peripheral and transmembrane proteins. MC simulations and other simulation techniques are very helpful to test theoretical concepts and to predict proper boundary conditions for differential equations needed for a macroscopic or mesoscopic description of bilayers and their interactions with membrane bound macromolecules.

Refining molecular models, MC simulations can also be useful to elucidate even more special problems related to lipid bilayers and other aggregates consisting of amphiphilic molecules. These simulations can help to estimate the validity of theoretical models and hypotheses on various self-assembled structures studied in the physical chemistry of amphiphiles.

ACKNOWLEDGMENT

We gratefully acknowledge the funding of parts of this work by a grant of the Deutsche Forschungsgemeinschaft (Grant No. MO 600/5-1).

REFERENCES

[1] D.F. Evans, H. Wennerstrom, The Colloidal Domain: Where Physics, Chemistry, Biology, and Technology Meet, Wiley-VCH Inc., New York, 1999.
[2] S.J. Singer, G.L. Nicolson, The fluid mosaic model of the structure of cell membranes, Science 175 (1972) 720–731.
[3] O.G. Mouritsen, Self-assembly and organization of lipid–protein membranes, Curr. Opin. Colloid Interface Sci. 3 (1998) 78–87.
[4] T. Gil, J.H. Ipsen, O.G. Mouritsen, M.C. Sabra, M.M. Sperotto, M.J. Zuckermann, Theoretical analysis of protein organization in lipid membranes, Biochim. Biophys. Acta 1376 (1998) 245–266.
[5] T.J. McIntosh, S.A. Simon, Roles of bilayer material properties in function and distribution of membrane proteins, Annu. Rev. Biophys. Biomol. Struct. 35 (2006) 177–198.
[6] R. Phillips, T. Ursell, P. Wiggins, P. Sens, Emerging roles for lipids in shaping membrane-protein function, Nature 459 (2009) 379–385.
[7] H.M. McConnell, M. Vrljic, Liquid–liquid immiscibility in membranes, Annu. Rev. Biophys. Biomol. Struct. 32 (2003) 469–492.
[8] L.A. Bagatolli, J.H. Ipsen, A.C. Simonsen, O.G. Mouritsen, An outlook on organization of lipids in membranes: searching for a realistic connection with the organization of biological membranes, Prog. Lipid Res. 49 (2010) 378–389.
[9] K. Binder, D.W. Heermann, Monte Carlo Simulation in Statistical Physics, Springer Series in Solid-State Sciences, 80, Springer, Berlin, 1992.
[10] M.P. Allen, D.J. Tildesley, Computer Simulation of Liquids, Clarendon Press, Oxford, 2002.
[11] H. Noguchi, M. Takasu, Self-assembly of amphiphiles into vesicles: a Brownian dynamics simulation, Phys. Rev. E 64 (2001) 041913-1–041913-7.
[12] R.D. Groot, P.B. Warren, Dissipative particle dynamics: bridging the gap between atomistic and mesoscopic simulation, J. Chem. Phys. 107 (1997) 4423–4435.
[13] S. Jury, P. Bladon, M. Cates, S. Krishna, M. Hagen, N. Ruddock, P. Warren, Simulation of amphiphilic mesophases using dissipative particle dynamics, Phys. Chem. Chem. Phys. 1 (1999) 2051–2056.
[14] A. Mayer, Membrane fusion in eukaryotic cells, Annu. Rev. Cell Dev. Biol. 18 (2002) 289–314.
[15] B. Alberts, A. Johnson, J. Lewis, M. Raff, K. Roberts, P. Walter, Molecular Biology of the Cell, 4th ed., Garland, New York, 2002.
[16] Z.-J. Wang, D. Frenkel, Modeling flexible amphiphilic bilayers: a solvent-free off-lattice Monte Carlo study, J. Chem. Phys. 122 (2005) 2347111–2347118.
[17] I.R. Cooke, K. Kremer, M. Deserno, Tunable generic model for fluid bilayer membranes, Phys. Rev. E 72 (2005) 011506-1–011506-4.
[18] T. Zehl, M. Wahab, H.-J. Mogel, P. Schiller, Monte Carlo simulations of self-assembled surfactant aggregates, Langmuir 22 (2006) 2523–2527.
[19] U. Seifert, Configurations of fluid membranes and vesicles, Adv. Phys. 46 (1997) 13–137.

[20] N. Dan, P. Pincus, S.A. Safran, Membrane-induced interactions between inclusions, Langmuir 9 (1993) 2768–2771.
[21] M. Goulian, Inclusions in membranes, Curr. Opin. Colloid Interface Sci. 1 (1996) 358–361.
[22] M. Goulian, R. Bruinsma, P. Pincus, Long-range forces in heterogeneous fluid membranes, Europhys. Lett. 22 (1993) 145–150.
[23] F. Schmid, Toy amphiphiles on the computer: what can we learn from generic models? Macromol. Rapid Commun. 30 (2009) 741–751.
[24] P. Garidel, A. Hildebrand, K. Knauf, A. Blume, Membranolytic activity of bile salts: influence of biological membrane properties and composition, Molecules 12 (2007) 2292–2326.
[25] C. Tanford, The Hydrophobic Effect: Formation of Micelles and Biological Membranes, Wiley, New York, 1980.
[26] J.N. Israelachvili, Intermolecular and Surface Forces, Academic Press, London, 1995.
[27] H.D. Deuling, W. Helfrich, Red blood cell shapes as explained on the basis of curvature elasticity, Biophys. J. 16 (1976) 861–868.
[28] D.D. Lasic, Liposomes: From Physics to Applications, Elsevier, Amsterdam, 1993.
[29] J. Käs, E. Sackmann, Shape transitions and shape stability of giant phospholipid vesicles in pure water induced by area-to-volume changes, Biophys. J. 60 (1991) 825–844.
[30] K. Berndl, J. Käs, R. Lipowsky, E. Sackmann, U. Seifert, Shape transformations of giant vesicles: extreme sensitivity to bilayer asymmetry, Europhys. Lett. 13 (1990) 659–664.
[31] S.T. Milner, S.A. Safran, Dynamical fluctuations of droplet microemulsions and vesicles, Phys. Rev. A 36 (1987) 4371–4379.
[32] D. Boal, Mechanics of the Cell, Cambridge University Press, Cambridge, 2002.
[33] U. Reimer, M. Wahab, P. Schiller, H.-J. Mögel, Monte Carlo simulation of the adsorption equilibrium of a model surfactant solution on hydrophilic solid surfaces, Langmuir 17 (2001) 8444–8450.
[34] S. Salaniwal, S.K. Kumar, A.Z. Panagiotopoulus, Competing ranges of attractive and repulsive interactions in the micellization of model surfactants, Langmuir 19 (2003) 5164–5168.
[35] G. Brannigan, F.L.H. Brown, Solvent-free simulations of fluid membrane bilayers, J. Chem. Phys. 120 (2004) 1059–1071.
[36] G. Brannigan, A.C. Tamboli, F.L.H. Brown, The role of molecular shape in bilayer elasticity and phase behavior, J. Chem. Phys. 121 (2004) 3259–3271.
[37] J.-P. Hansen, H. Löwen, Effective interactions for large-scale simulations of complex fluids, in: P. Nielaba, M. Mareschal, G. Ciccotti (Eds.), Bridging the Time Scales: Molecular Simulations for the Next Decade, Lecture Notes in Physics, Springer, Berlin, 2002.
[38] O. Farago, "Water-free" computer model for fluid bilayer membranes, J. Chem. Phys. 119 (2003) 596–605.
[39] O. Farago, P. Pincus, Statistical mechanics of bilayer membrane with a fixed projected area, J. Chem. Phys. 120 (2004) 2934–2950.
[40] T. Zehl, M. Wahab, H.-J. Mögel, P. Schiller, Monte Carlo simulations of small vesicles under osmotic pressure, Langmuir 25 (2009) 7313–7319.
[41] B. Lerebours, E. Wehrli, H. Hauser, Thermodynamic stability and osmotic sensitivity of small unilamellar phosphatidylcholine vesicles, Biochim. Biophys. Acta Biomembr. 1152 (1993) 49–60.
[42] J.T. Jenkins, Static equilibrium configurations of a model red blood cell, J. Math. Biol. 4 (1977) 149–169.
[43] G. Denisov, S. Wanaski, P. Luan, M. Glaser, S. McLaughlin, Binding of basic peptides to membranes produces lateral domains enriched in the acidic lipids phosphatidylserine

and phosphatidylinositol 4,5-bisphosphate: an electrostatic model and experimental results, Biophys. J. 74 (1998) 731–744.
[44] H.W. Huang, Structural basis and energetics of peptide membrane interactions, in: K. Merz Jr., B. Roux (Eds.), Biological Membranes, Birkhäuser, Boston, 1996.
[45] T. Heimburg, B. Angerstein, D. Marsh, Binding of peripheral proteins to mixed lipid membranes: effect of lipid demixing upon binding, Biophys. J. 76 (1999) 2575–2586.
[46] O.G. Mouritsen, K. Jørgensen, Small-scale lipid-membrane structure: simulation versus experiment, Curr. Opin. Struct. Biol. 7 (1997) 518–527.
[47] P. Schiller, M. Wahab, H.-J. Mögel, Forces between colloidal particles adsorbed on fluid membranes, J. Non-Newtonian Fluid Mech. 119 (2004) 145–153.
[48] S. May, D. Harries, A. Ben-Shaul, Macroion-induced compositional instability of binary fluid membranes, Phys. Rev. Lett. 89 (2002) 268102-1–268102-4.
[49] H.T. Davis, Statistical Mechanics of Phases, Interfaces, and Thin Films, Wiley-VCH Inc., New York, 1996.
[50] P.M. Chaikin, T.C. Lubensky, Principles of Condensed Matter Physics, Cambridge University Press, Cambridge, 1997.
[51] P. Schiller, H.-J. Mögel, M. Wahab, U. Reimer, Cooperative effects induced by adsorbed polypeptides in mixed membranes, J. Phys. Chem. B 107 (2002) 12323–12330, Erratum: J. Phys. Chem. B 107 (2003) 4478.
[52] J.J. Binney, N.J. Dowrick, A.J. Fisher, M.E.J. Newman, The Theory of Critical Phenomena, Clarendon Press, Oxford, 1992.
[53] S. Loew, A. Hinderliter, S. May, Stability of protein-decorated mixed lipid membranes: the interplay of lipid–lipid, lipid–protein, and protein–protein interactions, J. Chem. Phys. 130 (2009) 0451021–0451028.
[54] G.B. Arfken, H.J. Weber, Mathematical Methods for Physicists, Academic Press, San Diego, 1995.
[55] P. Schiller, M. Wahab, F. Bagusat, U. Reimer, H.-J. Mogel, Adsorption of colloidal particles on mixed membranes, Progr. Colloid Polym. Sci. 128 (2004) 143–145.
[56] A. Evans, M.S. Turner, P. Sens, Interactions between proteins bound to biomembranes, Phys. Rev. E 67 (2003) 041907-1–041907-10.
[57] B.J. Reynwar, M. Deserno, Membrane composition-mediated protein–protein interactions, Biointerphases 3 (2008) FA117–FA124.
[58] M. Wahab, H.-J. Mögel, P. Schiller, Indirect interaction of inclusions in mixed membranes, Mol. Phys. 99 (2001) 2045–2053.
[59] T.R. Weikl, M.M. Kozlov, W. Helfrich, Interaction of conical membrane inclusions: effect of lateral tension, Phys. Rev. E 57 (1998) 6988–6995.
[60] H.W. Huang, Elasticity of lipid bilayer interacting with amphiphilic helical peptides, J. Phys. II France 5 (1995) 1427–1431.
[61] N. Dan, A. Berman, P. Pincus, S.A. Safran, Membrane-Induced interactions between inclusions, J. Phys. II France 4 (1994) 1713–1725.
[62] T.A. Harroun, W.T. Heller, T.M. Weiss, L. Yang, H.W. Huang, Theoretical analysis of hydrophobic matching and membrane-mediated interactions in lipid bilayers containing gramicidin, Biophys. J. 76 (1999) 3176–3185.
[63] D.J. Struik, Lectures on Classical Differential Geometry, 2nd Ed., Dover Publications Inc., New York, 1988.
[64] P. Sens, M.S. Turner, Theoretical model for the formation of caveolae and similar membrane invaginations, Biophys. J. 86 (2004) 2049–2057.
[65] K.G. Rothberg, J.E. Heuser, W.C. Donzell, Y.-S. Ying, J.R. Glenney, R.G. W. Anderson, Caveolin, a protein component of caveolae membrane coats, Cell 68 (1992) 673–682.

[66] B.J. Reynwar, G. Illya, V.A. Harmandaris, M.M. Müller, K. Kremer, M. Deserno, Aggregation and vesiculation of membrane proteins by curvature-mediated interactions, Nature 447 (2007) 461–464.
[67] H. Mueller, H.-J. Butt, E. Bamberg, Adsorption of membrane-associated proteins to lipid bilayers studied with an atomic force microscope: myelin basic protein and cytrochrome c, J. Phys. Chem. B 104 (2000) 4552–4559.
[68] P. Schiller, Indirect interaction of colloidal particles adsorbed on smectic films, Phys. Rev. E 62 (2000) 918–926.
[69] P. Schiller, Molecular statistical model for adsorbed membrane particles, Mol. Phys. 98 (2000) 493–503.
[70] P. Schiller, H.-J. Mögel, Indirect interaction of colloidal particles adsorbed on soft surfaces, Phys. Chem. Chem. Phys. 2 (2000) 4563–4568.
[71] C. Nielsen, M. Goulian, O.S. Andersen, Energetics of inclusions-induced bilayer deformations, Biophys. J. 74 (1998) 1966–1983.
[72] P. Sens, S.A. Safran, Inclusion induced phase separation in mixed lipid film, Eur. Phys. J. E 1 (2000) 237–248.
[73] G. Brannigan, F.L.H. Brown, A consistent model for thermal fluctuations and protein induced deformations in lipid bilayers, Biophys. J. 90 (2006) 1501–1520.
[74] G. Brannigan, F.L.H. Brown, Contributions of Gaussian curvature and non-constant lipid volume to protein deformation of lipid bilayers, Biophys. J. 92 (2007) 864–876.
[75] B. West, F.L.H. Brown, F. Schmidt, Membrane–protein interactions in a generic coarse-grained model for lipid bilayers, Biophys. J. 96 (2009) 101–115.
[76] G. Jenkins, L.J. Hardie (Eds.), Bile Acids: Toxicology and Bioactivity, RSC Publishing, Cambridge, 2008.
[77] M.M.A. Elsayed, G. Cevc, The vesicle-to-micelle transformation of phospholipid-cholate mixed aggregates: a state of the art analysis including membrane curvature effects, Biochim. Biophys. Acta. Biomembr. 1808 (2011) 140–153.
[78] C. Martin, J. Thongborisute, H. Takeuchi, H. Yamamoto, Y. Kawashima, H.O. Alpar, Cholesterol-bile salt vesicles as potential delivery vehicles for drug and vaccine delivery, Int. J. Pharm. 298 (2005) 339–343.
[79] K. Andrieux, L. Forte, S. Lesieur, M. Paternostre, M. Ollivon, C. Gabrielle-Madelmont, Solubilisation of dipalmi-toylphosphatidylcholine bilayers by sodium taurocholate: a model to study the stability of liposomes in the gastrointestinal tract and their mechanism of interaction with a model bile salt, Eur. J. Pharm. Biopharm. 71 (2009) 346–355.
[80] A. Hildebrand, Physikochemische Charakterisierung von Gallensalz-Mischmizellen als Grundlage fur innovative Arzneistofftragersysteme, Thesis (2002), Martin-Luther University Halle-Wittenberg, Germany.
[81] M. Cardenas, K. Schillen, V. Alfredsson, R.-D. Duanc, L. Nyberg, T. Arnebrant, Solubilization of sphingomyelin vesicles by addition of a bile salt, Chem. Phys. Lipids 151 (2008) 10–17.
[82] N.A. Mazer, G.B. Benedek, M.C. Carey, Quasielastic light-scattering of aqueous biliary lipid systems. Mixed micelle formation in bile salt-lecithin solutions, Biochem. 19 (1980) 601–615.
[83] A. Walter, P.K. Vinson, A. Kaplun, Y. Talmon, Intermediate structures in the cholate-phosphatidylcholine vesicle-micelle transition, Biophys. J. 60 (1991) 1315–1325.
[84] R. Schmidt, Monte Carlo Simulation der Assoziation von Cholaten in cholesterolhaltigen Lipid-Bilayern und Mizellen, Diploma Thesis (2009), TU Bergakademie Freiberg, Germany.

[85] S.J. Marrink, A.H. deVries, A.E. Mark, Coarse grained model for semi-quantitative lipid simulations, Phys. Chem. 108 (2004) 750–760.
[86] G. Brannigan, P.F. Philips, F.L. Brown, Flexible lipid bilayers in implicit solvent, Phys. Rev. E 72 (2005) 011915-1–011915-4.
[87] S.J. Marrink, J.H. Risselada, S. Yefimov, D.P. Tielman, A.H. deVries, The MARTINI forcefield: coarse grained model for biomolecular simulations, J. Phys. Chem. 111 (2007) 7812–7824.

CHAPTER SEVEN

Coarse-Grained Computer Simulations of Multicomponent Lipid Membranes

Mohamed Laradji[1,*] *and* P.B. Sunil Kumar[2]

Contents

Abstract

Based on indirect observations, there currently exists a consensus that the plasma membrane of mammalian cells exhibits nontrivial lateral heterogeneities in the form of nanoscale lipid domains known as lipid rafts which are rich in cholesterol and sphingolipids. Lipid rafts have been implicated in a range of biological functions, including signal transduction, endocytosis, trafficking, virus uptake, and regulation of the membrane tension. The elucidation of the finite size of lipid rafts in the plasma membrane has been a challenging problem since multicomponent lipid vesicles composed of saturated lipid, an

* Corresponding author. Tel.: +901-678-1676; Fax: +901-678-473.
E-mail address: mlaradji@memphis.edu

[1] Department of Physics, The University of Memphis, Memphis, Tennessee, USA
[2] Department of Physics, Indian Institute of Technology Madras, Chennai, India

Advances in Planar Lipid Bilayers and Liposomes, Volume 14
ISSN 1554-4516, DOI: 10.1016/B978-0-12-387720-8.00007-8

unsaturated lipid, and cholesterol also exhibit domains, but these are much larger than the lipid rafts in the plasma membrane. Many computational studies have recently been performed to address the phase separation in multicomponent membranes and potential mechanisms leading to nanoscale phase separation in the plasma membrane. This chapter provides an overview of major computational studies of multicomponent lipid membranes with a particular focus on time-dependent Ginzburg–Landau models, dynamic triangulation Monte Carlo models, coarse-grained molecular dynamics, and dissipative particle dynamics.

1. Introduction

The plasma membrane provides structural integrity to the cell and acts as a functional interface between its cytoplasm and its outer environment, through the support of a variety of transmembrane and anchored proteins that are involved in various physiological processes including transmembranous transport, signaling and act as linkers with the subjacent cytoskeleton [1]. It is now widely accepted that many physiological functions of the plasma membrane including signaling, trafficking, endocytosis, cytokinesis, and apoptosis, require in-plane compositional heterogeneities of the plasma membrane [1–3]. This view has challenged the fluid mosaic model of Singer and Nicholson [4], which considers the plasma membrane as a two-dimensional fluid where the self-assembled lipid bilayer acts as a homogeneous solvent to membrane proteins. By 1982, Karnovsky *et al.* [5] had shown that the plasma membrane may exhibit heterogeneous lipid domains. This concept formed the basis of the lipid raft hypothesis by Simons and van Meer [6]. Since then, it became widely accepted that the plasma membrane of eukaryotic cells exhibits distinct lateral heterogeneities in the form of nanoscale domains called lipid rafts [3]. Although there remains some confusion regarding the definition of lipid rafts and the biological roles that they play [7], there was a consensus at the 2006 Keytstone Symposium on *Lipid Rafts and Cell Function* in defining lipid rafts as small structures (10–200 nm), heterogeneous, highly dynamic, with time scales ranging between 10^{-3} and 10^{2} s [8,9], and enriched in cholesterol and sphingolipids [10]. Although lacking translational order, the sphingolipid tail groups in lipid rafts are ordered, implying that lipid rafts are in the liquid-ordered state (L_o), in contrast to the surrounding regions which, due to the fact that they are rich in unsaturated lipids, are in the liquid-disordered state (L_d) [11].

Lipid rafts have been implicated in many biological functions including signaling [12,13], trafficking [12], caveolin-mediated endocytosis [14,15], virus uptake [16], and tension-regulation of the plasma membrane [17,18]. Due to their small scale, below the spatial resolution of light microscopy, the

existence of lipid rafts in the plasma membrane has been mainly based on the observation that detergent-resistant membranes obtained by extraction of mammalian cells using nonionic surfactants, such as Triton X-100, mainly contain cholesterol, sphingolipids and GPI-anchored proteins [19,20]. More recently, *in vitro* studies of the organization of GPI-anchored proteins, using Foster's resonance energy transfer (FRET), have revealed more details on the structure of lipid rafts [21].

Due to the vast complexity of the plasma membrane, as a result of the presence of a large number of components and protein-mediated active processes, studies of the lateral organization of the plasma membrane *in vivo* conditions have been very challenging. As a result, the majority of experimental and computational studies of this problem have been carried out during the last few years on simple multicomponent membranes as models of the much more complex plasma membrane. Experimental studies of the lateral organization in multicomponent membranes are based on supported bilayers and giant unilamellar vesicles (GUVs) composed of a saturated lipid, an unsaturated lipid and cholesterol [11]. In these experiments, micron-scale phase separated L_o regions rich in cholesterol and the saturated lipid, coexisting with L_d regions, rich in the unsaturated lipids, are observed, thus suggesting that the plasma membrane should exhibit similar behavior [22–32].

Spinodal decomposition, which refers to the kinetics of phase separation, is a generic phenomenon observed in multicomponent liquids and solids and proceeds when a multicomponent system is rapidly quenched from a disordered homogeneous state to a two-phase region of the phase diagram [33]. Right after the quench, small-amplitude long-wavelength compositional fluctuations of the initial homogeneous structure become unstable [33]. This instability leads to the development of small domains and their growth in order to minimize the excess energy due to the presence of interfaces between them. The domain structure is interconnected (labyrinth-like) in the case of a critical quenches and globular in the case of off-critical quenches [33]. Many details of domain growth during spinodal decomposition tend to be generic and depend on few aspects of the system such as spatial dimension, presence or absence of hydrodynamic interactions and, in some cases, the topology of the domain structure [33,34]. An interesting feature of spinodal decomposition, that up to date has attracted a lot of attention, is that the average domain size scales with time as a power law, $R \sim t^{\alpha}$, where the exponent α is a signature of the physical mechanism driving the phase separation process.

Spinodal decomposition in multicomponent lipid membranes differs from that in other multicomponent systems, in that lipid membranes are two-dimensional fluids embedded in a three-dimensional fluid. Lipid membranes are prone to curvature fluctuations which are controlled by a bending modulus, $\kappa \sim 10$ to $100\ k_B T$, where k_B and T are the Boltzmann's constant and absolute temperature, respectively. The interplay between the

local composition, the local membrane curvature, and the hydrodynamic interactions mediated by momentum transport through the embedding fluid and the fluid membrane itself produce kinetics of phase separation in multicomponent membranes that is far richer than that of Euclidean systems, and morphologies marked by coupling between the membrane morphology and the lateral compositional organization of the membrane. The main factors that control domain growth and morphology of phase separating lipid membranes are (1) line tension between the coexisting regions, (2) composition of the coexisting phases, (3) lateral tension on the membrane or equivalently area-to-volume ratio in the case of closed vesicle, and (4) the hydrodynamic interactions mediated by the surrounding fluid and the fluid membrane itself.

In order to gain some insight into the interplay between line tension and membrane curvature [35], consider a circular domain of a B-phase with area a coexisting with an A-phase, as shown schematically in Fig. 1. Let c be the absolute value of the domain's curvature assumed to be almost uniform. The excess energy of the membrane is therefore dominated by the line energy due to the interface and the domain's curvature,

$$\varepsilon = 2\kappa a c^2 + \lambda l, \tag{1}$$

where the perimeter of the interface is given by

$$l = 2\pi r = 2\pi \left(\frac{a}{\pi}\right)^{1/2} \left(1 - \frac{ac^2}{4\pi}\right)^{1/2}. \tag{2}$$

The free energy can then be rewritten as

$$\varepsilon = 8\pi\kappa \left[\tilde{c}^2 + \frac{\lambda}{2\kappa c_{\max}^2}\left(1 - \tilde{c}^2\right)^{1/2}\right] + \lambda l, \tag{3}$$

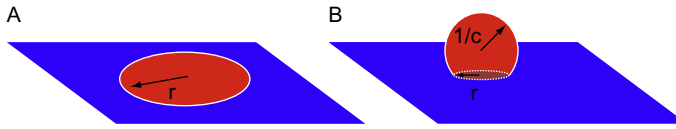

Figure 1 Three-dimensional rendering of (A) a flat lipid domain of radius r and area a, and (B) a curved spherically shaped (budded) lipid domain with same area as in (A) of radius $1/c$ and interfacial length $l = 2\pi r$. The shape of its lipid domain is determined by a competition between its line energy, $2\pi r\lambda$, and its curvature energy, $2\kappa a c^2$. In the case of a tensionless membrane, the budded domain adopts a limit-shape with an infinitesimally small neck (i.e., a neck determined by the thickness of the lipid bilayer).

where $a = 4\pi/{c_{\max}}^2$ and $\tilde{c} = c/c_{\max}$. The free energy in Eq. (3) has a minimum at $c = 0$. This minimum is absolute if the area of the domain is smaller than $a_0 = 4\pi(\kappa/\lambda)^2$. Otherwise, the free energy is lower for $c > 0$, with a specific value depending on the lateral tension on the membrane. In the case of a tensionless membrane, the domain has a shape of a complete bud, with the curvature $c = \sqrt{4\pi/a}$. These calculations imply that for a given κ/λ, the onset of domain capping occurs when its average radius exceeds $R_0 = 2\kappa/\lambda$. These simple arguments imply that the interplay between line tension and curvature energy leads to an early time dynamics dominated by flat domains. At later times, when the average domain size exceeds κ/λ, the domains cap. The line tension between the coexisting liquid-ordered and liquid-disordered phase close to the critical point is typically of order $\lambda \sim 1$ pN [28], and the bending rigidity is of order 10^{-19} J [36], implying that the onset of capping occurs at $R_0 \sim 100$ nm which is interestingly about the size of a lipid raft. In multicomponent membranes, phase separation proceeds until the domain size becomes comparable in size to the vesicle itself.

Many experiments on multicomponent GUVs undergoing phase separation have revealed the existence of large (micron-scale) domains, seemingly limited in size only by the finite size of the vesicle itself, implying that multicomponent GUVs do achieve thermodynamic phase separation [28]. Therefore, there is a notable difference between the sizes of lipid domains in model membranes and lipid rafts in the plasma membrane. As a result, one of the challenging questions regards the mechanisms that maintain the nanoscale size of lipid rafts. It is important to note that there are important differences between model multicomponent membranes and the plasma membrane. Chief among these are (1) a symmetric transbilayer lipid distribution in model membranes, whereas the transbilayer lipid distribution in the plasma membrane is highly asymmetric with the saturated lipid (mainly sphingolipids) mostly located on the exoplasmic leaflet; (2) absence of lipid trafficking in model membranes; (3) the presence of transmembrane proteins which partition preferably in the L_d domains; (4) the presence of a subjacent actin–myosin cytoskeleton in the plasma membrane which may lead to the confinement of some transmembrane proteins; and (5) activity of most of the proteins that are bound to the plasma membrane, making the plasma membrane a driven nonequilibrium system.

Several mechanisms have been put forward to explain the finite nanoscale size of lipid rafts in the plasma membrane. Mayor and Rao hypothesized that lipid rafts are equilibrium compositional fluctuations due to the closeness of the multicomponent system to its critical point [37]. Veatch *et al.*'s recent investigations of vesicles reconstructed from plasma membranes suggest that the physiological temperature of plasma membranes is higher than the critical point, thus implying that lipid rafts might simply be critical fluctuations [38,39]. The stability of nanoscale lipid rafts has also been attributed to the

presence of transmembrane proteins confined by the cortical cytoskeleton, which act as quenched impurities [9,40–42]. The finite size of lipid rafts has also been linked to the lipid recycling as well as trafficking [43,44]. The authors of this chapter also suggested that the finite size of lipid rafts is the result of asymmetry in the transbilayer lipid distribution in the plasma membrane [45]. This asymmetric lipid distribution leads to a spontaneous curvature of the domains and an effective repulsive interaction between curved domains [45,46]. It is plausible that the finite size of lipid rafts is due to a combination of the effects above. The understanding of phase separation in multicomponent membranes and the finite size of lipid rafts has thus been the subject of an increasing amount of computational studies during the last few years. These have been carried through phenomenological time-dependent Ginzburg–Landau models on Euclidean [42–44] and non-Euclidian surfaces [47–50], dynamic triangulation Monte Carlo (DTMC) [51–54], atomistic molecular dynamics (AMD) [55,56], coarse-grained molecular dynamics of implicit-solvent models [57,58] and explicit-solvent models such as that based on the MARTINI force field [59], and dissipative particle dynamics (DPD) [35,45,60,61]. The aim of this chapter is to present an overview of the recent computational studies of multicomponent membranes.

2. Time-Dependent Ginzburg–Landau Simulations

The earliest study of the phase separation kinetics in multicomponent lipid membranes using a time-dependent Ginzburg–Landau (TDGL) model was due to Taniguchi [47]. In this model, a free-energy functional of the local composition, $\phi(\mathbf{r})$, and local curvature, $c(\mathbf{r})$, of the multicomponent lipid bilayer on a vesicle, $\mathcal{S}$, parameterized by curvilinear coordinates (u_1, u_2) is given by

$$\begin{aligned}\mathcal{F}(\{\phi\},\{c\}) = &\int^{(\mathcal{S})} \sqrt{g}d^2u\left[\frac{a}{2}\phi^2+\frac{b}{4}\phi^4+\frac{1}{2}\xi^2 g^{\alpha\beta}\frac{\partial\phi}{\partial u^\alpha}\frac{\partial\phi}{\partial u^\beta}\right]\\ &+\frac{\kappa}{2}\int^{(\mathcal{S})}\sqrt{g}d^2u(c-c_0)^2+\Lambda\int^{(\mathcal{S})}\sqrt{g}d^2u\ \ c\ \ \phi+V\Delta P,\end{aligned} \tag{4}$$

where $\sqrt{g}d^2u$ is the element of area, $g^{\alpha\beta}$, with α, $\beta = 1$ or 2, is the contravariant metric tensor, c_0 is the spontaneous curvature, V is the enclosed volume, and ΔP is the pressure difference across the vesicle. The first integral in Eq. (4) is the usual Ginzburg–Landau free energy functional on

a generalized non-Euclidian surface. The second integral in Eq. (4) is the usual Helfrich Hamiltonain without the Gaussian term. The third integral in Eq. (4) describes the simplest bilinear coupling between the lipid composition and the local curvature. Langevin equations, without noise, describing the kinetics of both the local composition and local curvature are then derived and iterated numerically on closed surfaces with spherical initial shape.

In Fig. 2, late times snapshots in the case of a bilinear coupling coefficient $\Lambda = 0.5$ are shown for different values of the average composition $\bar{\phi}$. In snapshots (B) to (D) of Fig. 2, the curvature of the domains is due to the finite value of Λ. Figure 2(E) and (F) show that in the case where the curvature and composition fields are decoupled and shape fluctuations are suppressed (rigid spheres), domain growth is not affected by the vesicle's shape, $R \sim t^{\alpha}$, with the growth exponent $\alpha = 1/3$ for both critical and off-critical quenches. This growth law is identical to that of Euclidean systems undergoing spinodal decomposition where domain growth is mediated by

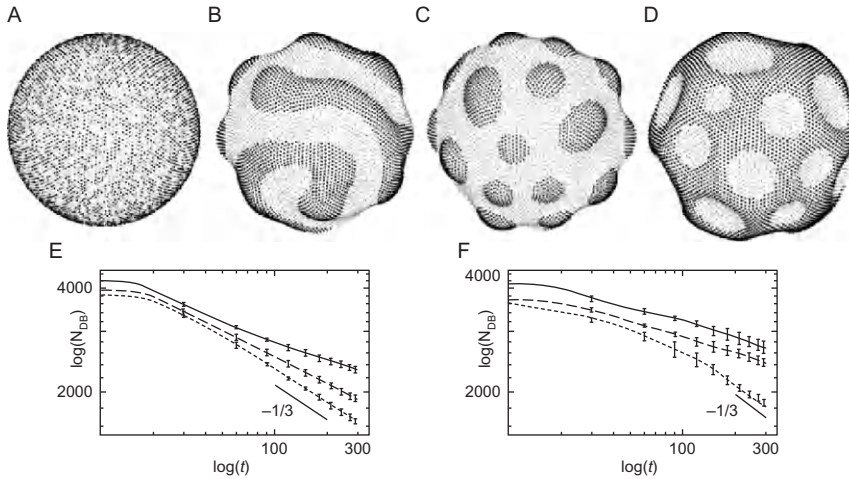

Figure 2 Configurations of vesicles as obtained from TDGL simulations of Taniguchi [47] in the case of $\Lambda = 0.5$. (A) corresponds to the initial configuration, (B) corresponds to a configuration at late times for a critical quench, $\bar{\phi} = 0$, (C) corresponds to a late-times configuration of an off-critical quench with $\bar{\phi} = 0.3$, and (D) corresponds to a late-times configuration for an off-critical configuration with $\bar{\phi} = -0.3$. Dark regions in (A)–(D) corresponds to $\phi(\mathbf{r}) < \bar{\phi}$. (E) shows a log–log plot of the interfacial length versus time for the case of critical quenches with different values of the bilinear coupling Λ between the composition and curvature. Graphs from top to bottom in (E) correspond to $\Lambda = 0.8$, 0.5, and 0, respectively. (F) Same as (E), but for off-critical quenches, $\bar{\phi} = -0.3$. Graphs from top to bottom correspond to $\Lambda = 0.8$, 0.5, and 0, respectively. The bottom graphs of both (E) and (F) are obtained in the context of rigid spheres. Reprinted with permission from [47]. Copyright 1996, American Physical Society.

the long-range evaporation–condensation mechanism [62]. When $\Lambda > 0$ and when curvature fluctuations are allowed, domain growth becomes significantly slower as shown by Fig. 2. This slowing down is probably due to the fact that the equilibrium state in these cases can be that of microphase-separated structures as has been shown by several mean field calculations of related models [63–67].

A two-dimensional version of the model above, with the membrane fluctuations described by the Monge representation was later investigated by Wallace *et al.* [68] and Thronton *et al.* [69,70]. A similar TDGL model coupled to a fluctuating elastic membrane model was later developed by McWhirter *et al.* [48–50]. It is worth noting that the bilinear coupling between the composition and curvature, often incorporated in TDGL models of multicomponent lipid membranes, implicitly assumes that the lipid composition of the two apposing leaflets is locally asymmetric. This assumption contradicts the experimental observation that domains in the two leaflets are in register [27,29].

In order to understand the finite-size of lipid rafts in the plasma membrane, Foret [44] proposed a two-dimensional TDGL model which neglects curvature fluctuations and where the lipid bilayer is coupled to a lipid reservoir in the cytoplasm that mimics the effect of lipids recycling. The model was later improved by Fan *et al.* [42,43] to account for the effect of immobilized proteins as well as critical fluctuations, two mechanisms which have also been associated with the arrest of domain growth in the plasma membrane [9,37]. The free energy functional of the system is given by the first integral of Eq. (4), but on a Euclidian nonfluctuating surface, $g = 1$ and $c = 0$. A Langevin equation describing the kinetics of the composition is derived with an additional term describing lipid exchange with the cytoplasm,

$$\frac{\partial}{\partial t}\phi(\mathbf{r},t) = -\frac{1}{\tau_r}\left[\phi(\mathbf{r},t) - \bar{\phi}\right] + M\nabla^2\frac{\delta\mathcal{F}}{\delta\phi} + \eta(\mathbf{r},t), \tag{5}$$

where M is the mobility of the composition field and τ_r is the relaxation time for the composition due to exchange with the lipid reservoir. η is a stochastic noise with zero mean and correlation

$$\langle\eta(\mathbf{r},t)\eta(\mathbf{r}',t')\rangle = -\frac{H^2}{2\pi}\nabla^2 K_0\left(\frac{|\mathbf{r}-\mathbf{r}'|}{l}\right)\ \delta(t-t'), \tag{6}$$

where H is either proportional to temperature or related to the rate of lipid exchange between the reservoir and the lipid membrane, and l defines the length scale over which spatial distribution of lipids takes place. K_0 is the modified Bessel function of the second kind and zeroth order. In this model, the free energy functional of the multicomponent lipid membrane is given by

$$\mathcal{F}(\{\phi\}) = \int^{(\mathcal{S})} d^2x \left\{ \frac{a}{2}\phi^2 + \frac{b}{4}\phi^4 + \frac{1}{2}\xi^2[1 - \alpha\rho(\mathbf{r})](\nabla\phi)^2 \right\}. \quad (7)$$

In the free energy functional, Eq. (7), $\rho(\mathbf{r})$ describes a local density of immobile transmembrane proteins, which act as quenched impurities for the lipid composition. These immobilized proteins may correspond, for example, to the protein complexes that link the actomyosin cytoskeleton to the lipid bilayer [9]. It is worth noting that, in Eq. (5), the term describing lipid exchange between the reservoir and the lipid bilayer, can be derived by adding to the free energy functional a bilinear long-range interaction, $(1/M\tau_r) \int d\mathbf{r} \int \mathbf{r}' \phi(\mathbf{r}, t) G(\mathbf{r}, \mathbf{r}') \phi(\mathbf{r}', t)$, where G is the Green's function satisfying $\nabla^2 G(\mathbf{r}, \mathbf{r}') = -\delta(\mathbf{r} - \mathbf{r}')$ [71]. The resulting free-energy functional is that of an effective diblock copolymer melt close to the order–disorder transition known to lead to various microphase-separated structures [72]. The model above was used to investigate four possible scenarios that have been associated with the stabilization of nanoscale lipid domains (rafts) in the plasma membrane: (1) the effects of critical fluctuations controlled by the coefficient a (<0 in the two-phase region and >0 in the one-phase region); (2) the effect of quenched proteins through the function $\rho(\mathbf{r})$; (3) the effect of lipids exchange between the reservoir and the lipid bilayer, which is controlled by the time scale τ_r; and (4) the effect of lipid recycling through the length scale l (an $l = 0$ implies no recycling). In Ref. [73], Fan *et al.* also investigated the effect of membrane compartmentalization (induced by cytoskeleton, for example) on domain growth. Typical late-time configurations obtained from this model are shown in Fig. 3.

Through the analysis of the correlation function of the composition, Fan *et al.* [43] determined a qualitative effect of each of the possible scenarios listed above on the correlation function of the composition scattering function. These analyses can, in principle, be mapped onto future experimental studies of lipid rafts in order to determine the mechanism(s) leading to finite size of lipid rafts. It is noted, however, that since the effects that may be involved in the stability of nanoscale lipid domains are nonequilibrium ones, the account for hydrodynamics may be very important. The coupling of the solvent velocity field to multicomponent membranes was recently investigated by Fan *et al.* [42] and Camley and Brown [74] using model H [75] in the low Reynolds number regime, where the inertia term in the Navier–Stokes equation can be neglected. In their analyses [42], Fan *et al.* found different regimes depending on the ratio, $R(t)/l_h$, where $R(t)$ is the domain size and $l_h = \eta_s/\eta_m$ is the hydrodynamic length with η_s and η_m are the viscosities of the solvent and membrane, respectively. Note that in their calculations, Fan *et al.* considered the membrane as a flat object without curvature deformations. The formulation of the problem while allowing for

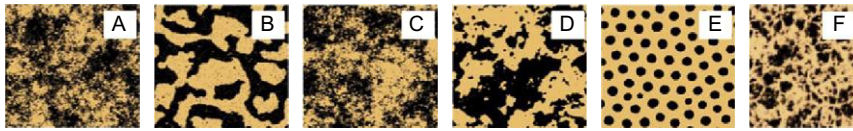

Figure 3 Late time configurations obtained from TDGL simulations of the model proposed by Fan *et al*. [43]. (A) corresponds to a system dominated by critical fluctuations (right below the critical point) without lipids recycling or immobilized proteins. (B) corresponds to a system in the two phase region (well below the critical point) without recycling and with immobilized proteins. (C) corresponds to a system in the one-phase region with recycling. (D) corresponds to a system in the two phase-region with recycling. (E) corresponds to a system with coupling to a lipid reservoir and in the two phase region. (F) corresponds to a system with cytoskeleton-induced compartmentalization. Reprinted with permission from [43,73]. Copyright 2010, the American Physical Society.

membrane deformation is a difficult task and has not yet been performed in the context of multicomponent membranes [76].

3. Dynamic Triangulation Monte Carlo

In the DTMC approach [77], the lipid membrane is approximated by a randomly triangulated sheet, with the vertex positions of the triangles specified by three-dimensional vectors. The vertices can move in three dimensions to allow for shape changes, with the topology of the membrane preserved by connecting the vertices with tethers, with a length $a = l_{\min} < l < l_{\max} = \sqrt{3}a$. The fluidity of the membrane is maintained by dynamic breaking and reconnecting of tethers. In the case of multicomponent membranes, an additional Kawasaki exchange move was introduced to facilitate phase separation [51,52]. The Monte Carlo moves are summarized in Fig. 4. The vertex moves and bond flips, leading to fluctuations in the shape of the membrane, are accepted using the Metropolis scheme and the conserved dynamics of the concentration field is ensured using Kawasaki exchange moves. In all cases, the configuration of the membrane is weighted by the discrete version of the Helfrich Hamiltonian,

$$\mathcal{H} = 2\kappa \sum_{\Delta} \left[H_{\Delta} - C_0(1+\phi_{\Delta})/2A_{\Delta}\right]^2 / A_{\Delta} - \sum_{ij} J\phi_i\phi_j, \qquad (8)$$

where $H_{\Delta} = (1/4)\sum_{ij} l_{ij}\Xi_{ij}$, is the contribution of every triangle to the total mean curvature integrated over the area of the vesicle and A_{Δ} is the area of a triangle [54]. l_{ij} is the length of the edge and Ξ_{ij} is the angle between the

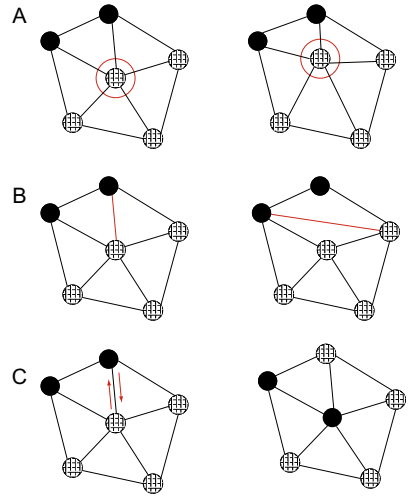

Figure 4 Schematic plot illustrating the moves used in the dynamic triangulation Monte Carlo approach to simulate a two-component fluid membrane. The two components are represented by crossed and solid spheres. (A) corresponds to a bead move, (B) corresponds to a bond flip, and (C) corresponds to a Kawasaki exchange move between the different types of particles.

normals of the triangles sharing the edge (i, j). The relative lipid concentration ϕ is discretized by assigning $\phi_\Delta = \pm 1$ to every triangle. J is the interaction parameter between neighboring patches. C_0 is the preferred mean curvature arising from the effective shape asymmetry of the two lipid components.

The early simulations performed on multicomponent membranes [53] used a slightly different form with discrete values for the mean curvature and concentration field assigned to the vertices of the triangles. The results obtained from these two discrete versions agree well with each other. Snapshot series of a membrane with its edges fixed to a hexagonal frame with $C_0 > 0$, and undergoing phase separation after a critical quench, are shown in Fig. 5, This figure indicates that during early times, the domain morphology is that of a labyrinth, typical to spinodal decomposition in two-dimensional Euclidian systems. The domain structure eventually breaks up into budded domains, leading to an increased tension of the membrane. This frame-induced tension prevents motion and coalescence of buds, eventually leading to a marked slowing down of the kinetics of phase separation [51].

The model was later used by Sunil Kumar *et al.* [54] to investigate the kinetics of phase separation of a closed multicomponent vesicle. Two particular cases corresponding to a spontaneous curvature (a) $C_0 = 0$ and (b) $C_0 > 0$ were investigated in detail. When the local composition and curvature are not coupled, that is,. when $C_0 = 0$, the kinetics proceeds

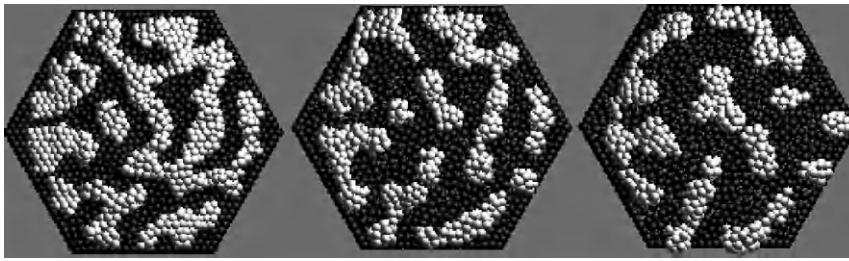

Figure 5 Three snapshots of a two-component membrane with its edges fixed on a hexagonal frame. Note the labyrinth domain morphology at early times, typical to spinodal decomposition. The labyrinth structure breaks up at late times. Reprinted with permission from [53]. Copyright 1998, the American Physical Society.

through two main regimes, as shown in Fig. 6. The first regime is characterized by the typical labyrinth domain structure observed in spinodal decomposition in Euclidian space. At later times, when the characteristic domain size exceeds κ/λ, the domain energy becomes dominated by its line energy leading the transformation of the domain structure into isolated buds connected to the main vesicle by narrow necks. The buds attain a limit shape configuration due to the absence of volume constraint in the DTMC approach, implying that the vesicles are in tensionless states (see arguments presented in the Introduction). Domain growth then proceeds via coalescence of these buds. The length scale $L(t)$ in these two regimes shows different dependence on time as can be seen in Fig. 7. After an initial transient, the length of the interface between domains scales with time as, $L(t) \sim t^{-\alpha}$, with the growth exponent $\alpha \approx 1/3$, typical to phase separating binary mixtures in Euclidean two- or three-dimensional systems without hydrodynamics [34,62]. This growth law could arise from the evaporation–condensation mechanism [62] or from capping of circular patches during the early stages. As quantitatively shown by Fig. 7, the duration of first regime is shorter for smaller κ. This is expected since the crossover domain size between the two regimes scales as κ/λ. At later times, as can be seen in Fig. 7, there is a clear crossover to the budding regime where the interfaces of the patches rapidly collapse into narrow necks due to absence of volume constraint. The crossover time at which domain growth changes to the budding regime increases as κ is increased, while the line tension is kept unchanged.

Situations wherein the two patches have different preferred mean curvatures are simulated by making $C_0 \neq 0$. Snapshots of the simulations with $C_0 > 0$, shown in Fig. 8, demonstrate a clear deviation of the kinetics from the path followed when $C_0 = 0$. When $C_0 \neq 0$, the interconnected patches do form as well during early stages, but they break up much earlier to form buds than in the case of zero spontaneous

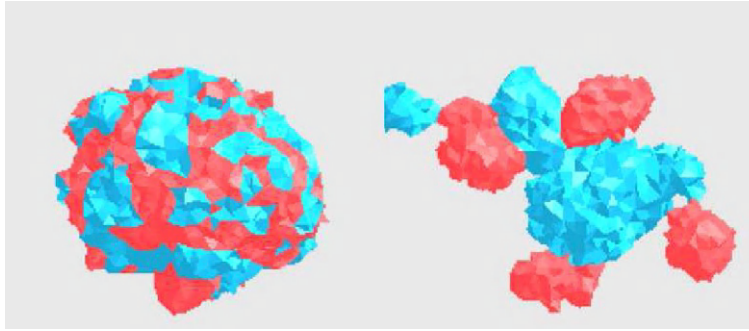

Figure 6 Two snapshots of a phase-separating two-component vesicle from a DTMC simulation following a critical quench, and with both components having no spontaneous curvature. The left snapshot is at early times during which the domains are flat and form a typical labyrinth morphology. The right snapshot is at later times and shows isolated budded domains. Reprinted with permission from [78]. Copyright 2009, The Physical Society of Japan.

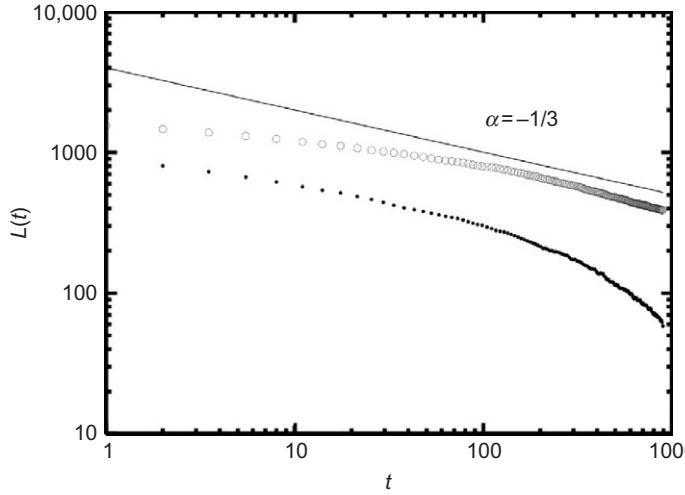

Figure 7 The net interfacial length, $L(t)$, versus time, t, for the case of zero spontaneous curvature. The upper curve corresponds to a membrane with a bending modulus eight times that of the lower curve. Reprinted with permission from [78]. Copyright 2009, The Physical Society of Japan.

curvature. Fig. 9 shows that the crossover time to the budding regime increases with decreasing C_0. The budding regime is identified by the sharp bend in $L(t)$ as a function of time. It is also noted that the critical patch size for budding increases with decreasing C_0, when all other parameters are held fixed.

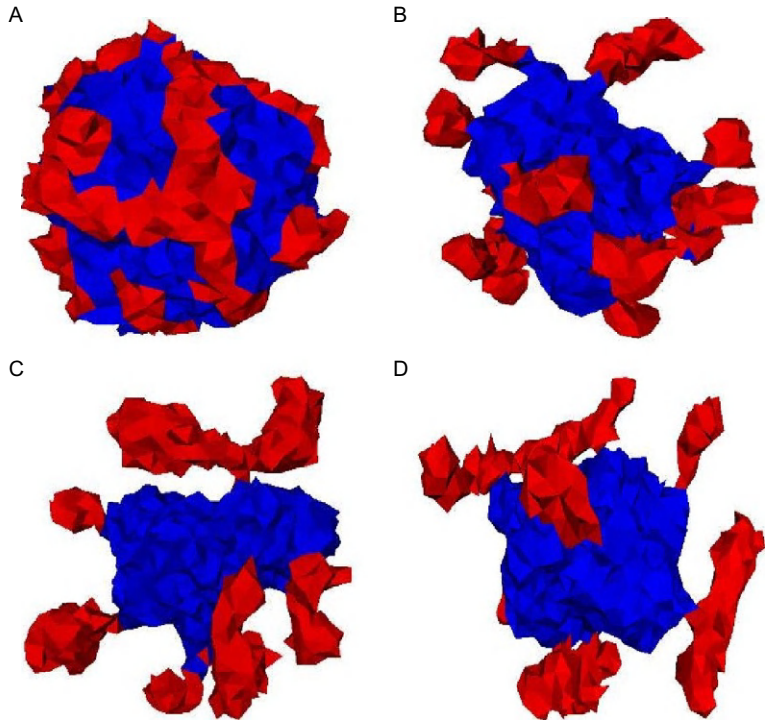

Figure 8 Time sequence of snapshots of a two-component vesicle from a DTMC simulation with $C_0 = 0.25$, $\kappa = 1.0$ and $J = 2.0$. (A), (B), (C), and (D) corresponds to $t = 1000$ MCS, 4.5×10^4 MCS, 1×10^5 MCS and 2×10^5 MCS, respectively. Reprinted with permission from [78]. Copyright 2009, The Physical Society of Japan.

The late time coarsening of the domains, once the buds are fully formed, is mediated by the Brownian diffusion of the buds and their coalescence on the surface of the vesicle. In this regime, all buds have a neck size of three triangles and thus the number of buds and the length $L(t)$ scale similarly. Diffusion-mediated coalescence of blebs is further substantiated by the correlation between $L(t)$ and the number of buds during late times [54] and the fact that the number of buds scales algebraically with time as $N(t) \sim t^{-1/2}$, agreeing with the bud coalescence model [54].

4. Coarse-Grained Molecular Dynamics

There have been few AMD simulations of three-component lipid membranes [55,56]. A typical AMD simulation will involve few thousands of lipids, and thus the linear system size is about 10 nm, smaller than a typical

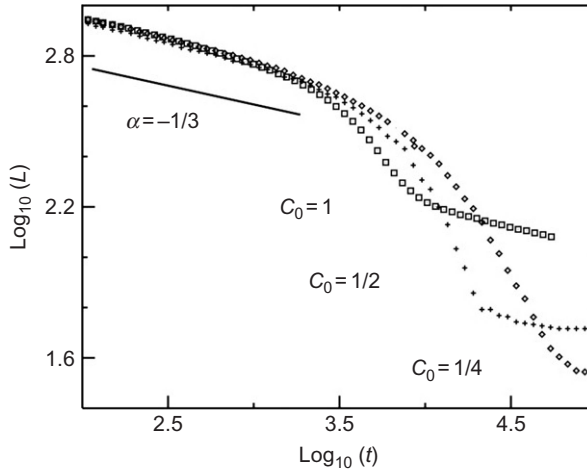

Figure 9 The total interfacial length, $L(t)$, as a function of time, t. The three sets of data are for different values of the spontaneous curvature C_0 of the patches. The slope of the straight line is $-1/3$. Reprinted with permission from [54]. Copyright 2001, The American Physical Society.

lipid raft. Furthermore, typical AMD simulation of lipid bilayers are run over few hundred nanoseconds. Thus, AMD only allows for short time-scale rearrangements of the lipid molecules. Therefore, as of now, there is no AMD study of lipid raft formation. An early molecular dynamics simulation based on Lenard–Jones interactions of a coarse-grained model for lipid membranes was performed by Goetz *et al.* [79,80] to investigate the mechanical properties of one-component lipid membranes. Goetz *et al.*'s model [79,80] is an effective molecular dynamics model in that a lipid molecule is coarse-grained into a short amphiphilic linear chain of beads composed of one hydrophilic particle and four hydrophobic particles. This model is generic, and has not been used for studying phase separation in multicomponent lipid membranes. More recently, Marrink *et al.* [81,82] proposed a more specific coarse-grained model, known as the MARTINI model, based on a four-to-one coarse-graining of heavy (carbon, oxygen, nitrogen, or phosphorous) atoms. For example, a dipalmitoylphosphatidylcholine (DPPC) molecule is coarse-grained into 12 beads, consisting of two hydrocarbon flexible chains, each composed of four hydrophobic beads, and a hydrophilic head group composed of four hydrophilic beads. Same mapping is used for water molecules, and a slightly different mapping is used for the ring structures present in cholesterol. A trial and error procedure was used to optimize the parameters of the MARTINI model in order to reproduce experimental densities of water and some alkanes at room temperature. An extensive force field library

of the MARTINI model has been developed, and is continuously being improved, for various types of lipids and amino acids [83].

Four main types of particles are used in the MARTINI model. These correspond to: polar (P), nonpolar (N), apolar (C), charged (Q), and apolar ring structure (SC). Each of the four beads, P, Q, N, or P, has between four and five subtypes. The time step in the MARTINI approach is typically around 20 fs, and is therefore about one order of magnitude higher than that of AMD [55]. The MARTINI approach has had an appreciable success during the last few years due to its ability to model specific systems, while being more coarse-grained than AMD, and thus allowing to investigate specific three-component mixtures over few microseconds The MARTINI model was recently used by Risselada and Marrink [59] to study domain formation in a ternary mixture of DPPC, dilinoleylphosphatidylcholine (DUPC) and cholesterol. Snapshots obtained from these simulations are shown in Fig. 10. In agreement with experiments, simulations based on the MARTINI force field [59] have shown that cholesterol has indeed an affinity for the saturated DPPC molecules. Furthermore, they also found that domains in the two leaflets do indeed exhibit a high degree of registration, again in agreement with experiments. Despite its successes, coarse-grained molecular dynamics with the MARTINI force field is still too slow to be used to investigate the kinetics of spinodal decomposition in large multicomponent membranes.

5. Dissipative Particle Dynamics

Due to its stochastic nature, the DTMC simulations of multicomponent lipid membranes cannot account for hydrodynamic interactions. Although Navier–Stokes equations can be coupled to the time-dependent Ginzburg–Landau equations in order to account for hydrodynamic interactions, these equations tend to be cumbersome, particularly in the case where out-of-plane deformations of the lipid membrane are allowed, and have thus far only been solved for the case of flat membranes without out-of-plane deformations [19,42]. Furthermore, the account for the constraint of area-to-volume ratio and topological changes of the membrane cannot readily be accounted for by either the TDGL approach or the DTMC approach. The effect of hydrodynamic interactions are inherently accounted for in molecular models such as atomistic and coarse-grained molecular dynamics, including molecular dynamics with the MARTINI force field, and the DPD. Although very promising, due to computer limitations, coarse-grained molecular dynamics with the MARTINI force field cannot yet be used to study the kinetics of phase separation in multicomponent membrane over long time scales.

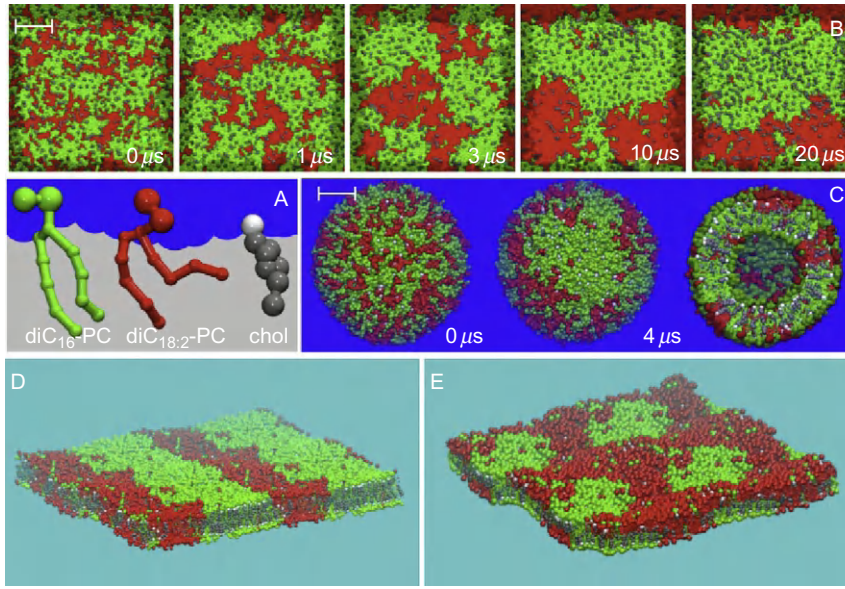

Figure 10 Domains in ternary lipid mixtures. (A) Color coding of the lipid components. Green is used for the DPPC lipids, and red is used for the DUPC lipids. Cholesterol is depicted in gray with a white hydroxyl group. (B) Time-resolved phase segregation of a planar membrane viewed from above, starting from a random mixture, ending with the L_o/L_d coexistence ($t = 20$ μs). (C) Phase segregation for the same lipid mixture in a liposome with 20 nm in diameter starting with a uniform mixture and ending at $t = 4$ μs. Both top view and cut through the middle are shown at late times. (D and E) Multiple periodic images (2×2) of the phase-separated DPPC/DUPC/cholesterol systems show striped pattern formation in the 0.42:0.28:0.3 system (D) and circular domains in the 0.28:0.42:0.3 system (E). (Scale bar: 5 nm.) Reprinted with permission from [59]. Copyright 2008, National Academy of Sciences, USA.

The relatively novel approach known as DPD, developed by Hoogerbrugge and Koelman [84] and then cast in its present form by Español and Warren [85] about 15 years ago, has proven to be extremely useful for investigations of soft materials, which are usually characterized by slow kinetics [86]. These include spinodal decomposition [87], transport of polymer solutions [88], microphase separation in diblock copolymers [89], nanocomposites [90–92], externally driven flow of polymeric systems [93–95], and living polymers [96]. DPD is reminiscent of molecular dynamics in that it is an explicit particle-based approach. Its essence lies in the fact that it uses soft conservative forces, and pairwise dissipative and random forces. The pairwise dissipative and random forces collectively act as a thermostat while locally conserving momentum. DPD thus implicitly and correctly describes the long-range hydrodynamic interactions in fluids [97]. The use of soft interactions in DPD allows for timesteps that are several orders of magnitude larger

than in coarse-grained molecular dynamics. Indeed the time step in DPD simulations of lipid membranes is typically of order 1 ps [56] and thus DPD is about two orders of magnitude faster than coarse-grained molecular dynamics with the MARTINI force field [56]. The success of DPD when compared to other methods used for studies of multicomponent membranes stems from the account of (1) hydrodynamic interactions mediated by both the lipid bilayer and ambient solvent, (2) area-to-volume constraint, and (3) topological changes of the lipid membrane.

There are several presentations of lipids in DPD simulations. These range from two-tailed models [98] to single tailed-lipids [60]. While some of the membrane physical constants like its bending modulus are not sensitive to the structure of the lipid, quantities such as the pressure profile, gel-fluid transition, and the structure of the gel phase, are sensitive to the lipid model. Since the phase separation of lipid membranes into coexisting L_o and L_d phases has been observed in many systems [11], with the main requirement being that the three components are a saturated lipids, an unsaturated lipid and cholesterol, keeping a simplified description of lipid particles is justified.

In the model of lipid membranes presented below [35,45,61,99], each lipid particle is represented by a hydrophilic head particle (h) connected to a linear strand of three hydrophobic tail particles (t). A multicomponent lipid membrane in the two-phase L_o–L_d coexistence is modeled within the DPD approach with two immiscible components, A and B, with their hydrophilic heads denoted by h_A and h_B, respectively, and their tail particles by t_A and t_B, respectively. The solvent also contains simple solvent particles denoted by w. A DPD particle, i, experiences the following net force from other particles,

$$\mathbf{F}_i = \sum_{j \neq i} \left(\mathbf{F}_{ij}^{(C)} + \mathbf{F}_{ij}^{(D)} + \mathbf{F}_{ij}^{(R)} \right), \tag{9}$$

where the conservative forces is given by

$$\mathbf{F}_{ij}^{(C)} = a_{ij} \omega\left(r_{ij}\right) \hat{\mathbf{r}}_{ij}, \tag{10}$$

with $\mathbf{r}_{ij} = \mathbf{r}_j - \mathbf{r}_i$, and $\hat{\mathbf{r}}_{ij} = \mathbf{r}_{ij}/r_{ij}$. The weight function ω is given by,

$$\omega(r) = \begin{cases} 1 - r/r_c & \text{for } r \leq r_c, \\ 0 & \text{for } r > r_c, \end{cases} \tag{11}$$

where r_c is a cutoff distance. The conservative forces between particles are therefore all repulsive. In this simple model, the hydrophobic and hydrophilic interactions are thus the result of the relative interaction

strengths a_{ij}. a_{ij} for w–w interaction is chosen such that water's compressibility at room temperature is reproduced [86]. Results presented below are obtained from the following set of interaction strengths

$$a_{ij} = \frac{\varepsilon}{r_c}\begin{pmatrix} & h_A & t_A & w & h_B & t_B \\ h_A & 25 & 200 & 25 & a_{AB} & 200 \\ t_A & 200 & 25 & 200 & 200 & a_{AB} \\ w & 25 & 200 & 25 & 25 & 200 \\ h_B & a_{AB} & 200 & 25 & 25 & 200 \\ t_B & 200 & a_{AB} & 200 & 200 & 25 \end{pmatrix}. \tag{12}$$

The dissipative and random forces are respectively given by

$$\mathbf{F}_{ij}^{(D)} = \gamma_{ij}\omega^2(r_{ij})\left(\hat{\mathbf{r}}_{ij}\cdot\mathbf{v}_{ij}\right)\hat{\mathbf{r}}_{ij}, \tag{13}$$

$$\mathbf{F}_{ij}^{(R)} = \sigma_{ij}(\Delta t)^{1/2}\omega(r_{ij})\zeta_{ij}\hat{\mathbf{r}}_{ij}, \tag{14}$$

where $\mathbf{v}_{ij} = \mathbf{v}_j - \mathbf{v}_i$ and Δt is the time step. ζ_{ij} is a symmetric random variable with zero mean and unit variance, uncorrelated for different pairs of particles and different times, that is,

$$\langle\zeta_{ij}(t)\rangle = 0, \tag{15}$$

$$\langle\zeta_{ij}(t)\zeta_{kl}(t')\rangle = \left(\delta_{ik}\delta_{jl} + \delta_{il}\delta_{jk}\right)\delta(t-t'), \tag{16}$$

with $i \neq j$ and $k \neq l$. The dissipative and random forces are related to each other through the fluctuation–dissipation theorem, leading to

$$\gamma_{ij} = \sigma_{ij}^2/2k_BT. \tag{17}$$

The integrity of a lipid particle is ensured by an additional harmonic interaction given by

$$\mathbf{F}_{i,i+1}^{(S)} = -k\left(1 - \frac{r_{i,i+1}}{b}\right)\hat{\mathbf{r}}_{i,i+1}, \tag{18}$$

where k is some spring constant and b is some preferred bond length. In Eq. (18), $k = 100\varepsilon$ and $r_c = 0.45r_c$ are used. The results presented here [45,61] were obtained from simulations performed at $\sigma = 3.0(\varepsilon^3 m/r_c^2)^{1/4}$, a fluid number density $r_c = 3.0{r_c}^{-3}$, and a temperature $k_BT = \varepsilon$. The velocity-Verlet algorithm was used with an integration time step $\delta t = 0.05\ \tau$ with the time scale $\tau = (m{r_c}^2/\varepsilon)^{1/2}$. The simulations are performed in cubic boxes of size $(80 \times 80 \times 80)\ {r_c}^3$ corresponding to

1,536,000 dpd particles. The number of lipid molecules is fixed at 16,000. The parameters of these DPD simulations [45,61] are such that solvent particles cannot translocate through the lipid bilayer, thus constraining the core volume of lipid vesicles. This corresponds to a typical experimental situation. In the simulations, vesicles are prepared by placing lipids on both inner and outer sides of a sphere with a pore at the pole. This pore eventually closes once the lipid surface densities on both leaflets are equilibrated. This process allows the vesicle to achieve a tensionless state with its equilibrium area-to-volume ratio and area between the two leaflets. After some equilibration time, lipids are randomly assigned types A and B on both leaflets with the desired composition, ϕ. In the presentation of the DPD results, a variety of systems will be discussed. The labels of these systems with their parameters are given in Table 1.

5.1. Domain Growth in Membranes with Equal Compositions

In Fig. 11, snapshots of systems $\mathcal{C}_1^{(100)}$, $\mathcal{C}_2^{(100)}$, and $\mathcal{C}_2^{(50)}$ (see Table 1 for a description of the labels) are shown, corresponding to the case of equal lipid compositions of the two lipids with two different area-to-volume ratios. This figure clearly shows the labyrinth-like domain structure during early times, typical to spinodal decomposition after a critical quench. At later times, however, the domain structure breaks up into more compact domains (see, e.g., system $\mathcal{C}_2^{(100)}$ at $t > 100\,\tau$). In system $\mathcal{C}_2^{(100)}$, which is characterized by high area-to-volume ratio and high tension, buckling of the compact

Table 1 Labels of the binary lipid systems simulated through DPD in Refs. [35,45]. v corresponds to the area-to-volume ratio parameter, defined as the total number of lipid particles over the number of solvent particles inside the vesicle. a_{AB} is the interaction strength between A and B lipids. $\phi_B^{(out)}$ and $\phi_B^{(in)}$ are the volume fraction of the B lipid in the outer and inner leaflet, respectively

System	v	a_{AB}	$\phi_B^{(out)}$	$\phi_B^{(in)}$
$\mathcal{A}_1^{(100)}$	0.462	100	0.3	0.3
$\mathcal{A}_2^{(100)}$	0.567	100	0.3	0.3
$\mathcal{A}_2^{(68)}$	0.567	68	0.3	0.3
$\mathcal{A}_2^{(50)}$	0.567	50	0.3	0.3
$\mathcal{C}_1^{(100)}$	0.462	100	0.5	0.5
$\mathcal{C}_2^{(100)}$	0.567	100	0.5	0.5
$\mathcal{C}_2^{(50)}$	0.567	50	0.5	0.5
$\mathcal{R}_1^{(50)}$	0.462	50	0.4	0.2
$\mathcal{R}_2^{(50)}$	0.567	50	0.4	0.2
$\mathcal{R}_3^{(50)}$	0.885	50	0.4	0.2

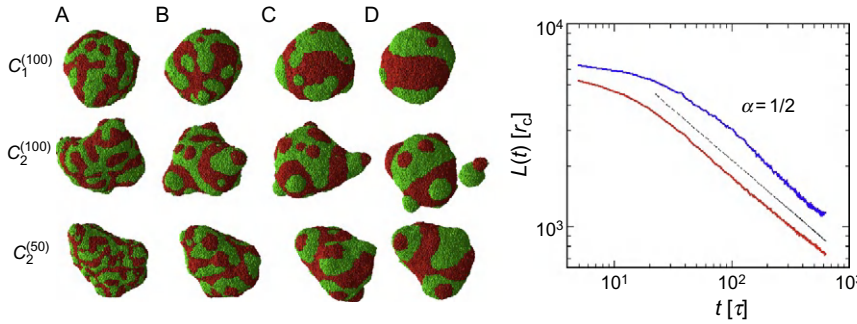

Figure 11 Snapshot sequences of closed vesicles with $\Phi_A = \Phi_B = 0.5$. Kinetics in systems $C_1^{(100)}$, $C_2^{(100)}$, and $C_2^{(50)}$ are shown. Columns (A) to (D) correspond to times $t = 100\ \tau$, $200\ \tau$, $400\ \tau$, and $700\ \tau$, respectively. The graph to the right depicts the total interfacial length as a function of time. The top and bottom solid lines correspond to $C_2^{(100)}$ and $C_2^{(50)}$, respectively. The slope of the dotted line is $-1/2$. Reprinted with permission from [35]. Copyright 2005, American Institute of Physics.

domains is clearly observed at $t \geq 100\ \tau$. This domain buckling is due to the fact that the line energy overcomes the bending energy of domains once they exceed a critical diameter $D_c \sim \kappa/\lambda$. This critical diameter is larger for the case of system $C_2^{(50)}$, and thus buckling is not observed for this system even at late times. The interfacial length of the domains, shown as a function of time in Fig. 11, scales with time as $L(t) \sim t^{-1/2}$, which is in contrast with the $t^{-1/3}$ growth observed in the DTMC simulations presented in Section 3 and TDGL simulations presented in Section 2. The $t^{-1/2}$ was also found in open membranes [45] following a critical quench, an indication that this growth law is independent of the membrane topology. Furthermore, as shown in Fig. 11, the $t^{-1/2}$ growth law in critical quenches of multicomponent membranes is robust and independent of the area-to-volume ratio (i.e., tension on the membrane). Recently, Ramachandran *et al.* [100], performed DPD simulations of a two-dimensional monolayer of simple particles embedded in a three dimensional fluid. The monolayer is kept in place through the action of an external potential. They found a domains' growth law, $R \sim 1/L(t) \sim t^{1/3}$, at late times for both critical and off-critical quenches. This growth law is different from that of binary lipid membranes after a critical quench. It must be emphasized, however, that the action of an external potential to constraint the monolayer in Ramachandran *et al.*'s simulations [100] leads to the breakdown of momentum conservation in vicinity of the monolayer. Therefore, the two systems are fundamentally different. The $t^{-1/2}$ growth law observed in the DPD simulation of a multicomponent membrane after a critical quench was independently confirmed by more recent TDGL simulations of model H in the viscous regime by Fan *et al.* [42] and Camley and

Brown [74]. Unfortunately, up to date, there is no detailed experimental study of phase separation kinetics in multicomponent membranes at critical quenches.

5.2. Effect of Area-to-Volume Ratio on Domain Growth in Multicomponent Membranes

As stated above, in the case of critical quenches, that is, for $\phi_{\rm B} = \phi_{\rm A} = 0.5$, the kinetics of phase separation is independent of area-to-volume ratio. However, the situation is different in the case of off-critical quenches. In Fig. 12, snapshots of systems $\mathcal{A}_1^{(100)}$ and $\mathcal{A}_2^{(100)}$ are shown. This figure indicates that the area-to-volume ratio has very little effect on the kinetics during the early times of the phase separation. Namely, the domains are circular during early times, with their curvature equal to that of the vesicle. During later times, however, one observes a noticeable qualitative difference between domain growths in the two systems: The domains remain mostly flat in the case of low area-to-volume ratio, $\mathcal{A}_1^{(100)}$, while becoming curved in the case of high area-to-volume ratio, $\mathcal{A}_2^{(100)}$. The buckling of the domains in the high area-to-volume ratio case is accompanied by a global reshaping of the vesicle into an almost spherical geometry, as demonstrated by the left graph of Fig. 12. During later times, many of the buckled domains reach the limit shape and detach from the vesicle, leading to a further reduction of the area-to-volume ratio. Once the vesicle becomes spherical in shape, no further domain vesiculation is observed [35,61]. The interfacial length is shown as a function of time in the right graph of Fig. 12. This figure substantiates the findings that during early times, the area-to-volume ratio has no effect on the dynamics. During this stage, the average domain size $R(t) \sim 1/L(t) \sim t^{1/3}$. To explain this growth law, monitored kinetics of the domains showed that the growth is the result of thermally induced Brownian motion of the domains and their coalescence. Two domains coalesce if they traveled a distance $l(t)$ determined by the average area on the membrane that is occupied by a domain, which is given by $l^2(t) = A_{\rm ves}/N(t)$, where $A_{\rm ves}$ is the area of the vesicle and $N(t)$ is the number of domains. Now, for a Brownian motion of the domains, $l^2(t) \sim D_R t$, where D_R is the domain diffusion coefficient, which for the case of a domain experiencing drag from the fluid above and below the domain is given by the well-known Stokes–Einstein relation, $D_R \sim 1/R$. This yield a domain radius, $R(t) \sim t^{1/3}$ and a number of domains $N(t) \sim t^{-2/3}$, in excellent agreement with the DPD findings in Refs. [35,61].

At intermediate times, the rapid decay in the interfacial length for the high area-to-volume ratio case, $\mathcal{A}_2^{(100)}$, is due to budding of domains with diameters exceeding κ/λ and the vesiculation of some of these domains [35,61]. At even later times, once the vesicle in the high area-to-volume ratio case reaches a spherical shape, the interfacial length decays as $L(t) \sim$

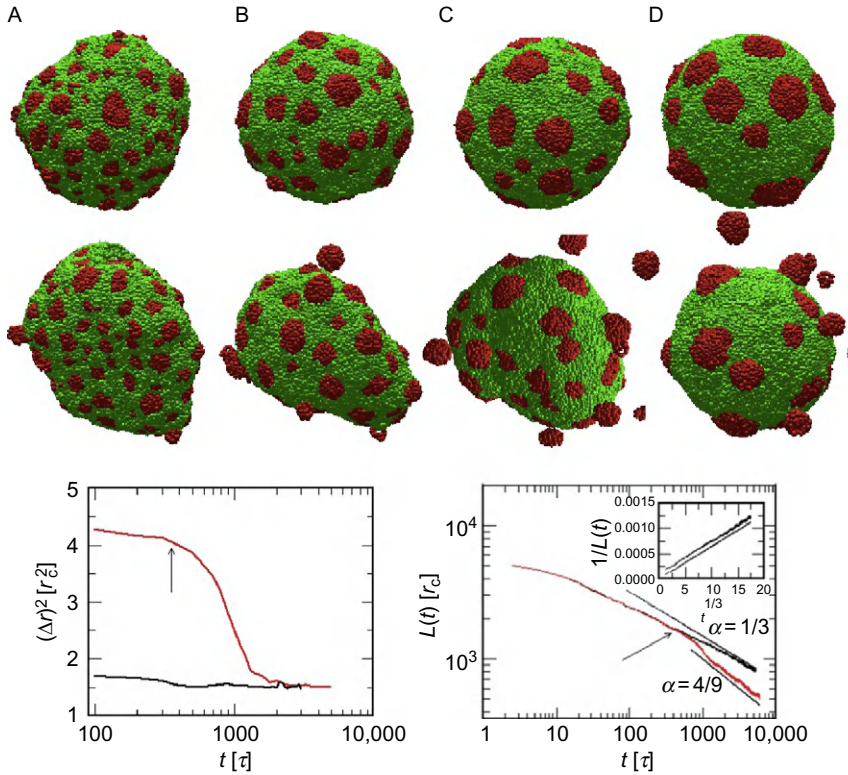

Figure 12 Snapshot sequences of closed vesicles showing the effect of area-to-volume ratio on domain growth. Systems correspond to $\phi_A = 0.7$, $\phi_B = 0.3$. The top and bottom row corresponds to $\mathcal{A}_1^{(100)}$ and $\mathcal{A}_2^{(100)}$. (A), (B), (C), and (D) correspond to $t = 100\ \tau$, $500\ \tau$, $1000\ \tau$, and $3000\ \tau$, respectively. The graph of the bottom left depicts the mean square of the distance of the majority (A) lipids from the vesicle's center of mass of the vesicle. The bottom and top curve corresponds to $\mathcal{A}_2^{(100)}$ and $\mathcal{A}_1^{(100)}$, respectively. The bottom right graph depicts the interfacial length for the same two systems. The top curve and bottom correspond to $\mathcal{A}_1^{(100)}$ and $\mathcal{A}_2^{(100)}$, respectively. The inset in the bottom left graph depicts $R(t) \sim 1/L(t)$ versus time in the low area-to-volume ratio case, $\mathcal{A}_1^{(100)}$. The inset shows clearly that the average domain size $R(t) \sim t^{1/3}$ in the low area-to-volume ratio case. Reprinted with permission from [35]. Copyright 2005, American Institute of Physics.

$t^{-\alpha}$, with $\alpha \approx 4/9$, markedly faster than in the case of low area-to-volume ratio, $\mathcal{A}_2^{(100)}$, as shown in Fig. 12. The faster growth law in the case of low area-to-volume ratio, $\mathcal{A}_1^{(100)}$, is due to the coalescence of well formed cap-shaped domains. In order to explain this growth regime, it is noted that the curvature of a cap is determined by a balance between its line energy and curvature energy. The average interfacial (neck) length of a single cap is therefore given by

$$l_{\text{cap}} \sim \left(\frac{\kappa a_{\text{cap}}}{\lambda}\right)^{1/3}. \tag{19}$$

As for the case of flat domains, the mean-square distance travelled by a capped domain is $l^2(t) \sim Dt$, where the diffusion coefficient, $D \sim a_{\text{cap}}^{-1/2}$ and $l^2(t) \sim A_{\text{ves}}/N(t)$. During late times, once there is no more fission of buds, $N(t)a_{\text{cup}} \sim$ const. Thus one obtains that the number of domains

$$N(t) \sim t^{-2/3}, \tag{20}$$

and the net interfacial length

$$L(t) = N(t)l_{\text{cap}} \sim t^{-4/9}, \tag{21}$$

in agreement with the computational findings presented above [35,61]. The decay of the number of domains as $t^{-2/3}$ was confirmed by Li *et al.* [31] in a study of a multicomponent tubular vesicles (very high area-to-volume ratio) composed of DPPC, DOPC and cholesterol. However, experimental measurements of the decay interfacial length during the phase separation process has not yet been done.

5.3. Effect of Line Tension on Domain Growth in Multicomponent Membranes

In this section, the effect of line tension on the phase separation kinetics is discussed. In Fig. 13, snapshot series for three systems, $\mathcal{A}_2^{(100)}$, $\mathcal{A}_2^{(68)}$, and $\mathcal{A}_2^{(50)}$ with decreasing values of the line tension are shown for comparison. All three systems have same compositions of the two components, corresponding to $\phi_{\text{B}} = 0.3$ and high area-to-volume ratio. The net interfacial lengths versus time of the three systems are also shown in Fig. 13. This figure clearly demonstrates that line tension has an important effect on domain growth in multicomponent membranes. In particular, Fig. 13 shows that the onset of domain budding is delayed to later times as the line tension is decreased. This is understood by recalling that a domain buds when its linear size, $R \approx \kappa/\lambda$. Figure 13 also shows that in the case of high line tension, $\mathcal{A}_2^{(100)}$, budding is followed by fission of many domains. In contrast, fission does not occur in the two other systems with lower line tension. This is quantitatively substantiated by the absence of a fast decay in the net interfacial length at intermediate times in systems $\mathcal{A}_2^{(68)}$, and $\mathcal{A}_2^{(50)}$. Figure 13 also shows that the net interfacial length exhibits two distinct regime with growth laws $L(t) \sim t^{-0.3}$ during early times, corresponding to the growth of flat domains, followed by a faster regime, $L(t) \sim t^{-4/9}$, during late times, which as discussed in Section 5.2 is due to the coalescence of capped domains.

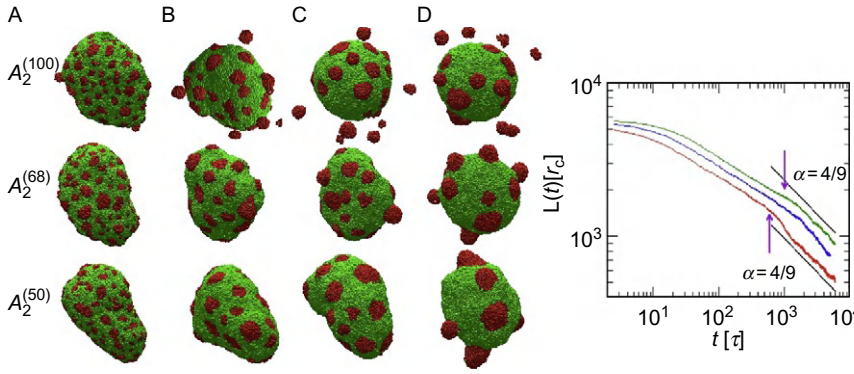

Figure 13 Snapshot sequences of closed vesicles showing the effect of line tension on domain growth for the case of $\phi_A = 0.7$, $\phi_B = 0.3$. Rows from top to bottom correspond to $\mathcal{A}_2^{(100)}$, $\mathcal{A}_2^{(68)}$, and $\mathcal{A}_2^{(50)}$, respectively. (A), (B), (C), and (D) correspond to $t = 100\,\tau$, $1000\,\tau$, $2000\,\tau$, and $4000\,\tau$, respectively. The graph at the bottom depicts the interfacial length for the three systems shown. Curves from bottom to top correspond to $\mathcal{A}_2^{(100)}$, $\mathcal{A}_2^{(68)}$, and $\mathcal{A}_2^{(50)}$, respectively. Reprinted with permission from [35]. Copyright 2005, American Institute of Physics.

5.4. Effect of Transbilayer Asymmetry in the Lipid Composition on Domain Growth in Multicomponent Membranes

In the previous subsections, DPD simulations of multicomponent membranes were performed for the case of a symmetric transbilayer composition of the lipids. However, the lipid distribution in the two leaflets of the plasma membrane of eukaryotic cells is asymmetric. Indeed, most of phosphatidylserine and phosphatidylethanolamine are located in the cytoplasmic leaflet of the plasma lipid bilayer. In contrast, sphingomyelin and phosphatidylcholine are predominately present in the outer leaflet [101]. This asymmetry is actively maintained by the cell and is essential to many biological functions. Since lipid rafts are rich in sphingomyelin and cholesterol, it is often assumed that lipid rafts are only on the outer leaflet of the plasma membrane. The absence of non- or partially overlapping domains in fluorescence micrographs of multicomponent giant vesicles, implies that lipid domains on both leaflets of the plasma membrane must be in register [11]. Since there exist, a small amount of sphingomyelin in the cytoplasmic leaflet, smaller lipid rafts are also expected on this leaflet, and a colocalization of these rafts with the larger ones on the outer leaflet is expected [45]. In order to minimize the interfacial energy between the L_o and L_d domains, the area difference between the inner and outer domains lead to their buckling, as shown schematically in Fig. 14. The induced spontaneous curvature is determined by the ratios of the compositions of the two leaflets,

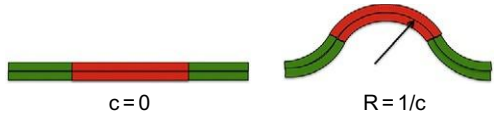

Figure 14 Domain configuration that minimizes the interaction energy between lipids for the case where the domains in the two leaflets have same area (left) and different areas (right).

$$c_0 = \left(\frac{2}{\varepsilon}\right)\left[\frac{\left(\phi_{\mathrm{B}}^{(\mathrm{out})}/\phi_{\mathrm{B}}^{(\mathrm{in})}\right)^{1/2} - 1}{\left(\phi_{\mathrm{B}}^{(\mathrm{out})}/\phi_{\mathrm{B}}^{(\mathrm{in})}\right)^{1/2} + 1}\right], \tag{22}$$

where, ε is the membrane thickness.

Motivated by the arguments above, DPD simulations of the effect of this transbilayer asymmetry in lipid composition was performed on vesicles with different values of the area-to-volume ratio [45]. Snapshots corresponding to systems, $\mathcal{R}_1^{(50)}$, $\mathcal{R}_2^{(50)}$, and $\mathcal{R}_3^{(50)}$ with increasing values of the area-to-volume ratio are shown in Fig. 15. These systems correspond to $\phi_{\mathrm{B}}^{(\mathrm{out})} = 0.4$ and $\phi_{\mathrm{B}}^{(\mathrm{in})} = 0.2$. Figure 15 demonstrates that the transbilayer asymmetry in the lipid distribution induces a spontaneous curvature since very early times, provided the vesicle has enough excess area to accommodate for this. Since the system, $\mathcal{R}_1^{(50)}$, has a low area-to-volume ratio, capping of the domains is not possible despite the fact that the domains have a finite intrinsic spontaneous curvature given by Eq. (22). Figure 15 also shows that the curvature of the domains in the case of system $\mathcal{R}_2^{(50)}$ is lower than that of system $\mathcal{R}_3^{(50)}$. This is due to the higher excess area in the latter.

A comparison between the interfacial length of system $\mathcal{R}_2^{(50)}$ and its counterpart with same parameters but with symmetric transbilayer lipid distribution, $\mathcal{A}_2^{(50)}$ is shown in Fig. 15. This figure clearly demonstrates that the asymmetry in the lipid distribution leads to a dramatic difference in the kinetics of the two systems. In particular, domain growth at late times in system $\mathcal{R}_2^{(50)}$ is markedly slower than in system $\mathcal{A}_2^{(50)}$. The weak growth law, $L(t) \sim t^{-0.14}$ is an indication that during late times, an asymmetric transbilayer lipid distribution may lead to a microphase separation. For the highest excess area, corresponding to system $\mathcal{A}_3^{(50)}$, growth of domain is again fast, with $L(t) \sim t^{-1/3}$. This implies that microphase separation is only observed at intermediate membrane tension. These results are in fair agreement with recent mean field calculations by Harden *et al.* [67]. The microphase separation observed at intermediate tension and in the presence of asymmetry in lipid distribution could be the result of an effective repulsive interaction between domains. Interestingly, arrest in domain growth was recently observed by Yanagisawa *et al.* in a study of a

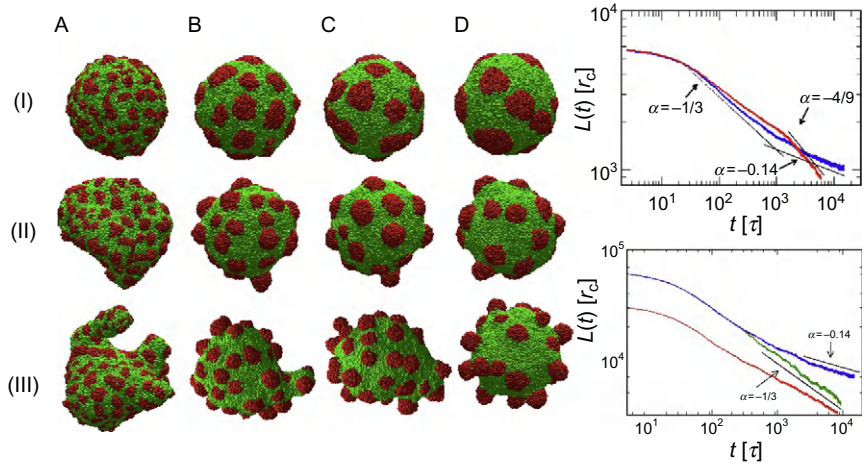

Figure 15 Snapshot sequences of closed vesicles showing the effect of transbilayer lipid distribution. Rows from top to bottom correspond to systems x, y, and z, respectively. (A), (B), (C), and (D) correspond to $t = 100\ \tau$, $1000\ \tau$, $2000\ \tau$, and $5000\ \tau$, respectively. The graph at the bottom left depicts the interfacial length for a symmetric transbilayer lipid distribution (bottom curve at $t = 2000\ \tau$) and asymmetric lipid distribution (top curve at $t = 2000\ \tau$). The graph at the bottom left depicts the interfacial length for the three systems. Reprinted with permission from [45]. Copyright 2006, American Physical Society.

ternary mixture composed of DPPC, DOPC, and cholesterol [32]. These results thus indicate that the finite size of lipid rafts might as well be the result of asymmetry in the transbilayer lipid distribution in the plasma membrane.

6. Conclusion

In this chapter, a review of coarse-grained computational studies of the phase separation of multicomponent membranes is presented. Four main coarse-grained approaches have been used to study the kinetics of phase separation in multicomponent membranes in recent years. These correspond to time-dependent Ginzburg–Landau (TDGL) models, DTMC, coarse-grained molecular dynamics, and DPD. Coarse-grained molecular dynamics based on the MARTINI force field [59] are very promising since this approach allows for the investigation of the phase separation in specific ternary mixtures. However, due to computer limitations, as of now the MARTINI approach cannot probe large systems and during late times, where the dynamics is most interesting. The DTMC approach is fully dissipative and, therefore, cannot account for hydrodynamic interactions.

Hydrodynamic interactions can be incorporated in the TDGL simulations. However, due to the complex nature of these simulations, the effect of hydrodynamics on the phase separation in TDGL models have thus far been accounted for in the context of flat membranes only. Due to the relatively low bending modulus of lipid membranes ($\kappa \sim 10\ k_B T$), membranes can easily deform, and these curvature deformations can play an important role on the kinetics. Furthermore, the constraint of inner volume, in the case of closed vesicles, cannot easily be accounted for in both the DTMC and TDGL simulations. Moreover, topological changes of the membrane cannot be easily accounted for in both TDGL and DTMC approaches. DPD is a particle-based model that inherently accounts for hydrodynamics, area-to-volume ratio, and topological changes of the membrane. This makes DPD a very promising approach to investigate the complex kinetics of the phase separation in multicomponent lipid membranes. DPD simulations, thus far performed, have shown complex kinetics that depend strongly on the area-to-volume ratio, line tension, and composition of the components. The DPD simulations have also shown that in the case where the transbilayer lipid distribution is not symmetric, a slowing down in the kinetics is observed, an indication that the system may approach a microphase separation. The transbilayer asymmetry in the lipid distribution has recently been proposed as a possible mechanism in maintaining the nanoscale size of lipid domain (i.e., lipid rafts) in the plasma membrane [45]. Other mechanisms have recently been proposed as an alternative for the finite size lipid rafts [43,44]. These include lipid recycling and the presence of transmembrane proteins that are pinned by the cortical cytoskeleton. These effects have recently been investigated through the TDGL model [43]. An investigation of these effects on the phase separation of multicomponent lipid membranes through DPD would, therefore, be very useful in providing a better understanding of the nanoscale size of lipid rafts.

ACKNOWLEDGMENTS

ML acknowledges financial support from NSF (DMR 0812470), NSF (DMR 0755447), NSF (EPS 1004083), and the Research Corporation (CC66879). PBSK acknowledges financial support from CSIR-India. The authors acknowledge Professors M. Haataja, S.J. Marrink, and T. Taniguchi, for allowing us to use their figures in this chapter.

REFERENCES

[1] B. Alberts, A. Johnson, J. Lewis, M. Raff, Molecular Biology of the Cell, 5th Ed, Garland Science, London, 2007.
[2] O.G. Mouritsen, Life as a Matter of Fat, Springer-Verlag, Berlin, 2005.
[3] L. Pike, The challenge of lipid rafts, J. Lipid Res. (2009) S323–S328.

[4] S.J. Singer, G.L. Nicolson, Fluid mosaic model of structure of cell-membranes, Science 175 (1972) 720–731.
[5] M.J. Karnocsky, A.M. Kleinfeld, R.L. Hoover, R.D. Klausner, Concept of lipid domains in membranes, J. Cell. Biol. 94 (1982) 1–6.
[6] K. Simons, G. van Meer, Lipid sorting in epithelial cells, Biochemistry 27 (1988) 6197–6202.
[7] L.J. Pike, Lipid rafts: heterogeneity on the high seas, Biochem. J. 378 (2004) 281–292.
[8] A. Pralle, P. Keller, E.L. Florin, K. Simons, J.K.H. Horber, Sphingolipid cholesterol rafts diffuse as small entities in the plasma membrane of mammalian cells, J. Cell. Biol. 148 (2000) 997–1008.
[9] A. Kusumi, I. Koyama-Honda, K. Suzuki, Molecular dynamics and interaction for creation of stimulation-induced stabilized rafts from small unstable rafts, Traffic 5 (2004) 213–230.
[10] L.J. Pike, Rafts defined: a report on the keystone symposium on lipid rafts and cell function, J. Lipid Res. 47 (2006) 1597–1598.
[11] L.A. Bagatolli, P.B. Sunil Kumar, Phase behavior of multicomponent membranes: experimental and computational techniques, Soft Matt. 5 (2009) 3234–3248.
[12] J.B. Helms, C. Zurzolo, Lipids as targeting signals: lipid rafts and intracellular trafficking, Traffic 5 (2004) 247–254.
[13] K. Simons, E. Ikonen, Functional rafts in cell membranes, Nature 387 (1997) 569–572.
[14] A. Schlegel, et al.Crowded little caves: structure and function of caveolae, Cell Signal 10 (1998) 457–463.
[15] G. van Mer, H. Sprong, Membrane lipids and vesicular traffic, Curr. Opin. Cell Biol. 16 (2004) 373–378.
[16] N. Chazal, D. Gerlier, Virus entry, assembly, budding, and membrane rafts, Microbiol. Mol. Biol. Rev. 67 (2003) 226–237.
[17] D. Raucher, M.P. Sheets, Characteristics of a membrane reservoir buffering membrane tension, Biophys. J. 77 (1999) 1992–2002.
[18] P. Sens, M.S. Turner, Budded membrane microdomains as tension regulators, Phys. Rev. E 73 (2006) 031918.
[19] D.A. Brown, E. London, Structure and function of sphingolipid- and cholesterol-rich membrane rafts, J. Biol. Chem. 275 (2000) 17221–17224.
[20] S. Sonnino, A. Prinetti, Membrane lipid domains and membrane lipid domain preparations: are they the same thing, Trends Glycosci. Glycotechnol. 20 (2008) 315–340.
[21] M. Rao, S. Mayor, Use of Forster Õs resonance energy transfer microscopy to study lipid rafts, Biochem. Biophys. Acta 1746 (2005) 221–233.
[22] J.R. Silvius, D. del Guidice, M. Lafleur, Cholesterol at different bilayer concentrations can promote or antagonize lateral segregation of phospholipids of differing acyl chain length, Biochem. 35 (1996) 15198–15208.
[23] J. Korlach, P. Schwille, W.W. Webb, G.W. Feigenson, Characterization of lipid bilayer phases by confocal microscopy and fluorescence correlation spectroscopy, Proc. Natl. Acad. Sci. 96 (1999) 8461–8466.
[24] L.A. Bagatolli, E. Gratton, A correlation between lipid domain shape and binary phospholipid mixture composition in free standing bilayers: a two-photon fluorescence microscopy study, Biophys. J. 79 (2000) 434–447.
[25] C. Dietrich, L.A. Bagatolli, Z.N. Volovyk, N.L. Thompson, M. Levi, K. Jacobson, E. Gratton, Lipid rafts reconstituted in model membranes, Biophys. J. 80 (2001) 1417–1428.
[26] S.L. Veatch, S.L. Keller, Organization in lipid membranes containing cholesterol, Phys. Rev. Lett. 89 (2002) 268101-1–268101-4.

[27] T. Baumgart, S.T. Hess, W.W. Webb, Imaging coexisting fluid domains in biomembrane models coupling curvature and line tension, Nature (London) 425 (2003) 821–824.
[28] A.R. Honerkamp-Smith, P. Cicuta, M.D. Collins, S.L. Veatch, M. den Nijs, M. Schick, S.L. Keller, Line tensions, correlation lengths, and critical exponents in lipid membranes near critical points, Biophys. J. 95 (2008) 236–246.
[29] S.L. Veatch, S.L. Keller, Miscibility phase diagrams of giant vesicles containing sphingomyelin, Phys. Rev. Lett. 94 (2005) 148101-1–148101-4.
[30] T. Baumgart, S. Das, W.W. Webb, J.T. Jenkins, Membrane elasticity in giant vesicles with fluid phase coexistence, Biophys. J. 89 (2005) 1067–1080.
[31] L. Li, X. Liang, M. Lin, Y. Wang, Budding dynamics of multicomponent tubular vesicles, J. Am. Chem. Soc. 127 (2005) 17996–17997.
[32] M. Yanagisawa, M. Imai, T. Masui, S. Komura, T. Ohta, Growth dynamics of domains in ternary fluid vesicles, Biophys. J. 92 (2007) 115–125.
[33] J.D. Gunton, M. San Miguel, P.S. Sahni, in: C. Domb, J.L. Lebowitz (Eds.), Phase Transitions and Critical Phenomena, Vol. 8, Academic Press, New York, 1983, p. 265.
[34] A. Bray, Theory of phase-ordering kinetics, Adv. Phys. 43 (1994) 357–459.
[35] M. Laradji, P.B. Sunil Kumar, Domain growth, budding, and fission in phase-separating self-assembled fluid bilayers, J. Chem. Phys. 123 (2005) 224902-1–224902-10.
[36] R. Lipowsky, E. Sackman, Structure and dynamics of membranes, Elsevier, Amsterdam, 1995.
[37] S. Mayor, M. Rao, Rafts: scale-dependent, active lipid organization at the cell surface, Traffic 5 (2004) 231–240.
[38] S.L. Veatch, O. Soubias, S.L. Keller, K. Gawrisch, Critical fluctuations in domain forming lipid mixtures, Proc. Natl. Acad. Sci. 104 (2007) 17650–17655.
[39] S.L. Veatch, P. Sengupta, A. Honerkamp-Smith, D. Holowka, B. Baird, Critical fluctuations in plasma membrane vesicles, ACS Chem. Bio. 3 (2008) 287–293.
[40] A. Yethiraj, J.C. Weisshaar, Why are lipid rafts not observed in vivo? Biophys. J. 93 (2007) 3113–3119.
[41] M.J. Swamy, L. Ciani, M.T. Ge, A.K. Smith, D. Holowka, B. Baird, J.H. Freed, Coexisting domains in the plasma membranes of live cells characterized by spin-label ESR spectroscopy, Biophys. J. 90 (2007) 4452–4465.
[42] J. Fan, T. Han, M. Haataja, Hydrodynamic effects on spinodal decomposition kinetics in planar lipid membranes, J. Chem. Phys. 133 (2010) 235101-1–235101-10.
[43] J. Fan, M. Sammakorpi, M. Haataja, Lipid microdomains: structural correlations, fluctuations and formation mechanisms, Phys. Rev. Lett. 104 (2010) 118101-1–118101-4.
[44] L. Foret, A simple mechanism of raft formation in two-component fluid membranes, Europhys. Lett. 71 (2005) 508–514.
[45] M. Laradji, P.B. Sunil Kumar, Anomalously slow domain growth in fluid membranes with asymmetric transbilayer lipid distribution, Phys. Rev. E 73 (2006) 040901-1–040901-4.
[46] T.S. Ursell, W.S. Klug, R. Philips, Morphology and interaction between lipid domains, Proc. Natl. Acad. Sci. 106 (2009) 13301–13306.
[47] T. Taniguchi, Shape deformation and phase separation dynamics of two-component vesicles, Phys. Rev. Lett. 76 (1996) 4444–4447.
[48] J.L. McWhirter, G. Ayton, G.A. Voth, Coupling field theory with mesoscopic dynamical simulations of multicomponent lipid bilayers, Biophys. J. 87 (2004) 3242–3263.

[49] G.S. Ayton, J.L. McWhirter, G.A. Voth, Coupling field theory with continuum mechanics: a simulation of domain formation in giant unilamellar vesicles, Biophys. J. 88 (2005) 3855–3869.
[50] G.S. Ayton, J.L. McWhirter, G.A. Voth, A second generation mesoscopic lipid bilayer model: corrections to field theory descriptions of membranes and nonlocal hydrodynamics, J. Chem. Phys. 124 (2006) 064906-1–064906-12.
[51] P.B. Sunil Kumar, M. Rao, Novel Monte Carlo approach to the dynamics of fluids: single-particle diffusion, correlation functions, and phase ordering of binary fluids, Phys. Rev. Lett. 77 (1996) 1067–1070.
[52] P.B. Sunil Kumar, M. Rao, Kinetics of phase ordering in a two-component fluid membrane, Mol. Cryst. Liq. Cryst. 288 (1996) 105–118.
[53] P.B. Sunil Kumar, M. Rao, Shape instabilities in the dynamics of a two-component fluid membrane, Phys. Rev. Lett. 80 (1998) 2489–2492.
[54] P.B.S. Kumar, G. Gompper, R. Lipowsky, Budding dynamics of multicomponent membranes, Phys. Rev. Lett. 86 (2001) 3911–3914.
[55] P.S. Niemela, S. Ollila, M.T. Hyvonen, M. Karttunen, I. Vattulainen, Assessing the nature of lipid raft membranes, PLoS Comput. Biol. 3 (2007) 304–312.
[56] T. Apajalahti, P. Niemela, P. Praveen, N. Govindan, M. Miettinen, E. Salonen, S.J. Marrink, I. Vattulainen, Concerted diffusion of lipids in raft-like membranes, Faraday Disc. 144 (2010) 411–430.
[57] I.R. Cooke, K. Kremer, M. Deserno, Tunable generic model for fluid bilayer membranes, Phys. Rev. E 72 (2005) 011506-1–011506-4.
[58] C. Zheng, P. Liu, J. Li, Y.-W. Zhang, Phase diagrams for multi-component membrane vesicles: a coarse-grained modeling study, Langmuir 26 (2010) 12659–12666.
[59] H.J. Risselada, S.J. Marrink, The molecular face of lipid rafts in model membranes, Proc. Natl. Acad. Sci. 105 (2008) 17367–17372.
[60] S. Yamamoto, S.A. Hyodo, Budding and fission dynamics of two-component vesicles, J. Chem. Phys. 118 (2003) 7937–7943.
[61] M. Laradji, P.B. Sunil Kumar, Dynamics of domain growth in self-assembled fluid vesicles, Phys. Rev. Lett. 93 (2004) 198105-1–198105-4.
[62] I.L. Lifshitz, V.V. Slyozov, The kinetics of precipitation from supersaturated solid solutions, J. Phys. Chem. Solids 19 (1962) 35–50.
[63] S. Leibler, D. Andelman, Ordered and curved meso-structures in membranes and amphiphilic films, J. Physique 48 (1987) 2013–2018.
[64] P.L. Hansen, L. Miao, J.H. Ipsen, Fluid lipid bilayers: intermonolayer coupling and its thermodynamic manifestations, Phys. Rev. E 58 (1998) 2311–2324.
[65] P.B. Sunil Kumar, G. Gompper, R. Lipowsky, Modulated phases in multicomponent fluid membranes, Phys. Rev. E 60 (1999) 4610–4618.
[66] Y. Jiang, T. Lookman, A. Saxena, Phase separation and shape deformation of two-phase membranes, Phys. Rev. E 61 (2000) R57–R61.
[67] J.L. Harden, F.C. MacKintosh, P.D. Olmsted, Budding and domain shape transformations in mixed lipid films and bilayer membranes, Phys. Rev. E 72 (2003) 011903-1–011903-13.
[68] E.J. Wallace, N.M. Hooper, P.D. Olmsted, The kinetics of phase separation in asymmetric membranes, Biophys. J. 88 (2005) 4072–4083.
[69] C.M. Funkhouser, F.J. Solis, K. Thornton, Coupled composition-deformation phase-field method for multicomponent lipid membranes, Phys. Rev. E 76 (2007) 011912-1–011912-15.
[70] F.J. Solis, C.M. Funkhouser, K. Thornton, Conditions for planarity in membranes: applications to multicomponent membranes with lamellar morphology, Europhys. Lett. 82 (2008) 38001-1–38001-6.

[71] L. Leibler, Theory of microphase separation in block copolymers, Macormolecules 13 (1980) 1602–1617.
[72] M. Bahiana, Y. Oono, Cell dynamical approach to block coploymers, Phys. Rev. A 41 (1990) 6763–6771.
[73] J. Fan, M. Sammalkorpi, M. Haataja, Influence of nonequilibrium lipid transport, membrane compartmentalization, and membrane proteins on the lateral organization of the plasma membrane, Phys. Rev. E 81 (2010) 011908-1–011908-15.
[74] B.A. Camley, F.L.H. Brown, Dynamic simulations of multicomponent lipid membranes over long length and time scales, Phys. Rev. Lett. 105 (2010) 148102-1–148102-4.
[75] B.I. Hohenberg, P.C. Halperin, Theory of dynamic critical phenomena, Rev. Mod. Phys. 49 (1977) 435–479.
[76] M.A. Lomholt, P.L. Hansen, L. Miao, A general theory of non-equilibrium dynamics of lipid-protein fluid membranes, Euro. Phys. J. E 16 (2005) 439–461.
[77] A. Baumgärtner, J.-S. Ho, Crumpling of fluid vesicles, Phys. Rev. A 41 (1990) 5747–5750.
[78] S. Ramachandran, M. Laradji, P.B. Sunil Kumar, Lateral organization of lipids in multi-component liposomes, J. Phys. Soc. Jpn. 78 (2009) 041006.
[79] R. Goetz, R. Lipowsky, Computer simulations of bilayer membranes: self-assembly and interfacial tension, J. Chem. Phys. 108 (1998) 7397–7409.
[80] R. Goet, G. Gompper, R. Lipowsky, Mobility and elasticity of self-assembled membranes, Phys. Rev. Lett. 82 (1999) 221–224.
[81] S.J. Marrink, A.H. de Vries, A.E. Mark, Coarse-grained model for semiquantitative lipid simulations, J. Phys. Chem. B 108 (2004) 750–760.
[82] S.J. Marrink, H.J. Risselada, S. Yefimov, D.P. Tieleman, A.H. de Vries, The MARTINI force field: coarse grained model for biomolecular simulations, J. Phys. Chem. B 111 (2007) 7812–7824.
[83] Details of the MARTINI force field parameters are found in the website, http://md.chem.rug.nl/cgmartini/index.php/downloads/force-field-parameters.
[84] P.J. Hoogerbrugge, J.M.V.A. Koelman, Simulating microscopic hydrodynamic phenomena with dissipative particle dynamics, Europhys. Lett. 19 (1992) 155–160.
[85] P. Espanol, P. Warren, Statistical-mechanics of dissipative particle dynamics, Europhys. Lett. 30 (1995) 191–196.
[86] R.D. Groot, P.B. Warren, Dissipative particle dynamics: bridging the gap between atomistic and mesoscopic simulation, J. Chem. Phys. 107 (1997) 4423–4435.
[87] M.J.A. Hore, M. Laradji, Dissipative particle dynamics simulation of the interplay between spinodal decomposition and wetting in thin film binary fluids, J. Chem. Phys. 132 (2010) 024908-1–024908-10.
[88] W. Jiang, J. Huang, Y. Wang, M. Laradji, Hydrodynamic interaction in polymer solutions simulated with dissipative particle dynamics, J. Chem. Phys. 126 (2007) 044901-1–044901-12.
[89] R.D. Groot, T.J. Madden, D.J. Tildesley, On the role of hydrodynamic interactions in block copolymer microphase separation, J. Chem. Phys. 110 (1999) 9739–9749.
[90] M. Laradji, M.J.A. Hore, Nanospheres in phase-separating multicomponent fluids: a three-dimensional dissipative particle dynamics simulation, J. Chem. Phys. 121 (2004) 10641–10647.
[91] M.J.A. Hore, M. Laradji, Microphase separation induced by interfacial segregation of isotropic, spherical nanoparticles, J. Chem. Phys. 126 (2007) 224903-1–224903-8.
[92] M.J.A. Hore, M. Laradji, Prospects of nanorods as an emulsifying agent of immiscible blends, J. Chem. Phys. 128 (2008) 054901-1–054901-8.

[93] J. Huang, Y. Wang, M. Laradji, Flow control by smart nanofluidic channels: a dissipative particle dynamics simulation, Macromolecules 39 (2006) 5546–5554.
[94] J.A. Millan, W. Jiang, M. Laradji, Y. Wang, Pressure driven flow of polymer solutions in nanoscale slit pores, J. Chem. Phys. 126 (2007) 124905-1–124905-9.
[95] J.A. Millan, M. Laradji, Cross-stream migration of driven polymer solutions in nanoscale channels: a numerical study with generalized dissipative particle dynamics, Macromolecules 42 (2009) 903–910.
[96] S. Thakur, K.R. Prathyusha, A.P. Deshpande, M. Laradji, P.B. Sunil Kumar, Shear induced ordering in branched living polymer solutions, Soft Matt. 6 (2010) 489–492.
[97] M. Ripoll, M.H. Ernst, P. Español, Large scale and mesoscopic hydrodynamics for dissipative particle dynamics, J. Chem. Phys. 115 (2001) 7271–7284.
[98] M. Venturoli, B. Smit, M.M. Sperotto, Simulation studies of protein-induced bilayer deformations, and lipid-induced protein tilting, on a mesoscopic model for lipid bilayers with embedded proteins, Biophys. J. 88 (2005) 1778–1798.
[99] S. Ramachandran, P.B. Sunil Kumar, M. Laradji, Lipid flip-flop driven mechanical and morphological changes in model membranes, J. Chem. Phys. 129 (2008) 125104-1–125104-5.
[100] S. Ramachadran, Effects of an embedding bulk fluid on phase separation dynamics in a thin liquid film, Europhys. Lett. 89 (2010) 56001-1–56001-6.
[101] P.F. Devaux, A. Zachowski, Maintenance and consequences of membrane phospholipid asymmetry, Chem. Phys. Lipid 73 (1994) 107–120.

CHAPTER EIGHT

Fluorescence Spectroscopy Study of Hyaluronan–Phospholipid Interactions

Filip Mravec,[1] Martina Klučáková,[1] *and* Miloslav Pekař[1,*]

Contents

Abstract

Capability of phospholipids with positive charge to form complexes with hyaluronan in aqueous solutions, in a similar way as traditional cationic surfactants, was investigated by fluorescence probes. DPPC and lecithin aggregate in aqueous solution to form micelle-like structures capable to solubilize hydrophobic molecules. Changes in aggregation behavior after adding hyaluronan were observed only in the case of lecithin. Further, nonionic biocompatible surfactant was used as additional dispersion environment in phospholipid–hyaluronan system with phospholipid molecules acting as a physical linker bonding micelles and biopolymer.

* Corresponding author. Tel.: +420-541149330; Fax: +420-541149398.
E-mail address: pekar@fch.vutbr.cz

[1] Centre for Materials Research, Faculty of Chemistry, Brno University of Technology, Brno, Czech Republic

Advances in Planar Lipid Bilayers and Liposomes, Volume 14
ISSN 1554-4516, DOI: 10.1016/B978-0-12-387720-8.00008-X

1. Introduction

Polysaccharides and their derivatives have become major components in the development of biocompatible and biodegradable materials with many areas of applications especially in beauty and health care (e.g., cosmetics, tissue engineering, or drug delivery). Phospholipids are another class of biomolecules with specific function particularly in forming cellular structures. Also, phospholipids have found practical applications in cosmetic and medical products, mainly in the form of liposomes.

Among polysaccharides, hyaluronan (HA) can be viewed as a rather unique macromolecule which has very simple chemical structure (repeating unit) but several and different physiological functions. Hyaluronan is a common name for hyaluronic acid or, more precisely, its sodium salt. Hyaluronan is a naturally occurring linear high molecular polysaccharide composed of repeating β-(1→4)-D-glucuronic acid β-(1→3)-*N*-acetyl-D-glucosamine disaccharide units [1–3] (see Fig. 1).

Hyaluronan is a polymer with a wide range of naturally occurring molecular masses from several hundred to 10 million g mol^{-1} [1,3] possessing one carboxylate group per disaccharide repeating unit, and is therefore a polyelectrolyte bearing a negative charge. Hyaluronan can be found primarily in the extracellular matrix [1–3] of all higher organisms, especially in connective tissues, synovial fluid, and eye vitreous and is produced by certain strains of bacteria. The biological functions of hyaluronan include maintenance of elastoviscosity of liquid connective tissues such as joint synovial fluid and eye vitreous, control of tissues hydration and water transport due to its immense ability to retain water [4,5]. Hyaluronan participates in supramolecular assembly of proteoglycans in the extracellular matrix and in numerous receptor-mediated roles in cell detachment, mitosis, migration, tumor development, metastasis, and inflammation [2,4,6].

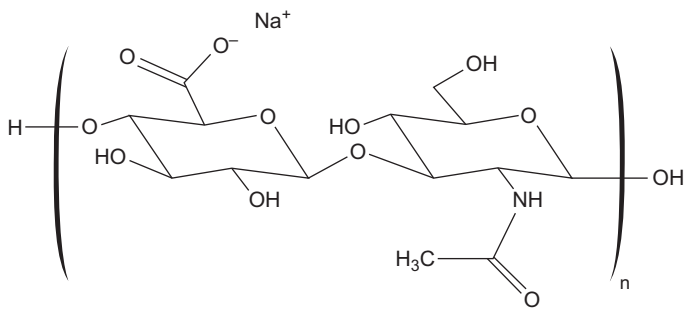

Figure 1 Structural unit of hyaluronan.

For these functions, multivalent interactions of HA with specific cell surface receptors such as CD44 and RHAMM are important [1,3,4,6]. Various tumors overexpress hyaluronan-binding receptors and consequently these tumor cells show enhanced binding and internalization of HA. Thus, HA coupled with, for instance, cytotoxic agents represents a nontoxic prodrug [6] and such conjugate is internalized into tumor cells through receptor-mediated endocytosis, followed by a release of active drugs, thus restoring their original toxicity.

Hyaluronan has, therefore, found important applications in drug delivery and surgery, and has been found to enhance absorption of drugs and proteins through mucus tissues [1,3,7]. It is used as an adjuvant for ophthalmic drug delivery [1,3] as a viscosity enhancing polymer for eye drops [1,8]. Hyaluronan has found important applications in the field of visco-surgery, visco-supplementation, and wound healing, furthermore as a supplementation of the synovial fluid in patients with osteoarthritis [3,7]. Hyaluronan is increasingly used in cosmetics, mainly as a moisturizing, epidermal renewal, and antiaging agent.

Phospholipids and phosphatidylcholine, in particular, are found as the most important constituents of many biological membranes. In cells, they work not only as a semipermeable barrier separating and protecting the cell from its environment and enabling transfer of ions but participate also in various cellular events. When used in cosmetic products, phospholipids show conditioning, softening, nourishing, and refattening effects. Conveniently, they are applied in liposomal form which is perhaps the most natural form of these molecules. However, just this form is not really substantial for turning out the desirable functions of phospholipids and their effectiveness is more a matter of the chemical composition of the cosmetic product than of the liposomal structure. Liposomes also have limited bearing capacity especially for lipophilic cosmetic ingredients and are not very suitable for lipid-rich cosmetic products. Different colloids or even nanosystems like nanoemulsions are, therefore, sought to extend applicability of phospholipids [8].

From the colloid chemistry point of view, phospholipids can be considered as a special type of surfactants. Hyaluronan, because of its negative charge, is known to interact with cationic surfactants, in particular, forming hyaluronan-surfactant complexes at concentrations well below the critical micellar concentration of pure surfactant. In this work, positively charged phospholipids were viewed and used as "common surfactants" and tested for their interactions with hyaluronan.

Study of hyaluronan–surfactant interactions is not a completely new field but the interest has been focused preferably on interactions between hyaluronan and liposomes.

The interactions of high molecular weight hyaluronan with di-palmitoyl phosphatidylcholine (DPPC) liposomes in aqueous buffer were investigated by Crescenzi *et al.* [9]. The superstructures resulting from co-incubation *in vitro*

were observed by means of negative staining and rotary shadowing electron microscopy. The existence of supramolecular complex between hyaluronan and DPPC was demonstrated. The complex would exist *in vivo* in the synovial fluid and should be responsible for the unique physiological properties.

Gómez-Gaete *et al.* [10] described the supramolecular organization of hybrid microparticles encapsulating dexamethasone (DXM) prepared by spray drying DPPC and hyaluronic acid. The effect of DXM concentration on size distribution and encapsulation efficacy was evaluated as a function of concentration of hyaluronic acid. *In vitro* release studies showed that hyaluronic acid does not influence DXM release kinetics. In the dry microparticles, DXM is probably mostly in amorphous domains within the DPPC–hyaluronic matrix. Upon hydration, the majority of the drug is released and only a small amount of DXM interacts with DPPC.

The chain flexibility of solutions of hyaluronan of different molecular weights in the absence and presence of the DPPC by ^{1}H-NMR spectroscopy, gel permeation chromatography, and multi-angle laser-light-scattering photometry were studied in [11] and [12]. Authors demonstrated that the sonication of high or low molecular weight hyaluronan with DPPC for periods markedly increased the chain flexibility of hyaluronan. They proposed that DPPC competes for the hydrophobic centers along the hyaluronan chain which are normally responsible for the inter and intra chain interactions and which confer stiffness to the molecule of hyaluronan.

Japan authors in [13] examined the effects of DPPC on the flexor tendon and its protective effect against postoperative adhesion. The friction coefficient was significantly lower with the mixture of DPCC and hyaluronan than with saline solution of hyaluronan. They concluded that the decreased friction coefficient indicates that DPPC could complement the boundary-lubricating ability of the tendon.

The lubrication systems in many sites in the body were reviewed in [14]. The systems consist of fluid adjacent to surfaces coated with an oligolamellar lining of surface-active phospholipid (SAPL) acting as a back-up boundary lubricant wherever the fluid film fails to support the load—a likely event at physiological velocities. It was explained how proteoglycans and hyaluronic acid could have carrier functions for the highly insoluble SAPL, while hyaluronic acid has good wetting properties needed to promote hydrodynamic lubrication of a very hydrophobic articular surface by an aqueous fluid wherever the load permits.

A standard (four-ball) test were used to study the anti-wear capabilities of ovine synovial fluid, the phospholipid extracted from it, a synthetic synovial fluid, and the phospholipid removed from the articular surface by a lipid solvent. The results were discussed as consistent with the hypothesis that the joints are lubricated by oligolamellar phospholipid as a lamellated solid (graphite-like) lubricant adsorbed onto the articular surface or otherwise deposited from synovial fluid [15].

Kawano *et al.* [16] examined *in vivo* the effects of a mixture of high molecular weight hyaluronic acid plus L-δ-dipalmitoyl phosphatidylcholine liposomes on joint lubrication and articular cartilage degeneration. Experimental osteoarthritis of the right knee was induced by anterior cruciate and medial collateral ligament in rabbits. The injected knees had a tendency to demonstrate less damage to the articular cartilage compared with control group.

The lubricating abilities of hyaluronic acid and the DPPC and mixture of both hyaluronic acid and DPPC were assessed in an *in vitro* model. Lubrication was found not to be concentration dependant for hyaluronic acid, but concentration was key for DPPC lubrication. Penetration of hyaluronic acid into bovine cartilage by up to 300 μm from the surface was observed over a 48-h period. It was observed that hyaluronic acid specifically targeted the chondrocytes as it was primarily found within the lacunae surrounding the cells [17].

Pasquali-Ronchetti *et al.* [18] studied *in vitro* interactions between hyaluronan of different molecular weights and phospholipids (DPPC and egg lecithin) in the form of either unilamellar particles or multilamellar vesicles. Both phospholipids changed their organization in the presence of hyaluronan, giving rise to the formation of huge perforated membrane-like structures lying on the substrate or thick cylinders with a tendency to aggregate and to form sheets. These structures were seen only in the presence of high-molecular weight hyaluronan, whereas low-molecular-weight one induced fragmentation of liposomes and formation of a few short rollers. They proposed that such interactions may not be as efficient in arthritic joints, where hyaluronan is degraded to low-molecular-weight fragments.

Steffan *et al.* [19] studied interactions of various polyanionic polysaccharides, including hyaluronic acid, with multilamellar dimyristoyl phosphatidylcholine liposomes. They concluded that the interactions of anionic polysaccharides with phospholipid membranes is due to the presence of divalent cations which require a certain electron configuration and ionic radius. They depend (among others) on chain length and on the kind of involved phospholipid. The observed temperature shift of the lipid phase transition is caused by a strong dehydration of the membrane surface, which can be inhibited by high concentrations of NaCl.

Taglienti *et al.* [20] utilized diffusional NMR techniques for investigation of the interactions between hyaluronan and phospholipids (DPPC and 1,2-Dipalmitoyl-*sn*-glycero-3-phospho-*rac*-(1-glycerol) sodium salt). They showed that they are dependent both on charge and hydrophobicity factors.

The complex of hyaluronic acid and egg lecithin (named Haplex) was prepared by film dispersion and sonication in [21]. The physico-chemical properties, studied by IR spectrometry and differential scanning calorimetry, of Haplex were different from hyaluronic acid or lecithin or their

mixture. After Haplex was administered to rats orally, the serum concentration of hyaluronic acid increased when compared with the mixture or control groups.

The role of hyaluronic acid in protecting SAPLs from lysis by exogenous phospholipase A_2 (PLA_2) was studied in [22]. It was found that hyaluronic acid adhered to the phospholipid membrane (liposomes), inhibited their lysis by PLA_2. However, in its degraded form, hyaluronic acid not only failed to inhibit PLA_2-lysing activity, but accelerated it. They concluded that when the rate of degradation of hyaluronic acid exceeds that of synthesis, there will be insufficient replacement of hyaluronic acid and/or SAPLs, resulting in denudation of the articular surfaces. These are then exposed to increasing friction, and hence increased danger of degenerative joint changes.

An active cosmetic solution based on hyaluronic acid and phospholipids in combination with other active substance (e.g., ceramide-6, chitosan derivative, vitamin C) was tested in order to improve health of very dry skin (xerosis). The obtained results were compared with simultaneously used placebo consisting phospholipids as vehicle for the active components. It was found that the improvement starts to be evident after 4 weeks of daily treatment, even if remarkable differences between the skin surface treated with vehicle and the active cream were not so strong. Probably that is due to the specific activity of the phospholipids which surely improve the skin appearance for their hydrating and restructuring properties [23].

Here, we investigate capability of phospholipids with positive charge to form complexes with hyaluronan in aqueous solutions in a similar simple way as traditional single- or double-alkyl chain cationic surfactants do. In particular, we were interested in solubilization properties of formed colloids towards hydrophobic molecules. For this purpose, fluorescence probe method is a suitable technique giving information both on complexation (aggregation) and solubilization behavior.

2. Fluorescence Probe Techniques

Determination of aggregation properties of phospholipid systems was based on fluorescence spectroscopy, a fluorescence probe method. Pyrene is a hydrophobic polyaromatic hydrocarbon with low solubility in water ($\sim 10^{-7}$ mol L^{-1}). Excitation and emission spectra of pyrene can be used to determine aggregation behavior of colloids. From these spectra, two polarity indexes are obtained—the emission polarity index (EmPI) and the excitation polarity index (ExPI). Photophysical origin of these two indexes is slightly different. The ExPI is based on the fact that in ground state the maximum absorption band is shifted bathochromically in nonpolar

environment. Because of extremely narrow interval of wavelengths, from ~333 nm to ~338 nm, it is difficult to precisely determine a maximum of excitation, consequently, the ExPI as a ratio of fluorescence intensity at two wavelengths is used.

The emission spectrum of pyrene presents a fine vibrational structure (Fig. 2) where the relative peak intensities are highly influenced by the polarity of the solvent molecules by which this probe is surrounded. The ratio of the fluorescence intensity of the highest energy vibrational band to that of the third highest energy band correlates with the solvent polarity and is denoted as EmPI. This unique property is based on the fact that the dipole moment of pyrene (3.24 ± 0.1 D) predicts in situations when some apolar domain exists in an aqueous solution that the pyrene is situated in less polar area and indicates local environment by changes in the value of EmPI. Both of these indexes, ExPI and EmPI, brought fully comparable results in our case.

In a system where the aggregation occurs, both indexes show the sigmoid decrease with increasing concentration of the aggregating molecules which form apolar domains within the aggregates (e.g., surfactants aggregating into micelles). The sigmoidal plots can adequately described by a decreasing Boltzmann curve, which is given by

$$\text{EmPI, ExPI} = \frac{\max - \min}{1 + e^{(x - x_0/\Delta x)}} + \min,$$

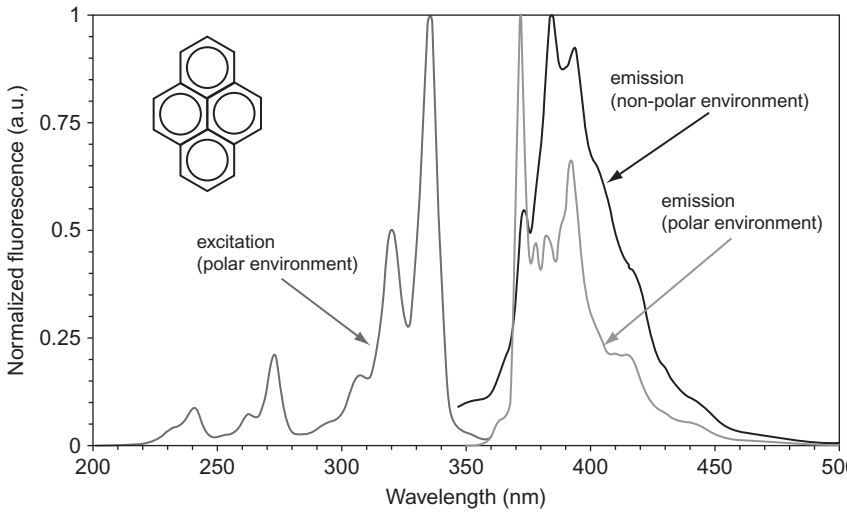

Figure 2 Fluorescence properties of pyrene in environments of different polarity.

where the independent variable x is the total surfactant concentration, max and min are the upper and lower limits of the sigmoid curve, x_0 is the center of the sigmoid (inflection point), and Δx is directly related to the independent variable range where abrupt change of dependent variable occurs. In this case, as aggregation concentration the x_0 point was taken.

In case of determination of surfactant binding on hyaluronan, a different type of fluorescence probe is appropriate. Acridine orange (AO), as a hydrochloride, has a positive charge located at the central nitrogen atom. Structure and fluorescence spectra and of AO are shown in Fig. 3. This type of dye forms in solution at high concentration the H-type of dye aggregate, an AO dimer. The AO dimers have the blue-shifted absorption band, from 492 nm to 465 nm and the fluorescence is forbidden (weak emission band at 650 nm). The monomer emission band has its maximum localized around 530 nm. In DNA, structure of AO dimer is sterically stabilized and probability of radiative transition in dimer strongly increases—e.g., DNA–AO associates show the red fluorescence instead of RNA–AO aggregates, which exhibits the green fluorescence.

The formation of nonfluorescent AO dimers in solution of polyanions is dependent on the number of dye molecules (D) and of polymer binding sites (P)—in our case, the number of negatively charged groups. This is described by the P/D ratio. In an ideal situation, when all negative groups are associated to AO dimers, the P/D value is 0.5.

Forming or breaking up of AO dimer can be observed in two different ways. Because of forbidden radiative transition from excited state of dimer, fluorescence intensity is inversely proportional to the dimer formation.

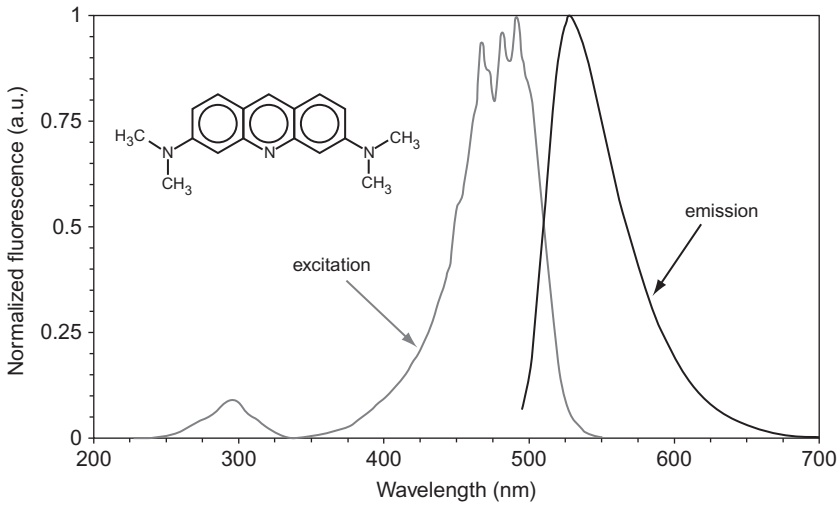

Figure 3 Fluorescence properties of acridine orange in aqueous environment.

As second parameter, a relative absorbance of dimer is used, expressed as ratio of absorbance at 465 nm (AO dimer) to absorbance at 492 nm (AO monomer) and denoted as "D:M."

As stated in introduction, our goal was an investigation of interactions between phospholipids and sodium salt of hyaluronic acid when the phospholipids play role of common surfactants.

The interaction between quaternary nitrogen and negatively charged carboxylic group can lead to the formation of electrostatically stabilized complex. This complex may result in the physically grafted copolymer, hydrophobically modified hyaluronan. The partially water-insoluble polymer can form aggregates with hydrophobic core and hydrophilic shell. This aggregate can solubilize amphiphilic and hydrophobic matters, for example, biologically active substances.

As was reported in introduction, phospholipids are mainly used in vesicular form. Phospholipid vesicles, liposomes, are initial colloidal particles in aqueous mixtures above the specific concentration, critical aggregation concentration. This fact is due to their packing parameter.

3. Materials and Methods

Selected phospholipids, DPPC (1,2-Dipalmitoyl-sn-glycero-3-phosphocholine, CAS # 63-89-8) and lecithin (1,2-diacyl-*sn*-glycero-3-fosfocholin, type XVI-E, CAS 8002 43 5) were purchased from Sigma-Aldrich. n-Dodecyl β-D-maltoside (C_{12}maltoside, CAS # 69227-93-6) was also purchased from Sigma-Aldrich company. Hyaluronan in different molecular weights were purchased from CPN Ltd., Czech Republic. All fluorescence probes, pyrene, and AO were of fluorescence grade and were purchased from Sigma-Aldrich. Solvents in this study were in spectrophotometric grade, and water was triple distilled.

Fluorescence spectra were recorded on AMINCO-Bowman Series 2 luminiscence spectrometer (ThermoSpectronics, Inc.) and absorption spectra were collected on Cary 50 (Varian, Inc.).

Stock solution of hyaluronan was prepared in triple distilled water and was stirred during 48 h at room temperature. Stock solutions of the phospholipids were prepared in chloroform. Pyrene's stock solution was prepared in acetone; on the other hand, stock solution of AO was prepared in triple distilled water.

In samples with lecithin or DPPC, phospholipid stock solution in chloroform was introduced into a vial and chloroform was evaporated. After evaporation stock solution of hyaluronan and/or dodecyl-maltoside was added.

Samples containing pyrene. Pyrene stock solution was introduced into a vial and acetone was evaporated. Final concentration of the pyrene in samples was $\sim 10^{-6}$ mol L^{-1}.The stock solution of the studied system was introduced into a flask with evaporating probe, was diluted to the desirable concentration, and the resulting solution was sonicated during 4 h and stored during next 20 h.

Samples containing acridine orange. AO stock solution was introduced into a vial. Final concentration of AO in samples was held to 5×10^{-6} mol L^{-1}. The stock solution of the studied system was introduced into a flask with probe solution.

4. Phospholipid Aggregation

As reported elsewhere [24], even phospholipids have their critical micelle concentrations. Above this concentration, only micelles or micelle-like aggregates are present in solution.

Concentration dependency of the aggregates formation process in solutions looks to be smooth. In a wide region of concentration, vesicles and micelles are coexisting in equilibrium. This can be one of the explanations of dependency of the ExPI on concentration of the phospholipid DPPC (see Fig. 4). From the Boltzman S-type curve the values of three independent variables, concentrations, which determine start and end of

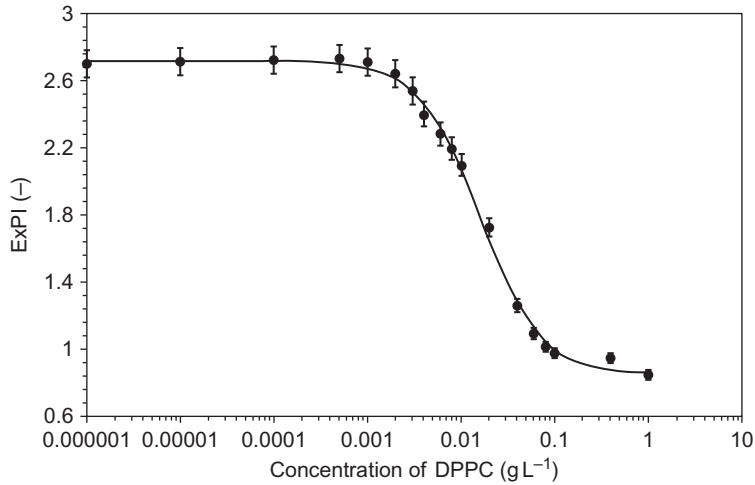

Figure 4 Dependency of the excitation polarity index (ExPI) on concentration of DPPC. Data were fitted by Boltzman sigmoidal curve and fitted parameters were used to characterize aggregation process, see Table 1.

the aggregation and the inflex point, were directly evaluated as the fit parameters.

The obtained fitted values of data from Fig. 4 are listed in Table 1 including fit parameters and goodness-of-fit statistics. As the data show, there is a wide range of concentrations between "start" and "end" point. The difference between these two points is nearby two orders of magnitude. As follows from the Boltzman equation, the parameter Δx is directly connected to the intensity of function decreasing.

This very slow decrease of polarity parameter can be explained in two different ways. At first, the resulting spectrum of fluorescence probes from each sample is a superposition of different signals coming from different probe's localizations. The solubility of pyrene probe in aqueous environment is sufficient to interfere with the signal of probe from nonpolar cores, especially in case when the system contains a small amount of these cores. Due to a low quantum yield of pyrene in aqueous environment, this effect takes a place only at extremely low micellar concentrations, or when a high amount of fluorescence probe is present in the sample. At second, when the concentration of phospholipid is increasing, the whole amount of added molecules is not used to form aggregates with nonpolar cores, or to form domains that are able to solubilize this type of probe. It is possible that added molecules are incorporated in existing aggregates and they are increasing the aggregation number of these aggregates. The enlargement of these aggregates leads to the phase transition of formed colloidal particles from micellar to vesicular type.

The other studied phospholipid, lecithin, showed similar aggregation behavior in aqueous solution like DPPC (see Fig. 5). Lecithin is 1,2-diacyl-*sn*-glycero-3-fosfocholin (type XVI-E, Sigma Aldrich, ~ 99%, CAS 8002-43-5). Lecithin is composed of different types of fatty acids—approx. 33% 16:0 (palmitic acid), 13% 18:0 (stearic acid), 31% 18:1(oleic acid), 15% 18:2 (linoleic acid), and minor residues. Compared to DPPC, the lecithin samples were transparent even at high phospholipid concentrations. Measurements performed with lecithin did not need to be corrected for the

Table 1 Fitted values from the Boltzmann fit of the dependency of ExPI on DPPC concentration (error given as the standard deviation)

Value	Concentration ($g\ L^{-1}$)	Error ($g\ L^{-1}$)				
start	0.004	0.002	*R*-Sq	0.9998	χ^2/DoF[a]	10^{-4}
inflex	0.016	0.005				
end	0.072	0.004				

[a] Goodness-of-fit—reduced chi-square is obtained by dividing the residual sum of squares by the degrees of freedom.

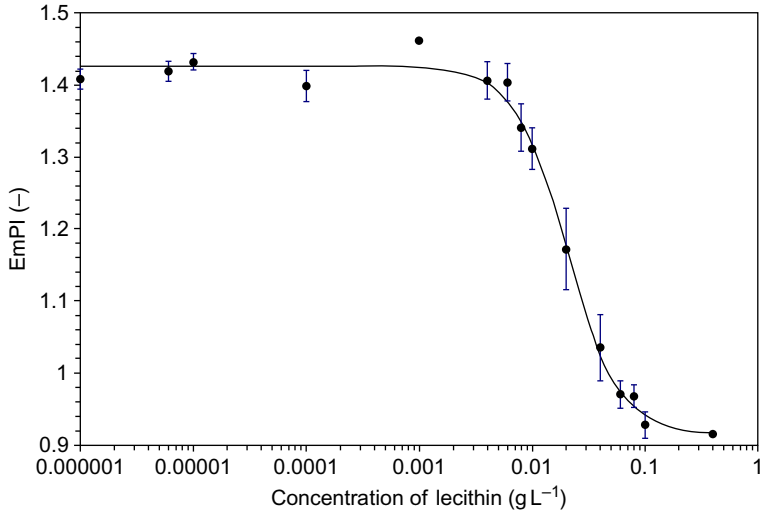

Figure 5 Dependency of the emission polarity index (EmPI) on concentration of lecithin. Data were fitted by Boltzman sigmoidal curve and fitted parameters were used to characterize aggregation process of lecithin, see Table 2.

Table 2 Fitted values from the Boltzmann fit of the dependency of EmPI on lecithin concentration (error given as the standard deviation)

Value	Concentration ($g\ L^{-1}$)	Error ($g\ L^{-1}$)				
start	0.007	0.001	*R*-Sq	0.9925	χ^2/DoF[a]	10^{-4}
inflex	0.021	0.003				
end	0.059	0.003				

[a] Goodness-of-fit—reduced chi-square is obtained by dividing the residual sum of squares by the degrees of freedom.

inner filter effect. Aggregation concentration of lecithin was determined from the dependency of the EmPI on PL concentration and obtained data are summarized in Table 2.

5. Presence of Hyaluronan

If we focus on aggregation behavior, expressed as a concentration dependency of some proper physical quantity, we should be able to prove interaction between phospholipid and hyaluronan. The phospholipid aggregation can be influenced by condensation of monomeric form of PL in solution on hyaluronan's chain. This condensation leads to formation of

some kind of different aggregates directly connected to the polymeric chain. This type of aggregate can form nonpolar cores, which are able to solubilize nonpolar species, one, two, or even more orders of magnitude below the critical aggregation concentration of phospholipid in pure aqueous solution. Formation of these aggregates is manifested as an "earlier" decrease of polarity index on the concentration axis. This decrease does not need to be intensive, but always should be marked. The intensity of this decrease is related to the fraction of pyrene molecule solubilized in these aggregates relatively to the amount of pyrene remaining in water. This fact must be taken into account especially in cases, when values of the polarity indexes are assigning to the polarity (relative permittivity, Δf function, etc.) of environment.

The aggregation behavior of lecithin, in the presence of native hyaluronan, is shown in Fig. 6. It is obvious that dependencies of the EmPI in the presence of hyaluronan are slightly shifted to the lower values comparing to the case when no hyaluronan is present in the solution. Numerical evaluation of this shift based on inflection points shows that aggregation in the presence of hyaluronan occurs at $\sim$3.8 mg L^{-1} compared with 5.6 mg L^{-1} in solution without biopolymer.

One can take into account that the added biopolymer is in fact a salt. With the biopolymer chain an equivalent amount of counter ions are added. These lead to increasing ionic strength, which can be responsible for slight shift of the aggregation dependencies. On the other hand, in case of absolute dissociation of sodium cation from hyaluronan backbone, the ionic strength

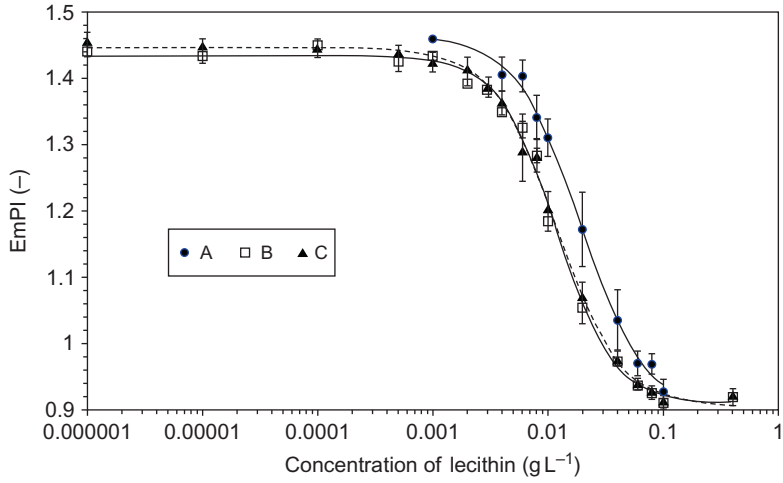

Figure 6 Aggregation behavior of lecithin in the presence of native hyaluronan (MW 73,000 g mol^{-1}) shown as dependency of the EmPI on the concentration of lecithin. (A) without HA; (B) with HA, $c = 1$ g L^{-1}; (C) with HA, $c = 15$ mg L^{-1}.

increases only for 0.0025 mol L^{-1}. In addition, showed dependencies for significantly different hyaluronan concentrations (1 g L^{-1} and 15 mg L^{-1}) seem to be independent on hyaluronan concentration.

The slight decrease of aggregation concentration can be directly connected to the interaction with hyaluronan chain (Fig. 7). This interaction is not strong but is present. This resulted in slightly "earlier" formation of the phospholipid aggregates. In this place, it can be noted that fluorescence spectroscopy refers only to cores which are able to solubilize hydrophobic species. These cores are in the center of interest, because they are potentially binding sites for drugs. This also means that in solution the phospholipid/biopolymer aggregates exist without a stable hydrophobic core.

Further experiments brought interesting information. Lecithin molecules were mixed with hyaluronans with higher molecular weight, viz. 300 kg mol^{-1} and 1460 kg mol^{-1}. Individual dependencies, together with the obtained aggregation concentration, clearly show that aggregation and the value of aggregation concentration are completely independent not only on the hyaluronan concentration but also on its molecular weight (see Table 3). Note that hyaluronan concentration spanned a broad region from 15 mg to 1 g per liter, which means that the concentration of biopolymer chains rapidly decreased in comparison with the first experiments described above but the number of monomers remained the same.

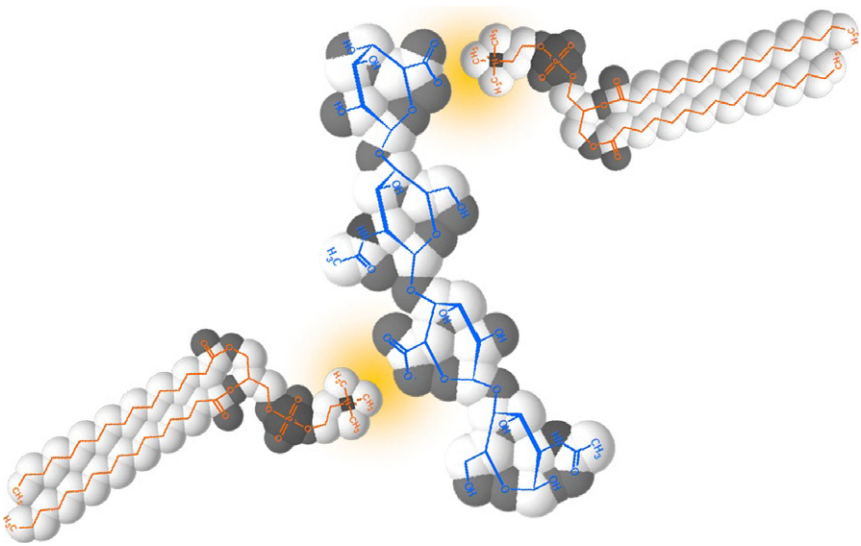

Figure 7 Illustration of supposed interaction between phospholipid and hyaluronan anion.

Table 3 Summary of hyaluronan effect on phospholipids aggregation concentration

HA MW (kg mol^{-1})	HA conc. (g L^{-1})	Aggregation concentration (mg L^{-1})	
		Lecithin	DPPC
Without HA		5.6 ± 0.1	0.8 ± 0.1
73	1	3.8 ± 0.3	0.9 ± 0.1
	0.015	3.3 ± 0.5	1.0 ± 0.1
300	1	3.8 ± 0.1	0.8 ± 0.1
	0.015	3.5 ± 0.3	1.4 ± 0.1
1460	1	3.9 ± 0.1	0.8 ± 0.1
	0.015	3.8 ± 0.1	0.9 ± 0.1

Another information extractable from the fluorescence experiments can be described as a "core quality." The final value of polarity index can be taken as its descriptor. From this point of view, formed aggregates are equal and there is no difference between free-formed aggregates and hyaluronan-complexed ones. Values of polarity indexes can be hardly assigned to a proper value of polarity, but can act as a good criterion for comparison of samples.

On the other hand, our experiments with DPPC in the presence of hyaluronan gave different results. Aggregation of free DPPC and in solution with biopolymer showed no difference. The obtained aggregation concentration values and other parameters of fit remained unchanged on the specified level of confidence.

Obtained results are summarized in Table 3. As can be seen, results for the DPPC only fluctuate around the mean value of 1 g L^{-1}. There is no obvious trend for this phospholipid.

Differences between aggregation behavior of lecithin and DPPC are quite interesting. This fact can be explained if we take into account what the name "lecithin" exactly covers. Lecithin used in this study consisted of 33% of DPPC the rest being various saturated and unsaturated analogues. The heterogeneity of this mixture allows the system to aggregate easily and to form smaller particles, which resulted in a clear solution even at higher concentrations in comparison with opalescent DPPC samples. This fact is inspiring for next work, which include combination of phospholipid and suitable surfactant. Another attempt was realized to prove interactions between DPPC and HA. Possible polymer binding sites were marked by AO dimers. These dimers showed no fluorescence when condensed on hyaluronan chain. If there is a stronger interaction between phospholipid and hyaluronan, than between AO and HA, AO dimers break-down and free monomers increase the fluorescence intensity from the sample. Of course, changes in absorption spectra, related to the absorbance of dimer, were also expected.

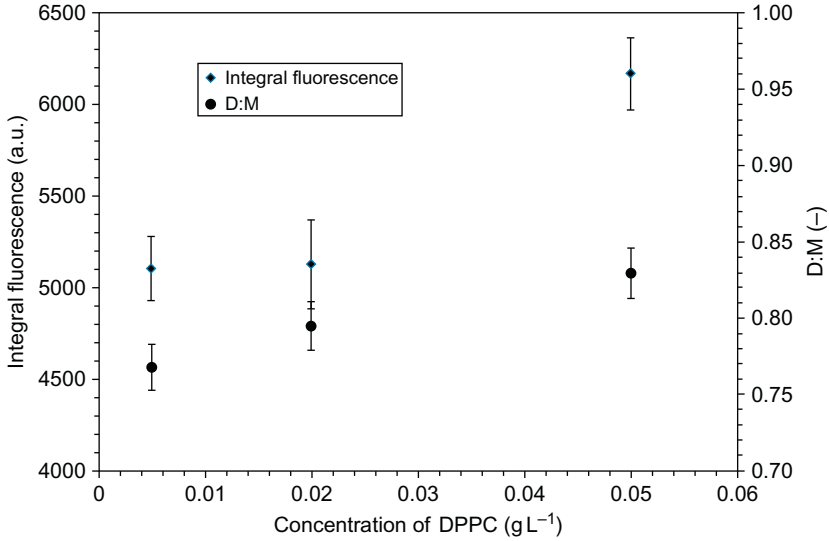

Figure 8 Dependency of the fluorescence intensity of acridine orange (as total integral) and D:M ratio on concentration of DPPC in the presence of hyaluronan (MW 73,000 g mol^{-1}; 15 mg L^{-1}).

From Fig. 8, it is obvious that increasing concentration of DDPC caused slightly increasing fluorescence intensity. The increasing intensity is accompanied by small increase of D:M ratio. These two opposite dependencies mean that there are no notable changes in this system and from the fluorescence-point-of-view there is no interaction between DPPC and native hyaluronan in aqueous solution.

6. Mixed System

Results obtained for DPPC failed to prove interactions of this phospholipid with hyaluronan but in the same time inspired additional experimentation. DPPC was further used only as an "interaction mediator." Main solubilization responsibility was transferred to suitable nonionic biocompatible surfactant and phospholipid should act as a linker to the hyaluronan macromolecule. In fact, formation of mixed surfactant-phospholipid micelles was supposed.

As surfactant for the experiments with mixed micelles, n-dodecyl β-D-maltoside (C_{12}maltoside, CAS #69227-93-6), a nonionic sugar-based amphiphile, was selected. The main idea was to use the nonionic surfactant as a medium for phospholipid dispergation and also as a solubilizing

environment. Phospholipid can act as a linking agent that bonds micelles and biopolymer together and also can act as an active nutritive component.

First, aggregation of nonionic surfactant in the presence of DPPC was investigated. Aggregation behavior as demonstrated by the dependency of the EmPI on surfactant concentration in the presence and absence of DPPC is shown on Fig. 8. Concentration of DPPC was set to 5 mg L^{-1}. From Fig. 9, it is evident that aggregation of C_{12}maltoside is quite simple, represented as simple sigmoidal curve, on contrary to the case when DPPC is present. Dependency of C_{12}maltoside aggregation in the presence of phospholipid showed local minimum nearby 0.05 mM. This concentration belongs to the induced aggregates of DPPC and maltoside. This fact is taken as a confirmation of interaction between DDPC and C_{12}maltoside surfactant. DPPC is directly solubilized into the sugar micelles and act as cosurfactant (Fig. 10).

These aggregates were used to interact with the AO labeled hyaluronan. From the previous measurements with DDPC, it was found out that the proper value of the dye amount on hyaluronan chain is nearby 0.3 mol of dye per mol of theoretical carboxylic groups. Complex of phospholipid and maltoside surfactant was prepared in the ratio of components PL:C12Mal 1:98. Value 98 came from aggregation number of maltoside surfactant in aqueous solution in region above its CMC, as were reported by producer [25]. In other words 1 mol of PL was present in the solution per 1 mol of theoretical C_{12}maltoside micelle.

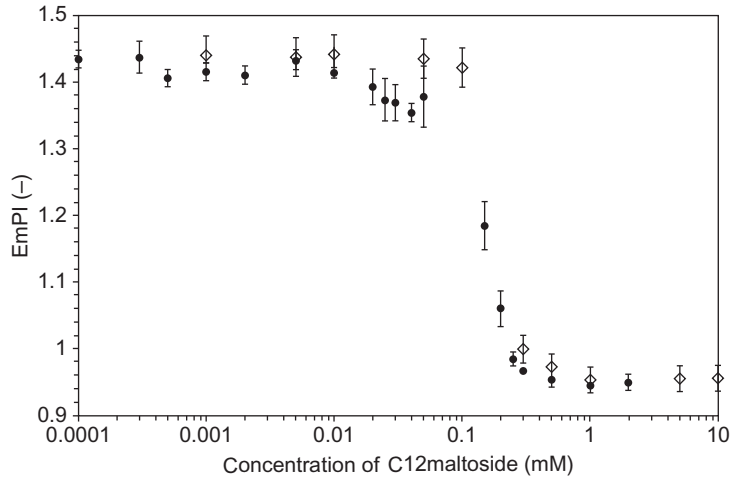

Figure 9 Dependency of the emission polarity index (EmPI) on C_{12}maltoside concentration in the presence (●) and absence (◇) of DPPC.

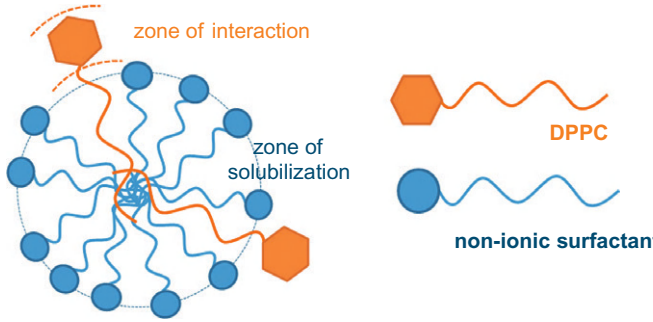

Figure 10 Illustration of supposed phospholipid–C_{12}maltoside complex.

The presence of the third component changes initial condition (besides the changed environment). Phospholipid was now only a minor part of the system from the "mass-point-of-view," but still remained the most important component. Phospholipid was used below its aggregation concentration and its presence could induce formation of nonionic surfactant micelles at lower concentration. All this made the experimental design a little bit problematic. A lot of parameters should be covered, for example, the ratio between PL and surfactant. Another problem was how to prove interactions between the amphiphiles complex and the biopolymer. One possible way was to mark the binding sites by the AO dimer, as reported above in the case of interaction of DPPC with hyaluronan.

Figure 11 displays dependencies of the fluorescence intensity of AO and D:M ratio on the concentration of the PL-surfactant complex. Addition of the complex increased fluorescence intensity that is related to the AO dimer breakdown. This was confirmed by the D:M dependency which showed that the amount of dimer in the system decreased. D:M ratio, as observable parameter, looked to be more sensitive to the changes in this complex solution. With respect to the error bars, there are three plateaus in this dependency. The plateaus indicate that complex should interact with nonlabeled parts of biopolymer. These parts can be primarily nonlabeled, due to interaction with complex these part are coming accessible for interaction, or they are firstly bonded aggregates and coming complexes only increase their aggregation number.

Fluorescence intensity slightly increased up to concentration around 5 mg L^{-1}. After this concentration, the fluorescence intensity increased rapidly. With respect to the D:M dependency, this increase can be explained as dimer breaking.

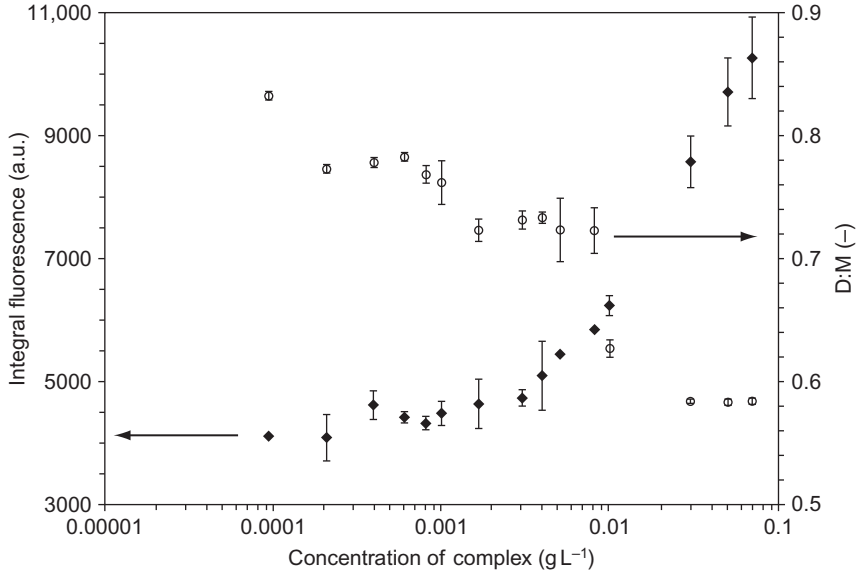

Figure 11 Dependency of the fluorescence intensity of acridine orange (as total integral; ◆) and D:M (○) ratio on concentration of DPPC–C_{12}maltoside complex.

7. Conclusion

Fluorescence probes showed that phospholipids, DPPC and lecithin, aggregate in aqueous solution to form micelle-like structures capable to solubilize hydrophobic molecules. Only in the case of lecithin, changes in its aggregation behavior were observable after adding hyaluronan. Presence of hyaluronan shifted aggregation concentration of the lecithin to the lower values. On the other hand, experiments with DPPC did not bring any evidence of interaction.

As a novel approach of this work in forming hyaluronan–phospholipid complexes, nonionic biocompatible surfactant was used as a dispersion environment for phospholipid molecules. Phospholipid than could act as a physical linker which bonds micelles and biopolymer together by physical forces and could also serve as an active nourishing agent. This new type complex can be used as a part of cosmetic formulation combining hydrating and nourishing effects or in pharmaceutics for the delivery of water insoluble active molecules.

ACKNOWLEDGMENTS

This work was supported by the Czech Ministry of Education, project No. OC08004 and COST action D43. The Centre for Materials Research at FC BUT is supported by project No. CZ.1.05/2.1.00/01.0012 from ERDF. Assistance of Tereza Halasová, Iva Maivaldová, and Jana Szewieczková in experimental work is gratefully acknowledged.

REFERENCES

[1] L. Lapčík, L. Lapčík, S. De Smedt, J. Demeester, P. Chabreček, Hyaluronan: preparation, structure, properties, and applications, Chem. Rev. 98 (1998) 2663–2684.
[2] M.K. Cowman, S. Matsuoka, Experimental approaches to hyaluronan structure, Carbohyd. Res. 340 (2005) 791–809.
[3] K.P. Vercruysse, G.D. Prestwich, Hyaluronate derivatives in drug delivery, Crit. Rev. Ther. Drug 15 (1998) 513–555.
[4] H.G. Garg, C.A. Hales (Eds.), Chemistry and Biology of Hyaluronan, Elsevier, Amsterdam, 2004.
[5] C.B. Knudson, W. Knudson, Hyaluronan-binding proteins in development, tissue homeostasis, and disease, FASEB J. 7 (1993) 1233–1241.
[6] S. Jaracz, J. Chen, L.V. Kuznetsova, I. Ojima, Recent advances in tumor-targeting anticancer drug conjugates, Bioorgan. Med. Chem. 13 (2005) 5043–5054.
[7] P. Prehm, Hyaluronan, in: E.J. Vandomme, S. De Baets, A. Steinbückel (Eds.), Biopolymers, Polysaccharides I: Polysaccharides from Prokaryotes, vol. 5, Wiley, Weinheim, 2002, pp. 379–406.
[8] M. Paye, A.O. Barel, H.I. Maibach (Eds.), Handbook of Cosmetic Science and Technology, Taylor & Francis, New York, 2006.
[9] V. Crescenzi, A. Taglienti, I. Pasquali-Ronchetti, Supramolecular structures prevailing in aqueous hyaluronic acid and phospholipid vesicles mixtures: an electron microscopy and rheometric study, Colloid. Surf. A 245 (2004) 133–135.
[10] C. Gomez-Gaete, N. Tsapis, L. Silva, C. Bourgaux, M. Besnard, A. Bochot, E. Fattal, Supramolecular organization and release properties of phospholipid-hyaluronan microparticles encapsulating dexamethasone, Eur. J. Pharm. Biopharm. 70 (2008) 116–126.
[11] P. Ghosh, N. Hutadilok, N. Adam, A. Lentini, Interactions of hyaluronan (hyaluronic-acid) with phospholipids as determined by gel-permeation chromatography, multi-angle laser-light-scattering photometry and H-1-NMR spectroscopy, Int. J. Biol. Macromol. 16 (1994) 237–244.
[12] P. Ghosh, N. Hutadilok, A. Lentini, Nuclear-magnetic-resonance studies of hyaluronan (HA): evidence of competitive-inhibition of interchain associations by phospholipids which may result in decreased antiinflammatory and cartilage protecting properties of HA, Heterocycles 38 (1994) 1757–1774.
[13] T. Moro-oka, H. Miura, T. Mawatari, T. Kawano, Y. Nakanishi, H. Higaki, Y. Iwamoto, Mixture of hyaluronic acid and phospholipid prevents adhesion formation on the injured flexor tendon in rabbits, J. Orthop. Res. 18 (2000) 835–840.
[14] B.A. Hills, Boundary lubrication *in vivo*, Proc. Inst. Mech. Eng. H J. Eng. Med. 214 (2000) 83–94.
[15] B.A. Hills, Remarkable antiwear properties of joint surfactant, Ann. Biomed. Eng. 23 (1995) 112–115.
[16] T. Kawano, H. Miura, T. Mawatari, T. Moro-Oka, Y. Nakanishi, H. Higaki, Y. Iwamoto, Mechanical effects of the intraarticular administration of high molecular weight phospholipid on synovial joint articular cartilage degeneration hyaluronic acid

plus lubrication and prevention of in experimental osteoarthritis, Arthritis Rheum-us 48 (2003) 1923–1929.
[17] R.W. Forsey, J. Fisher, J. Thompson, M.H. Stone, C. Bell, E. Ingham, The effect of hyaluronic acid and phospholipid based lubricants on friction within a human cartilage damage model, Biomaterials 27 (2006) 4581–4590.
[18] I. Pasquali-Ronchetti, D. Quaglino, G. Mori, B. Bacchelli, P. Ghosh, Hyaluronan–phospholipid interactions, J. Struct. Biol. 120 (1997) 1–10.
[19] G. Steffan, S. Wulff, H.J. Galla, Divalent cation-dependent interaction of sulfated polysaccharides with phosphatidylcholine and mixed phosphatidylcholine phosphatidylglycerol liposomes, Chem. Phys. Lipids 74 (1994) 141–150.
[20] A. Taglienti, F. Cellesi, V. Crescenzi, P. Sequi, M. Valentini, N. Tirelli, Investigating the interactions of hyaluronan derivatives with biomolecules. The use of diffusional NMR techniques, Macromol. Biosci. 6 (2006) 611–622.
[21] S.L. Huang, P.X. Ling, T.M. Zhang, Oral absorption of hyaluronic acid and phospholipids complexes in rats, World J. Gastroentero. 13 (2007) 945–949.
[22] D.W. Nitzan, U. Nitzan, P. Dan, S. Yedgar, The role of hyaluronic acid in protecting surface-active phospholipids from lysis by exogenous phospholipase A(2), Rheumatology 40 (2001) 336–340.
[23] P. Morganti, G. Fabrizi, B. James, A new cosmetic solution for a mild to moderate xerosis, J. Appl. Cosmetol. 17 (1999) 86–93.
[24] D. Marsh, Handbook of Lipid Bilayers, first ed., CRC Press, Boca Raton, 1990.
[25] http://www.sigmaaldrich.com, (accessed on February 24, 2011).

CHAPTER NINE

Dynamics of Lipid Vesicles: From Thermal Fluctuations to Rheology

Victoria Vitkova[1,*] *and* Chaouqi Misbah[2]

Contents

Abstract

Deformability is a key feature of the lipid membrane, being of importance for numerous processes taking place in biological cells, as well as for the flow behavior of cells in blood circulation. In the first part of the chapter, the potentials of investigating the dynamics of membrane fluctuations as an experimental tool for probing the membrane material properties are presented and discussed. By analysing the dynamics of thermally induced shape fluctuations of nearly spherical lipid vesicles, important mechanical constants of the bilayer are possible to be extracted, namely bending elasticity modules at free and blocked exchange of molecules between the two monolayers, comprising the lipid membrane, and the intermonolayer friction coefficient of the bilayer.

* Corresponding author. Tel.: +359-2-9795825/5725; Fax: +359-2-9753632.
E-mail address: victoria@issp.bas.bg

[1] Liquid Crystals Laboratory, Institute of Solid State Physics, Bulgarian Academy of Sciences, Sofia, Bulgaria
[2] Laboratoire interdisciplinaire de physique (LiPHy), CNRS and Université J. Fourier Grenoble I, Saint Martin d'Hères, France

Advances in Planar Lipid Bilayers and Liposomes, Volume 14
ISSN 1554-4516, DOI: 10.1016/B978-0-12-387720-8.00009-1

The second part of this contribution is dedicated to the dynamics of unconfined lipid vesicles in linear hydrodynamic fields. The current state of theory and experiment of single vesicle dynamics in simple shear flows is reviewed. Special attention is given to the relation between the overall rheological properties of vesicle suspensions and the individual vesicle dynamics in the flow.

1. Introduction

Representing the fundamental structural unit of every living organism, the biological cell is a natural object of investigation for biologists, biochemists, and biophysicists, who try to reveal and describe the various properties, mechanisms and processes making cells well functioning entities, properly communicating with their dynamical environment [1]. The basic common feature of biological cells despite their strong differentiation is that the cellular integrity is assured by a plasma membrane and numerous intracellular structures (organelles) are formed by internal membranes of different types and functions. Biological membranes play also the major role in many cellular processes such as cellular division, endo-, and exocytosis, where membrane deformations are important and are controlled by the membrane mechanical properties [2]. The permeability of biomembranes for various molecules and ions governs their barrier function, which is one of the basic functions of biological membranes and realizes the connection between the interior of the cell and the exterior environment. All biological membranes, including the plasma membrane and the internal membranes of eukaryotic cells, have a common general structure: they are assemblies of lipid and protein molecules, held together mainly by noncovalent interactions. The mass ratio between both constituents varies as a function of the membrane type [3]. Cell membranes are highly dynamic, fluid structures, which are made functional by lipid–lipid, lipid–protein, and protein–protein interactions. Most of their lipid and protein molecules are able to migrate in the membrane. The first insight into the general structural organisation of biological membranes was proposed in the early 1970s [4]. In its initial form, the celebrated Singer–Nicolson fluid mosaic model considers the cell membrane as a two-dimensional sea of lipid molecules with integral proteins, floating in it. Ever since the initial concept of the fluid mosaic model significantly evolved. It is now admitted that the membrane constituents do not diffuse freely in the two-dimensional lipid matrix, but are structured in 2D domains [5,6]. These small (10–200 nm) domains are called rafts [6–8] and are heterogeneous, sterol- and sphingo-lipid-enriched, highly dynamic, and compartmentalize cellular processes. It has been observed that small rafts can sometimes be stabilized to form larger platforms through protein–protein and protein–lipid interactions [9].

Conceived as part of a mechanism for the intracellular trafficking of lipids and lipid-anchored proteins, the raft hypothesis has been enriched and developed during the last decade [8]. Concerning the important role of the lipid bilayer in functional aspect, recent experimental observations have proven the bending-mediated force transduction and molecular organization in lipid membranes [10].

The investigation of the dynamics of the membrane organization is a challenging task for biophysicist. Following the so-called "bottom-up" approach, it is useful to introduce a simple model system with controlled experimental physicochemical parameters in order to be able to distinguish the contribution of every component to the studied membrane property, morphology and stability. The simplest physical model of biological membranes is the lipid bilayer [11]. Giant unilamellar vesicles (GUVs) with diameters at the micrometer scale are exploited successfully in the biophysical research for modeling basic physical properties of biomembranes [12,13]. Besides having characteristic diameters in the same range as the typical cell sizes (5–100 μm), GUVs allow controlling numerous parameters as membrane composition, viscosity, and concentrations of solutes in the aqueous environment, and thus, give the opportunity for direct visualization of particular membrane-related phenomena at the level of single vesicles [14].

With respect to biological cells, the well-known asymmetry of the bilayer and the proteins spanning the membrane add additional barriers to reconstituting membrane organization and function *in vitro*. In addition, most saturated lipids that are thought to underlie raft formation reside in the exoplasmic leaflet of the membrane, and the principles of raft organization in the cytosolic leaflet remain unknown [15]. Despite these fundamental difficulties, there is significant progress in reconstitution of natural membrane structure in artificial GUVs. Recent developments of the conventional methods for vesicle formation made possible the preparation of GUVs from native membranes or organic lipid mixtures in physiological conditions (high ionic strengths) [16]. Another important step toward better modeling of structural particularities of cell membranes is the successful reconstitution of membrane proteins into GUVs [17]. By means of fluorescence techniques, it has been proven that in artificial GUVs composed of native membranes, the membrane proteins and glycosphingolipids preserve their natural orientation after electroformation [18]. Such methodical achievements open new horizons to experimental studies of biologically important physical properties of inhomogeneous membrane systems in simplified laboratory conditions.

Another important application of lipid vesicles that gives special priority to the investigation of their physical properties, dynamics, and stability is their usage as drug and gene carriers [19].

The present contribution is focused on two different aspects of vesicle dynamics, both closely related to the unique material properties of the lipid bilayer. The first of the problems considered here is the dynamics of the

thermally induced shape fluctuations (TISF) of quasispherical lipid vesicles. Through a detailed review of the current state of theory and experiment in Section 2, it is shown how the analysis of the dynamics of the lipid membrane bending fluctuations can give information about important membrane properties such as the bilayer bending elasticity at blocked intermonolayer exchange of molecules (otherwise, immeasurable), the intermonolayer friction coefficient [20,21], and the lateral diffusion coefficient of a guest molecule in the bilayer [22]. Our experimental data are presented for the membrane bending elasticity at free and blocked exchange of molecules between the two monolayers composing a single-component synthetic bilayer and for the coefficient of its intermonolayer friction deduced from fluctuation analysis.

The dynamics of deflated lipid vesicles in linear flows is the subject of Section 3. The theoretical background of the problem [23–32] and the experimental work performed so far [33–39] are reviewed and discussed. In Section 4, it is shown how the overall rheology of dilute suspensions of lipid vesicles is related to the single vesicle dynamics in flow [40–42]. Similar measurements for red blood cell (RBC) suspensions in the dilute limit are presented. The micro–macro link experimentally detected [42] is discussed in the light of potential clinical applications as complementary diagnostic tools of blood pathologies and disorders.

2. Dynamics of Thermally Induced Membrane Fluctuations of Quasispherical Lipid Vesicles

2.1. Background

Lipid membranes in their liquid-crystalline state possess unique mechanical properties, combining area incompressibility and very low resistance to bending. The grounds of the elastic theory of lipid membranes were developed by Helfrich in the 1970s [43,44]. Typical thickness of lipid bilayers is of the order of nanometers, which is about thousand times smaller than the mean radius of GUVs and membranes are considered as sheets, thus every change of their shape being decomposed into three elementary deformations—shear, stretching, and bending (Fig. 1) [45]. If a lipid bilayer is discussed only in its liquid crystal state, it can be considered as a two-dimensional liquid. Consequently, the mechanical properties of such an object are characterized by its stretching and bending elastic moduli. This is exactly the case of phospholipid membranes in liquid crystal phase L_α [46], when lipid molecules can freely slide one to another and the shear elastic modulus is equal to zero. Evidently, in the case of natural membranes, containing a cytoskeleton, shear deformations cannot be neglected.

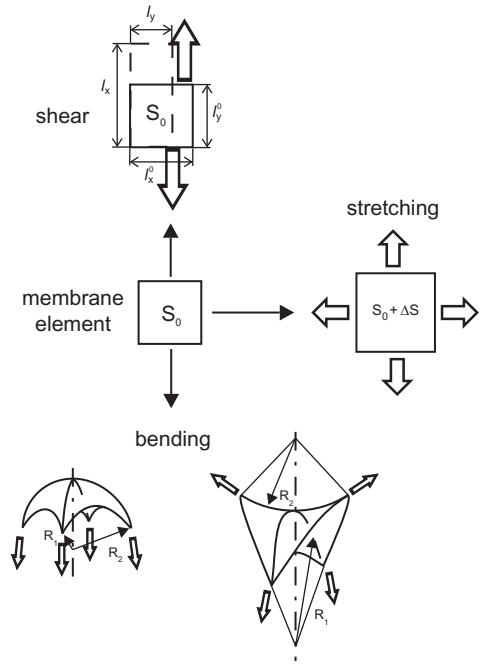

Figure 1 Elementary deformations of an infinitely thin membrane element. In the case of bending deformation, there are two possibilities: $R_1.R_2 > 0$ (left) and $R_1.R_2 < 0$ (right).

The expression for the surface density of stretching elastic energy reads [43]:

$$g_s = \frac{1}{2} k_s \left(\frac{\Delta S}{S_0} \right)^2, \tag{1}$$

where S_0 is the area of a flat tension-free membrane (Fig. 1), $\Delta S/S_0$ is the relative area change of the bilayer and k_s is the stretching elastic modulus (with dimension J/m^2 or N/m). Helfrich defines the membrane tension as

$$\sigma = k_s \frac{\Delta S}{S_0}. \tag{2}$$

If a tension-free membrane is bent, its shape can locally be characterized by its principal curvatures:

$$c_1 = \frac{1}{R_1}, \qquad c_2 = \frac{1}{R_2},$$

where R_1 and R_2 are respectively, the largest and the smallest radii of curvature in two mutually orthogonal directions (Fig. 1).

In the expression for the free bending energy for a bilayer in its liquid crystal state, the total curvature $c_1 + c_2$ and the Gaussian curvature $c_1 c_2$ participate. To the second order the density of the bending energy is given by [43]:

$$g_c = \frac{1}{2} k_c (c_1 + c_2 - c_0)^2 + \bar{k}_c c_1 c_2, \tag{3}$$

where k_c and $\bar{k}_c$ are elastic moduli of the curvature and the saddle curvature (with dimension of energy) and c_0 is the so-called spontaneous curvature. For symmetrical bilayers bathed by identical solvents, the condition $c_0 \equiv 0$ is fulfilled.

In fact, two different bending elastic moduli exist: k_c^{fr}, when the exchange of lipid molecules between the monolayers of the bilayer is allowed, and k_c^{bl}, when it is blocked [44]. When the exchange is forbidden, the number of the molecules in each monolayer of the bilayer is constant. At free exchange, the bending elasticity energy is lower because it has been minimized with respect to the difference between the number of the molecules in each monolayer and consequently, $k_c^{fr} < k_c^{bl}$. In all phenomena, related to the out-of-plane fluctuations of membranes, the relevant quantity is k_c^{fr} [21,47,48]. These phenomena include the thermal fluctuations of quasispherical vesicles [49,50], as well as the vesicle suction in micropipettes at very low suction pressures [51].

The energy, required to bend an initially flat membrane element with area 100 μm^2 to a cylinder with radius R_c equal to 10 μm, can be estimated by taking for k_c the value of 10^{-19} J [49] and is obtained to be

$$W_c = \frac{k_c}{2} \frac{S_0}{R_c^2} \approx 10^{-20} - 10^{-19} \text{J}. \tag{4}$$

These energies are of the order of thermal excitations energy $k_B T$. Therefore, the thermal excitation energy is sufficient to provoke curvature changes. Brochard and Lennon [52] used this argument to give a theoretical interpretation of the flicker phenomenon in erythrocytes. The shape fluctuations of giant liposomes are also explained by the same arguments. Membrane undulations are due to local pressure differences, resulting from the thermal (Brownian) motion of water molecules in the bilayer surroundings.

The second term in Eq. (3) depends on the Gaussian curvature $c_1 c_2$. The integral of the Gaussian curvature over a closed surface depends only on its topology. Consequently, this term is neglected when the

elastic properties of closed membranes are discussed. When the membrane continuity is not disrupted by cuts or contours [43] it is fulfilled that:

$$\oint_S c_1 c_2 ds = 2\pi\chi, \tag{5}$$

where the integral is over the whole surface S and χ is an integer called the Euler characteristic of the surface (related to the genus p of the surface by $\chi = 2(1 - p)$ for a closed surface). The Euler characteristic decreases with increasing number of holes (e.g., for a sphere (no holes) $p = 0$ and $\chi = 2$, for a torus (one hole) $p = 1$ and $\chi = 0$).

For stability reasons, it is easily understandable that the elastic modulus k_c has to be positive ($k_c > 0$). A simple variation calculus [53] also demonstrates that in the framework of the quadratic approximation a free deformable piece of monolayer possesses a stable configuration only if the following condition is fulfilled:

$$-2k_c < \bar{k}_c < 0. \tag{6}$$

Therefore, the equilibrium is characterized by spherical curvature $c_1 = c_2 = c_{eq}$, where:

$$c_{eq} = \frac{k_c}{2k_c + \bar{k}_c} c_0. \tag{7}$$

If $\bar{k}_c < -2k_c$, the quadratic approximation predicts the layers to "sphere up" without limits for all values of c_0 (higher order terms will then limit the deformation, cf. Mitov [54]). For $\bar{k}_c > 0$, elastic energy can be released, independently of k_c, by saddle-like deformations, for example, of the type $c_1 + c_2 = c_0$, $c_1 > 0$, $c_2 < 0$ (cf. Fig. 1). Harbich *et al.* [55] gave some early examples of this type.

After the first study of Brochard and Lennon [52], Schneider *et al.* [56] proposed a method for measurement of the bending elastic modulus of quasispherical vesicles by analysis of their TISFs. They employed fluorescence microscopy of labeled lipid bilayers and analyzed the fluctuations of vesicle diameter in two mutually perpendicular directions. This work was the first theoretical model for the dynamics of the shape fluctuations of quasispherical lipid vesicles. In their experiments, the time correlation function of the difference of two perpendicular diameters of the fluctuating circumference, representing the equatorial cross-section of the lipid vesicle, was calculated and analyzed. For the analysis, only the contribution of the second mode was taken into account. Their original theory contained some errors, as pointed out thereafter by Helfrich [57] and Milner and Safran [58], who introduced some corrections, and built a precise model of the dynamics of fluctuation of a giant

vesicle. The group of Sackmann worked on the same problem [2,59] and proposed a method based on Fourier decomposition of the shape fluctuations of quasispherical vesicles. The theoretical and experimental requirements of the method were defined by Faucon *et al.* [49], who elaborated the experimental approach of bending elastic modulus determination by thermal fluctuations analysis. Méléard *et al.* [60] considered the statics and dynamics of thermal membrane fluctuations with respect to the membrane curvature elasticity.

If the radius-vector of a point at the surface of the vesicle in the direction determined by its spherical coordinates (θ, ϕ) is considered as depicted in Fig. 2, its small deviation (or its fluctuation) in spherical coordinates at the moment t can be written in the following way:

$$\rho(\theta, \phi, t) = R_0[1 + u(\theta, \phi, t)]. \tag{8}$$

Here, R_0 denotes the radius of a sphere with the same volume as the volume of the vesicle and $u(\theta, \phi, t)$ is the normalized function, describing the shape fluctuations. The fluctuations can be decomposed in a series of spherical functions [61]:

$$u(\theta, \phi, t) = \sum_{n=2}^{n_{\max}} \sum_{j=-n}^{n} U_i^j(t) Y_i^j(\theta, \phi). \tag{9}$$

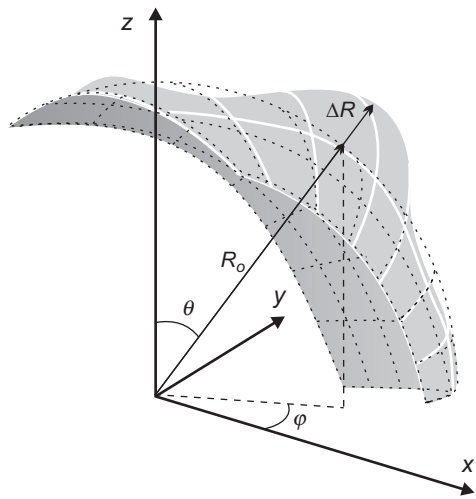

Figure 2 Schematic presentation of a piece of the fluctuating membrane of a quasispherical vesicle with radius R_0. The origin of the laboratory frame coincides with the vesicle's centre.

The mean square value of the fluctuations depends on the number n only, and is given by Milner and Safran [58] considering all modes as independent and applying the equipartition theorem:

$$\left\langle \left| U_n^m(t) \right|^2 \right\rangle = \frac{k_B T}{k_c} Q^{-1}(\bar{\sigma}, n), \tag{10}$$

where, k_B is the Boltzmann constant, T is the absolute temperature, $Q(\bar{\sigma}, n) = (n-1)(n+2)[\bar{\sigma} + n(n+1)]$ and $\bar{\sigma} = (\sigma R/k_c)$ is the dimensionless membrane tension.

From Eq. (10), it follows that the product:

$$\left\langle \left| U_n^m(t) \right|^2 \right\rangle \cdot Q(\bar{\sigma}, n) = \frac{k_B T}{k_c}, \tag{11}$$

does not depend on n and $\bar{\sigma}$ and this fact can be used for the determination of the (very small and otherwise immeasurable) membrane tension $\bar{\sigma}$, by treating it as an adjustable parameter. Such a possibility was not systematically exploited in the Fourier static analysis of shape changes in the contour [62], in contrast to the other variant of the method—Legendre analysis of the autocorrelation function of the vesicle contour [47,61].

What is observed experimentally is an equatorial cross-section of the vesicle with the focal plane of the microscope (Fig. 3). In this case it is fulfilled that $\theta = \pi/2$ (Fig. 2) and Eq. (8) reads

$$\rho(\phi, t) = R_0 \left[1 + u\left(\frac{\pi}{2}, \phi, t \right) \right]. \tag{12}$$

For the static fluctuation analysis, the calculation of the normalized angular autocorrelation function $\xi(\gamma, t)$ of the vesicle radius at a given moment of time, has been proposed by Bivas *et al.* [47]:

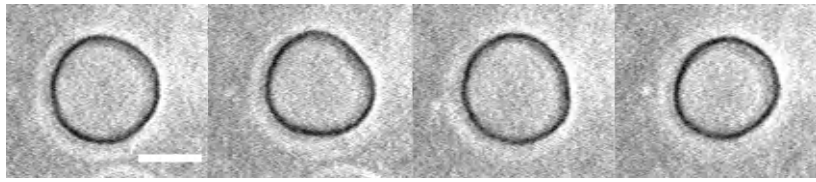

Figure 3 Phase-contrast images of a fluctuating DOPC vesicle as observed by phase-contrast microscopy. The bar corresponds to 10 μm. Time lapse between two adjacent images is 1 s.

$$\xi(\gamma,t)=\left\langle \frac{1}{{R_0}^2}\left[\int_0^{2\pi}\rho(\phi+\gamma,t)\rho^*(\phi,t)d\phi-\rho^2(t)\right]\right\rangle. \tag{13}$$

It has been shown [47,61] that the angular autocorrelation function, $\xi(\gamma)$, can be represented as a series of Legendre polynomials, $P_n(\cos\ \gamma)$, with coefficients $B_n(\bar{\sigma},k_c)$:

$$B_n(\bar{\sigma},k_c)=\frac{k_B T}{4\pi k_c}\frac{(2n+1)}{Q(\bar{\sigma},n)},\quad n\geq 2. \tag{14}$$

The comparison with Eq. (10) gives the direct relation between the amplitudes of the vesicle fluctuations $\langle|U_n^m(t)|^2\rangle$, and the vesicle radius $\rho(\phi,\ t)$, which is experimentally measurable through its autocorrelation function $\xi(\gamma)$:

$$B_n(\bar{\sigma},k_c)=\frac{(2n+1)}{4\pi}\left\langle\left|U_n^m(t)\right|^2\right\rangle.o \tag{15}$$

In the dynamic analysis of the thermally induced fluctuations in the shape of a quasispherical vesicle, a space–time autocorrelation function $\xi(\gamma,\ \tau)$ of its radius is introduced [61,63]:

$$\xi(\gamma,\tau)=\left\langle \frac{1}{2\pi{R_0}^2}\left[\int_0^{2\pi}\rho(\phi+\gamma,t+\tau)\rho^*(\phi,t)d\phi-\rho(t+\tau)\rho^*(t)\right]\right\rangle. \tag{16}$$

Milner and Safran, following Schneider *et al.* [56], studied theoretically the hydrodynamic behavior of fluctuating vesicles. In their considerations, the inertial and convective terms in the Navier–Stokes equations were neglected and from the balance of forces on the vesicle surface the following expression for the time autocorrelation function of the amplitudes U_n^m was derived [58]:

$$\left\langle U_n^m(\tau)U_{n'}^{m'*}(0)\right\rangle=\delta_{nn'}\delta_{mm'}\left\langle\left|U_n^m(t)\right|^2\right\rangle\exp\left(-\frac{\tau}{\tau_n}\right), \tag{17}$$

where τ_n is the correlation time of the n-th mode of fluctuations, given by

$$\tau_n = \frac{\eta R_0{}^3}{k_c} \frac{(2n+1)}{Q(\bar{\sigma}, n)} \frac{(2n^2+2n-1)}{n(n+1)}. \tag{18}$$

Mitov *et al.* [61,63] showed that the autocorrelation function (Eq. (16)) can be decomposed in series of Legendre polynomials with coefficients, related to the autocorrelation time of each fluctuation mode via the expression:

$$\beta_n(\tau) = \frac{k_B T}{4\pi k_c} \frac{(2n+1)}{Q(\bar{\sigma}, n)} \exp\left(-\frac{\tau}{\tau_n}\right). \tag{19}$$

Thus, the relaxation of a fluctuating membrane was predicted to be influenced solely by the viscosity of the surrounding medium, the bilayer bending elasticity and the vesicle excess area (the difference between the vesicle's area and the surface area of a sphere with the same volume as the volume of the vesicle).

Later on, a theoretical revision of the dynamics of the shape fluctuations of quasispherical giant vesicles was made [21,48,64], taking into account the bilayer structure of the lipid membrane, and the friction between the monolayers of the bilayer of the vesicle membrane was predicted to influence the dynamics of membrane fluctuations. Using the measurements of the interlayer friction coefficient b_s [65], the second dissipative mechanism was predicted to be considerable or negligible for the dynamics, depending on the fluctuation wavelength [20,21,48]. According to the theoretical predictions of Yeung and Evans [48] and Bivas *et al.* [21], the interlayer coupling affects the membrane fluctuations' dynamics and another relaxation process is involved, thus leading to a two-exponential decay of the normalized amplitudes in the decomposition of the autocorrelation function (Eq. (16)) in Legendre polynomials:

$$\frac{\beta_n(\tau)}{\beta_n(0)} = \psi_n \exp(-\omega_n \tau) + (1-\psi_n) \exp(-\Omega_n \tau), \tag{20}$$

where $\omega_n < \Omega_n$ and $\psi_n = f(\omega_n, \Omega_n)$ [21,22,48].

If an additive molecule is present in the bilayer, an additional relaxation process has been predicted to affect the dynamics of the shape fluctuations [22]. When the vesicle changes its shape due to the TISF of its membrane, a re-distribution of the additive molecules will occur in each of the monolayers by means of their lateral displacement to the vesicle poles at the outer monolayer and – to its equator in the inner leaflet (Fig. 4). Thus, the lateral diffusion coefficient of the additive molecule will influence the dynamics of the vesicle shape fluctuations. It has been shown theoretically that this

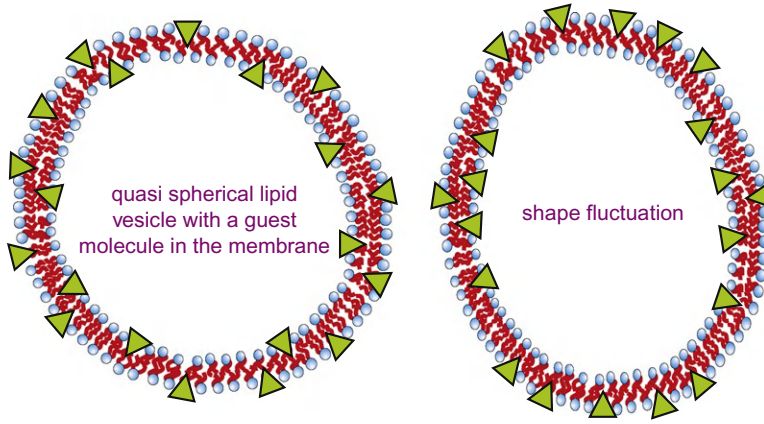

Figure 4 Sketch of the equatorial cross-section of a fluctuating vesicle with a guest molecule (depicted as triangles) in its membrane: qualitative demonstration of the impact of the diffusion of an inclusion to the dynamics of the shape fluctuations (see text).

autocorrelation function for a membrane, containing an additive with molar concentration C, is given by the expression [21,22]:

$$\frac{\beta_n(\tau)}{\beta_n(0)} = \psi_n \exp(-\omega_n \tau) + (1-\psi_n)\exp(-\Omega_n \tau) + \psi_n^{\mathrm{add}}(C)\exp\left[-D\frac{n(n+1)}{(R_0)^2}\tau\right], \tag{21}$$

where D is the two-dimensional diffusion coefficient of the additive and the pre-exponential factor before the third exponent $\psi_n^{\mathrm{add}}(C)$ is expressed by [22]:

$$\psi_n^{\mathrm{add}}(C) \approx -\frac{1}{k_c^{\mathrm{fr}}}\frac{\partial\left[k_c^{\mathrm{fr}}(c)\right]}{\partial C}\Bigg|_{C=0} C. \tag{22}$$

These theoretical results of Bivas and Méléard [22] reveal that the analysis of the TISF of lipid vesicles containing inclusions in their membranes, is an appropriate tool for the determination of the diffusion coefficient of the guest molecules in the lipid matrix.

Very recently, another dissipative mechanism of the mechanical energy stored in the thermally induced membrane fluctuations has been considered theoretically by taking into account the viscous friction of the flow in the

liquid around the vesicle caused by this displacement [66]. The time correlation functions of the vesicle's fluctuation modes have been calculated as a function of the mechanical and rheological properties of the system, namely, the tension of the vesicle bilayer, its bending elasticity at free and blocked intermonolayer exchange of molecules, the viscosities of the liquids in contact with the bilayer, the friction coefficient between the two monolayers, as well as the vesicle's radius and its bilayer thickness.

To summarize, by investigation and analysis of the TISFs of giant lipid vesicles and the dynamics of these fluctuations, one is able to determine in a completely noninvasive way the following membrane characteristics: (i) the membrane bending moduli at free, k_c^{fr}, and blocked, k_c^{bl}, exchange of molecules between the two monolayers of the vesicle's membrane; (ii) the intermonolayer friction coefficient, b_s, of the membrane; (iii) the coefficient of diffusion, D, of an inclusion in the bilayer.

The latter three constants are essentially new element from experimental point of view.

2.2. Experimental Determination of the Intermonolayer Friction Coefficient and the Bending Elasticity of Lipid Bilayers at Blocked Exchange of Molecules Between the Two Monolayers

It is important to recall that the analysis of the TISF of quasispherical lipid vesicles gives the value of the membrane bending modulus at free exchange of molecules between the two monolayers. This follows from the fact that the relative slipping of the monolayers is equivalent to the exchange of molecules between them in the limit of small enough fluctuations, compared to the radius of the vesicle.

The first experimental study of the dynamics of the TISF of GUVs has been performed by Schneider *et al.* [56] who measured the time correlation function of the difference between two perpendicular diameters of the fluctuating vesicle's contour observed microscopically. Later on, Duwe *et al.* [67] experimentally determined the time correlation functions of Fourier amplitudes for the second and the third mode. The first detailed dynamic study of TISF of quasispherical vesicles was published by Méléard *et al.* [60] who confirmed the mono-exponential character of the time correlation function using short time video image sequences of fluctuating GUVs.

As discussed in Section 2.1, when taking into account the double layer structure of the lipid membrane, the theory [20,21] predicts that the attenuation of the bending fluctuations of a pure lipid membrane will obey a double exponential-decay law. The typical accuracy of the experimental determination of the mean square amplitudes of vesicle's radius fluctuations is $\sim$10% for continuous illumination [49,61] and $\sim$5% when

applying stroboscopic illumination [68]. It has been estimated that in the former case the effect of the mutual displacement of the monolayers on the membrane fluctuation dynamics is not measurable for the highest wave numbers ($n \geq 16$) [21]. The first experimental study proving the presence of a second relaxation mechanism in the dynamics of TISF of GUVs has given a relation between the intermonolayer friction coefficient and the bilayer bending elasticity, obtained experimentally by analysis of the membrane fluctuation dynamics [69]. More recently, the value of the friction coefficient between the two monolayer leaflets of the membrane, b_s, and the bending elasticity modulus k_c^{bl}, were estimated from our stroboscopic illumination study of the dynamics of fluctuating vesicles, prepared from two types of single-component synthetic bilayers and this result, to the best of our knowledge, represents the only experimental data published so far for this otherwise immeasurable quantity [70].

Here, an example will be given for an experimental study of the statics and dynamics of TISF of GUVs composed of the synthetic lipid dioleoyl phosphatidylcholine (DOPC, Avanti Polar Lipids Inc., AL, USA). The electroformation method [71] was applied to prepare vesicles. Our electroformation chamber consisted of two (indium-tin oxide) ITO-coated plates, separated by a silicone spacer (polydimethylsiloxane—PDMS, Sylgard 184 silicone elastomer kit, Dow Corning GmbH, Germany), previously soaked in double-distilled water as indicated in [72]. The latter is necessary to wash away all no cured rests in the elastomer and thus to avoid any undesirable ion contamination of the aqueous phase of the electroformed vesicle suspension. For the same reason, the metal contacts between the conductive plates and the electrical wires were situated outside the cell. Lipid depositions were made by the careful and uniform spreading of ~100 μL of DOPC solution with concentration of 1 g/L in chloroform-methanol (Fluka Inc., Germany) mixture (9:1 volume parts) on the ITO-side of each ITO-coated glass plate. In our experiments freshly prepared organic solution of the lipid (previously lyophilized and kept under vacuum at −20 °C) was used. After the complete drying of the lipid for at least 2 h under vacuum, the electroformation chamber was assembled in a way to completely fill the internal volume (~5 ml) with double-distilled water, previously obtained in a quartz distiller without ion-exchange filter at the outlet and equilibrated in air (*p*H 5.5). Then, AC electric field (~10 Hz) was applied to the chamber, successively increased up to E_{pp}= 0.3 V/mm (where E_{pp} denotes the peak-to-peak amplitude of the electric field applied). In several hours, a high yield of unilamellar vesicles without microscopically observable defects and with radii (~5–20 μm), appropriate for fluctuation analysis, was obtained.

For sample observation and registration an inverted Axiovert 100 (Zeiss, Germany) microscope in phase contrast was used with a water-immersed 63× (NA 0.75, Ph3) objective. The video signal from the CCD camera

control unit (C2400-60, Hamamatsu, Japan) was fed to a frame grabber board (DT3155, Datatranslation, USA) mounted in a computer for proper digitization (768 × 576 8-bit pixels). Images were acquired in real time (25 frames per seconds), and recorded on the PC to obtain a long (7–10 min total duration of the record, or more than 10^4 frames) image sequence of the equatorial cross-section of the fluctuating vesicle with the focal plane of the objective (see Fig. 3). A stroboscopic illumination was applied in order to overcome the smearing effect of the camera integration time on the highest fluctuation modes and thus, to improve the precision of the fluctuation analysis [68].

First, the bending modulus at free exchange of molecules between the monolayers, comprising the bilayer, k_c^{fr}, was measured independently. To this aim, every 25-th frame from a given image sequence was taken in order to extract a succession of images of the vesicle contour fluctuations, captured every second. The substitution of typical experimental values for the vesicle radius, the bending elasticity modulus, the membrane tension and viscosity of the suspending medium ($n = 2$, $k_c^{fr} \approx 10^{-19}$ J, $\bar{\sigma} \approx 0.01$, $\eta \approx 10^{-3}$ Pa s, $R_0 = 10$ μm) in Eq. (18) permits to estimate the correlation time of the slowest fluctuations as $\tau_2 \approx 0.5$ s. In this way, taking one frame per second, it was assured to deal only with independent fluctuations for every captured contour. For each registered image of the fluctuating vesicle (Fig. 3), the contour representing the equatorial cross-section of the vesicle membrane was extracted as explained in details in [61]. All the "out-of-focus contours" were disregarded and not taken into account in the following analysis. The next step was to determine the exact position of the vesicle contour in every frame, the centre of mass and the instantaneous radius-vectors at 128 angularly equidistant points of the vesicle contour. The instantaneous value $B_n'(t)$ of the quantity B_n from Eq. (14) was calculated for each of the extracted contours of the fluctuating vesicle as the amplitude of the n-th mode of the development in Legendre polynomials of the instantaneous angular autocorrelation function $\xi(\gamma, t)$ from Eq. (13). Evidently, $B_n = \langle B_n'(t) \rangle$. The root mean square:

$$\Delta B'_n = \sqrt{\left\langle \left(B'_n(t)\right)^2 \right\rangle - \left(\left\langle B'_n(t) \right\rangle\right)^2} \tag{23}$$

was also calculated.

For each studied vesicle, the function $\chi^2\left(k_c^{fr}, \bar{\sigma}\right)$, defined in a standard way, was used

$$\chi^2\left(k_c^{fr}, \bar{\sigma}\right) = \sum_{n=2}^{N_{max}} \frac{\left[\left\langle B'_n(t) \right\rangle - B_n\left(k_c^{fr}, \bar{\sigma}\right)\right]^2}{\left(\Delta B'_n\right)^2}, \tag{24}$$

where $N_{\max}$ was the highest number of the index n used for the fitting. The values of k_c^{fr} and $\bar{\sigma}$ minimizing the function $\chi^2\left(k_c^{fr}, \bar{\sigma}\right)$ were determined numerically, as well as their confidence intervals. While $\bar{\sigma}$ can vary from vesicle to vesicle, k_c^{fr} is expected to be the same for all studied vesicles. The condition requiring the goodness of fit for each selected vesicle to be more than 0.1 was imposed. The second criterion for selecting a vesicle was its volume to be constant. If the vesicle's volume is constant in time, its excess area will be constant too and the amplitudes B_n for a given mode, n, will not increase or decrease during the measurement. Since the second (elliptical) fluctuation mode is the most sensitive in the case of any change of the vesicle's volume, B_2 will change the most. Therefore, in order to quantify any undesirable trend, the squares of the amplitudes of the second mode of fluctuations $(B_2)^2$ from Eq. (14) were plotted as a function of time for every analyzed vesicle (Fig. 5). The best linear fit of the experimental data with a function of the type $y = C + D \cdot x$ (with $x \in [0, N]$) gave the values of the coefficients and their errors $C \pm \Delta C$ and $D \pm \Delta D$. For an ensemble of N experimental measurements of the quantity y_i, the following relation between the dispersion, α_y, of the data and the dispersion, $\alpha_{\bar{y}}$, of the mean value $\bar{y} = \left(\Sigma_{i=1}^{N} y_i\right)/N$ exists

$$\alpha_y = \alpha_{\bar{y}}\sqrt{N}. \tag{25}$$

A vesicle can be considered as good for analysis, if the slope of the linear regression of the second mode amplitudes, B_2, is negligible compared to the dispersion of the data, namely:

$$|D| \ll \frac{\alpha_{\bar{y}}}{N\sqrt{N}}, \quad \text{where} \quad \alpha_{\bar{y}} = \sqrt{\frac{\sum_{i=1}^{N}\left(y_i - \bar{y}\right)^2}{N(N-1)}}. \tag{26}$$

The fulfillment of the above condition was imposed as a criterion for the stationarity of vesicles. Under this criterion of selection, only stationary vesicles were processed further and their membrane bending elastic modulus, k_c^{fr}, and tension, $\bar{\sigma}$, were deduced from the static analysis of their fluctuations as discussed in the previous section and described in details in [49,61].

Further, dynamic analysis of the vesicle's TISF was performed. To this aim, the vesicle contours were extracted from the continuous (25 frames per second) image sequence and the experimental Legendre amplitudes β_n of the space–time autocorrelation function $\xi(\gamma, \tau)$ of the fluctuations, defined in Eq. (16), were calculated for $2 \leq n \leq 11$ [61]. For those vesicles, for which the amplitudes of the spherical harmonics can be determined with high

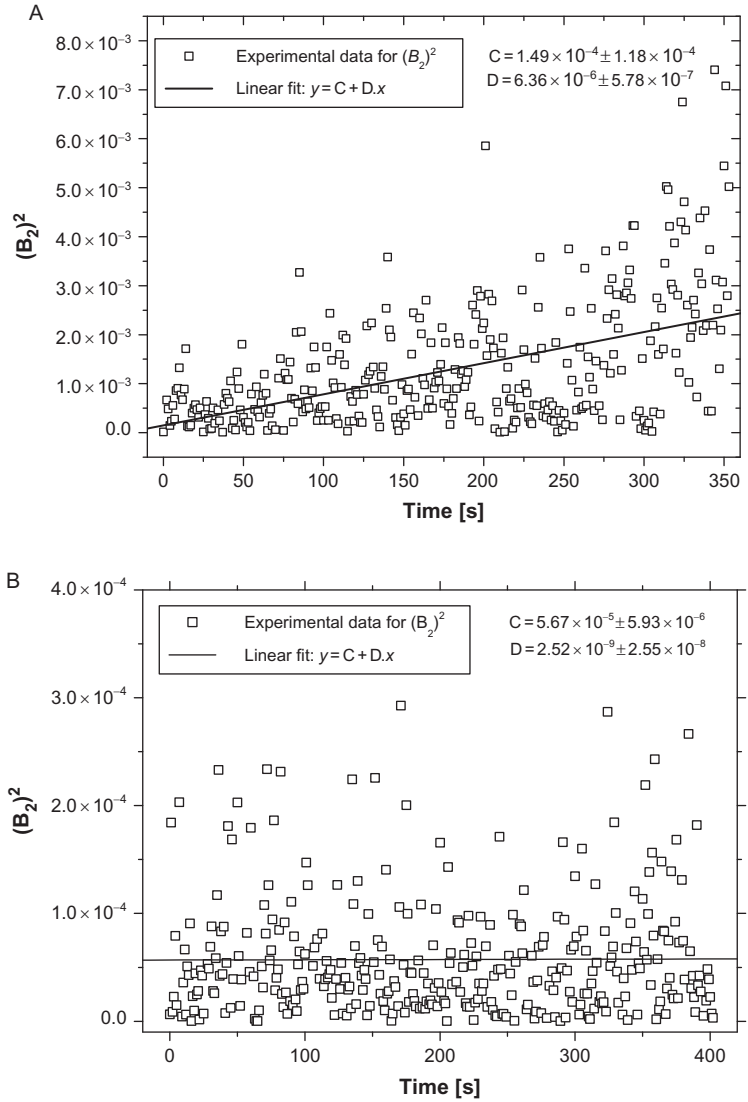

Figure 5 Time dependency of the squares of the second mode amplitudes in the decomposition of the autocorrelation function in a series of Legendre polynomials (points) for two quasispherical DOPC vesicles with linear fits of the data (solid lines): (A) example of a vesicle not satisfying the condition (26); (B) stationary vesicle, good for analysis.

enough precision, a double-exponential fit of the data for the long-wave modes of fluctuations can be performed [21]. The pre-exponential factors and the exponential indexes for the two exponents in Eq. (20) were

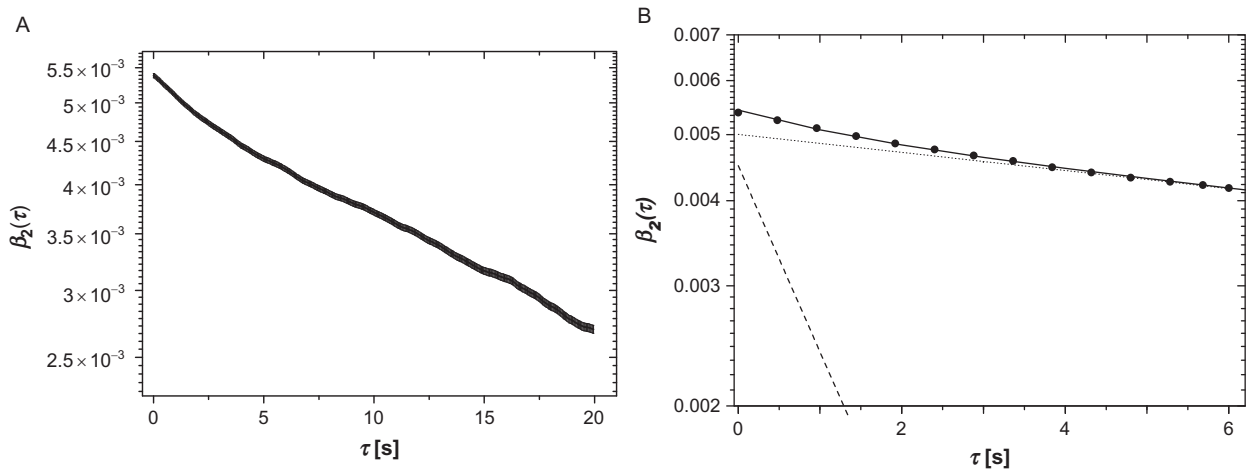

Figure 6 (A) Experimental data for the Legendre polynomial amplitudes of the second mode in the decomposition of the time–space autocorrelation function for DOPC vesicle with radius 8.4 μm; (B) Experimental points and the two exponential decays fitting the data (for sake of clarity, every tenth point and only the first part of the time interval are shown): $\beta_2 = 5 \times 10^{-3} \exp(-0.031\tau) + 4.3 \times 10^{-4} \exp(-0.618\tau)$; $\tau_\omega = 32.8$ s; $\tau_\Omega = 1.62$ s.

determined for each mode of fluctuations up to the sixth mode. In the analysis of the acquired experimental data for the dynamics of the TISF of DOPC vesicles, the theoretical description by Bivas *et al.* [21] was used. The experimental results for the second mode of the spherical harmonics for a DOPC vesicle with radius $R_0 = 8.4$ μm and $\bar{\sigma} = -5.2$ are presented in Fig. 6.

The experimental data for the second and the third modes of fluctuations were analyzed. The bending elasticity coefficient at blocked intermonolayer exchange of molecules was calculated independently using the relation between the experimentally determined frequency in the first exponent in Eq. (20) $\omega_n = f(\eta, k_c^{fr}, k_c^{bl}, R_0, \sigma)$ and the two bending coefficients [21]:

$$\omega_n = \frac{k_c^{bl}}{\eta (R_0)^3} \times \frac{\alpha_n}{Z(n)}, \quad \text{where } Z(n) = \frac{(2n+1)(2n^2+2n+1)}{n(n+1)} \quad \text{and}$$
$$\alpha_n = (n-1)(n+2)\left[n(n+1) + \frac{\sigma (R_0)^2}{k_c^{bl}} - \frac{1}{8\pi} \frac{k_c^{bl}}{\Delta k_c} \left(c_0^0\right)^2 \right] + \frac{1}{\pi} \frac{\Delta k_c}{k_c^{bl}} \left(c_0^0\right) \tag{27}$$

where η, k_c^{fr}, R_0, and σ are known, $\Delta k_c = k_c^{bl} - k_c^{fr}$ and c_0^0 has the meaning of induced spontaneous curvature that was found to be important for the dynamics of the second fluctuation mode when dealing with vesicles with molecular density difference of its two monolayers, close to its equilibrium value. For vesicles far from equilibrium, it has been obtained that the influence of c_0^0 can spread over higher fluctuation modes also and therefore, c_0^0 has to be one of the adjustable parameters in the analysis of the TISF of vesicles [21].

It was experimentally obtained that for DOPC bilayers, $k_c^{bl}/k_c^{fr} = 1.73$ (see Table 1), and consequently, it is fulfilled that $\Delta k_c \approx k_c^{fr}$. Our result is an experimental confirmation of the theoretical estimations of Bivas and Méléard [22] and is in accordance with the evaluation $\Delta k_c \approx k_B T$, experimentally obtained by Pott and Méléard [69] for SOPC bilayers.

The theoretically derived relation between the measured quantity and the bending elasticities at free and blocked intermonolayer exchange of molecules, the vesicle radius and the distance between the neutral surfaces of the two monolayers, permitted us to calculate the intermonolayer friction coefficient:

Table 1 Mechanical properties of DOPC membrane: experimental values deduced from the static and dynamic analysis of the thermally induced shape fluctuations of quasispherical GUVs (results for a vesicle with $R_o = 8.4$ μm and $\bar{\sigma} = -5.2$)

k_c^{fr} [10^{-1} J]	k_c^{bl}/k_c^{fr}	$(k_c^{bl} - k_c^{fr})/[b_s(d_0)^2]$ (10^{-12} m^2/s)	b_s (10^9 N s/m^3)
0.86 ± 0.09	1.73 ± 0.3	4.71	2.6

$$\Omega_n = \frac{k_c^{bl} - k_c^{fr}}{b_s (d_0 R_0)^2} n(n+1). \tag{28}$$

The results from the analysis of the experimental data permitted to determine the value of the combination $(k_c^{bl} - k_c^{fr})/[b_s(d_0)^2] = 4.71 \times 10^{-12}\,\mathrm{m}^2/\mathrm{s}$, where d_0 stands for the distance between the neutral surfaces of the monolayers comprising the bilayer.[1] The value for d_0, obtained from the best fit of our data, is close to the value, reported for the hydrophobic thickness of DOPC bilayers $\left(d_0 \approx 26\dot{A}\right)$ [73]. Our estimation of the membrane bending coefficient at blocked lipid exchange between the monolayers, k_c^{bl}, permitted us to calculate the intermonolayer friction coefficient, b_s, for DOPC bilayers (cf. Table 1). The intermonolayer friction coefficient, obtained here, is in good agreement with the value, calculated on the basis of the theoretical estimations of the quantities, participating in the above combination [21,69], as well as with the results of Merkel *et al.* [65] for the same quantity, measured in the case of bilayers deposited on glass substrates, and with our previous results for b_s of DOPC membranes [70].

In conclusion, the analysis of the TISFs of quasispherical vesicles represents a powerful tool to study membrane mechanical properties. Static and dynamic fluctuation analysis, performed together, allows deducing important material constants of the bilayer, such as the bending rigidity coefficients at free and blocked intermonolayer lipid exchange, the friction coefficient of the mutual displacement of the two monolayers comprising the membrane, as well as the diffusion coefficient of an inclusion in the bilayer. An important advantage of the discussed method is the fact that it is completely nondestructive, and one can obtain information about important physical properties of the membrane in a noninvasive way.

3. Dynamics of Vesicles in Unconfined Shear Flows: Overview of Theory and Experiments

The investigation of the lipid vesicle dynamics in hydrodynamic fields is a step forward to the better understanding of the behavior and the stability of these objects in flow. Recently, an important progress in this direction was made. Considerable knowledge about the individual dynamics of vesicles in different types of flow has been accumulated thanks to the intensive theoretical [23–27,29–32,74] and experimental [33–39,75] investigations performed so far. The key experimental observations and advances in theoretical description of vesicle and RBC dynamics in various

[1] Neutral surfaces are these surfaces at which the surface area per molecule is kept constant when the bilayer is cylindrically bent at allowed intermonolayer exchange of molecules.

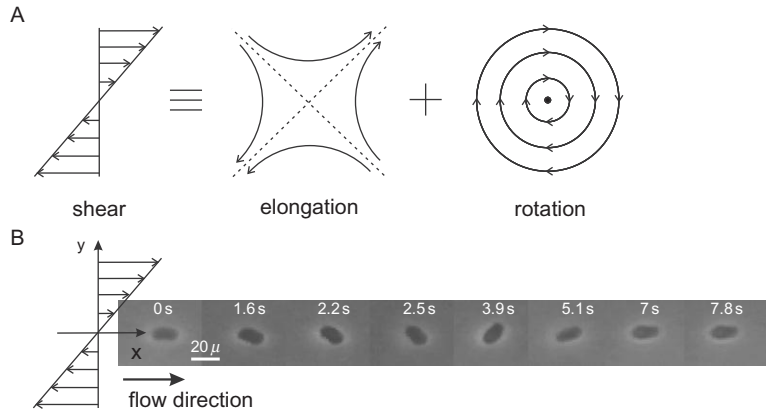

Figure 7 (A) Schematic presentation of the velocity field in a linear flow (equal to superposition of extension and rotation). (B) Experimental picture of a tumbling vesicle in simple shear flow.

unconfined flows as well as in capillary flows, relevant to the microcirculation, have been reviewed recently by Vlahovska *et al.* [32].

Here, we focus on the theoretical and experimental aspects of vesicle dynamics in linear hydrodynamic fields. A simple shear flow can be decomposed in an elongation component (pure deformation of extension) and a rotational part (rigid body rotation) as depicted in Fig. 7A. Deformable objects such as lipid vesicles become ellipsoids in shear flows (Fig. 7B). To assume this shape, a vesicle must possess some excess area, Δ, compared to the surface area of a sphere with the same volume (equivalent sphere), V [76]:

$$\Delta = \frac{S}{R_0} - 4\pi, \quad \text{where} \quad R_0 = \sqrt[3]{3V/4\pi}, \tag{29}$$

and S is the vesicle surface area.

Another quantity often used to quantify the vesicle deformability in hydrodynamic flows, is the so-called "'reduced volume", υ, representing the ratio between the vesicle volume and the equivalent sphere volume [77]:

$$\upsilon = \frac{3\sqrt{4\pi}V}{S^{3/2}} \quad \text{and} \quad \Delta = 4\pi\left(\upsilon^{-2/3} - 1\right). \tag{30}$$

For a spherical object $\upsilon = 1$ and $\Delta = 0$. For a normal (not pathological) RBC (erythrocyte) the same quantities are $\upsilon \approx 0.6$ and $\Delta \approx 5$.

Another important parameter when considering vesicle and RBC dynamics in linear hydrodynamic fields is the ratio between the viscosity of the fluid, enclosed by the lipid bilayer (for vesicles) and plasma membrane (for RBCs), $\eta_{\rm in}$, and the viscosity of the surrounding medium, $\eta_{\rm out}$:

$$\lambda = \eta_{\rm in}/\eta_{\rm out}. \tag{31}$$

At physiological temperatures (37 °C) erythrocytes are characterized by $\lambda \approx (7-13)$ for young and old cells, respectively [78]. For vesicles, this parameter is easily tunable thanks to the advanced experimental protocols for GUV formation, permitting good control of the physicochemical properties of the internal and external aqueous phases [13].

One more parameter, which is relevant to the dynamics of vesicles in shear flows, is the dimensionless capillary number, $Ca = \eta_{\rm out}\dot{\gamma}R_0^3/k_{\rm c}$, depending on the shear rate of the flow,$\dot{\gamma}$, the viscosity of the suspending medium, $\eta_{\rm out}$, as well as on the vesicle radius, R_0, and the bending coefficient of its membrane, $k_{\rm c}$.

It has been reported that in shear flows, vesicles and RBCs show various dynamical behaviors. For vesicles the following types of motion in linear hydrodynamic fields have been observed: (i) tank-treading (*TT*): the vesicle orients its long axis at a fixed angle with respect to the flow direction while its (fluid) membrane undergoes a tank-treading like motion [23,33,79], (ii) tumbling (*TB*) (or flipping) of the vesicle [35], (iii) vacillating-breathing (*VB*) (called also "trembling" [36,39] or "swinging" [80]) for vesicles (oscillation of the long axis about the flow direction, accompanied with breathing of the shape) or swinging, for RBC (nearly shape preserving oscillation about a nonzero angle) [81], *(iv)* spinning [30] or kayaking [82], where the main axis describes a cone about the perpendicular to the plane of the shear flow. As a consequence of the richer mechanical properties of RBC's membrane, namely the elasticity of the spectrin network, other more complex dynamics of RBCs have been predicted (under the assumption that the shape is fixed) [83] and observed [84]. New features of the RBC's dynamics compared to vesicles is that for small viscosity ratios, λ, and depending on the applied shear rate, $\dot{\gamma}$, erythrocytes can exhibit various types of motion. At low shear rates RBCs tumble, while at intermediate shear rates they perform swinging motion and finally, at high shear rates RBCs behave similarly to vesicles and show pure tank-treading [38,81]. A new theory [85], including the deformation of the RBC shape has been recently presented. This theory shows that the intermittent regime (tumbling interrupted by few cycles of swinging) reported in [83] disappears. In other words the intermittent regime seems to be an artifact of the shape preserving assumption.

In the limit of nearly spherical shapes ($\Delta \ll 1$) an analytical theory with an arbitrary viscosity contrast between the interior and the exterior of the vesicle has been developed in [28]. The vesicle shape evolution has been described by

the angle of inclination of the major axis of the ellipsoid, ψ, and its length, R (Fig. 7B). Neglecting the membrane thermal fluctuations, the following evolution equations of the vesicle shape have been obtained at leading order [28]:

$$\frac{\partial \psi}{\partial t} = -\frac{1}{2} + \frac{h}{2R(t)} \cos[2\psi(t)], \tag{32}$$

and

$$\frac{\partial R}{\partial t} = h\left(1 - 4\frac{R^2(t)}{\Delta}\right) \sin[2\psi(t)], \tag{33}$$

where $h = 4\sqrt{30\pi}/(32 + 23\lambda)$.

It has been shown also that the *TT*–*TB* transition occurs at a critical viscosity ratio, given by [28]:

$$\lambda_c = -\frac{32}{23} + \frac{120}{23}\sqrt{\frac{2\pi}{15\Delta}}. \tag{34}$$

Unlike capsules and droplets, vesicle dynamics does not depend on the mechanical properties of the interface (vesicle membrane), which follows from the fact that the above equations do not contain *Ca* but only Δ. This particularity reflects the condition of constant surface area of the vesicle membrane (membrane incompressibility) and accounts for the effect of the membrane tension on the vesicle dynamics. Another interesting point is that the evolution equations for vesicles are nonlinear, while at leading order capsules [86] and droplets [87] respond linearly to external flows.

If instead of a vesicle, a nondeformable ellipsoid in shear flow is considered, then $R(t) = 0$ and the analytical result (32) reduces to the Keller and Skalak's expression for the rotation of a rigid tank-treading ellipsoid with fixed shape [88], thus only *TT* and *TB* exist. The new type of motion of *VB* has been discovered by allowing the vesicle shape to freely evolve [28]. Initially coexistence of *VB* and *TB* modes has been obtained theoretically [28,29]. Experimentally, *VB* has been observed at intermediate *Ca*, respectively at intermediate λ [36]. A major consequence of increasing the capillary number on vesicles in *TB* regime is the decrease of the tumbling frequency with approaching the transition to *VB* [27,35]. The phase diagram, representing the three types of vesicle dynamics in linear flows, has the general form given in Fig. 8. Recently, Deschamps *et al.* [35] performed an extensive experimental study and explored in details the influence of all parameters on the vesicle dynamics in shear flow. Their experimental phase diagram is in good qualitative agreement with the theoretical results obtained previously for nearly spherical vesicles [30,41,90] (cf. Fig. 9).

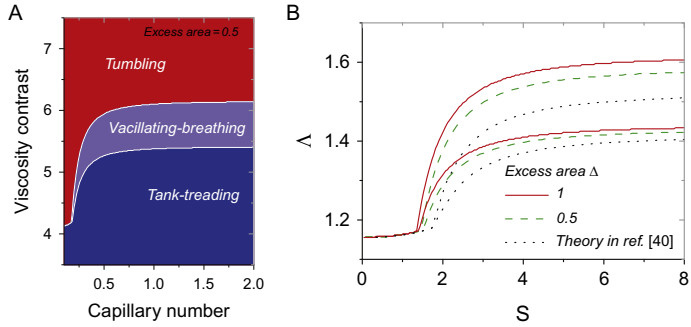

Figure 8 (A) A typical phase diagram representing the three regimes: TT (black area), VB (dark grey), and TB (light grey) in the ($\lambda - Ca$) plane (obtained in [89] for $\Delta = 0.5$). (B) Comparison between the two phase diagrams obtained by Kaoui *et al.* [89] (full and dashed lines) and the one reported in [40] (dotted black line) for three different values of the excess area. In both cases, the phase diagram is drawn in the ($S - \Lambda$) plane as in [90]. (Graphics reproduced from [89] with permission; Copyright (2009) by the American Physical Society).

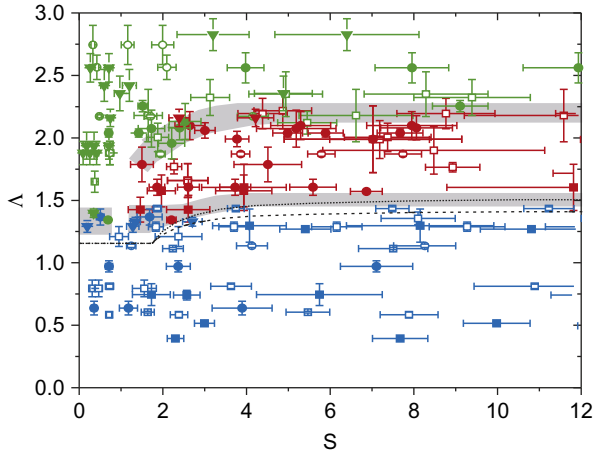

Figure 9 Phase diagram of the vesicle dynamical states in a shear flow: ■ [0–0.55], □ [0.55–0.8], ● [0.8–1.05], ○ [1.05–1.25], ▼ [1.25–2]. Black points correspond to the TT regime; dark grey points – to the VB regime; and light grey points stand for TB vesicles. Grey bands are guides for the eye. Dashed, dotted, and dash-dotted black lines are the theoretical boundaries between TT and VB; VB and TB; TT and TB, respectively (theory from [30]) (Graphics reproduced from [39] with permission; Copyright (2009) by the American Physical Society).

According to the theoretical results of Lebedev *et al.* [30,90], the parameters determining the dynamical regime of a vesicle in simple shear flow, are two, defined as $S = 7\pi\dot{\gamma}\eta_{\text{out}}R_0^3/3\sqrt{3}k_c\Delta$ and $\Lambda = 4(1 + 23\lambda/32)\sqrt{\Delta}/\sqrt{30\pi}$.

The experimental data of Fig. 9 (reproduced from [39]), are mixed with respect to Δ, since the authors assume that only S and Λ are relevant as reported in [30]. The perturbation theory developed by Danker *et al.* [41] has shown that the independent parameters, which are important for the dynamics of a vesicle in linear flow, are three, namely Ca, λ, and Δ. The pertinence of these parameters has been extensively discussed by Kaoui *et al.* [89]. It has been shown that when S and Λ are constant, the variation of the third parameter Δ, shifts significantly the boundaries of the phase diagram (Fig. 8B). Other quantities also, such as the amplitude of oscillation of the vesicle's long axis in *VB* mode, have been obtained to be extremely sensitive to the third parameter Δ at constant S and Λ [89]. A more recent analytical calculation [91] has revealed the necessity of including higher order harmonics (fourth order harmonics, albeit a linear shear flow predominantly excites second harmonics) even though the shape is arbitrarily close to a sphere. This study was motivated by a full 3D numerical simulation [82] that showed that even in the quasispherical limit the previous theories including only second order harmonics had a significant quantitative gap with the full numerics. The recent analysis [91] is a very good agreement with the full numerical solutions. Both the full numerical solution and the new analytical theory confirmed the relevance of three control parameters, in accord with Danker *et al.* [41] and Kaoui *et al.* [89]. A critical comparison between experiments and theory is provided in [82] and in [91].

An interesting question is whether the thermal fluctuations affect vesicle dynamics in shear flow. Experiments at very low shear rates have shown their significant influence on the vesicle shape and orientation in shear flow [24,36]. The important effect of membrane thermal fluctuations on the vesicle orientation has been registered in the *TT* regime [33] and also, on the vesicle shape in the *VB* mode [35,36,39] especially in the contraction phase, when the membrane is strongly fluctuating. Nevertheless it has been shown, that the average behavior is well described by the traditional models not taking into account the thermal noise [33]. It has been observed that oscillatory shear reduces membrane fluctuations [37], possibly as a consequence of increase in the membrane tension [92]. The same study of the effects of time-dependent external flows on the vesicle dynamics, reported the appearance of transient membrane wrinkles upon reversal of the flow direction [37]. The observed membrane undulations have been attributed to the appearance of negative tension [31].

The signature of the membrane bending elasticity on vesicle dynamics in shear flows is possible to be captured by higher-order theory. The perturbation analysis has been extended by including thermal fluctuations [24,93] and membrane bending elasticity [30,41]. It has been obtained that thermal fluctuations induce intermittent tumbling and alter the *TT*-to-*TB* transition [93,94]. It has to be pointed out that the analytical theories developed so far

for vesicle dynamics in shear flow [30,41] obtain the same qualitative shape of the phase diagram (Fig. 8), but compared to experiments, these models predict significantly lower transition values of viscosity ratios λ (or Λ as in [30]) (cf. Fig. 9). This quantitative discrepancy has been overcome in recent analytical [91] and numerical [82] studies by taking into account higher order spherical harmonics in the vesicle shape equation, while previous studies accounted only for the second mode of the shape decomposition in spherical harmonics. The latest analytical results of Farutin *et al.* [91] revealed that higher order terms and harmonics (even if they are not directly excited by the shear flow) is necessary to be included when the vesicle dynamics in shear flow is being analyzed. Furthermore, as a result of the excitation of the four-order harmonic in the shape evolution equations of a vesicle in a linear flow, a qualitatively new feature of the phase diagram has been obtained, namely an important widening of the *VB* regime band over a critical shear rate of the flow [91].

4. Microscopic Signature on the Rheology of Vesicle and Red Blood Cell Suspensions

The rich phase diagram of the vesicle dynamics in shear flows draws the attention to the possible impact of the microscopic dynamics (*TT, VB*, and *TB*) of these deformable particles and the transitions between the various dynamic states on the rheology of vesicular suspensions. Here, an example will be given for an experimental study of the rheology of dilute suspensions of vesicles and RBCs. By focusing simultaneously on GUV and RBC suspensions, information can be drawn regarding rheology, about similarities and differences of the two systems. As discussed in details in Section 1, besides constituting a relatively simple system, easily reproducible in laboratory conditions, vesicles are believed to capture some features of erythrocytes. In rheological studies, the parallel experiments with suspensions of vesicles and such of erythrocytes give the possibility to reveal and quantify the contribution of the cytoskeleton to the studied properties.

In order to answer the naturally arisen question about the signature of the vesicle or erythrocyte dynamics on the macroscopic level of rheology, viscosities of diluted suspensions were measured as a function of the viscosity ratio λ between the inner and outer fluids (relative to the vesicle or erythrocyte membrane). Rheology of dilute RBC suspensions was studied experimentally for the case, where the intercellular adhesion is absent. Hydrodynamic interactions between cells were weak and rouleaux formation was inhibited by removal of plasma proteins.

Vesicle suspensions were obtained from the synthetic lipid dioleoylphosphatidylcholine via electroformation [71] in the desired internal

solution containing sugars (sucrose or glucose) and/or dextran. All chemical substances used for preparation of suspensions in the present study, were purchased from Sigma-Aldrich (France). After dilution in the relevant external solution, which was chosen in a way to assure the necessary λ, suspensions were centrifuged and supernatants and sediments were collected separately. Viscosity measurements of the internal solution, the supernatant and the sediment, give respectively η_{in}, η_{out} and the effective viscosity of the suspension, η_{eff}. The microscopic characterization permits to calculate the volume fraction of vesicles in each suspension [42].

Whole blood from healthy donors was provided by the French National Centre of Blood (Etablissement Français du Sang—EFS, Grenoble) and the University Hospital (CHU) in Grenoble. Blood washing in PBS (Phosphate-buffered saline) buffer solution by gentle centrifugation permitted to remove plasma proteins and the other cellular fractions thus obtaining only erythrocyte concentrate in buffer solution. After the subsequent dilution in the desired external solution (containing dextran and/or PBS), the measurement of the suspension viscosity, η_{eff}, was performed. The experimental determination of the outer viscosity was carried out on the supernatant after the centrifugation of RBC suspensions till the complete cell sedimentation. All experimental procedures are described in detail in [42].

In the dilute limit, the variations of suspension viscosities compared to the viscosity of the suspending medium are proportional to the volume fraction. The intrinsic viscosity is defined as [42]:

$$[\eta] = \frac{\eta_{eff} - \eta_{out}}{\varphi \cdot \eta_{out}}, \tag{35}$$

where ϕ is the volume fraction of particles.

All viscosity measurements were performed at the constant temperature of 22 °C with different instruments whose choice depended on the expected value of the measured viscosity: for low viscosities a Schott capillary viscometer or a LS30 low-shear rheometer (Contraves, Switzerland) with cylinder-Couette geometry were used, otherwise we applied a stress-controlled Bohlin Gemini 150 rheometer (Malvern Instruments, Germany) with a cone-plate geometry.

Viscosity measurements were carried out in a large range of shear rates in order to detect possible viscoelastic or aggregation effects and determine the range of shear rates where measurements are accurate and correspond to the dilute suspension limit (Fig. 10). For RBCs in PBS buffer, measurements were made at different hematocrit values in order to check the applicability of dilute suspension theories and the appearance of hydrodynamic interactions [42]. It has been derived that for a suspension of vesicles in the *TT* branch of the phase diagram, the intrinsic viscosity reads [28]:

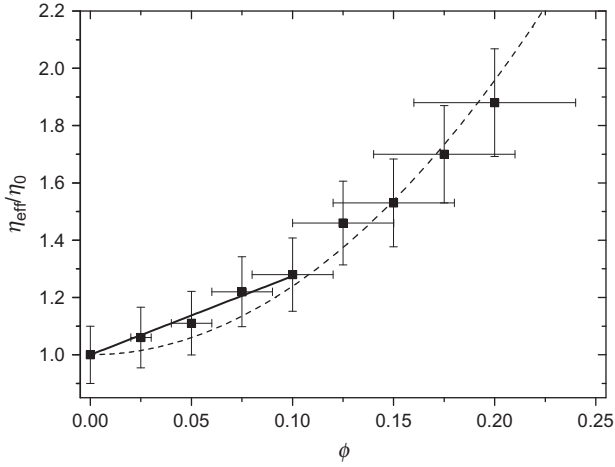

Figure 10 Experimental data for the relative viscosities of RBC suspensions vs. the volume fraction of the cells; parabolic fit (dashed line) of the data: $y = A + B \cdot x + C \cdot x^2$ with $A = 1$, $B = 0$, $C = 23.95 \pm 2.9$. Limits of dilute approximation for RBC suspensions: for small volume fractions, ϕ, of RBCs, relative viscosity increases linearly with ϕ (the solid line represents linear fit for $\phi \leq 0.1$: $y = C + D \cdot x$ with $C = 1$, $D = 2.75 \pm 0.12$).

$$[\eta]_{TT} = \frac{5}{2} - \Delta \frac{23\lambda + 32}{16\pi}. \tag{36}$$

If spherical particles are considered (i.e., $\Delta = 0$), the above expression reduces to the classical result of Einstein for the intrinsic viscosity of a dilute suspension of rigid spheres.

In the small excess area limit, the following expression has been obtained analytically for the intrinsic viscosity of a dilute suspension of tumbling vesicles [40]:

$$[\eta]_{TB} = \frac{5}{2} + \sqrt{\frac{30}{\pi}} \left[\frac{\sqrt{\Delta - 4h^2}}{\sqrt{\Delta + 4h^2} + \sqrt{\Delta}} - h \right], \tag{37}$$

where $h = 60\sqrt{2\pi/15}/(23\lambda + 32)$ with TB corresponding to $\Delta > 4h^2$, and TT—to the opposite condition.

In their experimental study, Kantsler *et al.* [95] found that at low λ the effective viscosity $[\eta]$ of vesicular suspensions increases with viscosity ratio λ. Our experimental results are shown in Fig. 11. The measured values of the intrinsic viscosities $[\eta]$ (35) are traced as a function of the viscosity ratio λ for vesicular suspensions with $0.03 \leq \phi \leq 0.12$. Our findings are consistent with recent theoretical studies on vesicle suspensions [40]. For every

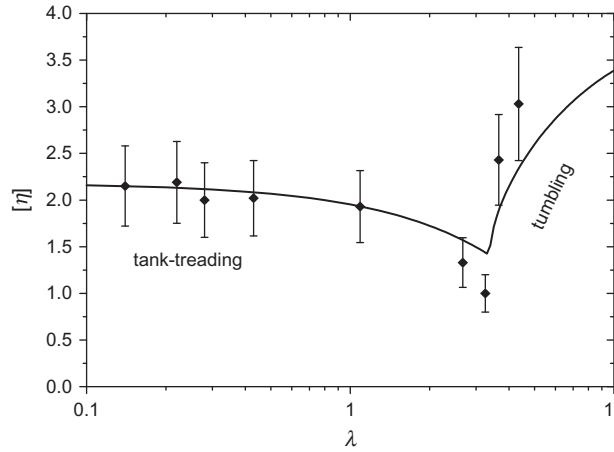

Figure 11 The intrinsic viscosity (Eq. (35)) of vesicular suspensions ($0.03 \leq \varphi \leq 0.12$) as a function of the viscosity ratio. The solid line represents the analytical results (Eqs. (36) and (37)) for vesicles with $\Delta = 0.5$ (Reprinted from [42]; Copyright (2008), with permission from Elsevier).

suspension it has been also checked if vesicles exhibit *TB* or *TT*. Vesicle samples are usually much more polydisperse in size than RBCs [42]. Despite their polydispersity, the viscosity of vesicle suspensions follows the general trend of a slow decrease in the tank-treading regime and a rapid increase after the transition to tumbling. Qualitatively, the pronounced decrease of the intrinsic viscosity $[\eta]$ in the vicinity of the *TT*-to-*TB* transition can be explained with the smaller viscous dissipation, resulting from the alignment with the flow of the particle's long axis, when approaching the transition to *TB*. In the *TB* regime already, larger fluid volume is disturbed by the flipping particle, thus leading to an increase of the viscosity.

With regards to erythrocytes, it is noteworthy that even if their biconcave cellular shape being far from that of a sphere, the rheology of RBC dilute suspensions has been obtained experimentally [42] to be in qualitative agreement with the theoretical results for vesicles [40]. Thus, the rheological constitutive law for dilute vesicular suspensions should serve as a first step from microscopic considerations toward blood rheology. Remarkably, the intrinsic viscosity decreases until the viscosity ratio reaches the range (2–3), and then sharply increases. This change of regime corresponds to the transition from tank-treading to tumbling that is observed at high shear rates when the relative viscosity is increased. The experimental results for RBC suspensions suggest that, as long as the viscosity is concerned, no qualitative effect of the cytoskeleton can be concluded. Quantitative effects are, however, quite significant. The intrinsic viscosity of dilute RBC suspensions exhibits a pronounced minimum, when the viscosity of the

ambient medium is close to the value at which the transition from *TT* to *TB* occurs. It was found [42] that the intrinsic viscosity of the suspension changes by about a factor four in the explored parameter range even at low volume fraction of erythrocytes ($\varphi \leq 0.1$).

A major result reported here is the fact that the experimental rheology of RBC suspensions shows the same general trend as the theory for vesicles: the effective viscosity exhibits a minimum around the *TT*–*TB* transition. This reveals a qualitative change due to the link between microscopic and macroscopic dynamics. This finding may be used to detect blood flow disorders linked to pathologies that affect erythrocyte's shape and mechanical properties and opens future perspectives on setting up new diagnostic tools, with high efficiency even at very low RBC concentration in the sample.

An important task for future research is to elucidate how pathological cells impact on rheology. This should open a new way toward setting up further diagnostic tools based on rheological measurements. Some pathological cells, for example, elliptocytes or spherocytes (see for ex. [96]) have larger reduced volume v, which can fall in the range from 0.7 up to 0.9 (to recall that for normocytes $v \approx 0.6$). Since the tumbling bifurcation significantly depends on the reduced volume v (or the excess area Δ) [26,89], the value of the viscosity ratio λ, at which the minimum of the intrinsic viscosity is found, should be shifted by a noticeable amount both in the horizontal and vertical directions. In addition, it is known that not only the shape but also the membrane mechanical properties could be altered due to a disorder of the cytoskeleton. A systematic investigation of the dynamics and rheology, and the link between micro and macro scales in pathological samples would therefore be relevant.

5. Concluding Remarks

The active research in the field of membrane biophysics, so far, led to a better understanding of the structural and functional membrane features playing major role in various processes with physiological relevance. The crucial interplay between the intrinsic bilayer properties and the physical phenomena, taking place in the membrane surroundings, has drawn the attention of theorists and experimentalists during the last decades.

In this chapter, we tried to present the potential of the shape fluctuation analysis of giant lipid vesicles as a powerful tool for the noninvasive determination of important membrane properties, such as its bending rigidity (at allowed and blocked intermonolayer exchange of molecules), the friction coefficient between the two monolayers, comprising the bilayer or the diffusion coefficient of a guest molecule in the lipid matrix. Modeling some basic characteristics of RBCs, giant lipid vesicles were shown to

recover qualitatively the basic rheological properties of RBC suspensions. Effective viscosity of suspensions exhibits minimum around the tank-treading-to-tumbling transition, thus making evident the relation between the structural dynamics at microscopic scale and the macroscopic properties of the suspension. These findings could be exploited in the conception of novel diagnostic tools for complementary detection of pathologies affecting the shape and/or rigidity of RBCs.

Despite the important progress achieved till now, numerous challenging questions remain to be answered from theoretical, as well as from experimental point of view. An example of them is the experimental investigation and the theoretical description of the behavior in hydrodynamic flows of vesicles with multicomponent membranes. The possible flow-induced lipid redistribution has to be taken into account as well as the new features in the vesicle shape dynamics, which would result from the complex membrane structure.

ACKNOWLEDGMENTS

We thank Prof. Isak Bivas and Assoc. Prof. Marin D. Mitov for their help with the thermal fluctuation analysis. We are grateful to Assoc. Prof. Hassan Chamati for the critical reading of the manuscript and to T. Podgorski and G. Coupier for enlightening discussions and experimental advice. Financial support from CNES (Centre National d'Etudes Spatiales) and ANR (MOSICOB project) is acknowledged. V. Vitkova was supported by grants from CNRS (Centre National de la Recherche Scientifique) and Université "Joseph Fourier" (Grenoble) and the National Science Fund (Bulgaria)—Grant HTC01-121.

REFERENCES

[1] B. Alberts, A. Johnson, J. Lewis, M. Raff, K. Roberts, P. Walter, Molecular Biology of the Cell, Carland, New York, 2002.
[2] E. Sackmann, H.P. Duwe, H. Engelhardt, Membrane bending elasticity and its role for shape fluctuations and shape transformations of cells and vesicles, Faraday Discuss. Chem. Soc. 81 (1986) 281–290.
[3] S. Singer, The molecular organization of membranes, Annu. Rev. Biochem. 43 (1974) 805–833; P.F. Devaux, M. Seigneuret, Specificity of lipid protein interactions as determined by spectroscopic techniques, Biochim. Biophys. Acta 822 (1985) 63–125; A.D. Dupuy, D.M. Engelman, Protein area occupancy at the center of the red blood cell membrane, Proc. Natl Acad. Sci. USA 105 (2008) 2848–2852.
[4] S.J. Singer, G.L. Nicolson, The fluid mosaic model of the structure of cell membrane, Science 175 (1972) 720–731.
[5] K. Jacobson, W.L.C. Vaz Test, Comments, Mol. Cell Biophys. 8 (1992) 17; E. London, How principles of domain formation in model membranes may explain ambiguities concerning lipid raft formation in cells, Biochim. Biophys. Acta 1746 (2005) 203–220.
[6] M. Edidin, The state of lipid rafts: from model membranes to cells, Annu. Rev. Biophys. Biomol. Struct. 32 (2003) 257–283.

[7] S.R. Shaikh, M.A. Edidin, Membranes are not just rafts, Chem. Phys. Lipids 144 (2006) 1–3.
[8] K. Simons, M.J. Gerl, Revitalizing membrane rafts: new tools and insights, Nat. Rev. Mol. Cell Biol. 11 (2010) 688–699.
[9] L.J. Pike, Rafts defined: a report on the Keystone symposium on lipid rafts and cell function, J. Lipid. Res. 47 (2006) 1597–1598.
[10] J.T. Groves, Bending mechanics and molecular organization in biological membranes, Ann. Rev. Phys. Chem. 58 (2007) 697–717.
[11] R. Lipowsky, E. Sackmann (Eds.), Structure and Dynamics of Membranes, Elsevier, Amsterdam, 1995.
[12] P.L. Luisi, P. Walde (Eds.), Giant Vesicles, John Wiley & Sons, Ltd., Chichester, 2000.
[13] R. Dimova, S. Aranda, N. Bezlyepkina, V. Nikolov, K.A. Riske, R. Lipowsky, A practical guide to giant vesicles: probing the membrane nanoregime via optical microscopy, J. Phys. Condens. Matter 18 (2006) S1151–S1176.
[14] L.A. Bagatolli, To see or not to see: lateral organization of biological membranes and fluorescence microscopy, Biochim. Biophys. Acta 1758 (2006) 1541–1556.
[15] P.F. Devaux, R. Morris, Transmembrane asymmetry and lateral domains in biological membranes, Traffic 5 (2004) 241–246.
[16] T. Pott, H. Bouvrais, P. Meleard, Giant unilamellar vesicle formation under physiologically relevant conditions, Chem. Phys. Lipids. 154 (2008) 115–119; P. Meleard, L.A. Bagatolli, T. Pott, Giant unilamellar vesicle electroformation: from lipid mixtures to native membranes under physiological conditions, Meth. Enzymol. 465 (2009) 161–176.
[17] N. Kahya, E.I. Pecheur, W.P. de Boeij, D.A. Wiersma, D. Hoekstra, Reconstitution of membrane proteins into giant unilamellar vesicles via peptide-induced fusion, Biophys. J. 81 (2001) 1464–1474; P. Girard, J. Pecreaux, G. Lenoir, P. Falson, J.L. Rigaud, P. Bassereau, A new method for the reconstitution of membrane proteins into giant unilamellar vesicles, Biophys. J. 87 (2004) 419–429; A. Varnier, F. Kermarrec, I. Blesneac, C. Moreau, L. Liguori, J.L. Lenormand, N. Picollet-D'hahan, A simple method for the reconstitution of membrane proteins into giant unilamellar vesicles, J. Membrane Biol. 233 (2010) 85–92.
[18] L.-R. Montes, A. Alonso, F.M. Goni, L.A. Bagatolli, Giant unilamellar vesicles electroformed from native membranes and organic lipid mixtures under physiological conditions, Biophys. J. 93 (2007) 3548–3554.
[19] M. Bloom, E. Evans, O.G. Mouritsen, Physical properties of the fluid lipid-bilayer component of cell membrane: a perspective, Quart. Rev. Biophys. 24 (1991) 293–397; T.M. Allen, P.R. Cullis, Drug delivery systems: entering the mainstream, Science 303 (2004) 1818–1822; G. Gregoriadis, Engineering liposomes for drug delivery, Trends Biotechnol. 13 (1995) 527–537; H. Harashima, H. Kiwada, Liposomal targeting and drug delivery: kinetic consideration, Adv. Drug Delivery Rev. 19 (1996) 425–444.
[20] U. Seifert, S.A. Langer, Viscous modes of fluid bilayer membranes, Europhys. Lett. 23 (1993) 71–76.
[21] I. Bivas, P. Meleard, I. Mircheva, P. Bothorel, Thermal shape fluctuations of a quasi spherical vesicle when the mutual displacements of its monolayers are taken into account, Coll. Surf. A Physicochem. Eng. Asp. 157 (1999) 21–33.
[22] I. Bivas, P. Meleard, Bending elasticity of a lipid bilayer containing an additive, Phys. Rev. E 67 (2003) 012901.
[23] I. Cantat, C. Misbah, Lift force and dynamical unbinding of adhering vesicles under shear flow, Phys. Rev. Lett. 83 (1999) 880–883.
[24] U. Seifert, Fluid membranes in hydrodynamic flow fields: formalism and an application to fluctuating quasispherical vesicles in shear flow, Eur. Phys. J. B 8 (1999) 405–415.

[25] T. Biben, C. Misbah, Tumbling of vesicles under shear flow within an advected-field approach, Phys. Rev. E 67 (2003) 031908; S.S. Vergeles, Rheological properties of a vesicle suspension, JETP 87 (2008) 511–515; K. Badr, A. Farutin, C. Misbah, Vesicles under simple shear flow: elucidating the role of relevant control parameters, Phys. Rev. E 80 (2009) 061905.
[26] J. Beaucourt, F. Rioual, T. Seon, T. Biben, C. Misbah, Steady to unsteady dynamics of a vesicle in a flow, Phys. Rev. E 69 (2004) 011906.
[27] M.-A. Mader, H. Ez-Zahraouy, C. Misbah, T. Podgorski, On coupling between the orientation and the shape of a vesicle under a shear flow, Eur. Phys. J. E 22 (2007) 275–280.
[28] C. Misbah, Vacillating breathing and tumbling of vesicles under shear flow, Phys. Rev. Lett. 96 (2006) 028104.
[29] P.M. Vlahovska, R. Gracia, Dynamics of a viscous vesicle in linear flows, Phys. Rev. E 75 (2007) 016313.
[30] V.V. Lebedev, K.S. Turitsyn, S.S. Vergeles, Nearly spherical vesicles in an external flow, New J. Phys. 10 (2008) 043044.
[31] K.S. Turitsyn, S.S. Vergeles, Wrinkling of vesicles during transient dynamics in elongational flow, Phys. Rev. Lett. 100 (2008) 028103.
[32] P.M. Vlahovska, T. Podgorski, C. Misbah, Vesicles and red blood cells in flow: from individual dynamics to rheology, C. R. Physique 10 (2009) 775–789.
[33] V. Kantsler, V. Steinberg, Orientation and dynamics of a vesicle in tank-treading motion in shear flow, Phys. Rev. Lett. 95 (2005) 258101.
[34] V. Vitkova, M. Mader, T. Biben, T. Podgorski, Tumbling of deformable lipid vesicles, enclosing a viscous fluid under a shear flow, J. Optoel. Adv. Mater. 7 (2005) 261–264.
[35] M.-A. Mader, V. Vitkova, M. Abkarian, A. Viallat, T. Podgorski, Dynamics of viscous vesicles in shear flow, Eur. Phys. J. E 19 (2006) 389–397.
[36] V. Kantsler, V. Steinberg, Transition to tumbling and two regimes of tumbling motion of a vesicle in shear flow, Phys. Rev. Lett. 96 (2006) 036001.
[37] V. Kantsler, E. Segre, V. Steinberg, Vesicle dynamics in time-dependent elongation flow: wrinkling instability, Phys. Rev. Lett. 99 (2007) 178102.
[38] M. Abkarian, A. Viallat, Vesicles and red blood cells in shear flow, Soft Matter 4 (2008) 653–657.
[39] J. Deschamps, V. Kantsler, V. Steinberg, Phase diagram of single vesicle dynamical states in shear flow, Phys. Rev. Lett. 102 (2009) 118105.
[40] G. Danker, C. Misbah, Rheology of a dilute suspension of vesicles, Phys. Rev. Lett. 98 (2007) 088104.
[41] G. Danker, T. Biben, T. Podgorski, C. Verdier, C. Misbah, Dynamics and rheology of a dilute suspension of vesicles: higher order theory, Phys. Rev. E 76 (2007) 041905.
[42] V. Vitkova, M. Mader, B. Polack, C. Misbah, T. Podgorski, Micro-macro link in rheology of erythrocyte and vesicle suspensions, Biophys. J. 95 (2008) L33–L35.
[43] W. Helfrich, Elastic properties of lipid bilayers: theory and possible experiments, Z. Naturforsch. 28c (1973) 693–703.
[44] W. Helfrich, Blocked lipid exchange in bilayers and its possible influence on the shape of vesicles, Z. Naturforsch. 29c (1974) 510–515.
[45] E. Evans, R. Skalak, Mechanics and Thermodynamics of Biomembranes, CRC Press, Boca Raton, Florida, 1980.
[46] V. Luzzati, A. Tardieu, Lipid phases: structure and structural transitions, Ann. Rev. Phys. Chem. 25 (1974) 79–94.
[47] I. Bivas, P. Hanusse, P. Bothorel, J. Lalanne, O. Aguerre-Chariol, An application of the optical microscopy to the determination of the curvature elastic modulus of biological and model membranes, J. Physique 48 (1987) 855–867.

[48] A. Yeung, E. Evans, Unexpected dynamics in shape fluctuations of bilayer vesicles, J. Phys. II 5 (1995) 1501.
[49] J.F. Faucon, M.D. Mitov, P. Meleard, I. Bivas, P. Bothorel, Bending elasticity and thermal fluctuations of lipid membranes. Theoretical and experimental requirements, J. Physique 50 (1989) 2389–2414.
[50] I. Bivas, L. Bivolarski, M.D. Mitov, A. Derzhanski, Correlations between the form fluctuation modes of flaccid quasispherical lipid vesicles and their role in the calculation of the curvature elastic modulus of the vesicle membrane. Numerical results, J. Physique II France 2 (1992) 1423–1438.
[51] E. Evans, W. Rawicz, Entropy-driven tension and bending elasticity in condensed-fluid membranes, Phys. Rev. Lett. 64 (1990) 2094–2097.
[52] F. Brochard, J.-F. Lennon, Frequency spectrum of the flicker phenomenon in erythrocytes, J. Physique 36 (1975) 1035–1047.
[53] W. Helfrich, Amphiphilic mesophases made of defects, in: R. Balian, M. Kleman (Eds.), Defects in Solids, North-Holland, Amsterdam, 1981, pp. 716–755.
[54] M.D. Mitov, Third and fourth order curvature elasticity of lipid bilayers, C. R. Acad. Bulg. Sci. 31 (1978) 513–517.
[55] W. Harbich, R.M. Servuss, W. Helfrich, Passages in lecithin–water systems, Z. Naturforsch. 33a (1978) 1013–1017.
[56] M.B. Schneider, J.T. Jenkins, W.W. Webb, Thermal fluctuations of large quasi spherical bimolecular phospholipid vesicles, J. Physique 45 (1984) 1457–1472.
[57] W. Helfrich, Size distributions of vesicles: the role of the effective rigidity of membranes, J. Physique (Paris) 47 (1986) 321–329.
[58] S.T. Milner, S.A. Safran, Dynamical fluctuations of droplet microemulsions and vesicles, Phys. Rev. A 36 (1987) 4371–4379.
[59] K. Fricke, K. Wirthensohn, R. Laxhuber, E. Sackmann, Flicker spectroscopy of erythrocytes: a sensitive method to study subtle changes of membrane bending stiffness, Eur. Biophys. J. 14 (1986) 67–81.
[60] P. Meleard, M.D. Mitov, J.F. Faucon, P. Bothorel, Dynamics of fluctuating vesicles, Europhys. Lett. 11 (1990) 355–360.
[61] M.D. Mitov, J.F. Faucon, P. Meleard, P. Bothorel, Thermal fluctuations of membranes, in: G.W. Gokel (Ed.), Advances in Supramolecular Chemistry, JAI Press, Greenwich, 1992, pp. 93–139.
[62] H. Engelhardt, H.-P. Duwe, E. Sackmann, Bilayer bending elasticity measured by Fourier analysis of thermally excited surface undulations of flaccid vesicles, J. Physique Lett. 46 (1985) L395–L400.
[63] P. Meleard, J.F. Faucon, M.D. Mitov, P. Bothorel, Dynamics of fluctuating vesicles, Europhys. Lett. 19 (1992) 267–271.
[64] M. Kraus, U. Seifert, Relaxation modes of an adhering bilayer membrane, J. Phys. II 4 (1994) 1117–1134.
[65] R. Merkel, E. Sackmann, E. Evans, Molecular friction and epitactic coupling between monolayers in supported bilayers, J. Phys. France 50 (1989) 1535–1555.
[66] I. Bivas, Shape fluctuations of nearly spherical lipid vesicles and emulsion droplets, Phys. Rev. E 81 (2010) 061911.
[67] H.P. Duwe, K. Zeman, E. Sackmann, Bending undulations of lipid bilayers and the red blood cell membrane: a comparative study, Progr. Colloid. Polym. Sci. 79 (1989) 6–10.
[68] J. Genova, V. Vitkova, L. Aladgem, M.D. Mitov, The stroboscopic illumination gives new opportunities and improves the precision of the bending elastic modulus measurement, J. Optoel. Adv. Mater. 7 (2005) 257–260.
[69] T. Pott, P. Meleard, Dynamics of vesicle thermal fluctuations is controlled by intermonolayer friction, Europhys. Lett. 59 (2002) 87–93.

[70] J. Genova, A. Zheliaskova, V. Vitkova, M.D. Mitov, Stroboscopic illumination study of the dynamics of fluctuating vesicles, J. Optoel. Adv. Mater. 11 (2009) 1222–1225.
[71] M. Angelova, D. Dimitrov, Liposome electroformation, Faraday Discuss. Chem. Soc. 81 (1986) 303–311.
[72] V. Vitkova, K. Antonova, G. Popkirov, M.D. Mitov, Y.A. Ermakov, I. Bivas, Electrical resistivity of the liquid phase of vesicular suspensions prepared by different methods, J. Phys. Conf. Ser. 253 (2010) 012059.
[73] R.P. Rand, V.A. Parsegian, Hydration forces between phospholipid bilayers, Biochim. Biophys. Acta 988 (1989) 351–376.
[74] S. Kessler, R. Finken, U. Seifert, Elastic capsules in shear flow: analytical solutions for constant and time-dependent shear rates, Eur. Phys. J. E 29 (2009) 399–413.
[75] N. Callens, C. Minetti, G. Coupier, M.-A. Mader, F. Dubois, C. Misbah, T. Podgorski, Hydrodynamic lift of vesicles under shear flow in microgravity, Europhys. Lett. 83 (2008) 24002; V. Vitkova, M. Mader, T. Podgorski, Deformation of vesicles flowing through capillaries, Europhys. Lett. 68 (2004) 398–404; G. Coupier, B. Kaoui, T. Podgorski, C. Misbah, Noninertial lateral migration of vesicles in bounded Poiseuille flow, Phys. Fluids 20 (2009) 111702; V. Vitkova, G. Coupier, M.-A. Mader, B. Kaoui, C. Misbah, T. Podgorski, Tumbling of viscous vesicles in a linear shear field near a wall, J. Optoel. Adv. Mater. 11 (2009) 1218–1221; V. Doyeux, T. Podgorski, S. Peponas, M. Ismail, G. Coupier, Spheres in the vicinity of a bifurcation, J. Fluid Mech. 674 (2011) 359–388.
[76] U. Seifert, Configurations of fluid membranes and vesicles, Adv. Phys. 46 (1997) 13–137.
[77] U. Seifert, K. Berndl, R. Lipowsky, Shape transformations of vesicles: phase diagram for spontaneous- curvature and bilayer-coupling models, Phys. Rev. A 44 (1991) 1182.
[78] P.D. Ross, A.P. Minton, Hard quasi-spherical model for the viscosity of hemoglobin solutions, Biochem. Biophys. Res. Commun. 76 (1977) 971–976; R. Tran-Son-Tay, S.P. Sutera, P.R. Rao, Determination of red blood cell membrane viscosity from theoscopic observations of tank-treading motion, Biophys. J. 46 (1984) 65–72.
[79] I. Cantat, C. Misbah, Dynamics and similarity laws for adhering vesicles in haptotaxis, Phys. Rev. Lett. 83 (1999) 235–238; B. Lorz, R. Simson, J. Nardi, E. Sakmann, Weakly adhering vesicles in shear flows: tank-treading and anomalous lift force, Europhys. Lett. 51 (2000) 468–474; M. Abkarian, C. Lartigue, A. Viallat, Tank-treading and unbiding of deformable vesicles in shear flow: determination of the lift force, Phys. Rev. Lett. 88 (2002) 068193.
[80] H. Noguchi, G. Gompper, Swinging and tumbling of fluid vesicles in shear flow, Phys. Rev. Lett. 98 (2007) 128103.
[81] M. Abkarian, M. Faivre, A. Viallat, Swinging of red blood cells under shear flow, Phys. Rev. Lett. 98 (2007) 188302.
[82] T. Biben, A. Farutin, C. Misbah, 3D vesicles under shear flow: numerical study of dynamics and phase diagram, Phys. Rev. E 83 (2011) 031921.
[83] J.M. Skotheim, T.W. Secomb, Red blood cells and other nonspherical capsules in shear flow: oscillatory dynamics and the tanktreading-to-tumbling transition, Phys. Rev. Lett. 98 (2007) 078301.
[84] J. Dupire, M. Abkarian, A. Viallat, Chaotic dynamics of red blood cells in a sinusoidal flow, Phys. Rev. Lett. 104 (2010) 168101.
[85] P. Vlahovska, Y.N. Young, G. Danker, C. Misbah, Dynamics of a non-spherical microcapsule with incompressible interface in a shear flow, J. Fluid Mech, (2011) in press.
[86] D. Barthes-Biesel, J.M. Rallison, The time-dependent deformation of a capsule freely suspended in a linear shear flow, J. Fluid Mech. 113 (1981) 251–267.

[87] G. Cox, The deformation of a drop in a general time-dependent fluid flow, J. Fluid Mech. 37 (1969) 601–623; N.A. Frankel, A. Acrivos, The constitutive equation for a dilute emulsion, J Fluid Mech. 44 (1970) 65–78.
[88] S.R. Keller, R. Skalak, Motion of a tank-reading ellipsoidal particle in shear flow, J. Fluid Mech. 120 (1982) 27–47.
[89] B. Kaoui, A. Farutin, C. Misbah, Vesicles under simple shear flow: elucidating the role of relevant control parameters, Phys. Rev. E 80 (2009) 061905.
[90] V.V. Lebedev, K.S. Turitsyn, S.S. Vergeles, Dynamics of nearly spherical vesicles in an external flow, Phys. Rev. Lett. 99 (2007) 218101.
[91] A. Farutin, T. Biben, C. Misbah, Analytical progress in the theory of vesicles under shear flow, Phys. Rev. E 81 (2010) 061904.
[92] N. Fa, C.M. Marques, E. Mendes, A.P. Schroder, Rheology of giant vesicles: a micropipette study, Phys. Rev. Lett. 92 (2004) 108103.
[93] R. Finken, A. Lamura, U. Seifert, G. Gompper, Two-dimensional fluctuating vesicles in linear shear flow, Eur. Phys. J. E 25 (2008) 309–321.
[94] H. Noguchi, G. Gompper, Dynamics of fluid vesicles in shear flow: effect of membrane viscosity and thermal fluctuations, Phys. Rev. E 72 (2005) 011901.
[95] V. Kantsler, E. Segre, V. Steinberg, Dynamics of interacting vesicles and rheology of vesicle suspension in shear flow, Europhys. Lett. 82 (2008) 58005.
[96] K. DeJong, S.K. Larkin, S. Eber, P.F.H. Franck, B. Roelofsen, F.A. Kuypers, Hereditary spherocytosis and elliptocytosis erythrocytes show a normal transbilayer phospholipid distribution, Blood 94 (1999) 319–325.

CHAPTER TEN

β-Carotene–Lipid Interactions in Liposomes with Different Lipid Composition

Antoaneta V. Popova[1,*] *and* Atanaska S. Andreeva[2]

Contents

Abstract

Carotenoids perform light harvesting, photoprotection, electron transfer, and structural role in photosynthetic membranes. To unravel the β-carotene contribution to the stability of membranes, liposomes with different lipid composition (resembling the photosynthetic membranes, containing mainly galactolipids with a high degree of unsaturation, and egg phosphatidylcholine) were used. The aim was to gain insight into the mechanism of β-carotene–lipid interactions with a special focus on the fluidity of the bilayer. Data from absorption, pyrene fluorescence, and resonance Raman spectroscopy revealed that the degree of lipids' unsaturation regulates the penetration of β-carotene molecules into the membrane, thus modifying the lipid–pigment interactions.

* Corresponding author. Tel.: +359-2-9793681; Fax: +359-2-9712493.
E-mail address: popova@bio21.bas.bg

[1] Institute of Biophysics and Biomedical Engineering, Bulgarian Academy of Sciences, Sofia, Bulgaria
[2] Department of Condensed Matter Physics, Faculty of Physics, Sofia University, Sofia, Bulgaria

Advances in Planar Lipid Bilayers and Liposomes, Volume 14
ISSN 1554-4516, DOI: 10.1016/B978-0-12-387720-8.00010-8

1. Introduction

Carotenoids are wide spread natural molecules, with over 600 structurally related compounds, both in plant and animal kingdom, which play multiple important physiological functions. From the spectroscopic and structural point of view the most typical feature of naturally occurring carotenoids is the long polyene chain with conjugated double bonds [1] that are responsible for the pigment properties of carotenoids, to absorb the electromagnetic radiation from the visual region. The double bond system constitutes a rod-like skeleton of the molecule that seems to play a key stabilization function of carotenoids, both in respect to lipid membranes and proteins [2].

In photosynthetic membranes, carotenoids perform different important functions as light harvesting, electron transfer, photoprotection, and structural role, stabilizing the membrane three-dimensional integrity [3–6]. They cover a spectral window lacking chlorophyll absorption (ca. 500 nm) [2,3] and play a protection role against high-light stress and reactive oxygen species, *via* quenching of electronic excited states of chlorophyll *a* molecules [5]. Carotenoids contribute also to the stability of the lipid molecules and preserve the three-dimensional integrity of bacterial and plant antenna complexes and the assembly of functional photosystem II under normal and potentially harmful environmental conditions [4,6].

The presence of carotenoids in the membrane influences, directly or indirectly, a vast range of physical and physiological processes. For investigation of the effects of various carotenoids on the membrane thermodynamic and mechanical properties, different model systems are used [7–10]. Carotenoids, being hydrophobic molecules, are predicted to be located within the hydrophobic core of the lipid bilayer. Their orientation within the membrane is dependent on the structure of the particular carotenoid and on the lipid composition of the host membrane. The orientational ordering of β-carotene, embedded in lamellar model lipid membranes and its effect on the membrane structural and dynamic properties have been investigated by variety of experimental methods: angle-resolved resonance Raman scattering, EPR, NMR, X-ray diffraction measurements, and computer simulation of molecular dynamics [7,9,11–13]. Localization of β-carotene, lacking polar groups in its molecule, in the lipid membrane environment is governed by van der Waals interactions with the hydrocarbon fatty chains of the lipids. The alterations in the angle-resolved Raman data have been used to monitor the phospholipid phase behavior in dipalmitoylphosphatidylcholine (DPPC) and distearoylphosphatidylcholine, one-component systems and binary mixtures [7]. The found orientational distribution functions have shown that β-carotene is oriented parallel to the bilayer plane (dioleoyl lecithin) or perpendicular to it

(soybean lecithin). For dimyristoyl lecithin, egg-lecithin, and digalactosyldiacylglycerol, two maxima have been found in the orientational distribution: one parallel and one perpendicular to the bilayer surface. In contrast, it has been shown that in carotenoid-egg phosphatidylcholine liposomes, β-carotene is randomly distributed in the hydrocarbon interior of the bilayer, without any preferred, well defined orientation and retains a substantial degree of mobility increasing motional freedom of both lipid headgroup and alkyl chains in liquid crystalline state [9]. EPR investigations have shown that β-carotene tends to fluidize the interior of phosphatidylcholine membranes and to decrease the penetration barrier to small molecules to the headgroup region [2,11]. X-ray diffraction measurements have confirmed that β-carotene disordered the packing of phospholipid acyl chains in a manner that correlated with its pro-oxidant actions [12]. The results obtained by a molecular dynamics simulation of the fully hydrated bilayer made of palmitoyl oleoyl phosphatidylcholine (POPC) and containing β-carotene molecules indicated that the β-carotene rings were located in the region occupied by the carbonyl groups of the lipids [13]. These results suggest two pools of the preferential orientation of β-carotene: a slightly bent structure corresponding to a small chain tilt angle and a rather stretched structure that corresponds to a higher chain tilt. All these data, contradictory to a certain extent, revealed that the orientation and conformation of β-carotene molecules in model membranes are strongly dependent on its lipid content.

Majority of investigations reporting on the effect of β-carotene on physical properties of model lipid membranes have been performed on phospholipid bilayers [2,7–11]. As β-carotene represents an important pigment component of the photosynthetic thylakoid membranes, where the photosynthetic processes take place, it was interesting to investigate its role on model membranes, resembling the lipid composition of photosynthetic membranes.

Thylakoid membranes of photosynthetic organisms contain various lipid species, the main being galactolipids, such as monogalactosyldiacylglycerol (MGDG), digalactosyldiacylglycerol (DGDG) and sulfoquinovosyldiacylglycerol (SQDG) [14,15]. MGDG comprises about half of the total thylakoid membrane lipid, the second most abundant lipid is DGDG which accounts to about 30% of the thylakoid lipids and SQDG that is found in a lower amount. The only phospholipid in the thylakoid membranes is phosphatidylglycerol (PG). MGDG and DGDG are neutral lipid molecules with a high degree of unsaturation of the fatty chains (predominantly 18:2 and 18:3). MGDG is a non-bilayer lipid forming hexagonal structures in aqueous medium. It has been shown that in native thylakoid membranes the non-bilayer lipids are arranged in a bilayer [16]. The other two components—PG and SQPG—are anionic lipids, providing negative charges to the thylakoid membrane [14,15].

The aim of the present work was to gain some insight into the mechanism of β-carotene–lipid interactions in liposomes with a special focus on the degree of unsaturation of the fatty chains. To investigate this effect, we used liposomes with lipid composition resembling that of photosynthetic thylakoid membranes, containing mainly galactolipids with a high degree of unsaturation of the fatty chains, and egg phosphatidylcholine liposomes. Absorption, pyrene fluorescence, and resonance Raman spectroscopy were applied to study the effect of β-carotene incorporation into the liposomes. The observed changes in β-carotene absorption and Raman spectra may be regarded as a result of the lipid–pigment interactions leading to a polyene geometry distortion, different in distinct lipid environment.

2. Materials and Methods

2.1. Materials

β-carotene, Tris-hydroxymethylaminomethane (TRIS), POPG, and pyrene were obtained from Sigma, EPC—from Avanti Polar Lipids. The chloroplast glycolipids SQDG, MGDG, and DGDG were purchased from Lipid Products (Redhill, Surrey, UK) and used as obtained.

2.2. Liposome Formation

The pigment was added to the lipids, before formation of liposomes, from a stock solution in chloroform to obtain following concentrations: 0.05, 1, 2, 3, 4, and 5 mol%. Concentrations of applied β-carotene were calculated as mol% in respect to the lipid concentration. Lipids equivalent to 1 mM (0.75 mg/ml) dissolved in chloroform, pure or mixed with different mol% β-carotene (1 mM in chloroform), were dried from the solvent under a gentle steam of N_2 to obtain a thin lipid layer on the bottom of a glass test tube. Thylakoid mix (TM) lipids were prepared as described in [17], 40% MGDG, 30% DGDG, 15% SQDG, and 15% POPG, on a weight base. Final traces of solvent were removed form the lipid film under deep vacuum over night followed by hydration with 50 mM TRIS buffer (*p*H 7.4). Small liposomes were formed by sonication for 40 s using ultrasound generator system. The residual, not integrated into liposomes β-carotene, was removed by two steps centrifugation at 15,000×g. Supernatant contained the β-carotene-doped TM or EPC liposomes and used for all experiments.

2.3. Determination of β-Carotene Concentration

The amount of β-carotene integrated into liposomes was determined by extraction of the pigment from the vesicles by ethanol and absorbance spectra were recorded on Specord 210 Plus in the spectral region

350–600 nm. Concentration of incorporated β-carotene was evaluated using molar extinction coefficient of β-carotene in ethanol at 453 nm, 141×10^3 M^{-1} cm^{-1} [18]. The results were used to determine the β-carotene incorporation yield (IY) as the ratio between the concentrations of integrated and applied β-carotene [19].

2.4. Steady-State Fluorescence Measurements

The fluorescent probe pyrene was added to TM and EPC liposomes, without and doped with different concentrations of β-carotene, at concentration 4 mol% in respect to lipids from a stock ethanol solution [19]. Care was taken the amount of added ethanol not to exceed 0.5%. Liposome–pyrene mixture was incubated at room temperature for 30 min and pyrene fluorescence was recorded with a Jobin-Ivon spectrofluorimeter. Fluorescence was excited at 332 nm and registered in the region 350–550 nm. Slit widths were 4 nm. After subtraction of the dark level, total fluorescence intensity (I) was determined as the total fluorescence area under the fluorescent contour. Pyrene, being apolar molecule, is completely buried within the hydrophobic region of the membrane [20]. Pyrene forms excimers (E) from monomers (M) by a diffusion-controlled process in fluid membranes that is directly related to membrane fluidity. In a monomeric form, pyrene gives a rise to a fluorescent peak at 393 nm (F393) and a broad one at 470 nm, emitted by the excimers (F470) [20].

2.5. Resonance Raman Spectra Measurements

Room temperature resonance Raman (RR) spectra were measured using a microRaman spectrometer (Jobin-Ivon, HR 800) with a grating 1800 g/mm. The excitation was provided by an argon ion laser (Innova 307, Coherent) at 514.5 nm. The laser intensity was 4 mW; the spectral resolution was 0.5 cm^{-1}.

All experiments were performed at room temperature, well above the phase transition of lipids.

3. Results

In Fig. 1, the chemical structures of the predominant lipid class of EPC (64% POPC)[A], of thylakoid mix lipids (MGDG) [B], and of β-carotene [C] are presented. DGDG and SQDG contain in the headgroup two or one galactose residue, respectively. Both galactolipids, MGDG and DGDG, contain highly unsaturated fatty chains, three double bonds per chain, which

determines the high degree of fluidity of the hydrophobic interior of the membrane [14]. The relative length of presented molecules is comparable.

Small liposomes were formed by sonication [17] without or in the presence of different concentrations of β-carotene. In Fig. 2A, the

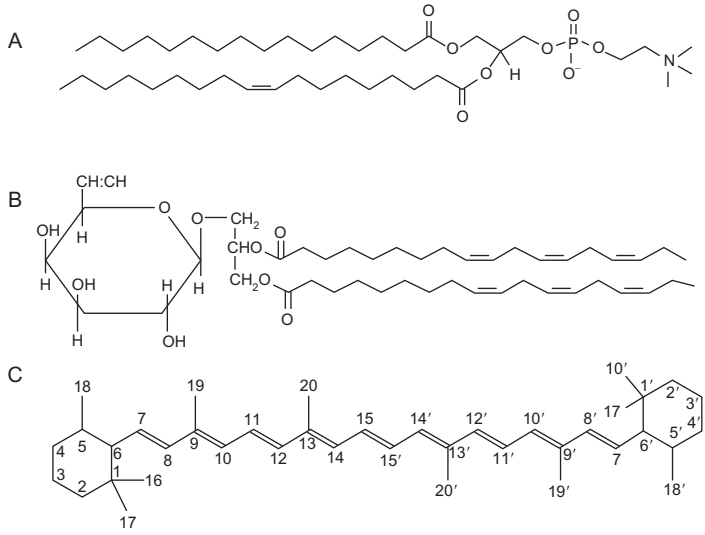

Figure 1 Chemical structure of predominant lipid species of EPC—POPC (A), of thylakoid mixture—MGDG (B), and of β-carotene (C).

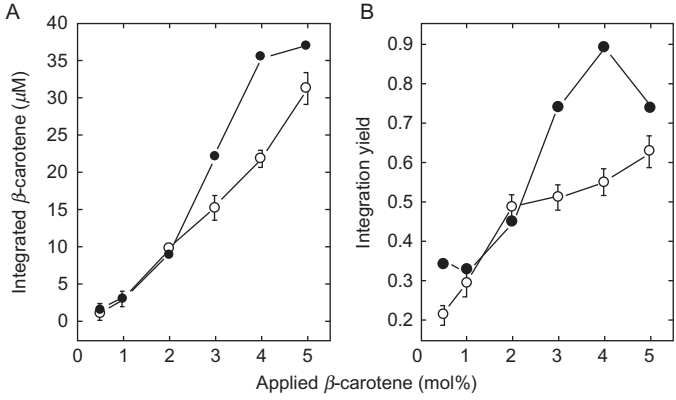

Figure 2 Concentration of β-carotene, integrated into small liposomes, EPC (-○-) or thylakoid mix ones (TM) (-●-) as a function of concentration of applied β-carotene (A). Integration yield of β-carotene into EPC (-○-) or into TM liposomes (-●-), determined as the ratio integrated/applied β-carotene (B). Mean values are determined from at least three independent experiments. Where SD bars are not seen, they are smaller than the value points.

calculated concentrations of integrated β-carotene in both types of liposomes as dependent on the concentration of applied pigment are presented. As expected, more β-carotene was integrated into liposomes with increase of concentration of applied pigment. For EPC liposomes, this dependence was nearly linear. For TM liposomes, integration of β-carotene at higher concentrations of applied pigment was higher than in EPC liposomes. The values of integrated and applied β-carotene concentrations were used to calculate the integration yield of the pigment (IY) (Fig. 2B). The obtained data for EPC liposomes were in a good agreement with the values obtained for IY of β-carotene in DPPC liposomes [21].

In Fig. 3, the absorbance spectra of β-carotene, extracted from EPC liposomes by ethanol, and the spectra of both investigated liposomes, dissolved in buffer and containing the highest concentration of integrated β-carotene, are shown. The spectra of ethanol extracts show a typical carotene contour, with two maxima, at 453 and 476 nm and a shoulder at 430 nm (Fig. 3, spectrum 1). The three spectra were normalized at 453 nm (0–1 transition).

In the spectra of EPC and TM liposomes, dissolved in buffer, three peaks were resolved, at 453, 480, and 518 nm. The shoulder at 430 nm (0–2 transition) was less expressed than in the ethanol extract of β-carotene. The peak at 480 nm (0–0 transition) in EPC and TM liposomes was higher than in the ethanol extract and its height was comparable with that at 453 nm.

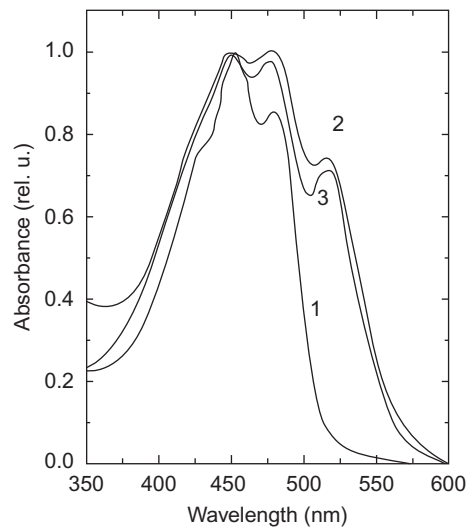

Figure 3 Absorbance spectra of β-carotene, extracted from liposomes by ethanol (1) and integrated into liposomes (EPC—2, TM—3), dissolved in TRIS buffer. Spectra are normalized to the intensity at 453 nm.

The most interesting difference in the spectra of ethanol extract and of liposomes, containing β-carotene, was the additional absorbance peak at 518 nm. Nevertheless that β-carotene was integrated into different liposomes and with different efficiency the resulting spectra were very similar. Here, we present only the spectra of liposomes with the highest concentration of integrated β-carotene because for the lower concentrations the shapes of the spectra were identical in respect to height and position of the peaks (data not shown).

The fluorescent probe pyrene is often used for determining membrane fluidity. Pyrene is an apolar molecule, composed of four fused benzol rings, completely buried into the hydrophobic interior of lipid membranes and forms excimers from monomers in fluid membranes by a diffusion controlled process [20]. The excimer formation is determined by the ratio of the excimer to monomer fluorescence quantum yield (E/M). In Fig. 4, the fluorescent spectra of EPC and TM liposomes, without and containing different concentrations of β-carotene, are presented. With increase of concentration of integrated β-carotene, the overall pyrene fluorescence for both types of liposomes was quenched. In Fig. 5, the total areas under the pyrene fluorescent spectra of EPC and TM liposomes containing increasing concentrations of β-carotene as a measure of the degree of quenching are presented. The observed decrease supposed that the pyrene fluorescence was quenched by β-carotene, due to an effective energy transfer from pyrene excimers to β-carotene since the excimer fluorescence

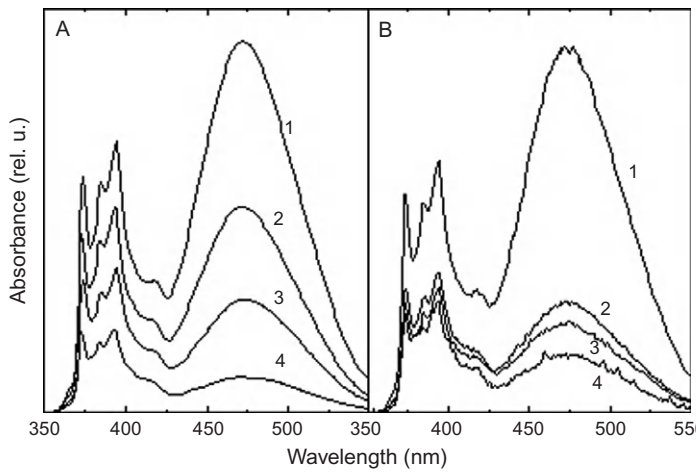

Figure 4 Fluorescence spectra of pyrene, integrated into EPC (A) or TM (B) liposomes, pure (1) and doped with different concentrations of β-carotene; concentration of applied β-carotene 3 μM (2), 9 μM (3) and 35 μM (4). Fluorescence was excited at 332 nm, slits—4 nm.

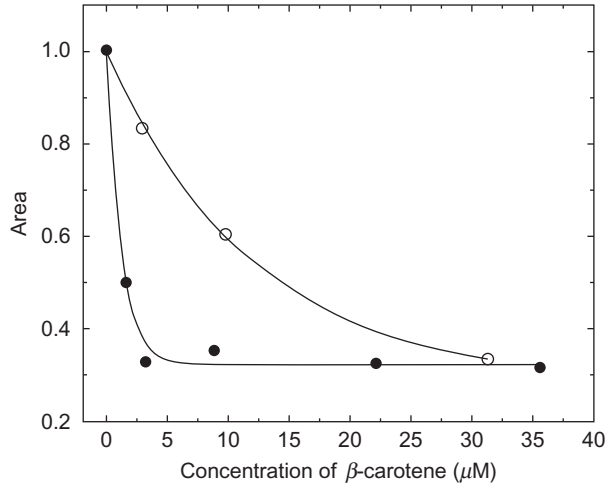

Figure 5 Area under the fluorescent spectra of pyrene in EPC (-○-) or TM (-●-) liposomes, without and containing different concentrations of β-carotene, in respect to concentration of integrated pigment. Area under the fluorescent spectra of pyrene in pure liposomes was taken as 1.

spectrum overlaps the carotene absorption. The quenching of pyrene fluorescence indicated that the pigment molecules were localized in the hydrophobic environment of the bilayer, in the vicinity of pyrene molecules, and the distance between them is estimated to be not higher than 7 Å in order the supposed energy transfer to take place. The more effective quenching for TM liposomes could be due to the higher motional freedom of the fatty chains of lipids that allows deeper penetration of β-carotene in the lipid bilayer and closer contact with the hydrophobic molecule of pyrene.

In an attempt to get more detailed information about β-carotene–lipid interactions in EPC and TM liposomes, we compared their RR spectra, excited at 514.5 nm, to the spectrum of β-carotene dissolved in pyridine. The comparison is presented in Fig. 6. Pyridine was chosen as a solvent as its refractive index ($n = 1.5092$) is close to that of membrane lipids. The excitation wavelength was near to the observed additional absorbance peak of β-carotene integrated into both types of liposomes (Fig. 3). The RR spectra manifest the characteristic for carotenoids' four main frequency bands in Raman spectrum (called from ν_1 to ν_4). The main bands have been assigned as follows: ν_1 to in-phase stretching vibrations of the C=C bonds, ν_2 to C–C stretching coupled to C_{15}–H in-plane (ip) bending, ν_3 to methyl CH_3 ip rocking vibrations, and ν_4 (around 960 cm^{-1}) have been attributed either to the out-of-plane wagging motions of the C–H groups of the carotenoid molecules and/or to the C–CH_3 stretching [22–25]. Differences are mainly observed in the region of ν_4 and ν_2 bands.

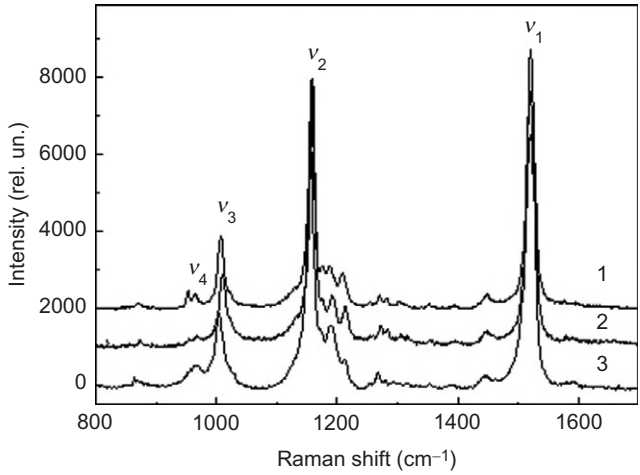

Figure 6 Characteristic resonance Raman spectra of β-carotene integrated into EPC (1), TM (2) liposomes and dissolved in pyridine (3) at room temperature excited at 514.5 nm. Spectra are up shifted for better visualization. Concentrations of β-carotene were 25, 24, and 100 μM, respectively.

In the region of ν_2 band (Fig. 6), we observed characteristic frequencies at 1175, 1190, and 1210 cm^{-1}. Their structure in the liposomes differed from that one in solution (pyridine). The 1175 cm^{-1} line could be assigned to methyl rocking at C_{18}. The other two lines have been attributed to localized stretching modes: 1190 cm^{-1} at C_8–C_9 and 1210 cm^{-1} at C_{12}–C_{13}, combined with C_{15}=$C_{15'}$, according to the recently published theoretical results for β-carotene Raman-active modes [26]. The relative intensity of the band at around 1210 cm^{-1} increased in both kinds of liposomes correlating with the changes in ν_4 band.

Structured ν_4 bands, indicative of out-of-plane distortions of conjugated backbone of the β-carotene molecule, were observed in both EPC and TM liposomes with incorporated β-carotene. They exhibited two transitions at 954 and 965 cm^{-1} becoming particularly clear from Fig. 7, where the bands were normalized to the intensity of the band at 965 cm^{-1} and compared to the unstructured band of β-carotene, dissolved in pyridine. Based on the normal coordinate analysis made for β-carotene by Saito and Tasumi [27], the mode around 950 cm^{-1} has been assigned to the torsion at C_7=C_8, whereas the mode at 965 cm^{-1} to the torsion at C_{11}=$C_{12'}$. These Raman-active modes have been recently predicted also by Tschirner *et al.* [26], at 974 and 982 cm^{-1} with low intensities, arising from methyl rocking $C_{16'}$ and CH out-of-plane wagging around C_{11}=C_{12}, but observed at 957 and 967 cm^{-1} [26].

The intensity of the band located at 954 cm^{-1} changed weakly with the pigment concentration in EPC liposomes (Fig. 7A), remaining lower than that at 965 cm^{-1}. In contrast, in TM liposomes, the 954 cm^{-1} intensity

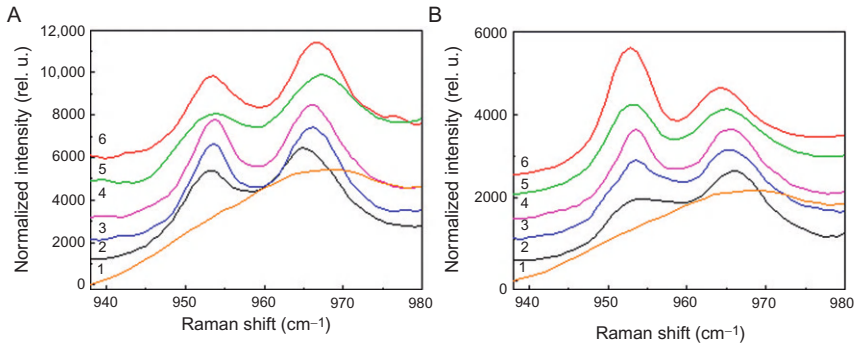

Figure 7 Resonance Raman ν_4 band of spectra of β-carotene integrated with different concentration into EPC (A) and TM (B) liposomes at room temperature excited at 514.5 nm. Spectra are up shifted for better visualization. Numbers next to the spectra correspond to the following concentration: 1–100 μM β-carotene in pyridine; in EPC liposomes: 2–3, 3–10, 4–15, 5–25, 6–31 μM and in TM liposomes: 2–3, 3–9, 4–12, 5–24, 6–38 μM.

increased gradually with the pigment concentration and became twice higher than that at 965 cm^{-1} at concentration 38 μM (Fig. 7B) indicating that the polyene geometry at $C_7=C_8$ was distorted stronger in TM liposomes with integrated higher concentration of the pigment. Thus, based on the observed different concentration, dependences of the intensity of these two modes in both EPC and TM liposomes, we can suppose that the out-of-plane distortions of conjugated backbones of the β-carotene molecules were different in respect to the type of liposomes.

4. Discussion

In order to study the β-carotene–lipid interactions in photosynthetic thylakoid membranes, we used liposomes, composed of lipids mimicking the lipid composition of plant chloroplast membranes, which are characterized with a high degree of unsaturation of their fatty chains. The alterations in absorption, pyrene fluorescence, and resonance Raman spectra, induced by β-carotene incorporation into TM and EPC liposomes, were compared to determine the role of lipid unsaturation for these interactions. When integrated into model membranes β-carotene can adopt various orientations, depending on the type of host lipids [7,9,11–13].

In majority of published data on the effect of carotenoids on the physicochemical properties of model membranes, only the concentration of the applied carotenoids is taken into account. It is uncertain how much of β-carotene molecules added to the sample during preparation can be

dissolved in the lipid bilayer in the form of monomers. Because of these solubility problems and uncertainties, the carotenoid concentration is discussed as the amount added to the sample during preparation of liposomes and not as the amount dissolved in the lipid bilayer [9,11–13,28]. To the best of our knowledge, there are only two reports on degree of incorporation of various carotenoids in different model membranes, phosphatidylcholine vesicles, finding high incorporation rate for xanthophylls and low incorporation for β-carotene [21,29]. In this study, we estimate the amount of integrated β-carotene into two different types of liposomes, composed of egg phosphatidylcholine and of lipids, found in photosynthetic thylakoid membranes. The results indicated that the integration rate of β-carotene was dependent on the fluidity of the hydrophobic interior of the bilayer. As expected, the amount of β-carotene integrated into TM liposomes was higher than in EPC ones, especially for high concentration of applied pigment (Fig. 2) due to the higher fluidity of the hydrophobic interior of TM liposomes. All presented results were given as a function of the real concentration of β-carotene, integrated into liposomes.

The higher degree of motional freedom of the hydrophobic interior of TM liposomes determined not only the higher concentration of integrated β-carotene but probably the molecules of the pigment were inserted deeper in the bilayer as evidenced by the accelerated quenching of pyrene fluorescence (Fig. 5). This quenching was realized by an effective energy transfer from the pyrene excimers to β-carotene molecules, situated in a close proximity, as the maxima of excimers' fluorescence emission and the β-carotene absorption overlap (see Figs. 3 and 4).

In the absorbance spectra of the two types of liposomes, containing β-carotene, we observed an additional peak at higher wavelengths, 518 nm (Fig. 3). We consider that this peak should be rather due to lipid/pigment interactions than to a possible formation of J-aggregates, characterized by a new absorption band at 530 nm [30,31]. The arguments in favor of this conclusion were the following. One of the key factors controlling the formation of interval J-aggregates has been shown to be the high initial concentration (100 μM), allowing the excitonic interactions between carotenoid molecules [30]. All used concentrations in this work were well below these values to induce aggregation. Another argument was the inverse correlation between the position of the absorption maximum of the aggregation band with the catotenoid's polarity, found by Ruban *et al.* [31]. Since the polar molecules of zeaxanthin had an aggregation maximum at 534 nm, the expected aggregation band for apolar β-carotene should be at higher wavelengths. The observed position of the additional absorption band in liposomes at 518 nm shows that the assignment of this peak to the formation of β-carotene aggregates is not feasible. So, we can attribute this band to lipid/pigment interactions.

Resonance Raman spectroscopy is a nondestructive method providing precise information on the type and conformation of carotenoid molecules

[22–25]. All presented resonance Raman spectra, excited by a narrow laser line coinciding with a new carotenoid absorption band, 514.5 nm, we assigned to the all-*trans* β-carotene. The following two reasons support this assignment. Firstly, we did not observe an upshift of the ν_1 band induced generally by *cis* isomerization [24,25,32]. Secondly, our experimental data (Fig. 6) showed a relatively very weak intensity around 1134 cm^{-1} in the so-called *cis*-isomerization fingerprint region ν_2 (1100–1300 cm^{-1}) [24,32]. It led us to the conclusion that the presence of other geometrical conformers in liposomes is not likely.

The structured ν_4 bands [22,25,27], observed in both types of liposomes containing β-carotene, indicated that the pigment incorporation led to out-of-plane distortions of conjugated backbone of the β-carotene molecules. Moreover, the degree of lipids' unsaturation exhibited pronounced difference in their effect on the molecular planar structure of all-*trans* β-carotene molecules during their integration. Induced stronger deformation of the carotenoid molecular geometry in the fluid environment of TM liposomes can be due to the deeper and easier insertion of pigment molecules between TM lipids as compared to the EPC ones. The more effective quenching of pyrene fluorescence in TM liposomes supported this notion. The deeper insertion should lead to the exhibited stronger distortion of carbon backbone of pigment molecules at $C_7{=}C_8$ in TM liposomes. The different penetration deepness of β-carotene molecules in liposomes suggested that the molecule orientation could be in different directions: parallel or perpendicular to the bilayer surface as it was concluded for dimyristoyl lecithin, egg-lecithin, and digalactosyldiacylglycerol liposomes [7]. The two different orientations into the bilayer could impose the distinct extent of the deviation from the planarity of β-carotene molecules at two different places in the conjugated backbone generating the two Raman-active modes at 954 and 965 cm^{-1} (Fig. 7). The perpendicularly orientated molecules to the membrane surface (being parallel to the lipid alkyl chains) are subjected to a slighter deformation than those, oriented parallel to the surface in the interior of the bilayer. These considerations are in accordance with the suggested two distinct deformations of β-carotene molecules, resulted from a molecular dynamics simulation of the fully hydrated bilayer composed of POPC [13].

In conclusion, our data imply that the degree of lipids' unsaturation regulate the penetration deepness of β-carotene molecules in liposomes thus modifying the lipid–pigment interactions leading to the polyene geometry distortion, different in distinct lipid environment.

ACKNOWLEDGMENTS

All lipids were a generous gift from Dr. D.K. Hincha, Max-Plant Institute for Molecular Plant Physiology, Golm, Germany. This work was supported by the Operational Program

"Human Resources Development" (BG 051PO001-3.3.04/42) co-financed by the European Social Fund of the European Union and by Grants: No. DO02-167-2008 from the National Science Fund of the Ministry of Education and Science of Bulgaria and No. 036-2011 from the Scientific Research Foundation at Sofia University, Bulgaria.

REFERENCES

[1] P.D. Fraser, P.M. Bramley, The biosynthesis and nutritional uses of carotenoids, Prog. Lipid Res. 43 (2004) 228–265.
[2] W.I. Gruszecki, K. Strzalka, Carotenoids as modulators of lipid membrane physical properties, Biochim. Biophys. Acta 1740 (2005) 108–115.
[3] I. Yruela, R. Tomas, M.L. Sanjuan, E. Torrado, M. Aured, R. Picorel, The configuration of β-carotene in the photosystem II reaction center, Photochem. Photobiol. 68 (1998) 729–737.
[4] A.A. Moskalenko, N.V. Karapetyan, Structural role of carotenoids in photosynthetic membranes, Z. Naturforsch. 51c (1996) 763–771.
[5] K.K. Nyogi, Photoprotection revisited: genetic and molecular approaches, Annu. Rev. Plant Physiol. Plant Mol. Biol. 50 (1999) 333–359.
[6] M. Havaux, Carotenoids as membrane stabilizers in chloroplasts, Trends Plant Sci. 30 (1998) 147–151.
[7] M. van de Ven, M. Katrenberg, G. Van Ginkel, Y.K. Levine, Study of the orientational ordering of carotenoids in lipid bilayers by resonance-Raman spectroscopy, Biophys. J. 45 (1984) 1203–1210.
[8] R. Mendelsohn, R.W. Van Holten, Zeaxanthin [(3R,3′R)-β,β-carotene-3-3′-diol] as a resonance Raman and visible absorption probe of membrane structure, Biophys. J. 27 (1979) 221–236.
[9] J. Gabrielska, W.I. Gruszecki, Zeaxanthin (dihydroxy-β-carotene) but not β-carotene rigidifies lipid membranes: a ^{1} H-NMR study of carotenoid-egg phosphatidylcholine liposomes, Biochim. Biophys. Acta 1285 (1996) 167–174.
[10] A. Andreeva, A. Popova, Integration of β-carotene molecules in small liposomes, J. Phys. Conference series 253 (2010) 012066.
[11] K. Strzalka, W.I. Gruszecki, Effect of beta-carotene on structural and dynamic properties of model phosphatidylcholine membranes: I. An EPR spin label study, Biochim. Biophys. Acta 1194 (1994) 138–142.
[12] H.P. McNulty, J. Byun, S.F. Lockwood, R.F. Jacob, R.P. Mason, Differential effects of carotenoids on lipid peroxidation due to membrane interactions: X-ray diffraction analysis, Biochim. Biophys. Acta 1768 (2007) 167–174.
[13] M. Jemiola-Rzeminska, M. Pasenkiewicz-Gierula, K. Strzalka, The behaviors of beta-carotene in the phosphatidylcholine bilayer as revealed by a molecular simulation study, Chem. Phys. Lipids 135 (2005) 27–37.
[14] P.J. Quinn, W.P. Williams, The structural role of lipids in photosynthetic membranes, Biochim. Biophys. Acta 737 (1983) 223–266.
[15] M.S. Webb, B.R. Green, Biochemical and biophysical properties of thylakoid acyl lipids, Biochim. Biophys. Acta 1060 (1991) 133–158.
[16] G. Garab, K. Lohner, P. Laggner, T. Farkas, Self-regulation of the lipid content of membranes by non-bilayer lipids, Trends Plant Sci. 5 (2000) 489–494.
[17] D.K. Hincha, Effects of α-tocopherol (vitamin E) on the stability and lipid dynamics of model membranes mimicking the lipid composition of plant chloroplast membranes, FEBS Lett. 582 (2008) 3687–3692.
[18] http://epic.awi.de/publications/jef1997f.pdf.

[19] C. Socaciu, C. Lausch, H.A. Diehl, Carotenoids in DPPC vesicles: membrane dynamics, Spectrochim. Acta A 55 (1999) 2289–2297.
[20] H.J. Galla, E. Sackmann, Lateral diffusion in the hydrophobic region of membranes: use of pyrene excimers as optical probes, Biochim. Biophys. Acta 339 (1974) 103–115.
[21] C. Socaciu, R. Jessel, H.A. Diehl, Competitive carotenoid and cholesterol incorporation into liposomes: effect on membrane phase transition, fluidity, polarity and anisotropy, Chem. Phys. Lipids 106 (2000) 79–88.
[22] B. Robert, Resonance Raman spectroscopy, Photosynth. Res. 101 (2009) 147–155.
[23] J.C. Merilin, Resonance Raman spectroscopy of carotenoids and carotenoid-containing systems, Pure Appl. Chem. 57 (1985) 785–792.
[24] Y. Koyama, R. Fujii, *Cis–Trans* carotenoids in photosynthesis: configurations, excited-state properties and physiological functions, in: H. Frank, A. Young, G. Britton, R. Cogdell (Eds.), The Photochemistry of Carotenoids, Kluwer, Dordrecht, 1999, pp. 161–188.
[25] B. Robert, The electronic structure, stereochemistry and resonance Raman spectroscopy of carotenoids, in: H. Frank, A. Young, G. Britton, R. Cogdell (Eds.), The Photochemistry of Carotenoids, Kluwer, Dordrecht, 1999, pp. 189–201.
[26] N. Tschirner, M. Schenderlein, K. Brose, E. Schloedder, M.A. Mroginski, C. Thomsen, P. Hildebrandt, Resonance Raman spectra of β-carotene in solution and in photosystems revisited: an experimental and theoretical study, Phys. Chem. Chem. Phys. 11 (2009) 11471–11478.
[27] S. Saito, M. Tasumi, Normal coordinate analysis of β-carotene isomers and assignments of the Raman and infrared bands, J. Raman Spectrosc. 14 (1983) 310–321.
[28] A. Wisniewska, J. Widomska, W.K. Subczynski, Carotenoid–membrane interactions in liposomes: effect of dipolar, monopolar, and nonpolar carotenoids, Acta Biochim. Polonica 53(3) (2006) 475–484.
[29] C. Socaciu, P. Bojarski, L. Aberle, H.A. Diehl, Different ways to insert carotenoids into liposomes affect structure and dynamics of the bilayer differently, Biophys. Chem. 99 (2002) 1–15.
[30] H.H. Billsten, V. Sundstrom, T. Polivka, Self-assembled aggregates of the carotenoid xeaxanthin: time resolved study of excited states, J. Phys. Chem. A 109 (2005) 1521–1529.
[31] A.V. Ruban, P. Horton, A.J. Young, Aggregation of higher plant xanthophylls: differences in absorption spectra and in the dependency on solvent polarity, J. Photochem. Photobiol. B: Biol. 21 (1993) 229–234.
[32] Y. Koyama, I. Takatsuka, M. Nakata, M. Tasumi, Raman and infrared spectra of the all-*trans*, 7-*cis*, 9-*cis*, 13-*cis* and 15-*cis* isomers of β-carotene: key bands distinguishing stretched or terminal-bent configurations form central-bent configurations, J. Raman Spectrosc. 19 (1988) 37–49.

Subject Index